Heat and electron conduction in microporous catalyst layers of polymer electrolyte membrane fuel cells

by

Mohammad Ahadi

M.Sc., Amirkabir University of Technology (Tehran Polytechnic), 2011
B.Sc., Isfahan University of Technology, 2009

Thesis Submitted in Partial Fulfillment of the
Requirements for the Degree of
Doctor of Philosophy

in the
School of Mechatronic Systems Engineering
Faculty of Applied Sciences

SIMON FRASER UNIVERSITY
Fall 2018

Approval

Name:	**Mohammad Ahadi**
Degree:	**Doctor of Philosophy**
Title:	**Heat and electron conduction in microporous catalyst layers of polymer electrolyte membrane fuel cells**
Examining Committee:	**Chair: Amr Marzouk** Lecturer
	Majid Bahrami Senior Supervisor Professor
	Michael Eikerling Supervisor Professor
	Byron Gates Supervisor Associate Professor
	Woo Soo Kim Internal Examiner Associate Professor
	Jon Pharoah External Examiner Professor Mechanical and Materials Engineering Queen's University
Date Defended/Approved:	November 28th, 2018

Abstract

Recent movement toward zero-emission mobility has propelled significant technological advancements in commercialization of polymer electrolyte membrane fuel cells (PEMFCs). PEMFCs provide electricity by reacting hydrogen with oxygen through two half-reactions occurring inside two respective anodic/cathodic microporous catalyst layers (CLs) with thicknesses of ~2-8 μm. Other products of the overall reaction include water and waste heat. All the electricity generation/consumption and most of the heat generation modes occur inside the CLs through a set of highly coupled multi-physics phenomena (a coupling between the electrochemical reactions, transport of species, electron conduction, and heat conduction). This necessitates knowing thermal and electronic conductivities of CLs for optimizing the fuel cell performance in various operating conditions.

In this thesis, novel procedures are developed to measure thermal and electronic conductivities of CLs at low error rates. The procedures are based on novel methods to increase the amount of catalyst in the testbeds for enhancing the signal to noise ratio while ensuring complete deconvolution of the CL bulk signal. Further, a comprehensive platform is developed to characterize microstructure of CLs from various aspects, including a complete scheme for characterizing cracks for the first time. Separate measurements of in-plane and through-plane electronic conductivities, for the first time, uncovers anisotropic microstructure of CLs. CL designs with various compositions and structures are made and characterized. Observed trends in the conductivity data are linked to various structural properties of the CLs to understand structure-property correlations. A complete set of closed-form multi-scale structural models are developed for the conductivities in different directions to understand the underlying physics and provide tools for development of CLs with desired conductivities. The developed models agree well with the experimental data and precisely predict the structural trends. The models also explain and predict effects of different operating conditions. Using the developed tools, design guidelines are proposed for fabricating CLs with desired thermal and electronic conductivities, whose proof of concepts were made and successfully tested in the experimental phase of this research. Order of magnitude analyses show significant potentials for enhancing the fuel cell performance by tuning the conductivities through engineering the microstructure.

Keywords: Fuel cell; catalyst layer; thermal conductivity; electronic conductivity; microstructure; structure-property correlations

To my love Negar and my dear parents and brothers for their support and encouragement

Acknowledgements

I would like to express my deep gratitude towards the many great people who made accomplishing this dissertation possible and enjoyable for me. My especial thanks go to my senior supervisor at Simon Fraser University (SFU), Dr Majid Bahrami, for his great support and guidance throughout my PhD studies, as well as my colleagues and friends at Automotive Fuel Cell Cooperation Corp. (AFCC), who accepted me, shared a vision with me, trained me, and guided me throughout my PhD studies and even beyond. I am especially grateful to Jürgen Stumper, Mickey Tam, Jasna Jankovic, Andreas Putz, Dorina Manolescu, Madhu S. Saha, Darija Susac, Helen Zhu, Beniamin Zahiri, and Keping Wang, who gave me their full support throughout all phases of the project, from essential trainings and technical support at AFCC to providing me with their expert knowledge and guidance at countless formal and informal meetings throughout the five years of the project.

I gratefully acknowledge the financial support received from the Natural Sciences and Engineering Research Council of Canada (NSERC) through NSERC Collaborative Research Development Grant no. 31-614105, which made this whole enterprise possible.

I would like to thank my co-op students at Simon Fraser University: Jason Wallace, Saeed Shokoya, and Adrian Wikarna, for assisting me in performing time-consuming thermal and electronic conductivity tests at Laboratory for Alternative Energy Conversion (LAEC) at SFU. My especial thanks go to Jason Wallace and Wendell Huttema (a previous lab engineer at SFU LAEC) who helped me through years to improve the design and performance of a Guarded Heat Flow thermal conductivity testbed at SFU LAEC. I am deeply grateful to previous and current lab engineers and post docs at SFU LAEC: Wendell Huttema, Marius Haiducu, and Claire McCague, for providing me with their technical support and expert guidance on various aspects of the project.

I am also thankful to Asahi Glass Co. for providing free ETFE samples, Ms. Marcia Reid from McMaster University for preparing TEM microtomed slices, and SFU 4D LABS for providing access to various tools for electron and optical microscopy, electrochemical impedance spectroscopy, porosimetry, X-ray photoelectron spectroscopy, etc.

Finally, I would like to express my gratitude to my family, who always supported me in all stages of my personal life and professional career, and, more importantly, to my lovely wife who always believed in me and supported me with her love and encouragement.

Table of Contents

List of Tables

List of Figures

List of Acronyms

ACL	Anode catalyst layer
AFC	Alkaline fuel cell
AFCC	Automotive Fuel Cell Cooperation Corp.
AGDL	Anode gas diffusion layer
Al	Aluminum
AM	Agglomerate model
AMPL	Anode microporous layer
BCC	Body centered cubic
BSE	Backscattered electron
C	Carbon
CCL	Cathode catalyst layer
CCM	Catalyst-coated membrane
CCS	Catalyst-coated substrate
CGDL	Cathode gas diffusion layer
CL	Catalyst layer
CMPL	Cathode microporous layer
DC	Direct current
DI	Deionized
DNS	Direct numerical simulation
ECR	Electronic contact resistance
ECS	The Electrochemical Society
EDX	Energy dispersive X-ray
EIS	Electrochemical impedance spectroscopy
ESEM	Environmental scanning electron microscope/microscopy
ETFE	Ethylene tetrafluoroethylene
eV	Electron volt
F	Fluorene
FCC	Face centered cubic
FIB	Focused ion beam
GDL	Gas diffusion layer
GHF	Guarded heat flow
H	Hydrogen

HAADF	High angle annular dark field
HOR	Hydrogen oxidation reaction
hr	Hour
IP	In-plane
IPA	Isopropanol alcohol
I/C	Ionomer-to-carbon weight ratio
LAEC	Laboratory for Alternative Energy Conversion (at Simon Fraser University)
MCFC	Molten carbonate fuel cell
MEA	Membrane electrode assembly
MHM	Macro-homogeneous model
ML	Membrane layer
MRM	Microstructural reconstruction model
O	Oxygen
ORR	Oxygen reduction reaction
P	Pressure
PAFC	Phosphoric acid fuel cell
PEFC	Polymer electrolyte fuel cell
PEM	Polymer electrolyte membrane
PEMFC	Polymer electrolyte membrane fuel cell
PFSA	Perfluorosulfonic acid
PSD	Pore size distribution
Pt	Platinum
PTC	Parallel thermal conductance
PTFE	Polytetrafluoroethylene
Pt/C	A carbon particle and Pt particles supported on it, as a whole
Pt/C/Nafion	A homogenous mixture of Pt, C, and Nafion
R&D	Research and development
RH	Relative humidity
S	Sulfur
SC	Simple cubic
SE	Secondary electron
SEM	Scanning electron microscope/microscopy
SFU	Simon Fraser University
SOFC	Solid oxide fuel cell

STD	Standard deviation
T	Temperature
TCR	Thermal contact resistance
TEM	Transmission electron microscope/microscopy
TP	Through-plane
TPS	Transient plane source
TTE	Trimethylolpropane triglycidyl ether
TUC-RUC	Thickness under compression-resistance under compression
VDP	van der Pauw
wt	Weight
XPS	X-ray photoelectron spectroscopy
XRF	X-ray fluorescence

Nomenclature

A	Area (m^2)
AR	Crack aspect ratio, defined as ratio of long over short edge of a crack
a	Contact or overlap radius (m)
B	A geometrical parameter (m), which appears in modeling the resistance of a mesopore
b	Y-intercept of a line
c	Specific heat capacity ($\mathrm{J \cdot kg^{-1} \cdot K^{-1}}$)
CD	Crack density, defined as fraction of total area of a CL covered by cracks
d	Diameter (m)
E	Output voltage of an electrochemical cell (V)
$\mathcal{E}$	Utilized fraction of a CL thickness in reaction inside a cell
ECR	Electronic contact resistance (Ω)
EW	Equivalent weight of ionomer ($\mathrm{g/mol\ of\ SO_3{}^-}$), defined as mass of dry ionomer per mole of sulfonic acid groups ($\mathrm{SO_3{}^-}$)
e	Counter variable
e^-	Electron
EP	Constant electric power of a TPS thin film sensor (W)
g	Gravitational acceleration constant ($9.81\ \mathrm{m \cdot s^{-2}}$)
H	Hydrogen atom
$\mathrm{H_2}$	Hydrogen molecule
$\mathrm{H_2O}$	Water molecule
$\mathrm{H^+}$	Hydrogen ion (proton)
h	Thickness (m)
$h_{\text{Kap\&adh}}$	Total thickness of the Kapton layer and the adhesive sticking the Kapton layer to the double spiral nickel in a TPS thin film sensor (m)
I	Electric current (A)
I_0	Modified Bessel function of the zeroth kind
i	Counter variable
j	Current density ($\mathrm{A \cdot cm^{-2}}$), defined as current per unit area of an MEA

K	A geometrical parameter (m), which appears in modeling the resistance of a mesopore
Kn	Knudsen number, defined as mean free path divided by a characteristic length
k	Thermal conductivity $(\mathrm{W \cdot m^{-1} \cdot K^{-1}})$
$k_{\text{Kap\&adh}}$	Total or effective bulk thermal conductivity of the Kapton layer and the adhesive sticking the Kapton layer to the double spiral nickel in a TPS thin film sensor $(\mathrm{W \cdot m^{-1} \cdot K^{-1}})$
Len	Length (m)
l	Loading
$l_{\mathrm{I/C}}$	Ionomer-to-carbon (I/C) weight ratio (i.e., I/C ratio)
l_{ion}	Ionomer loading, defined as mass of ionomer over total mass of a CL
l_{Pt}	Areal Pt loading $(\mathrm{kg \cdot m^{-2}})$, defined as mass of Pt over area of a CL
$l_{\text{Pt}/\mathrm{C}}$	Pt loading, defined as Pt-to-carbon (Pt/C) weight ratio
M	A fluid parameter (m)
m	Mass (kg)
MFP	Mean free path (m)
MW	Molecular weight $(\mathrm{kg \cdot kmol^{-1}})$
N	Total number of measurement points
N_{A}	Avogadro's number (6.022×10^{23})
n	A number
O	Oxygen atom
$\mathrm{O_2}$	Oxygen molecule
P	Pressure (Pa)
$Parameter$	A CL design parameter, e.g., I/C ratio, Pt loading, etc.
P_i	Legendre polynomial of degree i
Pr	Prandtl number
p	A dimensionless parameter related to crack aspect ratio, which appears in modeling the in-plane conductivity of a cracked CL
$\dot{Q}$	Heat flow rate (W)
q	An arbitrary function
R	Resistance $(\mathrm{K \cdot W^{-1}}$ if thermal; Ω if electronic)

R_{res}	A residual resistance as a part of a total through-plane thermal resistance measured for a sample by a GHF or a TPS testbed, which consists of either TCRs between the sample and the GHF fluxmeters in the case of GHF measurements or effects of through-plane bulk resistance of the TPS sensor's insulating layer and TCRs in the TPS test column in the case of TPS measurements $(\mathrm{K \cdot W^{-1}})$
R'	Summation of TCRs in a TPS test column and residual resistances related to the TPS thin film sensor, which is a part of the total through-plane resistance measured during a TPS measurement of a thin film $(\mathrm{K \cdot W^{-1}})$, $R' = \frac{h_{\text{Kap\&adh}}}{k_{\text{Kap\&adh}}A_{\text{sen}}} + TCR = \frac{h_{\text{Kap\&adh}}}{k_{\text{Kap\&adh}}A_{\text{sen}}} + R_{\text{c,bm-s}} + R_{\text{c,s-Kap}} + R_{\text{c,adh-sen}}$
R''	A share of through-plane bulk thermal resistance of a substrate-CL-CL-substrate sandwich which does not include through-plane bulk resistances of the CLs $(\mathrm{K \cdot W^{-1}})$, $R'' = 2R_{\text{b,sub}} + 2R_{\text{c,sub-cl}} + R_{\text{c,cl-cl}}$
R'''	A constant part of total through-plane thermal resistance measured for a substrate-CL-CL-substrate sandwich by a GHF or a TPS testbed, including effects of bulk resistances of the substrates and TCRs in the sandwich as well as residual resistance of the measurement device $(\mathrm{K \cdot W^{-1}})$, $R''' = R'' + R_{\text{res}} = 2R_{\text{b,sub}} + 2R_{\text{c,sub-cl}} + R_{\text{c,cl-cl}} + R_{\text{res}}$
R''''	Summation of all the measured resistances except for bulk of the CLs in measuring total through-plane electronic resistance of n catalyst-coated Al samples with GDLs at every interface (Ω), $R'''' = n\left(R_{\text{b,Al}} + R_{\text{c,Al-cl}}\right) + (n+1)R_{\text{b,gdl}} + nR_{\text{c,cl-gdl}} + nR_{\text{c,Al-gdl}} + 2R_{\text{gdl-sen}}$
$R_{\text{b,Kap\&adh}}$	Effective through-plane bulk thermal resistance of the Kapton layer and the adhesive layer together in a TPS thin film sensor $(\mathrm{K \cdot W^{-1}})$
r	Radius (m)
$reps$	Total number of measurement repetitions
S	A geometrical parameter (m), which appears in modeling the resistance of a mesopore
s	Integration variable
s_b	Standard deviation of the intercept of a linear regression, $s_b = s_{y,x}\sqrt{\left(\frac{1}{N} + \frac{x_{\text{ave}}^2}{SS_{xx}}\right)}$
s_{sl}	Standard deviation of the slope of a linear regression, $s_{sl} = \frac{s_{y,x}}{\sqrt{SS_{xx}}}$
$s_{y,x}$	Standard deviation of $y(x)$ in a linear regression, $s_{y,x} = \sqrt{\frac{SS_E}{N-2}}$
sl	Slope of a line

SS_E	Error sum of squares, $SS_E = \sum_{i=1}^{N}(y_i - \widehat{y_i})^2$
SS_{xx}	Sum of squares, $SS_{xx} = \sum_{i=1}^{N}(x_i - x_{\mathrm{ave}})^2$
SS_{xy}	Sum of squares, $SS_{xy} = \sum_{i=1}^{N}(x_i - x_{\mathrm{ave}})\,(y_i - y_{\mathrm{ave}})$
T	Temperature ($\mathrm{^\circ C}$ or K)
t	Time (s or hr)
TCR	Thermal contact resistance ($\mathrm{K \cdot W^{-1}}$)
$T_{\Omega/2,N-2}$	The upper $100 \times \Omega/2\%$ point of the t-distribution with $N-2$ degrees of freedom
V	Volume ($\mathrm{m^3}$)
v	Speed ($\mathrm{m \cdot s^{-1}}$)
vis	Viscosity ($\mathrm{Pa \cdot s}$)
W	Weight (N)
Wid	Width (m)
w	Mass fraction
x	Location variable (m) / An arbitrary variable
y	An arbitrary variable
z	An arbitrary variable

Greek letters

α	An accommodation parameter
α_T	Accommodation coefficient of a surface at temperature of T
β	A fluid parameter
$\mathit{\Gamma}$	Electrical resistivity of nickel element in a TPS thin film sensor ($\Omega \cdot \mathrm{m}$)
γ	Ratio of specific heats
Δ	Difference operator
δ	Uncertainty operator
ε	Porosity
ϵ	Temperature coefficient of resistivity of the nickel element in a TPS thin film sensor ($\mathrm{K^{-1}}$)
ζ	A dimensionless parameter related to cracks, which appears in modeling the in-plane conductivity of a cracked CL

η	Molality of a solute in a solution, defined as mass of the solute per mass of the solvent
Θ	A characteristic time parameter (s), $\Theta = r_{\mathrm{sen}}^2/\kappa_{\mathrm{bm}}$
θ	Overlap angle (rad)
κ	Thermal diffusivity $(\mathrm{m}^2 \cdot \mathrm{s}^{-1})$
Λ	Conductivity $(\mathrm{W} \cdot \mathrm{m}^{-1} \cdot \mathrm{K}^{-1}$ if thermal; $\mathrm{S} \cdot \mathrm{m}^{-1}$ if electronic)
λ	Water content of ionomer, defined as mole of water per mole of sulfonic acid groups $(\mathrm{SO_3}^-)$
μ	Ratio of molecular weight of a fluid on a surface to molecular weight of the material of the surface, $\mu = MW_{\mathrm{f}}/MW_{\mathrm{s}}$
ξ	Contact effectiveness factor (dimensionless)
ρ	Volumetric mass density $(\mathrm{kg} \cdot \mathrm{m}^{-3})$
Σ	Summation operator
σ	Electronic conductivity $(\mathrm{S} \cdot \mathrm{m}^{-1})$
ς	A dimensionless function, which appears in modeling transient heat conduction from a circular heat source on a half space
τ	A dimensionless time parameter, $\tau = \sqrt{t/\Theta}$
φ	An angle related to crack aspect ratio, which appears in modeling the in-plane conductivity of a cracked CL
ϕ	Volume fraction
χ	Volume fraction of micropores
ψ	Ionomer coverage, defined as a fraction of total area of an aggregate covered by ionomer
Ω	Significance level in a linear regression analysis
ω	Overlap depth (m)

Subscripts

0	Reference conditions of $101.3\ \mathrm{kPa}$ and $298\ \mathrm{K}$
AI	Armco iron
Al	Aluminum
a	Air
adh	Adhesive, sticking the Kapton layer to the nickel probe in a TPS sensor

app	Apparent
ave	Average
ac	Agglomerate cluster
agg	Aggregate of Pt/C particles inside an agglomerate
aggl	Agglomerate: a microstructural unit of CLs, made from an aggregate of Pt/C particles and the ionomer film around it
b	Bulk
bm	Background material
bot	Bottom
C	Carbon
CB	Carbon black
c	Contact
ccs	Catalyst-coated substrate
cell	A single cell in a PEMFC
Chem comp	Chemical composition
cl	Catalyst layer
col	Collision
cr	Crack
ct	Catalyst
dm	Dry milling
dry	Dry conditions (no hydration)
e	Electron
eff	Effective
etfe	Ethylene tetrafluoroethylene
f	Fluid
g	Gas
gdl	Gas diffusion layer
geo	Geometric
i	in (indication of place)
init	Initial
ink	Catalyst ink

ion	Ionomer
ip	In-plane
Kap	Kapton insulating layer of a TPS thin film sensor
mep	Mesopore
meu	Mesoscale unit cell
mip	Micropore
Nafion	Nafion membrane or ionomer
np	Nanopore
o	Octane
obj	Object
Pt	Platinum
Pt/C	A carbon particle together with platinum particles supported on it, as a whole
p	Pore
ph	Phonon
ref	A reference CL design, defined as the CL with I/C=1.1, 0 hr dry milling time, and 55 °C drying temperature
res	Residual
ring	One of the concentric rings (or sources) of the double spiral nickel of a TPS thin film sensor
rod	Coating rod
s	Sample
sen	Sensor (fluxmeters of a GHF testbed or nickel probe of a TPS testbed)
sol	Solid
st	Stack
sub	Substrate
surf	Surface
th	Thermal
top	Top
tot	Total
tp	Through-plane
w	Water

wet	Wet conditions (full hydration)

Superscripts

*	A modified property or a property divided by a reference property
–	Average (mean) property
′	Signifying an extra part of a resistance
~	Preliminary form of a property to be modified or corrected later
^	Predicted by linear regression

Executive Summary

Motivation

Polymer electrolyte membrane fuel cells (PEMFCs) are considered one of the alternative technologies for sustainable clean power generation due to their promising features, such as potentially zero greenhouse gas emissions, high efficiency, and abundance of their fuel source, i.e., hydrogen, which could be produced from various sources including electrolysis of water and reformation of hydrocarbons. The basics of operation of PEMFCs could be summarized as the chemical reaction between hydrogen and oxygen producing electricity, water, and heat. This chemical reaction is split into two half-reactions happening inside two respective catalyst layers (CLs), which are microporous materials and parts of a membrane electrode assembly (MEA) making the core of a PEMFC. The exothermic nature of the electrochemical reaction and conduction of the resultant electricity through the MEA could induce significant local temperature variations inside the MEA which could highly affect performance and degradation of the PEMFC during normal operation as well as special operating conditions like freeze-start and warm-up. Further, ohmic losses through different MEA components limit the performance of PEMFCs. Accordingly, performance and degradation of PEMFCs are closely linked to thermal and electrical properties of the MEA components. Among the different components of an MEA, CLs with thicknesses of ~2-8 μm could be regarded as the hotbed of performance and degradation issues due to occurrence of most of the heat and all the electricity generation inside these layers, yet their thermal and electronic properties have not been studied in-depth and are relatively unknown due to the many existing challenges in measurement and modeling of such properties for the very thin CLs. In addition, there is a great need for data on various microstructural properties of traditional ink-based CLs as well as geometrical models which could be representative of the underlying complex microstructure.

Accordingly, in this PhD dissertation, CL sample preparation, measurement procedures, and new analytical models are developed to obtain an in-depth understanding of heat and electron conduction phenomena inside the microporous thin CLs; the underlying microstructure is also studied in-depth and modeled. Moreover, several in-house standards are established for the first time for systematic and accurate measurement of thermal and electronic conductivities of CLs at Automotive Fuel Cell Cooperation Corp. (AFCC), the industrial partner of the project, and design guidelines are proposed according to the models for designing CLs with desired conductivities. Although the focus of this research has been on the CL of PEMFCs, the findings can be directly applied and used in modeling and characterizations of a wide range of thin films and membranes that have applications in numerous engineering and biological systems.

Objectives

The objectives of this research are to understand heat and electron conduction phenomena inside microporous CLs of PEMFCs and provide guidelines for designing CLs with desired conductivities.

Methodology

A systematic approach is adopted to achieve the goals of this research, as follows:

- Fabrication and preparation of CL samples by selecting an appropriate coating method and suitable substrates for thermal and electronic conductivity tests;
- Geometric characterization and modeling of CLs, used as a foundation for modeling the targeted transport properties (i.e., thermal and electronic conductivities in this thesis);
- Establishing new and accurate procedures for measuring thermal and electronic conductivities of CLs ex-situ;
- Mechanistic modeling of heat and electron conduction phenomena inside CLs using the developed geometrical platform; and
- Performing parametric studies to establish effects of salient geometrical and compositional parameters (e.g., porosity, crack density, and ionomer-to-carbon (I/C) weight ratio) on the targeted properties to provide guidelines for designing CLs with desired conductivities.

The above systematic approach was developed in form of a project roadmap, shown below, as a guideline for various phases of the research:

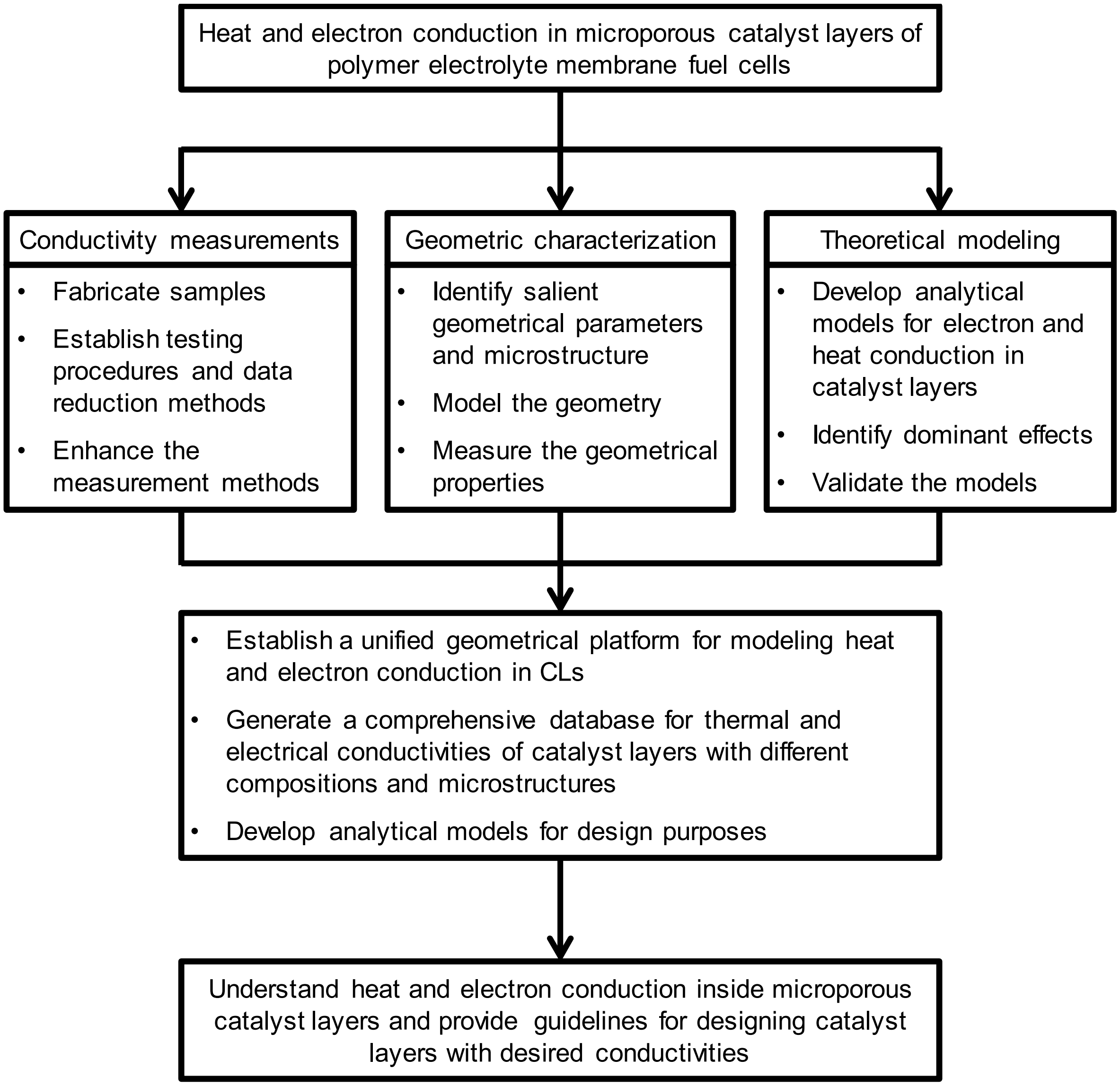

Project roadmap

Contributions

Contributions of this study include a set of new analytical and experimental tools for studying heat and electron conduction phenomena inside traditional ink-based CLs as well as comprehensive databases for microstructural properties and the conductivities, for different CL compositions and microstructures. Effects of operating conditions on the conductivities are also discussed in depth. The main outcomes of this research are summarized here:

- Developed a new data reduction method for eliminating a systematic error in thin film thermal conductivity tests by transient plane source (TPS) method;
- Determined an efficient coating method for fabricating uniform thicknesses of CLs required for accurate measurements of thermal and electronic conductivities;
- Established suitable non-masking substrates for through-plane thermal, through-plane electronic, and in-plane electronic conductivity measurements;
- Developed new accurate test procedures for ex-situ measurements of through-plane thermal, through-plane electronic, and in-plane electronic conductivity of CLs;
- Developed a new and comprehensive procedure for experimental characterization of the bulk and interfacial microstructure of CLs using a set of experimental tools;
- Investigated effects of substrate type, areal Pt loading, and hot-pressing on the microstructure as well as through-plane thermal and in-plane electronic conductivity of CLs;
- Developed a new geometrical model for conventional ink-based CLs, which could be used as a platform for modeling different transport properties inside CLs;
- Developed the first analytical models for predicting thermal and electronic conductivities of CLs for both through-plane and in-plane directions;
- Performed analytical and experimental parametric studies of through-plane thermal, through-plane electronic, and in-plane electronic conductivities for several CL designs under various operating conditions;

Scholarly Contributions

1. Mohammad Ahadi, Mickey Tam, Jürgen Stumper, and Majid Bahrami, "Electronic conductivity of catalyst layers of polymer electrolyte

membrane fuel cells: Through-plane vs. in-plane," (*International Journal of Hydrogen Energy*, Accepted, 2018).

2. Mohammad Ahadi, Mickey Tam, Madhu S. Saha, Jürgen Stumper, Majid Bahrami, "Thermal conductivity of catalyst layer of polymer electrolyte membrane fuel cells: Part 1 - Experimental study," *Journal of Power Sources,* vol. 354, p. 207–214, 2017.

3. Mohammad Ahadi, Andreas Putz, Jürgen Stumper, Majid Bahrami, "Thermal conductivity of catalyst layer of polymer electrolyte membrane fuel cells: Part 2 - Analytical modeling," *Journal of Power Sources,* vol. 354, p. 215–228, 2017.

4. Mohammad Ahadi, Mehdi Andisheh-Tadbir, Mickey Tam, Majid Bahrami, "An improved transient plane source method for measuring thermal conductivity of thin films: Deconvoluting thermal contact resistance," *International Journal of Heat and Mass Transfer,* vol. 96, p. 371–380, 2016.

5. Sadegh Hasanpour, Mohammad Ahadi, Majid Bahrami, Nedjib (Ned) Djilali, Mohsen Akbari, "Woven gas diffusion layers for polymer electrolyte membrane fuel cells: Liquid water transport and conductivity trade-offs", *Journal of Power Sources*, vol. 403, p. 192–198, 2018.

6. SFU Team: Mohammad Ahadi, Claire McCague, Majid Bahrami; AFCC Team: Mickey Tam, Andreas Putz, Ehsan Sadeghi, Madhu Saha, Jasna Jankovic, Juergen Stumper, "Gate 2 review: Catalyst layer through-plane thermal resistance tool," Automotive Fuel Cell Cooperation (Internal report), Vancouver, August 23rd, 2016.

7. SFU Team: Mohammad Ahadi, Claire McCague, Majid Bahrami; AFCC Team: Mickey Tam, Andreas Putz, Madhu Saha, Jasna Jankovic, Juergen Stumper, "Gate 2 review: Cathode catalyst layer through-plane electronic resistance tool," Automotive Fuel Cell Cooperation (Internal report), Vancouver, December 12th, 2016.

8. Mohammad Ahadi, Sina Salari, Ali Malekian, Mickey Tam, Juergen Stumper, Majid Bahrami, "PEMFC catalyst layers: Recent advances in process-structure-property correlations", in *AiMES 2018*, Cancun, September 30th–October 4th, 2018.

9. Mohammad Ahadi, Mickey Tam, Andreas Putz, Jürgen Stumper, Claire McCague, Majid Bahrami, "Electrical conductivity of PEM fuel cell catalyst layers: Through-plane vs. in-plane", in *European Hydrogen Energy Conference 2018*, Costa del Sol, March 14–16th, 2018.

10. Mohammad Ahadi, Mickey Tam, Andreas Putz, Jürgen Stumper, Claire McCague, and Majid Bahrami, "Challenges facing thermal and electrical conductivity measurements in catalyst layer of PEM fuel cells", in *European Hydrogen Energy Conference 2018*, Costa del Sol, March 14–16th, 2018.

11. Mohammad Ahadi, Mickey Tam, Madhu S. Saha, Jürgen Stumper, Majid Bahrami, "Thermal conductivity of the catalyst layer of polymer electrolyte membrane fuel cells: modeling and experiment," in *The 27th International Symposium on Transport Phenomena*, Hawaii, September 23rd, 2016.

12. Mohammad Ahadi, Mehdi Andisheh-Tadbir, Mickey Tam, Majid Bahrami, "Improving the transient plane source method for measuring thermal conductivity of thin films by deconvoluting thermal contact resistance with applications in fuel cell technology," in *The 27th International Symposium on Transport Phenomena*, Hawaii, September 22nd, 2016.

13. Mohammad Ahadi, Mickey Tam, Madhu S. Saha, Jürgen Stumper, Majid Bahrami, "Heat transfer in micro/nano porous layers of polymer electrolyte membrane fuel cells," in *ECS-Canada Section Fall Meeting*, Vancouver, October 24th, 2015.

14. Mohammad Ahadi, Mickey Tam, Madhu S. Saha, Jürgen Stumper, Majid Bahrami, "Experimental study of thermal conductivity of catalyst layer of polymer electrolyte membrane (PEM) fuel cells," in *228th ECS Meeting, Polymer Electrolyte Fuel Cells 15 (PEFC 15)*, Phoenix, October 14th, 2015.

15. Mohammad Ahadi, Jürgen Stumper, Majid Bahrami, "Analytical modeling of thermal conductivity of catalyst layer of polymer electrolyte membrane (PEM) fuel cells," in *228th ECS Meeting, Joint General Session: Batteries and Energy Storage -and- Fuel Cells, Electrolytes, and Energy Conversion*, Phoenix, October 13th, 2015.

16. Mohammad Ahadi, Hamidreza Sadeghifar, Sina Salari, Mehdi Andisheh-Tadbir, Claire McCague, Majid Bahrami, "Transport Phenomena in Micro/Nano Porous Layers of Polymer Electrolyte Membrane (PEM) Fuel Cells," in *Nanolytica Symposium, Simon Fraser University*, Vancouver, March 14th, 2014.

17. Sina Salari, Claire McCague, Mohammad Ahadi, Mickey Tam, Ehsan Sadeghi, Jürgen Stumper, Majid Bahrami, " Characterization of transport properties of catalyst layer of a PEMFC," in *Pacific Centre for Advanced Materials and Microstructures (PCAMM) Meeting*, University of Victoria, Victoria, December 5th, 2014.

Chapter 1.

Introduction

An ever-accelerating movement toward alternative energy sources and power generation technologies has been triggered in recent decades mainly due to: i) desire for lower dependence on fossil fuels due to their crucial role in greenhouse gas emissions leading to environmentally detrimental phenomena of manmade climate change, ii) necessity of lowering pollution due to its relevant health hazards and adverse effects on ecosystems and economy, and iii) need for higher efficiency for economical and sociological advancements. Fuel cells are considered one of the alternative future technologies for power generation due to their promising potentials in lowering the pollution and dependence to fossil fuels as well as increasing the power generation efficiency. They produce potentially zero greenhouse gases due to their sole production of water and heat along with electrical work. They could reduce the major pollutants by more than 90% with pollution emissions being strictly limited to fuel production processes, and their electrical energy conversion efficiency could reach up to 60% (compare with the average ~20% efficiency of conventional internal combustion engines) [1, 2].

Fuel cell is defined as an electrochemical device/engine that directly converts the chemical energy stored in a fuel and an oxidizer (i.e., the reactants) into useful electrical work. Figure 1-1 shows a schematic of a generic fuel cell and its main components. As shown in Figure 1-1, fuel and oxidizer streams (reactants) enter the fuel cell through flow channels and move (by diffusion or advection) to the electrodes, where they undergo reduction and oxidation reactions to produce the external electric current. The reactions are facilitated by catalyst layers in the electrodes. The entering fuel to the anode undergoes an oxidation electrochemical reaction and turns into to ions and electrons; the electrons, collected by the anode current collector, are passed to the external circuit (i.e., the resistance *R*) to provide the electric work, and the ions pass through the electrolyte to recombine with the electrons arriving from the external circuit and the oxidizer arriving from the oxidizer flow channels in a reduction electrochemical reaction and complete the cell reaction. Products of the whole cell reaction are electric work, chemicals, and waste heat [1].

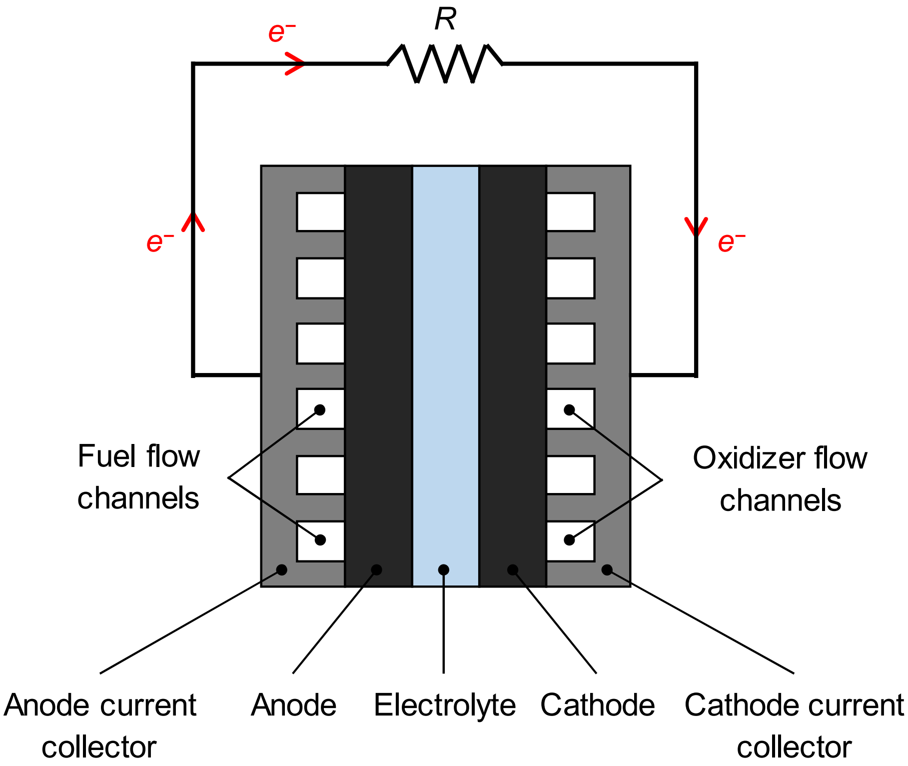

Figure 1-1. Schematic of a generic fuel cell and its main components

Fuel cells are generally categorized according to the utilized material for their electrolyte to the following classes [1]:

1. Alkaline fuel cells (AFCs), employing an aqueous solution of potassium hydroxide as their electrolyte;
2. Phosphoric acid fuel cells (PAFCs), employing a solution of phosphoric acid in porous silicon carbide matrix as their electrolyte;
3. Solid oxide fuel cells (SOFCs), having a solid ceramic oxide electrolyte (Yttria (Y_2O_2) stabilized zirconia (ZrO_2));
4. Molten carbonate fuel cells (MCFCs), making use of molten alkali metal (Li/K or Li/Na) carbonates in a porous ceramic matrix as their electrolyte; and

5. Polymer electrolyte membrane fuel cells (PEMFCs), utilizing a flexible solid perfluorosulfonic acid (PFSA) polymeric membrane as their electrolyte.

Among all the mentioned types of fuel cells, PEMFCs are envisioned as the most viable candidate to replace heat engines and batteries in automotive, stationary, auxiliary, and portable power applications, due to their main following advantages over the other types of fuel cells: i) High relative performance (or power density), ii) Low operating temperatures (~20-90 °C), making them also more capable of rapid start-up, and iii) Facile anode kinetics of the hydrogen oxidation reaction, making them have the lowest utilization of the precious catalyst (usually platinum (Pt) or its alloys) [1]. In the following section, the basics of operation of the PEMFCs and the underlying electrochemical reactions are described.

1.1. Basics of Operation of PEMFCs

Schematic of a typical PEMFC is shown in Figure 1-2. As shown in Figure 1-2, core of a PEMFC, also called the membrane electrode assembly (MEA), is consisted of: i) a PFSA membrane layer (PFSA ML) made of hydrophobic polytetrafluoroethylene (PTFE) backbone sulfonated with hydrophilic acid clusters to provide the required ionic conductivity, ii) anode/cathode gas diffusion layer (AGDL/CGDL), made of carbon nanofibers and PTFE to provide the required pathways for distribution of reactants and products and transport of electrons, iii) anode/cathode microporous layer (AMPL/CMPL), made of carbon nanoparticles and PTFE to enhance the transport of reactants, products, and electrons in the electrodes, and iv) anode/cathode catalyst layer (ACL/CCL), made of Pt and carbon nanoparticles and a PFSA ionomer (like the ML) to provide facile kinetics of the electrochemical reactions as well as facile transport of ions, electrons, reactants, and products in the electrodes [1].

In a typical PEMFC, hydrogen is used as fuel and oxygen is used as oxidizer. The fed hydrogen to the anode is split into hydrogen ions and electrons in the ACL during a hydrogen oxidation reaction (HOR), as follows:

$$2H_2 \rightarrow 4H^+ + 4e^- \tag{1.1}$$

The produced electrons in anode travel through the external circuit to provide the electric work, and the hydrogen ions pass through the PFSA ML and reach the cathode, where they react with the oxygen molecules and the arriving electrons from the external circuit through the following oxygen reduction reaction (ORR):

$$O_2 + 4H^+ + 4e^- \rightarrow 2H_2O \tag{1.2}$$

Accordingly, overall reaction of the PEMFC could be summarized by combining the half-cell reactions (1.1) and (1.2), as follows:

$$O_2 + 2H_2 \rightarrow 2H_2O \tag{1.3}$$

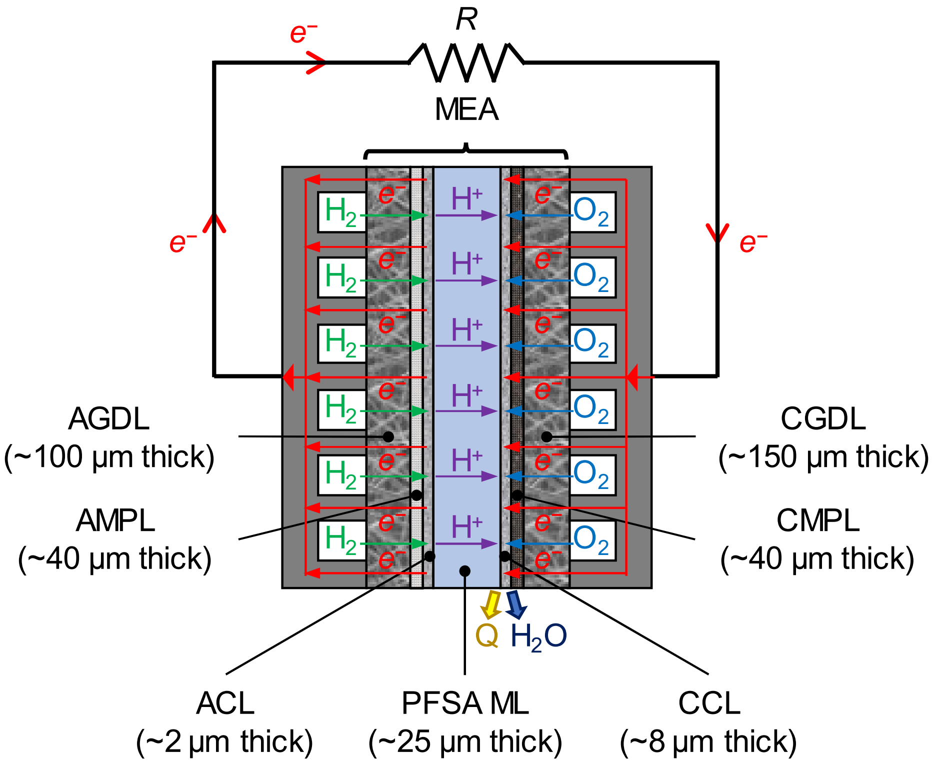

Figure 1-2. Schematic of a PEMFC

1.2. Importance of Heat and Electron Conduction in Catalyst Layers (CLs)

Because of the electrochemical reactions occurring inside the ACL and CCL and the transport of electrons through different layers of the MEA, various heat generation modes occur inside a PEMFC, which could be categorized as [3-6]:

1. Reversible (or entropic) heat of the electrochemical reactions in the CLs, due to entropy changes during the reactions;
2. Irreversible heat, due to losses caused by over-potential in the CLs;
3. Latent heat, due to phase change in the CCL;
4. Joule heating in all the MEA layers including the CLs; and
5. Heat of sorption of water vapor inside the ionomer in the CLs.

The above heat sources could induce significant local temperature variations inside the MEA, which could highly affect water management, performance, and degradation of the fuel cell during normal operation as well as special operating conditions like freeze-start, warmup, and others [4-12]. Despite the comparatively low thickness of the CLs (~2-8 μm) within the current state of the art MEAs, Burheim at al. [13] predicted a significant change in MEA temperature profile due to saturation of the CLs alone. Burheim [14] further investigated effects of thermal conductivity of CLs on temperature profile across the MEA and reported significant increase in temperature profiles of the membrane and the CLs in case of low thermal conductivity of the CLs. This could lead to creation of hot spots in the membrane, which are one of the main mechanisms of MEA failure [15-20]. Further, an order of magnitude analysis, performed in Chapter 6 section 6.10 of this thesis, shows that conduction heat transfer through CLs accounts for ~60% of the total heat transfer through a PEMFC. Another factor to be considered is that ohmic losses through different MEA layers, including the CLs, limit the performance of PEMFCs. For a typical PEMFC with an ideal thermal voltage of ~1.3 V performing at 0.6 V and 1 A/cm^2 (total loss of ~1.3 V – 0.6 V = 0.7 V), breakdown of performance losses due to different modes could be described as [1]: i) ~0.1 V due to reversible (entropic) loss of the overall reaction (~14 % of the total loss), ii) ~0.2 V due to contamination, cross over, and electron leakage (~29 %

of the total loss), iii) ~0.3 V due to activation losses (~43 % of the total loss), and iv) the rest ~0.1 V due to ohmic losses through the layers (~14 % of the total loss). Accordingly, study of heat and electron conduction in CLs is of significant interest for performance optimization during normal and special operating conditions as well as for degradation minimization.

In addition to the above-standard operating conditions, there are several nonstandard situations where heat and electron conduction through the CLs may become a concern:

- Detachment of the gas diffusion layers (GDLs) from the CLs, which may lead to significant increase in thermal contact resistances (TCRs) and electronic contact resistances (ECRs) between the GDLs and the CLs. This, in turn, may lead to high local temperatures and significant temperature gradients over large distances (in the in-plane direction of the CLs), which would potentially be sensitive to the thermal and electronic conductivities of the CLs;
- Localized heat generation due to membrane damage/shortage;
- Designs without GDL, in which case the impact of heat and electron conduction phenomena through the GDLs would disappear, and sensitivity to the CLs would increase drastically; and
- New materials with significantly different thermal and electronic properties (ceramic or organic support materials, etc.).

The factors necessitating understanding heat and electron conduction phenomena in CLs are, however, not limited to the above operational issues and include concerns related to manufacturing process as well as quality control of the CLs. Depending on the manufacturing process, a CL may be exposed to several drying, heating, annealing, and lamination steps. If a catalyst-coated membrane (CCM) is assembled, all the layers involved in the process have a similar thickness. Therefore, if one wants to model the manufacturing process, the knowledge of the effective thermal conductivity is of significant interest. Additionally, as the catalyst manufacturing typically starts with coating a catalyst ink, a theoretical prediction of the thermal conductivity based on the ink composition would be desirable before a measurement value can be obtained. From the quality control aspect, measurement of electronic conductivity of the CLs may be employed as a forensic tool for assessing degradation level (e.g., carbon corrosion [21, 22]) and structural defects like cracks which could be created due to certain conditions during the CL manufacturing process (e.g., low ionomer content of the ink, low drying temperature, high areal Pt loading) or due to operational degradation [23-25].

1.3. Literature Review

The non-isothermal MEA models cited in section 1.2 (refer to [6, 8-11, 13]) rely on approximate explicit prescription of thermal and electronic conductivities for the CLs and, therefore, are limited to sensitivity studies on these parameters alone. However, to enable a model-guided structural and compositional optimization of the MEA, predictive descriptions of the thermal and electronic conductivities of different MEA components (including the CLs) with respect to the relevant structural parameters, backed by accurate measurements of these properties, are necessary.

Some studies have been performed on thermal and electronic conductivities of different MEA components [5, 13, 24, 26-49]. However, the reported studies on thermal and electronic conductivities of CLs [5, 13, 24, 38, 39, 47-49] are mostly experimental, and, to the authors' best knowledge, no closed-form expression for the conductivities that could account for structural and compositional variations can be found in the open literature. Moreover, the reported thermal/electronic conductivity data in literature contain effects of TCRs/ECRs together with some other residual bulk resistances present in the tests, whose effects are uncertain and not debated much in literature. Specifically, the effective electronic conductivity measurement methods employed in Refs. [24, 47, 48] are under the assumption of isotropic CL, which could easily fail for the generally cracked CLs or in case of microstructural inhomogeneities or gradients.

1.3.1. Existing Literature on Thermal Conductivity of CLs

Khandelwal and Mench [5] measured effective through-plane thermal conductivity of various fuel cell materials using the guarded heat flow (GHF) method [50] and reported 0.27±0.05 ($W \cdot m^{-1} \cdot K^{-1}$) for some CLs, deconvoluted from measurements of an MEA. As mentioned in Ref. [5], this is an effective value that also contains TCRs between the CLs and the GDLs as well as TCRs between the CLs and the membrane. Alhazmi et al. [38] employed parallel thermal conductance (PTC) technique [51] and measured in-plane thermal conductivity of some CLs by deconvoluting the conductivity from measurements of an MEA and catalyst-coated GDLs, neglecting: 1) TCRs between the GDLs and the CLs present in measurements of both the MEA and the catalyst-coated GDLs, 2) TCRs between the membrane and the CLs in the MEA, and 3) possible effects of compression of the MEA on thermal conductivities of the MEA components. Alhazmi et al. [38] reported insensitivity of the in-plane thermal conductivity to temperature, its slight increase with areal Pt loading (in terms of mg Pt/cm^2), and in-plane thermal conductivity values of 0.29-0.39 W$\cdot$m$^{-1}\cdot$K^{-1}. Alhazmi et al. [39] used a GHF device to measure through-plane thermal conductivity of catalyst-coated GDLs (spray-coated); they deconvoluted through-plane conductivity of the CLs from the measurements of the catalyst-coated GDLs, neglecting TCRs present in their measurements including the ones between the CLs and the GDLs. Alhazmi et al. [39] reported insensitivity of the through-plane conductivity to temperature and ~0.34 W$\cdot$m$^{-1}\cdot$K^{-1} for a 0.4 mg Pt/cm^2 CL which was comparable with in-plane conductivity of the same CL. Burheim et al. [13] made CLs (~30 and 60 μm thick) by spraying several layers of catalyst ink onto copper substrates, stacked copper-catalyst-aluminum sandwiches in a GHF device, and reported overall through-plane conductivity values of 63-98 mW$\cdot$m$^{-1}\cdot$K^{-1} for dry CLs with different compositions under compression; they neglected effects of thermal resistances of the metal foils and TCRs within the stacks.

1.3.2. Existing Literature on Electronic Conductivity of CLs

Gode et al. [47] used van der Pauw (VDP) method [52] to study effective electronic conductivity of CLs with 20 wt% Pt on Vulcan and different ionomer contents, spray-coated onto a Nafion membrane, and reported values of 90-390 S$\cdot$m^{-1} for the CLs, measured in ambient conditions. Morris et al. [48] also used the VDP method [52] to measure effective electronic conductivity of four different CL formulations under different relative humidity (RH) ratios and reported values of ~7-300 S$\cdot$m^{-1} for dry (0% RH) CLs. However, as also mentioned in Ref. [48], the VDP method [52] assumes that the material is isotropic for data reduction. This could introduce substantial errors into the conductivity results of Refs. [47] and [48] if their CLs were highly anisotropic. The isotropy assumption was also employed by Suzuki et al. [24], who measured electronic conductivity of a CL with different volume fractions of carbon and Pt particles (or alternatively Pt/C particles defined as carbon particles and the Pt particles supported on them), by employing a four probe technique in accordance with the Japanese Industrial Standard JIS-K7194; Suzuki et al. [24] reported conductivity values of ~10-100 $S \cdot m^{-1}$. Du et al. [49] assumed that CLs consisted of a simple cubic (SC), body centered cubic (BCC), or face centered cubic (FCC) arrangement of spherical agglomerates, each made of a homogenous mixture of Pt/C particles and Nafion; they numerically solved the Laplace equation inside the assumed geometry for diffusion of electrons and protons and fitted correlations through their numerical results for different radii of agglomerates, contact angles, ratios of contact radius to agglomerate radius, and bulk conductivity values of Pt/C/Nafion mixture inside the agglomerates. However, Du et al. [49] neglected the complex microstructure of agglomerates and considered them as solid (non-porous) structural units made of a homogenous Pt/C/Nafion mixture, which may result in two main sources of error in their numerical results: i) despite the assumption made by Du et al. [49], an increasing number of recent studies [53-57] indicate that ionomer (Nafion) does not penetrate into the agglomerates but, rather, stays as a thin layer on the surface of agglomerates, and ii) the complex microstructure of Pt/C particles and porosity inside the agglomerates are neglected in the study of Du et al. [49]. From the range of porosities that they proposed for different packing arrangements of solid agglomerates, the maximum was 0.5 which belonged to the SC arrangement, whereas in reality porosity of CLs could way exceed the value of 0.5 [47, 48]. Du et al. [49] also spray-coated CLs with different Nafion volume ratios onto a hollow glass cylinder and measured their electronic conductivity using an electrochemical impedance spectroscopy (EIS) method introduced by Pantea et al. [58]. In their experimental work, Du et al. [49] deconvoluted the electronic resistance from the total (electronic plus protonic) resistance, applied definition of slab resistance to obtain the electronic conductivity, and reported values of ~25-225 $S \cdot m^{-1}$. However, the experimental procedure used by Du et al. [49] did not account for deconvolution of possible ECRs or other residual resistances in their measurements and yielded effective conductivity values.

1.4. Research Motivation

In summary, based on the discussion in sections 1.2 and 1.3, the main motivations of this research could be categorized under two main topics as follows:

- *Need for fundamental understanding of heat and electron conduction in CLs:* for performance optimization, degradation minimization, fabrication, and forensic purposes; and

- *Deficiencies in the literature:* such as lack of mechanistic models which could lead to fundamental understanding of heat and electron conduction in CLs and could be used for development of new CLs, lack of noise-free procedures, ensuring deconvolution of all the effective parasitic resistances (noises) existing in the measurements, for accurate measurements of the conductivities in both through-plane and in-plane directions, and lack of comprehensive thermal/electronic conductivity databases for CLs with various compositions, microstructures, and operating conditions.

1.5. Research Objectives

The objectives of this research were to satisfy the contemporary needs of the cutting-edge PEMFC technology in fundamental understanding of heat and electron conduction inside CLs and to provide design guidelines for development of CLs with desired thermal and electronic conductivities. Moreover, due to close correlation of CL microstructure with its transport properties, advancement of knowledge on the underlying microstructure was also expected as another objective of this research.

1.6. Research Roadmap

A roadmap, shown in Figure 1-3, was prepared to achieve the goals of this research. The roadmap consisted of the following main steps:

- *CL sample preparation for geometric characterization and conductivity tests:* Three main criteria were defined to be met in this step, including: i) selecting an appropriate coating method which could yield uniform CL thicknesses with a relatively high yield rate, ii) selecting suitable substrates for thermal and electrical tests, which could have the minimum possible contribution in the tests in order to have the maximum possible signal to noise ratio, and iii) the highest possible resemblance of microstructure of the coated CLs to CLs prepared for use in a real PEMFC product.

- *Measurements of thermal and electronic conductivities:* In this step, efforts were made to modify/develop the existing/new measurement procedures in order to enhance the signal to noise ratio (reduce the uncertainty) in the tests and effectively deconvolute the effects of TCRs/ECRs and other residual resistances (e.g., related to the substrate or artifacts from the measurement

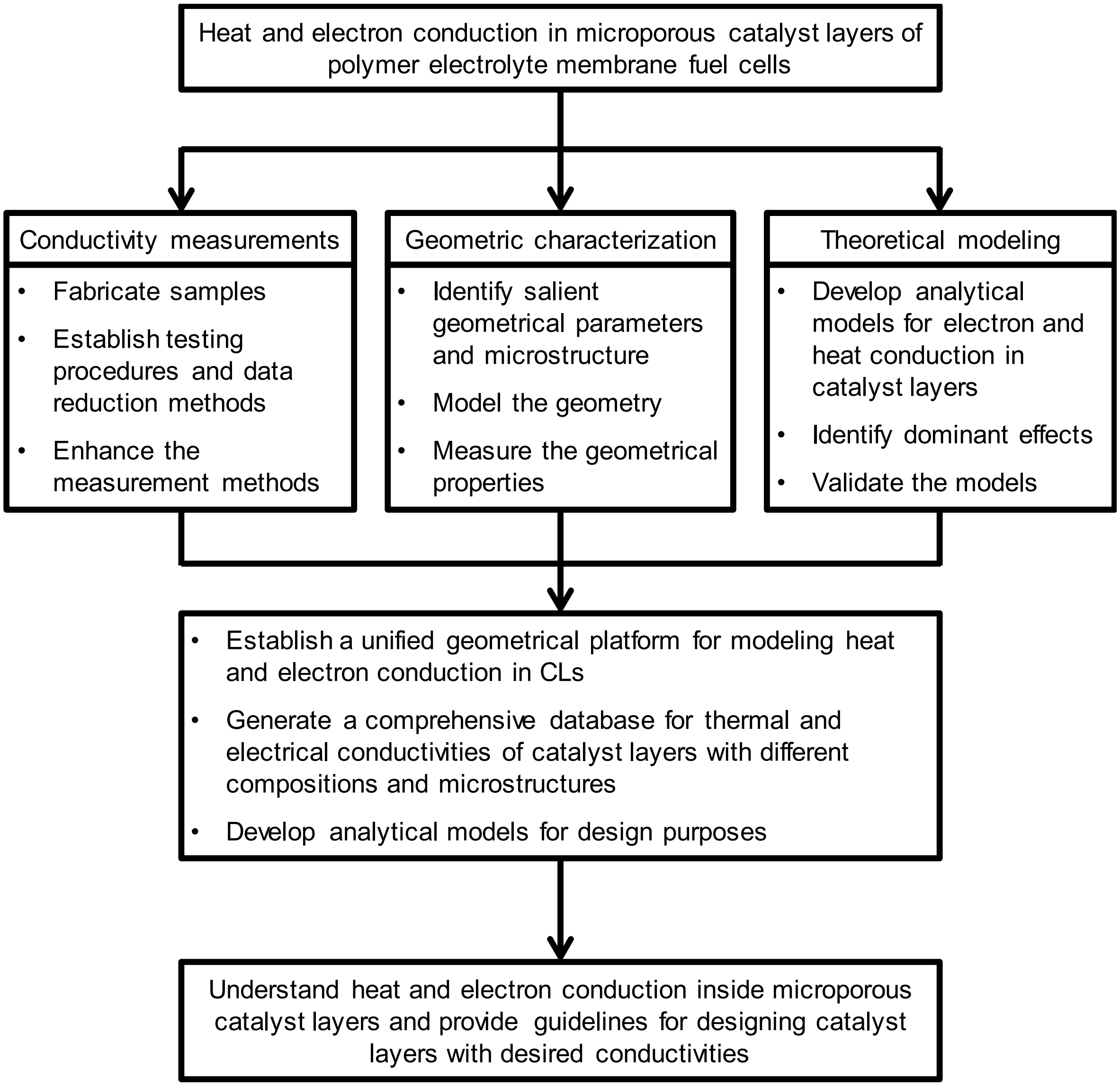

Figure 1-3. Roadmap of the project

sensors) from the measured data for accurate determination of the bulk conductivities. The modified/developed procedures were then used to measure the conductivities for CLs with various compositions and microstructures. Effects of various operating conditions, resembling the conditions occurring in a state-of-the-art PEMFC, were also studied.

- *Geometric characterization and modeling:* In this step, the building block of the modeling work was founded by determining, modeling, and measuring the salient geometrical parameters of CLs.
- *Modeling the thermal and electronic conductivities:* In this step, the built geometrical platform was used to develop mechanistic models for the

conductivities, which could cover the structural and compositional effects of CLs as well as various operating conditions.

- *Developing design guidelines:* In this step, parametric studies were performed on the developed models to identify the dominant effects and parameters, which were then used to provide guidelines for designing CLs with desired thermal and electronic conductivities. The modeling parametric study was backed up by an experimental parametric study, performed by coating and measuring CLs with various compositions and structures. Model predictions for effects of different operating conditions were also backed up by experimental data.

Chapter 2.

CL Fabrication

2.1. Ink Preparation

Traditional ink-based CLs are complex porous composites of three distinct materials: 1) nano-sized (~2-5 nm) catalyst particles (typically Pt or its alloys), 2) nano-sized (~20-30 nm) carbon particles which support the Pt particles, and 3) an ion-conducting polymeric material for which perfluorosulfonic acid (PFSA) ionomers are generally used. Catalyst ink is prepared by mixing catalyst powder (in form of carbon supported Pt or Pt/C catalyst powder) with ionomer, deionized (DI) water, and solvent, in certain weight ratios to prepare a specific composition. Amounts of water and volatile solvent (AFCC's proprietary solvent) were optimized (at AFCC) for each coating technique and device to obtain the desired coating and drying speeds.

Sequence of steps for mixing the ingredients was significantly important and was not violated as it could result in fire hazards in case of direct contact between the dry catalyst powder with the volatile solvent. Accordingly, based on the desired composition, first, the catalyst powder was mixed with water in a vial and shaken manually for ~3 min to ensure fully wetting of all the powder; then, the ionomer and solvent were added to the wet catalyst and shaken manually for ~3 min to ensure good mixing of the ink and breaking large Pt/C agglomerates. Afterwards, the ink inside the vial was sonicated in a sonication dismembrator (Fisher Scientific Sonic Dismembrator – Model 500) at 40% amplitude for a total (on/off) time of 1 hr (net time of 15 min: 1 sec on/3 sec off) to ensure complete mixing of the ink constituents and maximal breakage of large Pt/C agglomerates. Breaking the large agglomerates was necessary to obtain a homogenous ink and prevent clogging of printing nozzles during coating. Careful cleaning of the sonication probe before and after the sonication was necessary for maintenance of the device and safety purposes as well as preventing contamination from entering the ink. The cleaning process consisted of several steps, including: i) cleaning the ink-wetted probe with dry tissues, ii) cleaning the probe using tissues wetted by a 50/50 solution of isopropanol alcohol (IPA) and DI water,

iii) turning on the sonicator for a few seconds several times while dipping the probe in a DI water-filled vial, iv) rinsing the probe with IPA, and v) touching the IPA-wetted probe gently by dry tissues to absorb the IPA and dry the probe. Cleaning the sonicator took ~15 min to complete. In the next steps of making the ink, a magnetic stirring bar (cleaned in an IPA-filled vial capped and kept inside a sonication bath for ~3 min) was placed inside the ink-filled vial, the vial was sealed by tightly putting on its cap and wrapping parafilm around the cap, and then the sealed vial was placed and left on a stirring plate to stir for 2 days to obtain a homogenous ink. It is worthy to mention that, during the ink preparation, the ionomer solution may strip Pt particles off the carbon supports and concentrate them within dried ionomer clumps due to poor attachment of Pt particles to their carbon support [53], which could be exacerbated by aggressive overnight stirring [53], ultrasonication [59], or ball milling, as explained later in this thesis.

2.2. Coating

CL is not a standalone layer and should be coated on a substrate. The following techniques were tried at AFCC for coating a catalyst ink on a substrate: i) printing using two printers, namely, Fujifilm Dimatix Inkjet Printer and Microfab Inkjet Printer, and ii) coating using a Mayer bar coater. To ensure maximal breakage of large Pt/C agglomerates in the ink, to prevent nozzle clogging in the printers, it was necessary to first sonicate the ink in a sonication bath for ~3 min and then use it for any of the mentioned printers. After coating, the sample could either be kept on a heated surface (at ~55 ºC) or just be left in ambient conditions (~24 ºC) to dry; in either case, the sample was further left in the open to ensure complete evaporation of all the volatile solvent. As it will be discussed in later chapters of this thesis, the two different drying temperatures led to different microstructures for the CLs by affecting density and aspect ratio of cracks. The mentioned printers and coater are described in the following sections.

2.2.1. Fujifilm Dimatix Inkjet Printer (DMP2800)

The Fujifilm printer, shown in Figure 2-1, made use of a piezoelectric cartridge for material deposition and was controlled by a software (Dimatix Drop Manager) installed on a computer. The software provided several capabilities, including setting patterning schemes, cleaning and printing scenarios (speed, direction, starting point, platen temperature, etc.), and monitoring quality of droplet formation on the cartridge nozzles. All the 16 nozzles of the cartridge had to be checked each time before starting the printing to ensure their optimal performance; if clogged nozzles were found at this stage, then one of the following actions would be performed depending on the situation: i) increasing the number and/or duration of automatic cleaning cycles during printing (the more the number/duration of the cleaning cycles, the shorter the ink would last), ii) cleaning the cartridge head by purging it several times with a 50/50 solution of IPA and DI water, using a syringe, or iii) using a new cartridge in case the cartridge failed after cleaning.

As indicated earlier, the printer had a platen for holding the substrate, whose temperature could be set to control the temperature of the substrate sitting on it. It also had some small holes on it which were connected to an internal vacuum system providing suction at the holes and resulting in better sticking of the substrate to the platen. Making use of this vacuum system ensured proper contact between the platen and the substrate and, consequently, uniform temperature of the substrate (i.e., uniform drying of the ink) during printing.

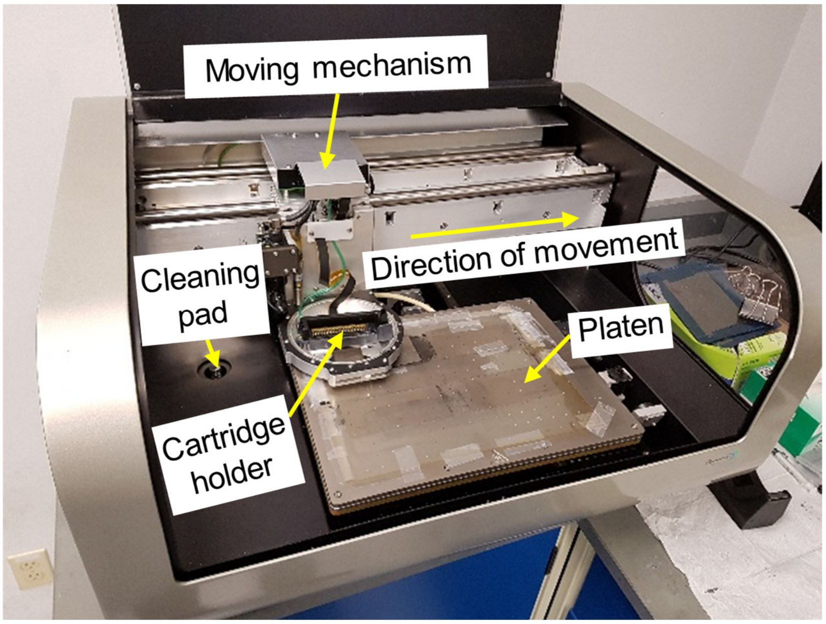

Figure 2-1. **Fujifilm Dimatix inkjet printer (DMP2800)**

To start printing, the cartridge was filled with the ink by a syringe, placed inside the cartridge holder in the printer, and then checked for optimal performance by the software. After ensuring proper operation of the nozzles and setting the options, the printing could be started. The cartridge, connected to a moving mechanism, moved horizontally across the platen with the specified speed and deposited the ink droplets on the substrate with the specified deposition rate. After completing a printing band, the platen moved vertically to print a new band. After printing a certain number of bands, based on the defined settings for the cleaning cycle, the moving mechanism moved the cartridge toward the cleaning pad to perform the cleaning.

While operating this printer at AFCC, the following issues were found to hinder its usage for this PhD program: i) clogging of the nozzles, requiring spending several hours on cleaning the cartridge using a syringe and the 50/50 solution of DI water-IPA, and ii) very slow rate of printing or small printing yield (1 day for printing 0.25 mg Pt/cm^2, equivalent to a CL thickness of ~7 μm, on a 10 cm × 40 cm area).

2.2.2. Microfab Inkjet Printer

The Microfab printer is shown in Figure 2-2. Unlike the Fujifilm printer which used 16 electrically operated nozzles in a cartridge to perform the printing, the Microfab printer used only a single jet which was connected to an ink container and operated by a pneumatic system. Moreover, unlike the Fujifilm printer in which the printing head moved during printing a band, the platen moved in a Microfab printer during coating. The single nozzle of this printer had a larger diameter than a nozzle of the Fujifilm printer, leading to formation of larger droplets and higher printing rates compared to the Fujifilm printer. The platen of this printer was also larger than the Fujifilm printer, making printing on larger areas possible, and had some vacuum holes on it for providing a better temperature control on the substrate. However, unlike the Fujifilm printer, the Microfab printer did not have a self-cleaning mechanism, and in case of blockage of its single nozzle, the operator had to stop the printing and clean the nozzle with injecting solvent or air through the nozzle using the pneumatic system. The Fujifilm printer could still perform the printing if only some of its nozzles became clogged, whereas printing by the Microfab printer would completely be terminated in the case of clogging of its single nozzle, giving it much less reliability.

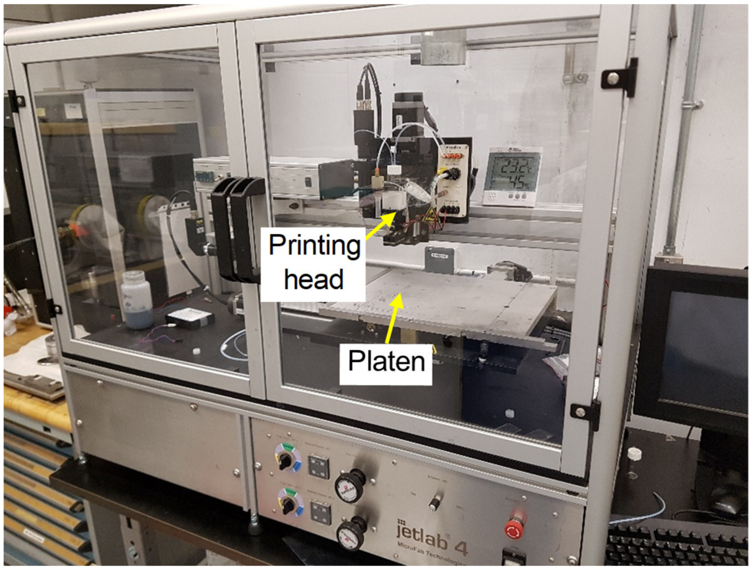

Figure 2-2. Microfab inkjet printer

There were many parameters which the operator had to play with to obtain a steady nice droplet for printing with a Microfab printer. Just like the Fujifilm printer, formation of ink droplets and their quality had to be checked before starting the printing. Another drawback of this printer was its much less control over the printing rate due to its usage of a pneumatic system for ink injection compared to the electrical injection system of the Fujifilm printer. Aside from the instability of the device due to pressure fluctuations of the pneumatic system and not having a self-cleaning mechanism, the vacuum system of the device did not work properly due to huge pressure drop through the system. In fact, for making vacuum on the platen, the printer used the same pneumatic pump which it used for injecting the ink. Overall, during operation of the device, it was found that the pressure fluctuations of the pneumatic system made the printer very unstable and inaccurate in terms of producing uniform and reproducible coatings, which hindered its usage for the purposes of this project.

2.2.3. Mayer Bar Coater

As shown in Figure 2-3, in a Mayer bar coater, a chunk of ink was poured onto the substrate, and the ink was coated on the substrate simply by moving a rod over it. Different areal Pt loadings of catalyst (or different CL thicknesses) could simply be made using coating rods with different grades. To clarify more, a certain grade of the coating rod had grooves with a certain spacing, which would control the amount of ink and, thus, thickness of the coating. The coating speed (adjustable) and quality were quite high. On the other hand, Mayer bar coating mimicked the same roll-coating process used for mass production of CLs in industry at the time of this PhD program. Accordingly, this method was used for preparing CL samples for this project. This method, however, was found to exert a huge amount of shear on the ink during coating, which may give the CLs anisotropic microstructure and conductivity. This is further discussed in Chapter 5.

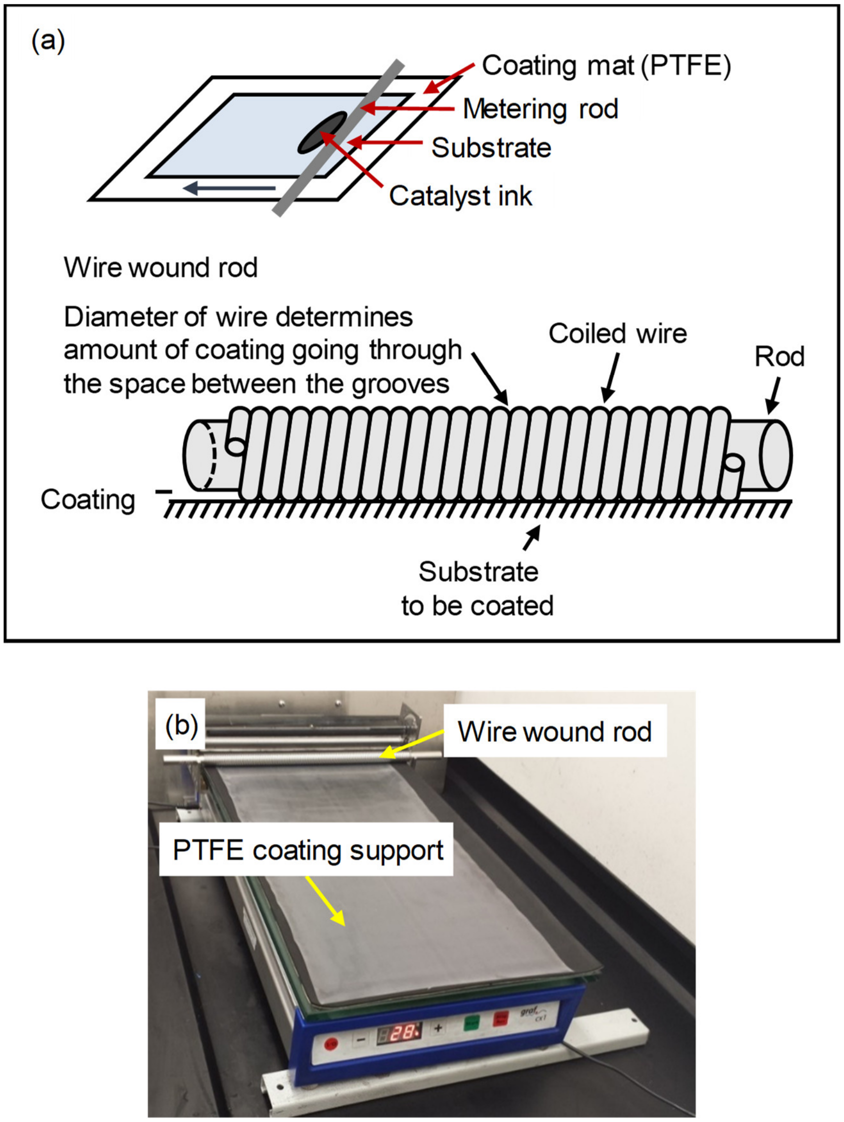

Figure 2-3. **Mayer bar coater: (a) a schematic of the coater and its basics of operation, and (b) a picture of the used Mayer bar**

2.3. Decal Transfer Technique

Normally, in the conventional method of MEA fabrication (see Figure 2-4), a CL is first coated on a dummy substrate (normally ethylene tetrafluoroethylene (ETFE)), also called decal, and then transferred onto the membrane by hot-pressing to construct the CCM in a process called “decal transfer” [60-64]. The purpose of hot-pressing is transferring the CL from its dummy ETFE substrate to the membrane by providing proper conditions of transfer (mainly related to surface energies of the different layers).

In fact, since the membrane absorbs water and solvents [65, 66], it is quite hard to coat a homogeneous and uniform CL by directly coating the ink onto the membrane; water and solvent absorption vary in different parts of the membrane, which makes the coated CL on the membrane to dry nonuniformly. Further, the membrane swells during coating because of the absorption of water and solvents, which makes the CL even more nonuniform and nonhomogeneous. Severity of these issues depends on several factors, such as coating technique, ink formulation, and type of the membrane. Accordingly, in the current practice, CLs are first coated on the hydrophobic ETFE and then transferred onto the membrane by hot-pressing, which results in a much more uniform and homogenous CL. Nonetheless, directly coating on the membrane is still desirable to eliminate the decal transfer step and make the coating process simpler and, thus, cheaper. This is currently an active area of research, and several fuel cell companies, such as AFCC, are trying to improve their techniques to be able to directly coat the CL on the membrane while mitigating the nonuniformity and nonhomogeneity issues. For instance, one mitigation strategy could be printing the CL band by band using a printer, as opposed to printing the whole layer at once using a coater. This was the main motivation behind trying the inkjet printers in this thesis. However, since the printing techniques were not fully developed at the time of this project, the produced CLs by the printers proved to be very nonuniform in terms of thickness, which made the author of this thesis to abandon the printers and proceed with the Mayer bar coater and the decal transfer process.

The usual decal transfer process at AFCC, optimized for the cleanest maximum transfer of a CL from an ETFE decal to a membrane, had two main steps: i) drying the catalyst-coated decal under 150 ˚C for 5 min, and then ii) hot-pressing the catalyst-coated decal on the membrane under 150 ˚C and 15 bar for 3 min. The drying step was necessary to remove moisture from the CL and prevent formation of vapor during hot-pressing; vapor formation would lead to imperfect contact between the CL and the membrane and, consequently, incomplete transfer of the CL to the membrane. To protect the membrane during hot-pressing, the ETFE-CL-membrane layers were wrapped by PTFE sheets. To provide a uniform pressure distribution on the layers during hot-pressing, a piece of flexible rubber was placed on the layers, and then the whole rubber-PTFE-ETFE-CL-membrane-PTFE sandwich was placed in between two grafoil sheets to facilitate handling the sandwich after hot-pressing; otherwise, the two end rubber and PTFE sheets would stick to the hot-press jaws, which would damage the CL when the jaws would get separated after hot-pressing. The drying step was simply performed in the hot-press by placing the materials on top of the lower jaw, without putting the rubber and upper graphoil sheets on top and without closing the jaws. After the drying, the layers were taken out from the hot-press and gently rolled by a roller from center outward in different directions to push the generated vapor out from the interface between the CL and the membrane. Afterwards, the rubber sheet and, then, the upper grafoil sheet were placed on top, and the whole sandwich was placed in between the jaws. After hot-pressing and separating the rubber and top grafoil sheets (normally stuck together at this point) from the rest of the layers, the layers were again gently rolled in the same way and put on a table to cool down. At the end, the membrane (having the CL transferred to it) was kept straight, and the ETFE layer was peeled off to prevent damaging/changing the CL by bending/stretching the membrane. As shown in Figure 2-4, hot-pressing may also be performed a second time during assembly of the MEA layers to enhance structural integrity of the MEA; for conciseness, Figure 2-4 does not show the described intermediate decal-transfer steps.

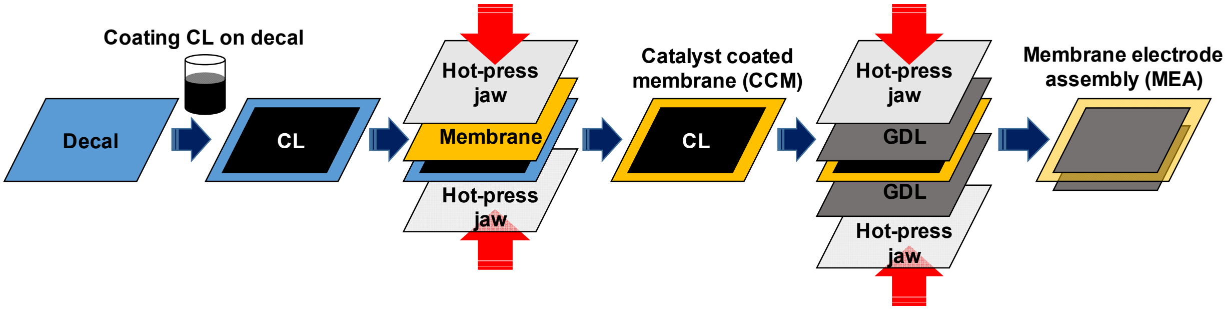

Figure 2-4. MEA fabrication, where CLs undergo two hot-presssing stages

2.4. Suitable Substrates for Thermal and Electronic Conductivity Tests

Reducing the substrate signal in the tests was crucial to increase the signal to noise ratio, leading to enhancement in accuracy (or reduction in uncertainty) of the tests. The substrate resistance is in parallel to the CL resistance in the in-plane tests and in series in the through-plane tests. Thus, to minimize the substrate signal, a highly thermally/electronically insulating substrate was needed for the in-plane tests, while a highly thermally/electronically conductive substrate was needed for the through-plane tests. Two available substrates were: i) ETFE decal, which is completely electronically insulating and has a low thermal conductivity (~ 0.17 $W \cdot m^{-1} \cdot K^{-1}$), and ii) aluminum (Al) foil, which is highly conductive both thermally and electronically (conductivities of ~ 205 $W \cdot m^{-1} \cdot K^{-1}$ and 37×10^6 $S \cdot m^{-1}$). Accordingly, these substrates were chosen for the tests. As shown in Chapter 3, it was ensured through a set of microstructural properties tests that CLs coated on these substrates would have the same microstructure.

2.5. Dry Milling the Catalyst Powder

Ball milling has been extensively used in literature for changing the structure of graphitic materials [67-75]. In this process, the material is mechanically grinded by steel or, more commonly, zirconia balls in a ball mill with a rotation speed of ~ 60-900 rpm. This process could be performed in dry conditions or in presence of a solvent/surfactant if surface modifications are desirable [73, 75]. Dry ball milling (or in short, dry milling) of graphite could lead to: formation of carbon nanoarches [67], nanoporous graphitic structures by ball milling in ambient temperature [68], and curved or closed-shell carbon nanostructures (onion-like structures) by bending the graphene sheets [69]. Similar bending effects have also been observed for dry milling of carbon blacks [72]; specifically, Ref. [72] reported enhancement of crystalline region of carbon blacks and graphitized carbon blacks as well as gradual change in the shape of carbon blacks from polyhedron to sphere by increasing the dry milling time. Aside from these effects, mechanical energy of the colliding balls could easily break and build chemical bonds [76]. For most of the carbon black types, primary carbon particles almost never exist in isolation but are strongly fused together by covalent bonds in aggregates [77-80]. During ball milling of the aggregates, all carbon blacks achieve a maximum level of breakdown in less than 30 minutes leading to enlargement of surface area due to wedging of the fragments; further ball milling leads to collapse of the porous structure, new bonding between the particles, and compacting the aggregates into micro agglomerates with less surface area [75, 80]. In this thesis, dry milling was used to compact the Pt/C catalyst aggregates (before making the ink) as a way to reduce the porosity without changing the composition. However, as discussed in Chapter 4 and Chapter 5, other possible effects such as bending the peripheral graphene sheets of carbon particles and their transformation from a polyhedron shape to a spherical shape were speculated to have significant effects on the conductivities.

2.6. Different CL Designs

To perform a comprehensive parametric study, CLs with different compositions and microstructures were produced and measured. Composition was altered by changing the ionomer-to-carbon (I/C) weight (wt) ratio of the ink. A catalyst powder made from Pt nanoparticles supported on partially graphitized carbon black particles (Pt/C catalyst) with 50 wt% of Pt was used in all the inks. Altering the composition changed the microstructure as well. In addition, different microstructures were made by: i) dry milling the Pt/C catalyst powder (before making the ink) to reduce the porosity and change the morphology of the aggregates, and ii) changing the drying temperature of the ink (after coating) to induce cracks. In the dry milling step, dry catalyst powder was grinded by zirconia balls on a jar mill for a desired length of time. A catalyst ink was prepared by mixing the (dry milled) Pt/C catalyst powder with water, solvent, and ionomer (Aquivion). The prepared ink was coated onto one side of ETFE sheets for in-plane tests and Al foils for through-plane tests, using the Mayer bar coater. To enable deconvolution of the bulk signal of a CL from the through-plane measurements, different thicknesses of the same ink (areal Pt loadings of ~150, 300, and 500 μg Pt·cm^{-2}) were made on ETFE and Al. Table 2-1 shows fabrication details of different CL designs coated for this study. Figure 2-5 shows a schematic of the CL fabrication process together with scanning electron microscope (SEM) images of three of the designs, indicating that the isotropy assumption could easily fail for cracked CLs. In later chapters, it is shown that cracks significantly affect the in-plane conductivities.

Table 2-1. **Fabrication details of different CL designs coated for this study**

Design #	I/C ratio	Dry milling time (hr)	Drying temperature (°C)
1	1.1	0 (None)	55
2	0.7	48	55
3	0.9	48	55
4	0.7	24	55
5	1.1	48	55
6	0.9	24	55
7	1.1	48	24 (Room temperature)
8	1.1	0 (None)	24 (Room temperature)

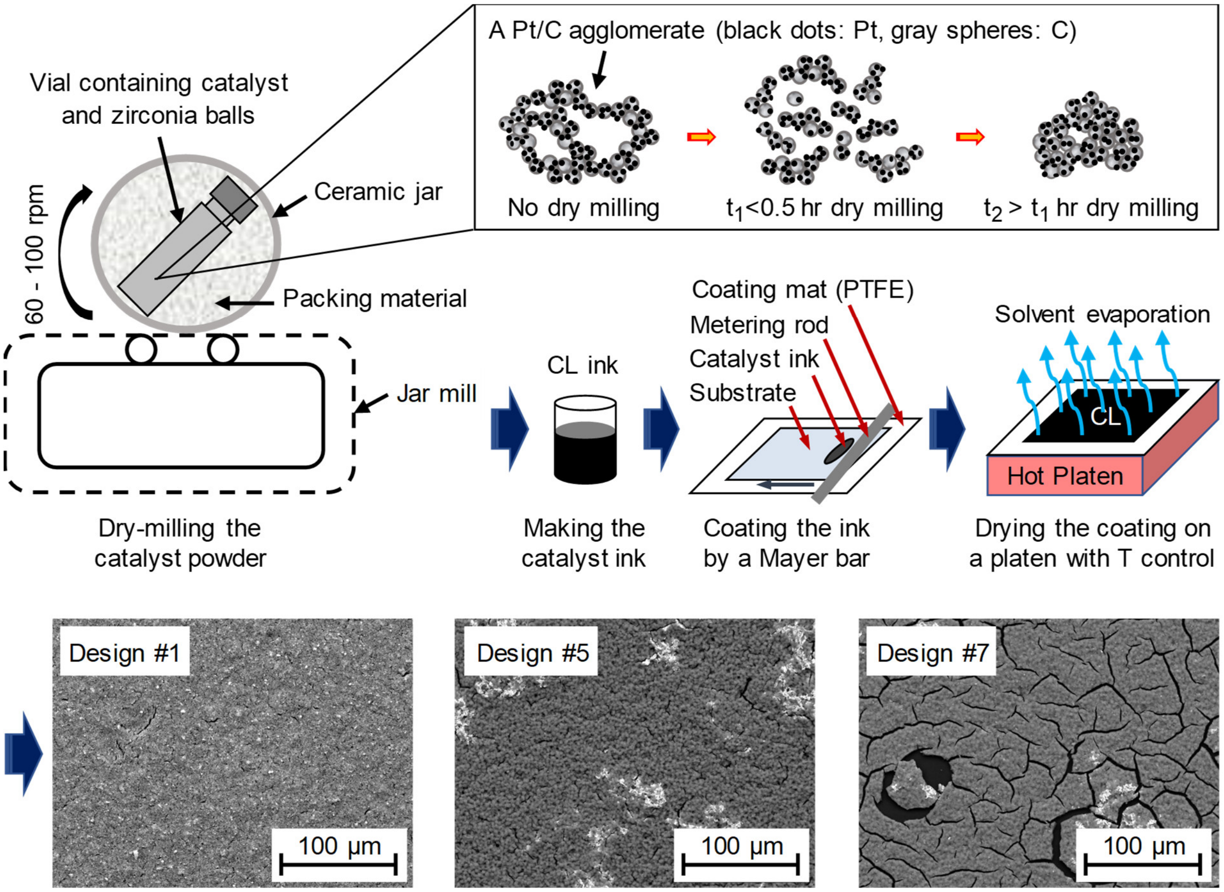

The least cracked CL

A moderately cracked CL

The most cracked CL

Figure 2-5. **A schematic of the CL fabrication process and SEM images of some of the coated designs showing differences in microstructure**

2.7. Conclusions

Among the different coating techniques tried in this thesis, Mayer bar coating was proved to be the most reliable one in terms of coating highly uniform CL thicknesses, required for accurate measurements of the conductivities, and having a high yield rate, which was necessary to keep up with the high rate of trials and errors during improvement of different testing procedures. As shown in the next chapter, the prepared CL samples for various designs showed a great deal of variety in terms of microstructural properties which made them suitable for the intended experimental parametric studies, described in later chapters. In the next chapter, procedures and results of microstructural characterizations are described in detail.

Chapter 3.

Microstructure of CLs

Knowing microstructure of CLs is of great importance in this thesis for two main reasons:

1. A geometrical model, representative of the complex microstructure of CLs, is needed for modeling the thermal and electronic conductivities. Microstructural data are further needed to be fed as geometrical inputs into the models.
2. As the developed characterization methods for measuring the conductivities entail using different thicknesses of fresh/hot-pressed CLs on different substrates, microstructural data of a CL under these conditions were needed to ensure the same microstructure, thereby validating the developed ex-situ characterization tools.

To explain the latter point mentioned above, studies on thermal and electronic conductivities of CLs in the current literature [5, 13, 24, 38, 39, 47-49] as well as the current thesis have used their own set of substrate(s) and sample preparation techniques. The coated CLs for the ex-situ characterizations in those studies also cover a broad thickness range. On the other hand, CLs in PEMFCs, manufactured for commercial use, are coated with a certain thickness on an ETFE decal first and then transferred onto the membrane by hot-pressing (which may be performed a second time during assembling the MEA). Accordingly, some questions have remained unanswered as whether the CLs on the substrates chosen for the ex-situ measurements differ from the CLs used in a fuel cell product. For these tests to be relevant, microstructure of the measured samples needs to be as comparable as possible to the microstructure of the CLs in an actual MEA. Accordingly, it is important to know whether the CL microstructure is influenced by changing the substrate type, hot-pressing, and CL thickness. Many studies could be found in the literature on the microstructure of PEMFC CLs [53-57, 81-92], and some works are available on the effects of hot-pressing on the performance of PEMFCs [93-96]. However, to the authors' best knowledge, the literature lacks a comprehensive and systematic study on the influence of substrate type, hot-pressing, and CL thickness on the CL microstructure and conductivities, which, as mentioned earlier, is needed to determine applicability of the ex-situ measurements.

In this chapter, a new geometrical model for CLs is developed to be used for modeling the conductivities. Then, the microstructural characterization tools, used in this thesis, are explained in detail and used to perform a systematic investigation of effects of substrate type, hot-pressing, and CL thickness on the microstructure of a typical CL design used in a typical PEMFC. Finally, the measured microstructural properties for all the CL designs of Table 2-1, needed as inputs for the conductivity models, are provided and explained.

3.1. Geometrical Modeling of Bulk Microstructure of CLs

High-resolution CL images [53] and molecular dynamics simulations of catalyst ink solidification [54] indicate that carbon particles cluster and form aggregate-like structures covered by a thin film of ionomer. To be consistent with the CL literature, in this work, the word “aggregate” is used to refer to a group of Pt/C particles covered by ionomer film, and the word “agglomerate” is used to refer to a Pt/C aggregate and its surrounding ionomer film together. In the carbon black literature, however, different definitions are used for aggregates and agglomerates [78]. SEM images of a CL (fractured in liquid nitrogen), reported by Ref. [53], show that existence of some microscale pores (~0.5-1 μm) between clusters of agglomerates, called “micropores” in this thesis, is possible and may be considered as another geometrical characteristic of a CL for modeling purposes. This observation was confirmed in this thesis (see Chapter 6, section 6.4.2, Figure 6-2). Further, crack characterizations in this thesis showed that CLs are generally covered by cracks, which are very slim and could range in size from 0.1 μm to 1 cm. Several approaches to geometrical modeling of CLs have been proposed in literature, none of which have considered effects of micropores or cracks to this point. Common approaches are: i) pseudo-homogeneous film or macro-homogeneous models (MHM) [97-99], ii) agglomerate models (AM) [100-103], and iii) microstructural reconstruction models (MRM) [104-106]. A brief review of these models is provided in Table 3-1.

In this study, a new geometrical model, shown in Figure 3-1, is proposed for a CL. This model does not have most of the limitations of the available models in literature, as described in Table 3-1. Further, the proposed model considers effects of micropores and cracks for the first time.

Table 3-1. **Summary of features of the available geometrical models for CLs in literature**

Model	Notes
MHM [97-99]	• Assuming a homogeneous configuration of Pt, C, and ionomer in the porous matrix of CL (treating CL as an effective porous medium) • Using prescribed transport properties for CLs, to be determined from experiments or structural models • Lacking microstructural or morphological details of the CLs
AM [100-103]	• Assuming structural units for CLs, as spherical Pt/C agglomerates filled with ionomer or liquid water • Assuming possible presence of a thin ionomer film around a cluster • Assuming possible presence of a thin liquid water film around a cluster • Existence of analytical solutions for specific cases
MRM [104-106]	• Obtaining a reconstruction of the CL microstructure from micrographs or random algorithms • Solving transport and reaction equations within the reconstructed microstructure via direct numerical simulation (DNS) • Necessity of performing numerical simulations with a suitable solver for a system of nonlinearly coupled partial differential equations on multiple domains (high calculation time and cost)

As shown in Figure 3-1, the proposed geometrical model consists of units of bulk catalyst and cracks whose sizes could cover a very wide range from a fraction of micrometer to a centimeter (as characterizations showed). The bulk catalyst units are made of overlapping agglomerates clustered around some micropores whose sizes were estimated to be tens to hundreds of nanometers. Overall, four scales of pores are considered in this geometrical model: i) micropores (tens to hundreds of nanometers) between the agglomerate clusters, ii) mesopores (tens of nanometers) between the agglomerates, iii) nanopores (a few nanometers) between the carbon particles inside the agglomerates, and iv) sub-nanometer pores inside the porous carbon particles. In this study, all the mentioned four types of pores are considered. Moreover, ionomer strands which may inhomogeneously be distributed in the mesopores are considered as part of the ionomer film around the agglomerates, and thickness of the ionomer film is considered to be uniform throughout the ionomer-covered surface of the agglomerates. Geometrical relations for the agglomerates and the Pt/C aggregates inside the agglomerates are provided in Appendix A. In this thesis, sizes of Pt/C aggregates were known from electron microscopy, and agglomerate sizes were calculated using the geometrical relations of Appendix A. Overlap angle calculations are explained in Chapter 6.

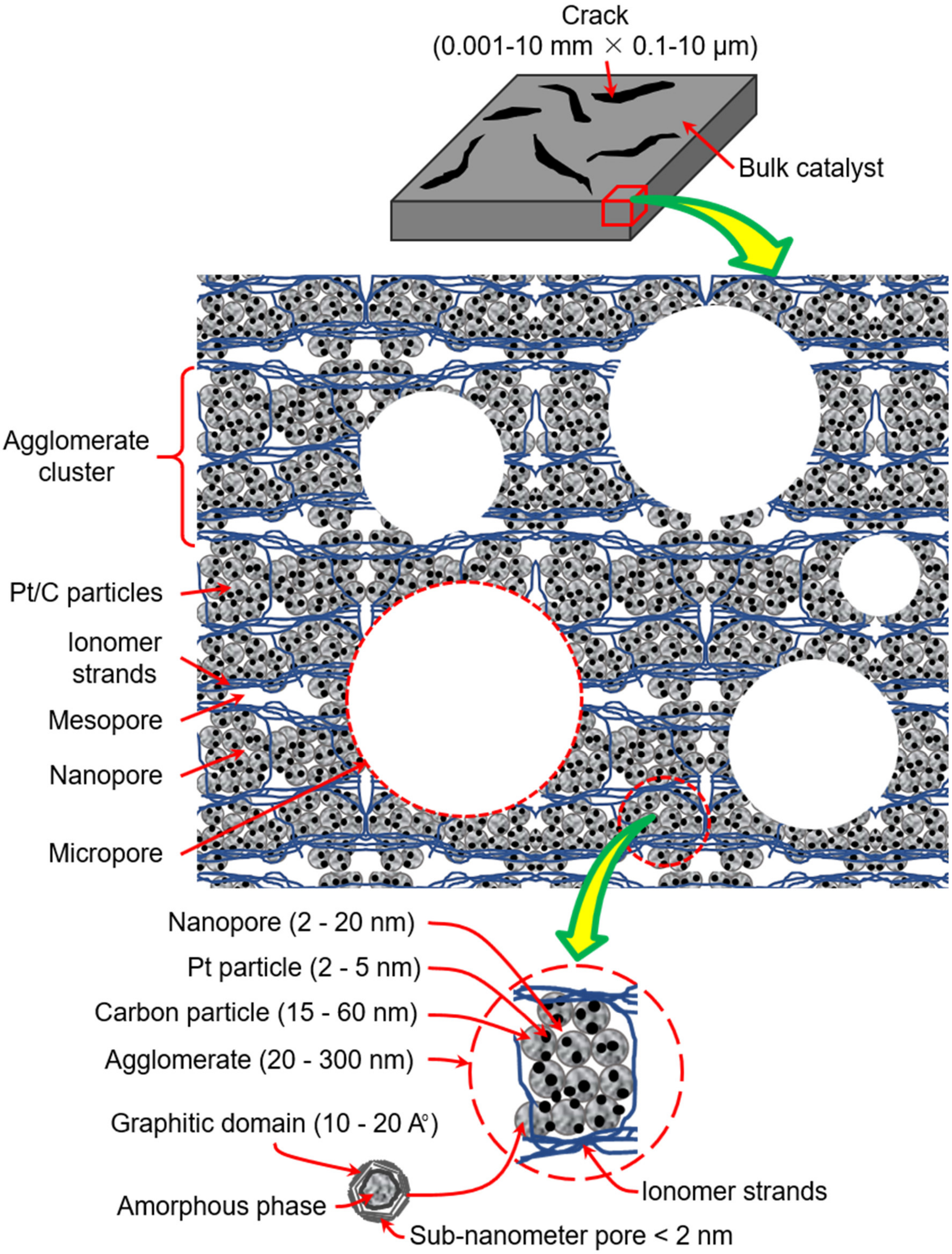

Figure 3-1. **Proposed geometrical model for CLs**

3.2. Measurements of Microstructural Properties

In this study, a set of experimental tools, described in Figure 3-2, were used to study the bulk and interfacial microstructure of CLs. As indicated in Figure 3-2, some of the properties were measured using two methods for cross-checking. In the following sections, each of the experimental tools, shown in Figure 3-2, are explained.

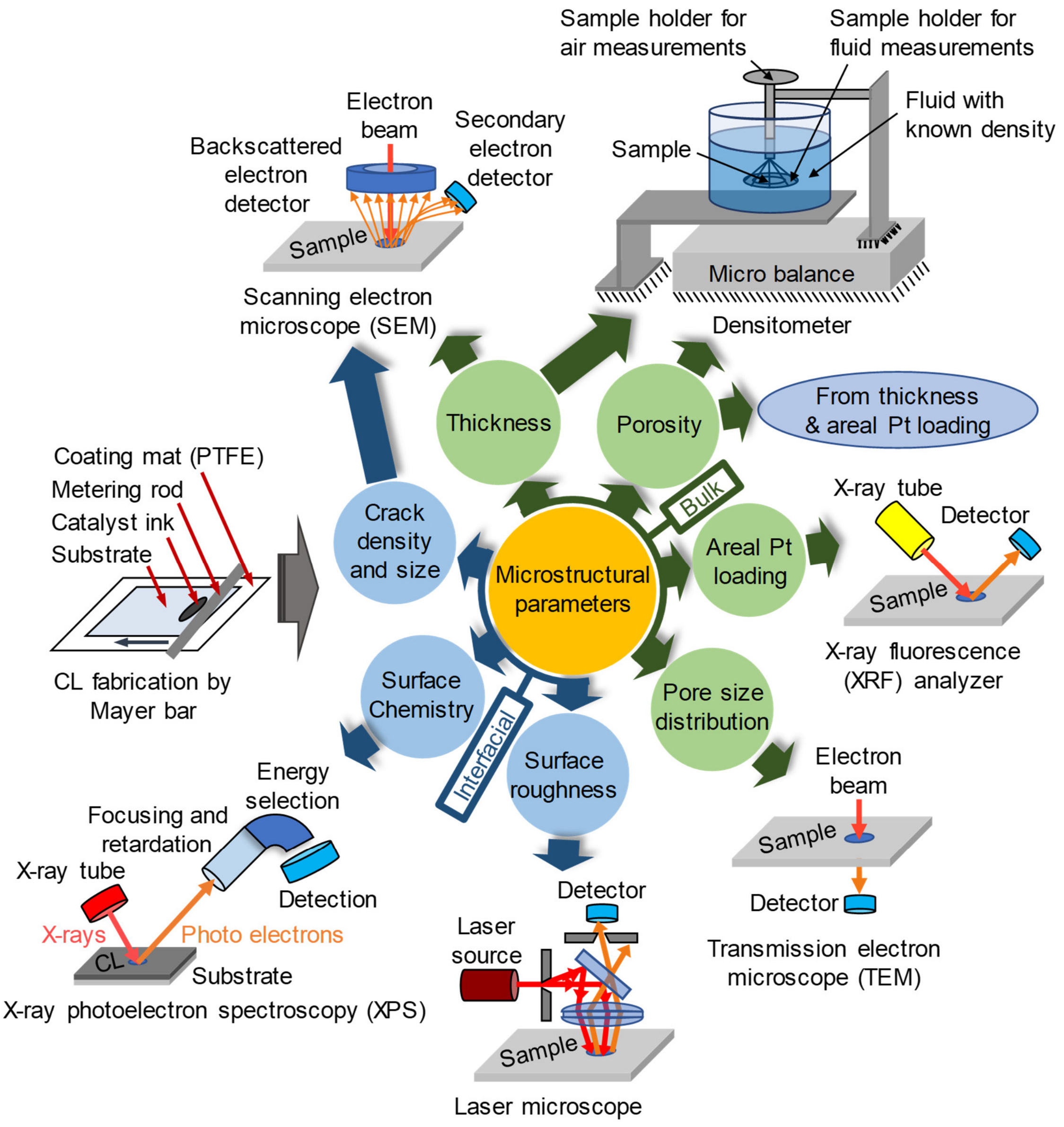

Figure 3-2. Experimental tools employed for the microstructural study

3.2.1. Areal Pt Loading Measurements by an X-ray Fluorescence (XRF) Analyzer

An XRF analyzer (Thermo Scientific, Niton XL3t) integrated with a portable test stand, providing a safe shielded test platform, was used to measure areal Pt loadings of catalyst-coated substrates (CCSs). Samples for XRF analysis were cut and measured from various locations of a CCS to obtain average areal Pt loading and its variation across the samples. A sample was placed inside the test stand with the XRF analyzer mounted on the stand. During operation, the analyzer emits excitation X-rays from an X-ray source inside the analyzer toward the target area of the sample and receives and analyzes characteristic X-rays emitted from the excited area, by a detector inside the analyzer. The detector detects each element by measuring its characteristic X-ray spectrum (unique X-ray energies acting like a fingerprint for each element), and it determines concentration of each element in the sample by counting the number of signals occurring at the energy emitted by the element.

3.2.2. Thickness Measurements by SEM

An Environmental SEM (ESEM) device at AFCC (Philips XL30 ESEM) was used for SEM imaging of the CLs. A standard method for preparing CL samples for SEM imaging was epoxy-embedding. As explained in Appendix B, this method proved to be very risky for CL thickness measurements, as it could potentially alter the CL cross section. Accordingly, another less risky method, called “freeze-fracture”, was developed for CL sample preparation for SEM imaging to cross-check the results. In this method, high quality cross sections of a sample for SEM imaging were made by cutting the sample under liquid nitrogen, which would ensure a clean cut by making the sample highly brittle. Selecting an appropriate cutter, however, depended on the material of the sample; for soft materials which would become highly brittle under liquid nitrogen, like Nafion membranes, a one-time cut by a sharp knife would easily do the job, whereas for harder materials which would not get brittle enough under liquid nitrogen to be cut by a one-time action of the knife, like ETFE and Al, a one-time cut could be performed by sharp scissors. To emphasize more, cutting a sample had to be performed only once in one action of the cutter to have a clean cut for the sample, or otherwise, blades of the cutter would smash the sample’s cross section during the second cutting action. The cut samples were then mounted vertically between carbon plates on a vertical SEM sample holder, shown in Figure 3-3, and then dried at 80˚C in a vacuum oven for ~1 hr to avoid absorption of ambient air humidity by the cold samples. Thickness of a CL was then measured by the SEM device (at AFCC) at various locations along its cross section, using the backscattered electron (BSE) detector, and average and standard deviation (STD) of the measurements were used in further analyses. Figure 3-4 shows SEM images of samples on different substrates along with average thicknesses and STDs of the thicknesses from the average values, clearly indicating high uniformity of the prepared CLs in terms of thickness.

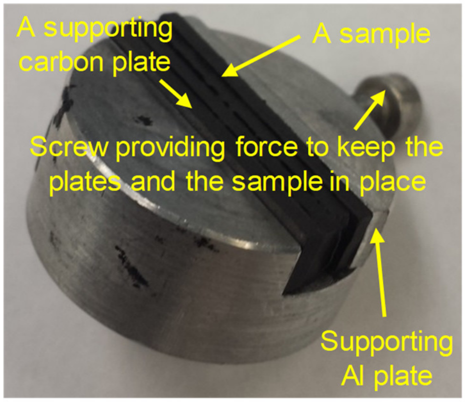

Figure 3-3. Vertical sample holder used for imaging cross sections of freeze-fractured samples

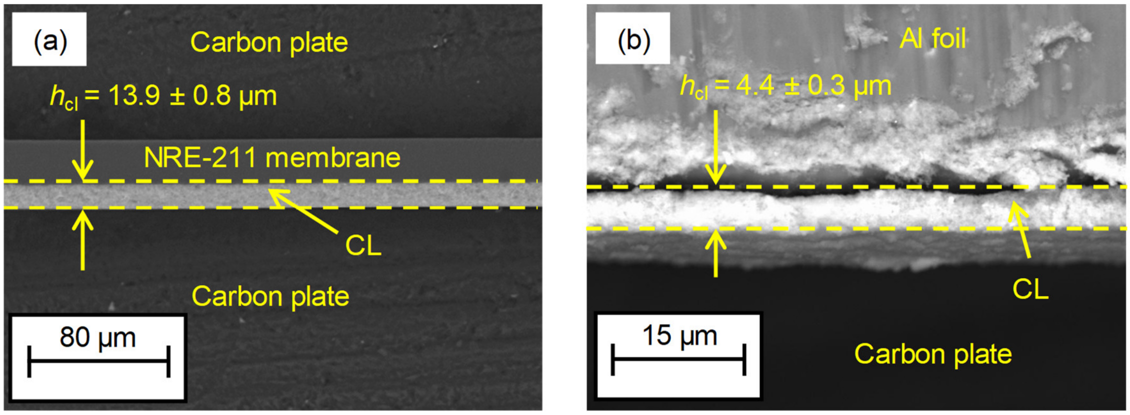

Figure 3-4. SEM images of cross sections of CL samples (errors: STDs): (a) decal-transferred from ETFE onto membrane, and (b) coated on Al foil

Accuracy of the thickness measurements was better than 0.3 μm for CLs transferred onto the membrane and better than 0.06 μm for CLs on Al, based on the pixel size and magnification of the taken SEM images. The mentioned accuracies should not be confused with the mentioned STDs in the images, as the latter show thickness variations along the CL samples. Since the STDs were much higher than the accuracy of the measurements, the STDs were used in error analyses.

A buoyancy thickness measurement method, called “densitometer”, was further developed for cross-checking the SEM results. Accordingly, two methods of thickness measurements by SEM on samples prepared by freeze-fracture and the buoyancy method consisted the package of thickness measurement methods in this project. In the following sections, these methods are explained.

3.2.3. Thickness Measurements by a Densitometer

This method is based on the Archimedes’ principle, stating that the upward buoyancy force exerted on an immersed object in a fluid is equal to the weight of the fluid displaced by the object. This principle allows for measuring the volume of an object by measuring the volume of the fluid it displaces upon submerging, using the measured weight change and the volumetric mass density of the fluid. Accordingly, if we measure the weights of an object in air and in a fluid with a known volumetric mass density using a densitometer setup (see the densitometer schematic included in Figure 3-2), volume of the object could be determined from:

$$V_{\mathrm{obj}} = \frac{W_{\mathrm{obj,ia}} - W_{\mathrm{obj,if}}}{\rho_{\mathrm{f}} g} \quad (3\text{-}1)$$

where V_{obj} is the object’s volume; ρ_{f} is the fluid’s density; g is the gravitational acceleration constant, and $W_{\mathrm{obj,ia}}$ and $W_{\mathrm{obj,if}}$ are the weights of the object in air and the fluid, respectively. One could also divide the numerator and denominator of Eq. (3-1) by the gravitational acceleration constant, g, and write this equation in terms of the equivalent masses shown by a microbalance as:

$$V_{\mathrm{obj}} = \frac{m_{\mathrm{obj,ia}} - m_{\mathrm{obj,if}}}{\rho_{\mathrm{f}}} \tag{3-2}$$

where $m_{\mathrm{obj,ia}}$ and $m_{\mathrm{obj,if}}$ are the masses shown by a microbalance for the object hanging from the balance in air and the fluid, respectively. See Figure 3-2 for a schematic of the densitometer setup and its sample holders for measurements in air and in a fluid. In this study, a density determination kit (Sartorius YDK01) integrated with an analytical balance (ML204T) was used to perform the measurements.

When a CL is submerged in water at room temperature, water penetration into the pores of the CL is negligible due to high surface tension of water at room temperature (72 mN·m^{-1} at 20˚C). See Figure 3-5 for a picture of a water droplet on the surface of a CL at room temperature; the obtuse contact angle of the water droplet on the CL surface shows hydrophobicity of the surface.

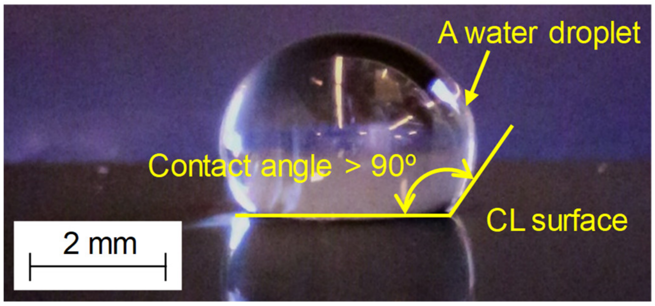

Figure 3-5. Image of a water droplet on the surface of a CL at room conditions (taken by a Dino-Lite Digital Microscope), showing its hydrophobicity

See Ref. [84] for further evidences regarding hydrophobicity of CLs. Making use of this property together with the Archimedes' principle, thickness of a CL coated on a substrate can simply be obtained from weight measurements of the CCS and the substrate (after removing the CL) in air and water. After performing such measurements on a sample in air and water and measuring volumes of the CCS and substrate using Eq. (3-2), thickness of the CL can be calculated using its area as:

$$h_{\mathrm{cl}} = \frac{V_{\mathrm{cl}}}{A_{\mathrm{cl}}} = \frac{V_{\mathrm{ccs}} - V_{\mathrm{sub}}}{A_{\mathrm{cl}}} \tag{3-3}$$

where h_{cl}, V_{cl}, and A_{cl} are the thickness, volume, and area of the CL, respectively, and V_{ccs} and V_{sub} are the volumes of the CCS and substrate, respectively. Due to negligible penetration of water into the CL bulk at room temperature, geometric volume of a CCS is measured from the water measurements at room temperature. Good agreement between SEM and densitometer results as well as the obtuse contact angle of a water droplet on a CL surface at room temperature support this claim (see Figure 3-5 and Figure 3-8).

3.2.4. Porosity Measurements by the Densitometer

Porosity measurements by the densitometer follow the same principle described in section 3.2.3. The only difference is that another measurement in a low surface tension liquid, capable of penetrating into the pores, should also be performed on a CCS, prior to removing the CL, to obtain the solid volume of the CL. In this study, n-octane with surface tension of 21.6 $\mathrm{mN \cdot m^{-1}}$ at 20˚C was used as the low surface tension liquid for porosity measurements. Assuming n-octane would fill all the pores, the total pore volume and porosity of the CL could be obtained from:

$$V_{\mathrm{p,cl}} = V_{\mathrm{geo,cl}} - V_{\mathrm{sol,cl}} \tag{3-4}$$

$$\varepsilon_{\mathrm{cl}} = \frac{V_{\mathrm{p,cl}}}{V_{\mathrm{geo,cl}}} \tag{3-5}$$

where $V_{\mathrm{p,cl}}$, $V_{\mathrm{geo,cl}}$, and $V_{\mathrm{sol,cl}}$ are pore volume, geometric volume, and solid volume of the CL, respectively, and $\varepsilon_{\mathrm{cl}}$ is porosity of the CL. The above volumes are obtained as:

$$V_{\mathrm{geo,cl}} = V_{\mathrm{geo,ccs}} - V_{\mathrm{geo,sub}} \tag{3-6}$$

$$V_{\mathrm{geo,ccs}} = \frac{m_{\mathrm{ccs,ia}} - m_{\mathrm{ccs,iw}}}{\rho_{\mathrm{w}}} \tag{3-7}$$

$$V_{\mathrm{geo,sub}} = \frac{m_{\mathrm{sub,ia}} - m_{\mathrm{sub,iw}}}{\rho_{\mathrm{w}}} \tag{3-8}$$

$$V_{\mathrm{sol,cl}} = V_{\mathrm{sol,ccs}} - V_{\mathrm{sol,sub}} \tag{3-9}$$

$$V_{\mathrm{sol,ccs}} = \frac{m_{\mathrm{ccs,ia}} - m_{\mathrm{ccs,io}}}{\rho_{\mathrm{o}}} \tag{3-10}$$

$$V_{\mathrm{sol,sub}} = \frac{m_{\mathrm{sub,ia}} - m_{\mathrm{sub,io}}}{\rho_{\mathrm{o}}} \tag{3-11}$$

where $V_{\mathrm{geo,ccs}}$ and $V_{\mathrm{geo,sub}}$ are geometric volumes of the CCS and substrate, respectively; $m_{\mathrm{ccs,ia}}$ and $m_{\mathrm{ccs,iw}}$ are masses of the CCS in air and water, respectively; $m_{\mathrm{sub,ia}}$ and $m_{\mathrm{sub,iw}}$ are masses of the substrate in air and water, respectively; $V_{\mathrm{sol,ccs}}$ and $V_{\mathrm{sol,sub}}$ are solid volumes of the CCS and substrate, respectively; $m_{\mathrm{ccs,io}}$ and $m_{\mathrm{sub,io}}$ are masses of the CCS and substrate in octane, respectively; and ρ_{w} and ρ_{o} are densities of water and octane, respectively. In this study, since the substrates (ETFE and Al) were non-porous, $V_{\mathrm{sol,sub}} = V_{\mathrm{geo,sub}}$, and the measurements of the substrates in octane were not necessary.

3.2.5. CL Thickness under Compression

Since the CL samples were put under mechanical pressure by clamping them between sensors during the ex-situ through-plane conductivity tests, there was a need to clarify if the CL thickness significantly changed under compression. Such a significant change could affect the conductivity values significantly as the thicknesses were directly used in data reduction to deconvolute the conductivities. Accordingly, in this section, investigation of such effects is explained.

To examine the behavior of CLs under compression, thicknesses of CCSs were monitored under contact pressures from 1 to 30 bar with accuracy of 1 μm using a custom-made testbed known as TUC-RUC (thickness under compression-resistance under compression) at AFCC. To make the effective thickness of a CL larger in the TUC-RUC device, two pristine CCSs were made into a sandwich by contacting them from their catalyst sides. The sandwich was then put in between the mechanical jaws of the TUC-RUC device for thickness measurements. Moreover, to detect any possible change in CL thickness due to hot-pressing/decal-transfer conditions, the same experiments were performed by the TUC-RUC device for hot-pressed CCSs. In addition, thickness of a pristine CL coated on ETFE was measured by SEM and compared to thickness of the same CL after decal-transferring it onto an NRE-211 Nafion membrane by hot-pressing. Thickness measurements at different contact pressures by the TUC-RUC device for fresh and hot-pressed CCSs and by SEM for the CL before and after decal-transfer did not show any meaningful change in the thickness which would go beyond the STDs in thickness or errors of the instruments. Thus, the SEM/densitometer thicknesses of fresh samples were used in deconvolution of the conductivities, and the relevant uncertainties in measurements of thickness were used in calculating uncertainties of the conductivities.

3.2.6. Porosity Calculations from Thickness and Areal Pt Loading Data (Theoretical Porosity)

Since composition of a CL (mass fractions of the components) is known from composition of the ink and since densities of different components are also known, volume fraction of each component can be calculated. Therefore, any set of measurements, which could yield information about volumetric spread of a component in the CL, could be used together with the compositional data to calculate a theoretical value for porosity. Thickness measurements (yielding volume per unit area) and areal Pt loading measurements (yielding mass of Pt per unit area) could provide such information. Such a calculated porosity is called theoretical because it would yield a value for all the pores inside the CL, including the open pores (accessible to gas) and the dead-end pores (inaccessible to gas). Details of such calculations are described fully in Ref. [48] and are not discussed here for conciseness; only the final formulas are mentioned here. Denoting the volume fractions of Pt/C particles (as a whole) and ionomer in a dry CL by $\phi_{\mathrm{Pt/C}}$ and ϕ_{ion}, respectively, the theoretical porosity could be obtained from:

$$\varepsilon_{\mathrm{cl}} = \phi_{\mathrm{p}} = 1 - \phi_{\mathrm{Pt/C}} - \phi_{\mathrm{ion}} \tag{3-12}$$

where ϕ_{p} is volume fraction of the pores (i.e., porosity of the CL), and $\phi_{\mathrm{Pt/C}}$ and ϕ_{ion} are obtained from:

$$\phi_{\text{Pt/C}} = \left(\frac{1}{\rho_{\text{Pt}}} + \frac{w_{\text{C}}}{w_{\text{Pt}}\rho_{\text{CB}}}\right)\frac{l_{\text{Pt}}}{h_{\text{cl}}} \tag{3-13}$$

$$\phi_{\text{ion}} = \frac{w_{\text{ion}}}{w_{\text{Pt}}}\left(\frac{1}{\rho_{\text{ion}}}\right)\frac{l_{\text{Pt}}}{h_{\text{cl}}} \tag{3-14}$$

where ρ_{Pt}, ρ_{CB}, and ρ_{ion} are densities of Pt, carbon black, and ionomer, respectively; w_{Pt}, w_{C}, and w_{ion} are mass fractions of Pt, carbon, and ionomer, respectively ($w_{\text{Pt}} + w_{\text{C}} + w_{\text{ion}} = 1$), and l_{Pt} and h_{cl} are areal Pt loading and thickness of the CL, respectively. h_{cl} can be determined by either densitometer or SEM, and ρ_{CB} (1.6 g·cm^{-3}) is different than density of bulk carbon/graphite (2.26 g·cm^{-3} [107]) due to porosity of the carbon particles themselves ($\phi_{\text{p,CB}} = 0.287$ [108]). This point was also mentioned by Ref. [48]. The porosity of carbon blacks (0.287) was further confirmed using a TEM-EDX (transmission electron microscope-energy dispersive X-ray spectroscopy) map analysis, developed by Dr. Jasna Jankovic at AFCC, who was a former AFCC scientist and is currently an Assistant Professor in the University of Connecticut.

3.2.7. Pore Size Distribution Measurements by a Transmission Electron Microscope (TEM)

Samples for TEM imaging were prepared by embedding small pieces of CCSs in TTE resin (trimethylolpropane triglycidyl ether and 4,4'-methylenebis (2-methylcyclohexylamine)), microtoming thin (~100-200 nm) TEM slices using a Leica Ultracut UCT ultramicrotome (Leica Microsystem, Wien, Austria), and depositing the TEM slices on 100-mesh Cu TEM grids. TEM imaging of the samples' cross sections was performed on FEI Tecnai Osiris S/TEM Transmission Electron Microscope, with 200 kV accelerating beam voltage, by scanning a focused electron beam in a raster and collecting the signal by the High Angle Annular Dark Field (HAADF) detector. Several TEM images in different areas were collected and analyzed for each sample. TEM imaging was chosen as the technique to obtain images for measuring pore size distribution because not only did it offer results which were comparable to a typically used 3D Focused Ion Beam-SEM (3D FIB-SEM), as tried by the author and Dr. Jasna Jankovic for some samples, but it also proved to be a faster approach through which a larger number of areas could be imaged in a shorter time. The taken TEM images were thresholded and analyzed using Fiji ImageJ software (available in the public domain) to separate and measure inter-agglomerate pores (segmented as black areas or 0 grayscale value in 8-bit images) and solid areas including intra-agglomerate nanopores (segmented as white areas or 255 grayscale value). The extracted data by ImageJ were then post-processed using an internally developed macro in Microsoft Excel software to: i) convert the measured pore areas and perimeters into their equivalent diameters ($4A_{\mathrm{p}}/P_{\mathrm{p}}$), ii) classify the diameters of the pores into bins (10 nm intervals), and iii) count the relative frequency of the pores falling into each bin.

3.2.8. Crack Characterization

In this thesis, cracks were characterized by their areal density on the CL surface as well as their aspect ratio (long over the short edge). Measurements were performed by analyzing surface images of CLs, taken by SEM. For this purpose, CCSs were mounted on SEM stubs by sticking the CCSs from their substrate sides on carbon tapes stuck onto the stubs; then, surface images of the CLs were taken by SEM. The images were then thresholded and analyzed by the Fiji ImageJ software to measure the surface crack density as well as area and perimeter of the cracks which were then converted into aspect ratios of the cracks by a simple mathematical manipulation. Cracks were generally found to penetrate through the whole CL thickness, as shown in Figure 3-6. Thus, the areal density of cracks could also be interpreted as their volume fraction inside the CL, which will come in handy for modeling the effect of cracks on the conductivities as shown in Chapter 6. Aspect ratio of cracks, defined here as the ratio of long over the short edge of a crack, is another parameter which will appear in the in-plane conductivity models. As shown in Figure 3-7, cracks are generally very slim objects with large aspect ratios. Therefore, length of a crack could simply be obtained by dividing its perimeter by a factor of 2 because thickness of slim cracks could be neglected compared to their length and, thus, one can write the relation $Perimeter \approx 2.0 \times (Length + Thickness) \approx 2.0 \times Length$ for perimeter of a crack. Thickness of the crack could then be obtained by dividing its area by the calculated length because $Area \approx Length \times Thickness$, which would then yield aspect ratio of the crack as $Aspect\ ratio = Length/Thickness$. Since longer cracks were expected to be more significant for in-plane conduction, the aspect ratios were averaged using crack length as the weight factor, and this weighted average was used in further analyses and calculations.

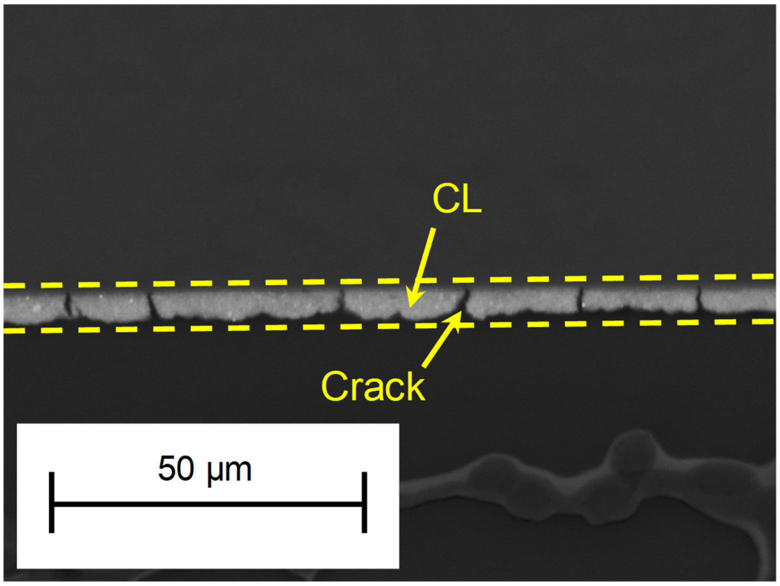

Figure 3-6. SEM image of a CL cross section (design #2), showing penetration of cracks through the whole CL thickness

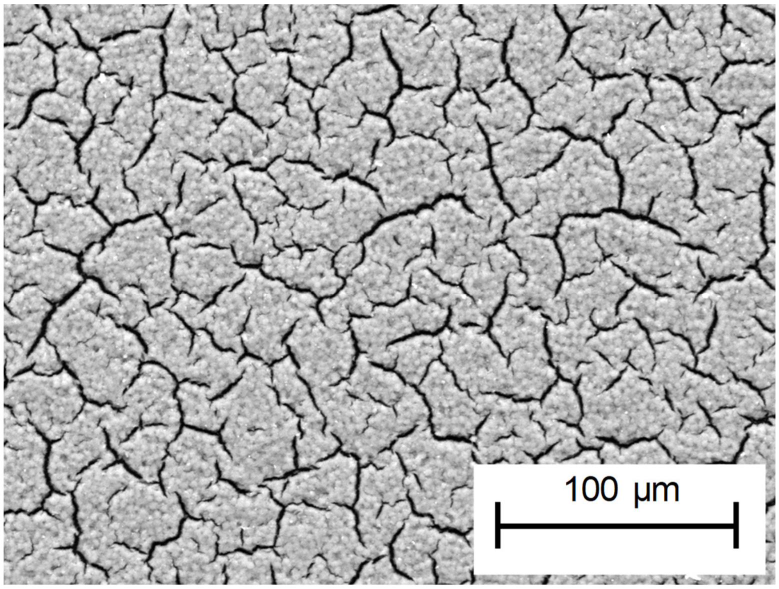

Figure 3-7. SEM image of a CL surface (design #2), showing slimness (large aspect ratio) of cracks

3.2.9. Surface Roughness Measurements by a Laser Microscope

Surface roughness of the CLs was measured by a laser microscope (Keyence VK-9500K Color 3D Profile Measurement Microscope) that worked based on penetration of a laser beam into roughness valleys on the surface of a sample. To ensure high flatness of the CLs and to eliminate any unevenness on the CCSs coming from the substrates, the CCSs were mounted on glass slides by sticking their substrate sides onto double-sided adhesive tapes stuck onto the slides. For each measurement, the laser beam scanned the sample surface at different depths, depending on the maximum depth of the roughness valleys, and, based on different reflections of the beam from the surface at different depths, topography of the surface was obtained by post-processing the reflection data.

3.2.10. Surface Chemistry by X-ray Photoelectron Spectroscopy (XPS)

Surface chemistry of the CLs was analyzed using an XPS tool (Kratos Analytical, Axis Ultra DLD) at SFU 4D LABS. XPS, like XRF, bombards the target material with X-rays. However, unlike XRF, which analyzes characteristic X-rays coming from several µm deep inside the material (due to the high 15-50 kV excitation energy), XPS analyzes photoelectrons emitted from the first 10 nm of the sample's surface (due to the relatively low 0-1200 eV excitation energy). Thus, unlike XRF whose signal comes from the bulk of the material, XPS is very surface sensitive, making it highly suitable for surface chemistry analyses. XPS graphs represent counts of photoelectrons per binding energy (in [eV]). Since kinetic energy of the photoelectrons is related to the strength of the atomic bond from which they are "knocked out", and the elements in the bond, XPS can distinguish both the types of bonds that the photoelectrons come from, as well as the chemical composition of a sample. To determine the composition, broad survey scans with energy ranges from 1200 to 0 eV are performed, while for finding the bonded state of an element (e.g., the fraction of CF_3 or C=C in a sample), high-resolution narrow scans with energy range of around 20 eV wide are performed.

In this study, XPS data of design #1 of Table 2-1 were taken and quantified to track changes in chemical composition of the CL surface, which could be imposed by different conditions such as different substrates, CL thicknesses, or hot-pressing. It should be noted that XPS signals taken for composite materials are generally hard to quantify, if not impossible, due to different sampling depths for materials with different densities. According to Beer-Lambert's law [109], penetration depth of X-rays is inversely proportional to the density of a sample. For CLs, carbon and ionomer have almost the same density of ~2,000 $kg\cdot m^{-3}$, and Pt has a density of 21,450 $kg\cdot m^{-3}$, which is very different than the other two components. However, for a typical CL with 50 wt% Pt in Pt/C catalyst, volume fraction of Pt is less than ~2%. For this reason, most of the scanned area of a CL by XPS consists of carbon and ionomer, and thus, assumption of a uniform sampling depth for CLs is quite reasonable. This assumption allows for quantification of the XPS signal taken from a CL for finding mass fractions of different components, which is more familiar and tangible than mass fractions of different chemical elements of the CL. Such quantification could also provide insight into interfacial and internal microstructure of CLs. One idea to quantify the XPS signal for a CL is to calculate the I/C ratio.

By performing a survey scan in an XPS measurement, the following information could be obtained from the XPS signal: i) atomic percentages of elements in the CL, including fluorene (F), carbon (C), sulfur (S), platinum (Pt), and oxygen (O), using areas of peaks from a broad survey scan, and ii) weight percentages of the different elements using the atomic percentages and molecular weights of the elements. However, a broad survey scan could not differentiate between C in the ionomer (C bonded to F) and C in the catalyst (C not bonded to F) because of the low resolution of such scans. Accordingly, weight percentages of all the elements in the CL including C were found from broad survey scans, and fractions of C in the ionomer and the catalyst were found either from narrow scans (followed by C 1s curve fitting) or from chemical composition of the ionomer (Aquivion), given by the manufacturer.

Overall, the I/C ratio was calculated using four different ways for cross-checking and validation. Three calculations were developed at AFCC by Dr Darija Susac, involving quantification of narrow scans, and one calculation was developed in this thesis without the need to perform any narrow scans. Results showed that all the calculations matched with less than 8% deviation. Further, good agreement was observed between calculations for a CL (design #1 of Table 2-1) scraped off of its ETFE substrate and calculations of this thesis on the surface of the same CL (the normal side as opposed to the substrate side) with less than 4% deviation between the results. Accordingly, only the fourth calculation/methodology was used in this thesis for further measurements as it could provide the same results without having to perform any high-resolution narrow scans.

In this thesis, to find the I/C ratio from the XPS data, weight percentage of ionomer was found by dividing weight percentage of F (found from a broad survey scan) by fraction of F in the ionomer (found from the chemical composition of the ionomer: $C_{14}F_{27}O_5S_1H_1$). For finding weight percentage of "C from catalyst", the weight percentage of ionomer was multiplied by fraction of C in ionomer (found from the chemical composition) to find weight percentage of "C from ionomer", and then the result was subtracted from the total weight percentage of C found from the survey scan. The final formula for calculating the I/C ratio, denoted by $l_{\mathrm{I/C}}$, could be expressed as:

$$l_{\mathrm{I/C}} = \frac{m_{\mathrm{ion}}}{m_{\mathrm{C\ from\ ct}}} = \frac{\dfrac{w_{\mathrm{F}}}{w_{\mathrm{F\ in\ ion\ from\ chem\ comp}}}}{w_{\mathrm{C}} - \dfrac{w_{\mathrm{F}}}{w_{\mathrm{F\ in\ ion\ from\ chem\ comp}}} \times w_{\mathrm{C\ in\ ion\ from\ chem\ comp}}} \tag{3-15}$$

3.3. Effects of Substrate, Hot-pressing, and CL Thickness

Using the tools explained above, effects of substrate type, hot-pressing, and CL thickness on the microstructure was investigated for design #1 of Table 2-1, which is a typical CL used in a typical fuel cell produced at AFCC. For this purpose, two thicknesses of ~ 8 μm and ~ 16 μm, corresponding to areal Pt loadings of ~ 250 and 500 μg Pt·cm^{-2}, respectively, were coated on ETFE sheets (100 μm thick) and Al foils (50 μm thick). Half of the samples were hot-pressed to include the factor of hot-pressing into the study.

3.3.1. Normalized Thickness Results

Figure 3-8 shows average CL thickness normalized by the relevant areal Pt loading for different cases, which is a measure of CL homogeneity (see Eqs. (3-13) and (3-14)). The uncertainties shown in Figure 3-8 (STDs) are all below 11 %. As shown in the figure, considering overlap of the error bars, densitometer and SEM measurements agree well with each other. This agreement along with the picture of a water droplet on the surface of a CL at room temperature, shown in Figure 3-5, confirm hydrophobicity of the CLs at room temperature. To test this observation in another way, weights of CCSs were monitored under DI water at room temperature in the densitometer setup for hours, and no weight change was observed. The overlap of the error bars in Figure 3-8 also shows that hot-pressing, substrate type, and CL thickness had insignificant effects on the normalized thickness. Insignificance of effects of hot-pressing and substrate type was also true for the CL thicknesses before normalizing them with the areal Pt loadings. The thickness increased, though, almost linearly with areal Pt loading, as expected. The observation that the normalized thickness remained constant by changing the areal Pt loading shows homogenous spread of Pt particles inside the CLs. Eq. (3-13) also shows that, in the case of homogenous distribution of Pt particles inside a CL with a certain composition, the normalized thickness should remain constant.

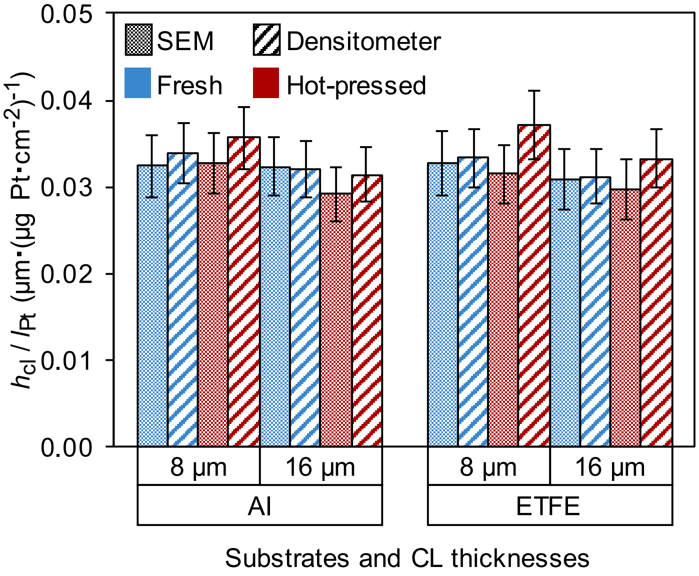

Figure 3-8. **Ratio of CL thickness over areal Pt loading, showing good agreement between the different methods, high homogeneity of the CLs, and insignificant effects from substrate type, hot-pressing, and thickness**

3.3.2. Porosity Results

Porosity results are shown in Figure 3-9. Overlap of the error bars shows good agreement between the different methods, which shows that porosity of a CL could simply be obtained by measuring its thickness and areal Pt loading which are much simpler measurements and entail fewer steps. All the uncertainties shown in Figure 3-9 (STDs) are below 4%. Uncertainties of the densitometer values as a direct measurement method were much lower compared to uncertainties of indirect derivations using the measured areal Pt loadings and thicknesses. More importantly, Figure 3-9 shows insignificant effects from hot-pressing, substrate type, and CL thickness on the porosity.

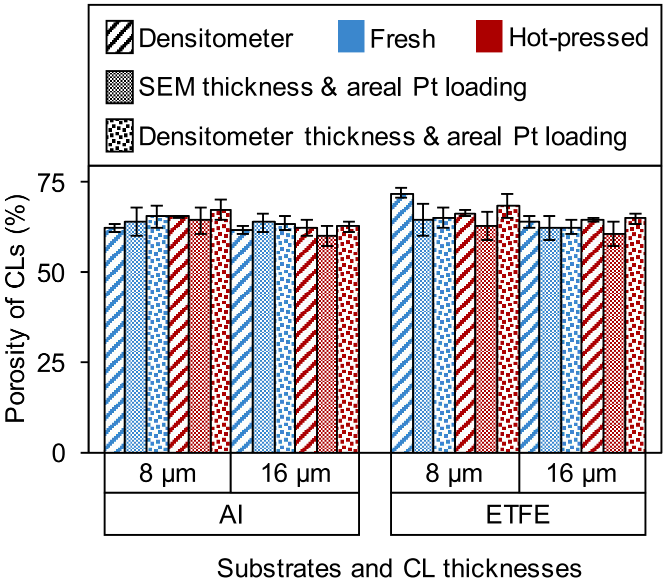

Figure 3-9. **Porosity from densitometer vs. theoretical values derived from areal Pt loading and thickness, showing agreement between the methods and no effect from hot-pressing, substrate type, and CL thickness**

3.3.3. Pore Size Distribution (PSD) Results

To distinguish pores from solid parts in a TEM image, contrast of the raw image was enhanced by the ImageJ software, and then, the (8 bit) image was thresholded to make pore pixels have a single greyscale value. A "watershed" segmentation algorithm was applied next, to consolidate boundaries between the pores. A raw and a processed image are shown in Figure 3-10 a and b. White regions in the images show the solid parts, and black regions show the pores. The processed image was analyzed by the software to measure areas and perimeters of the pores, which were then used in the developed macro in Microsoft Excel to yield the PSD. PSDs for all the CLs are shown in Figure 3-10 c and d, with Figure 3-10 c also showing the uncertainty bars (vertical bars: STDs of the measurements, and horizontal bars: 14 nm pixel size of the images). The PSDs show the same pattern and indicate insignificant effects from hot-pressing, substrate type, and CL thickness, within the error range. Further, on average, more than 90% of the resolved pores had sizes smaller than 180 nm, and there was no pore larger than 400 nm.

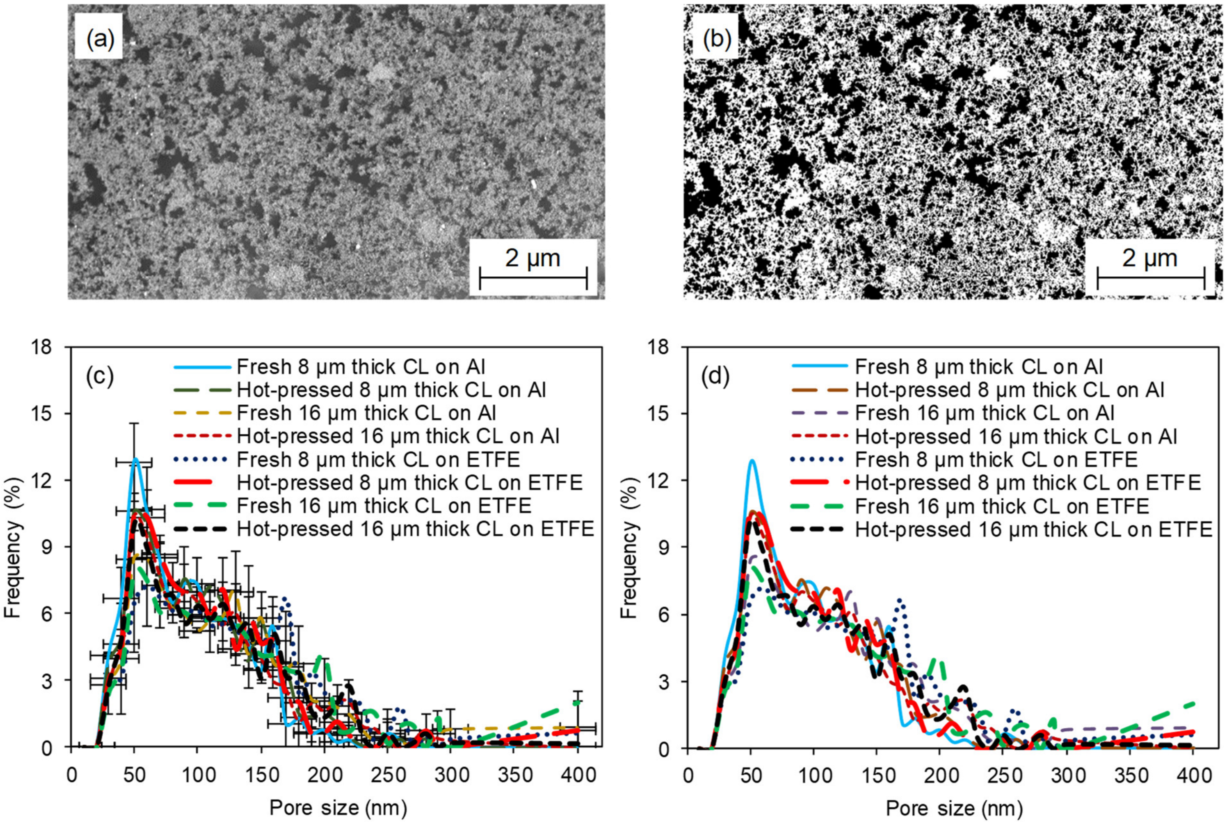

Figure 3-10. PSD results: (a) raw TEM image of a CL, (b) processed TEM image of the same CL, (c) and (d) the measured PSDs (one with the error bars and one without the error bars), showing insignificant effects from hot-pressing, substrate type, and CL thickness

Two interesting observations can be made by comparing the pore size distribution in Figure 3-10 d with results of N_2 adsorption porosimetry for CLs with similar compositions from Refs. [56, 64]. First, the N_2 adsorption results of Refs. [56, 64] do not show pore sizes larger than 100 nm, whereas the TEM image analysis of this thesis could find pores close to 400 nm. This difference could be due to the very different nature/principles of these measurement techniques and demands a more in-depth investigation of the underlying roots, which is not in the scope of this thesis. Another interesting observation is that despite these differences, both techniques yielded a peak size of around 50 nm.

3.3.4. Crack Characterization Results

The measured crack densities for all the cases were below 6% and within the uncertainty ranges of one another; uncertainty in this context refers to STD of the measurements. Accordingly, hot-pressing, substrate type, and CL thickness were found to have insignificant effects on crack density of the CL. However, larger crack aspect ratios were observed for higher CL thicknesses, as shown in Figure 3-11. This may be due to slower drying of higher amounts of catalyst ink in case of coating a higher CL thickness due to higher thermal resistance of the thicker ink, which could give the coating enough time to develop larger cracks as it dried. However, as crack densities for all the samples of this CL (i.e., samples of design #1 of Table 2-1 with different substrates, thicknesses, and hot-pressing) were small, the differences in crack aspect ratio were not expected to affect the ex-situ conductivity tests of this CL. This was further confirmed through ex-situ measurements of the conductivities. More clarifications regarding effects of crack properties on the conductivities are provided in Chapter 6, when cracks are modeled.

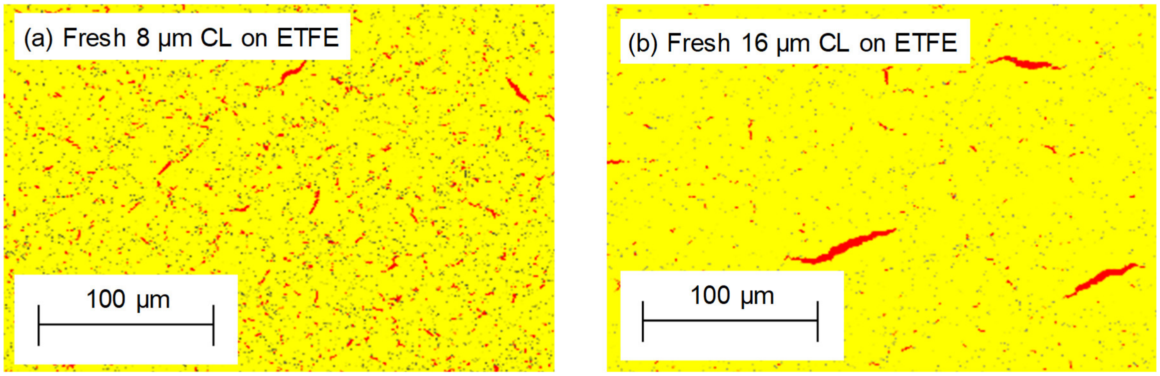

Figure 3-11. Processed SEM surface images of CLs (red: crack) for: (a) an 8 µm CL on ETFE, and (b) a 16 µm CL on ETFE, showing formation of larger cracks on the CL surface by increasing the coating thickness

3.3.5. Surface Roughness Results

Surface roughness results are shown in Figure 3-12 for bare substrates and the CLs. As shown in the figure, despite the very different surface roughness values of the Al and ETFE substrates, the CLs coated on them had same surface roughness, which did not change statistically with hot-pressing or increasing the CL thickness. Therefore, Figure

3-12 shows insignificant effects from hot-pressing, substrate type, and CL thickness on surface roughness of the CL. An implication of this conclusion is that contact resistances between a CL surface and surfaces of probe(s) or other samples/materials, used during measurements of thermal and electronic conductivities, remain the same with increasing the CL thickness. As explained in the next chapters, this enables deconvolution of the through-plane conductivities, as measuring these conductivities for a CL entails measuring resistances of different thicknesses of the CL in stacks of CL samples. The uncertainties shown in Figure 3-12 (STDs) are all below 15%.

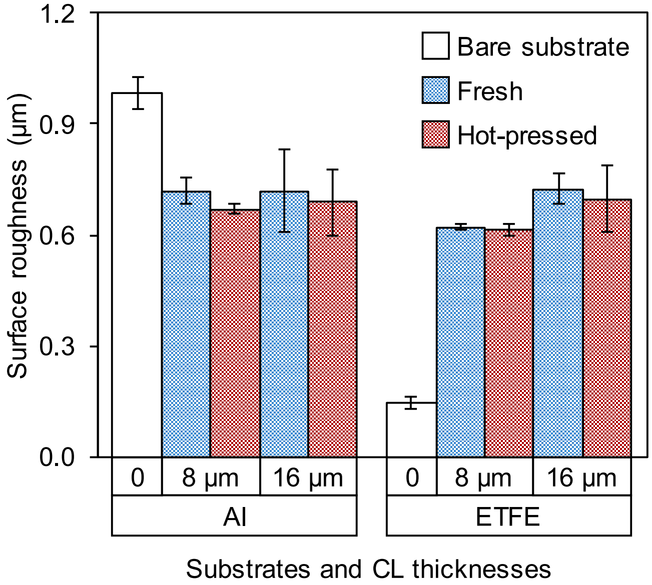

Figure 3-12. Surface roughness results for bare substrates and CLs coated on them, showing insignificant effects from hot-pressing, substrate type, and CL thickness (error bars: STDs)

3.3.6. Surface Chemistry Results

Chemical composition of the CL surface (normal side as opposed to the substrate side) is shown in Figure 3-13 for CLs with different substrates, thicknesses, and hot-pressing. As shown in the figure, composition of the surface did not change by hot-pressing, substrate type, or CL thickness. Hydrogen (an element of ionomer) is absent in the results because it cannot be detected by XPS due to participation of its single valence electron in chemical bonding [110]. The calculated I/C ratio for the CL surface was ~2.7 which was significantly higher than the value of 1.1 expected from the catalyst ink composition, suggesting that portion of the sample measured by XPS (the first 10 nm thickness below the surface) had a higher amount of ionomer than the bulk or average of the sample. On the other hand, XPS-based I/C calculations at AFCC for the same CL scraped off of its ETFE substrate showed the same value of ~2.7. This can be explained based on the agglomerate-like structure of CLs. The very surface-sensitive XPS technique, detecting only the first 10 nm of a sample's surface, only captured surface of agglomerate-like structures covered with ionomer and did not capture much signal from inside of the agglomerates filled with Pt/C particles; thus, an I/C ratio higher than the bulk I/C was measured. This observation can be served as a proof for having an agglomerate-like structure in CLs.

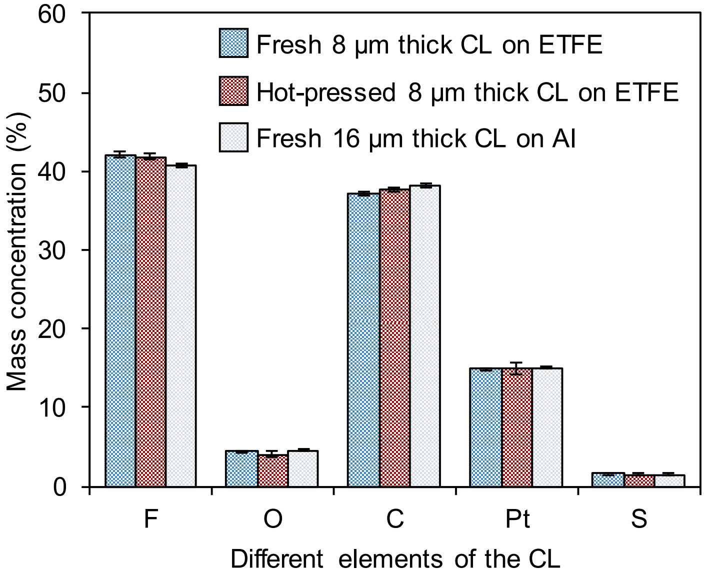

Figure 3-13. Chemical composition of the CL surface (normal side), showing insignificant effects from hot-pressing, substrate type, and CL thickness (error bars: STDs)

Similar XPS analyses and I/C calculations were performed for substrate side of fresh and hot-pressed CL samples on ETFE. The substrate (or decal) side was exposed by peeling off the CL by a tape as well as by decal-transferring the CL onto a Nafion membrane. Results showed that I/C calculations for fresh and hot-pressed decal side on the tape (exposed by peeling off) agreed with each other, and those calculations agreed with the calculations for the decal side on the membrane (exposed by hot-pressing). Further, the decal side I/C was much higher than the normal side I/C, as shown in Figure 3-14, indicating having more ionomer on the decal side compared to the normal side.

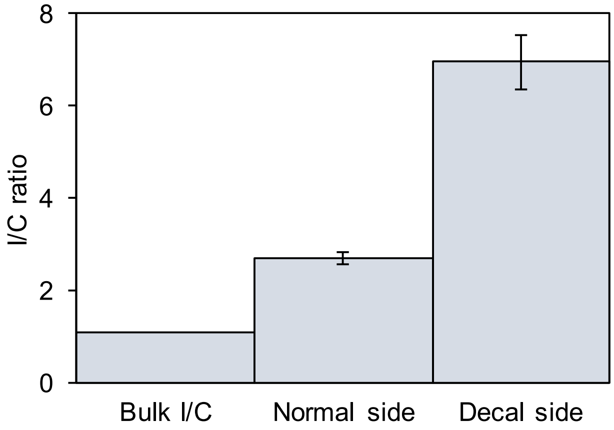

Figure 3-14. I/C ratio in different regions of the CL (data: average values of different measurements, error bars: STDs)

Having more ionomer on the decal side could also be visually verified by comparing the decal side to the normal side in front of the light (see Figure 3-15). The much shinier surface of the decal side could be a result of having more ionomer on the decal side, which could reflect the light and lead to such a shininess.

Figure 3-15. Pictures of normal and decal sides of the CL (decal side exposed by a tape), showing more reflection of light from the decal side

As discussed in later chapters, CLs are electronically conductive in the through-plane direction. Thus, the more ionomer on the decal side cannot be in form of a continuous film of ionomer, which was also confirmed by detecting Pt on the decal side in the XPS tests.

In another effort, TEM Energy Dispersive X-ray (TEM-EDX) maps of the CL cross section were taken to investigate depth of penetration of ionomer on the decal side into the CL bulk, by looking at the F signal. However, no thick film of ionomer was visible near the decal side, perhaps due to the very small thickness of the decal side ionomer which could not be resolved by the 14 nm pixel size of TEM-EDX maps. This means that the decal side ionomer should just be located on the decal side surface and should have a thickness of ~14 nm or less, much like the ionomer film covering an agglomerate in the CL bulk.

Thus, the higher amount of ionomer on the decal side should just be a normal part of the ionomer film covering the substrate side agglomerates, much like the bulk agglomerates with the only difference that the decal side agglomerates should be closer (less open) at their bottom parts ending on the decal side. The less-open agglomerates on the decal side may just contribute to a higher electronic contact resistance between the CL and its substrate. For heat conduction, the effect should be less because, unlike electrons, heat can still pass through the ionomer. As shown in later chapters, effects of such contact resistances will be deconvoluted during measurements of the bulk conductivities. Thus, having less-open agglomerates on the decal side does not affect the measurements and modeling of the bulk conductivities in this thesis. However, the resultant contact resistances could potentially affect the performance of an actual fuel cell as the decal side of a CL will be the CL surface contacting a GDL. To clarify more, decal-transferring a CL onto a membrane, in order to make a CCM, exposes the decal side which will then contact a GDL in an MEA. Investigation of such contact resistances and their effects on the fuel cell performance is a highly interesting area of research. However, such investigation is out of the scope of this thesis and is only suggested here as a future work.

Overall, effects of CL thickness, substrate type, and hot-pressing on the microstructure of the CL are insignificant. As discussed in the next chapters, among all the above microstructural properties, crack properties (i.e., density and aspect ratio) and porosity are key parameters for modeling the bulk conductivities. Accordingly, in the following section, measurements of these properties are presented and discussed for all the CL designs.

3.4. Porosity, Crack Density, and Crack Aspect Ratio for all the CL Designs

Figure 3-16 shows microstructural properties, including porosity, crack density, and crack aspect ratio, for different CL designs. Figure 3-16 a-c show that porosity decreases with increasing the I/C ratio and dry milling time but does not change with drying temperature of the ink. Reasons behind the decreasing trends could be: i) filling more pores with ionomer by increasing the I/C ratio, and ii) more compactness of the Pt/C aggregates with increasing the dry milling time.

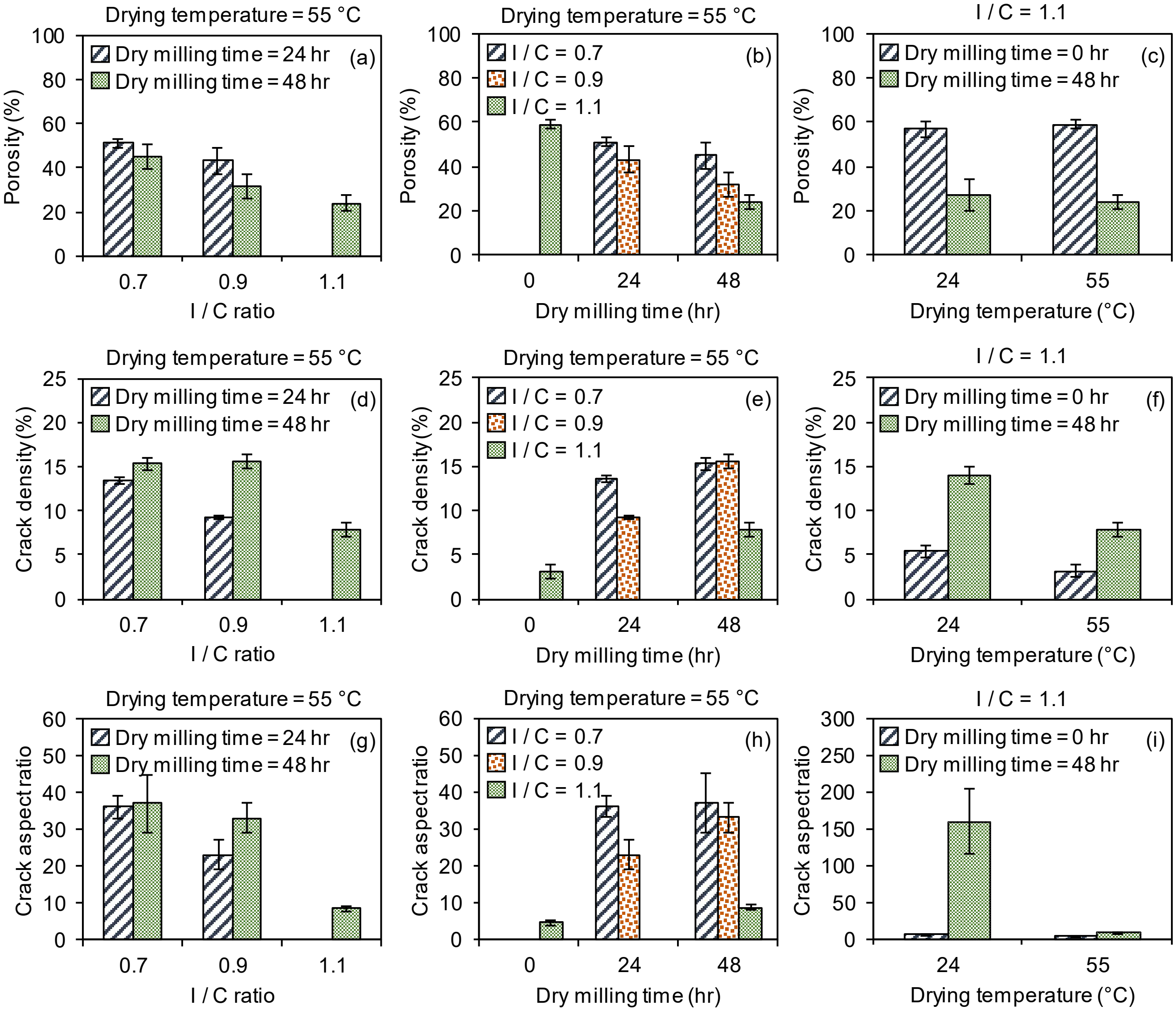

Figure 3-16. Microstructural parameters for different CLs (error bars: STDs): (a-c) porosity, (d-f) crack density, and (g-i) crack aspect ratio

Figure 3-16 d-f show that crack density decreases with increasing the I/C ratio and drying temperature but increases with increasing the dry milling time. Reasons behind these trends could be: i) enhancing structural integrity of the CL by increasing the I/C ratio (i.e., more ionomer as a binder), ii) quicker solidification of the ionomer, when the ink dries, by increasing the drying temperature, giving less time to the aggregates to move around and rearrange themselves and, thus, freezing the after-coating structure faster, and iii) smaller contacts between the aggregates (hence, weaker to forces from the solidifying ionomer) by increasing the dry milling time due to increase in sphericity of the particles [72].

Figure 3-16 g-i show that crack aspect ratio follows the same trends as the crack density does; the same reasons mentioned for the trends of crack density apply for explaining the trends of crack aspect ratio. Most of the CLs had aspect ratios below 40 except for design #7 with I/C=1.1, 48 hr dry milling time, and 24 °C drying temperature, which had a crack aspect ratio of ~160. This very high aspect ratio was a direct result of long dry milling and low drying temperature of the ink. As shown in Figure 3-16, this CL had one of the lowest porosities and one of the highest crack densities as well. Sample SEM surface images taken from all the CL designs are shown in Figure 3-17. The very different surface texture and microstructure of the different designs is clear in the images. As shown in later chapters of this thesis, the diverse surface texture of these designs was one of the main reasons leading to a diverse set of in-plane conductivities for the CLs.

One point is worth mentioning regarding the SEM surface images of Figure 3-17. The SEM images were acquired using the BSE detector. Since heavy elements (i.e., elements with high atomic numbers) backscatter electrons more strongly than light elements (i.e., elements with low atomic numbers), heavy elements appear brighter in an SEM image. Thus, the white marks observed in some of the images of Figure 3-17 are, in fact, made of the heavy element of Pt. This shows that, for the CL designs having the white marks in their images, some Pt particles could be removed from their carbon support by long dry milling and could make localized Pt aggregates (i.e., the white marks in the images). This effect is only observed for designs #2, #3, #5, and #7, whose catalyst powder was dry-milled for 48 hours. The designs with 0 or even 24 hours dry milling time, on the other hand, did not show this effect. For simplicity, these changes are not considered in the modeling work of this thesis. However, as also mentioned in Refs. [53, 59], such Pt detachment leads to loss of electrochemical surface area and, thus, lower catalytic activity, which is detrimental to fuel cell performance. Thus, aggressive dry milling of the catalyst powder is not desirable in general.

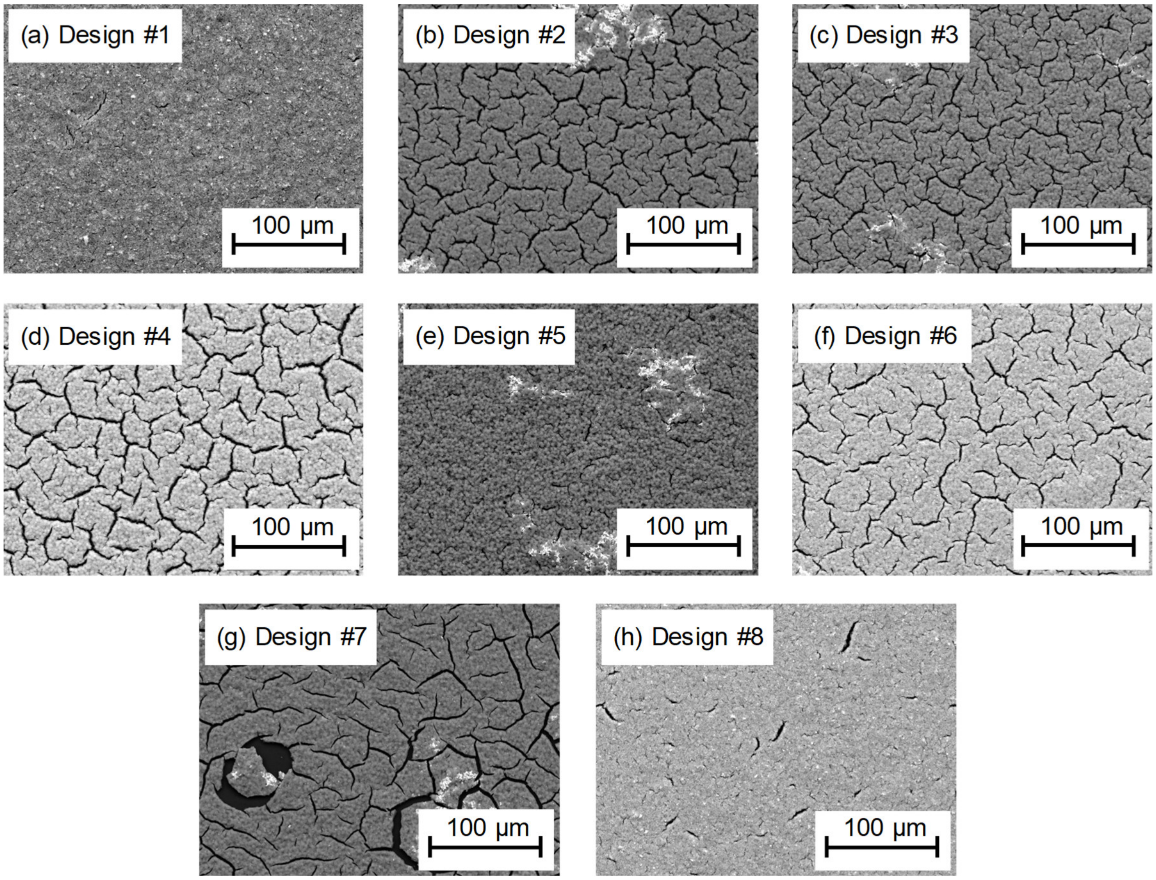

Figure 3-17. Sample SEM surface images of all the CL designs, showing the very different texture and microstructure of the CLs

3.5. Conclusions

In this chapter, a comprehensive experimental platform was developed to study microstructure of CLs from various aspects. The studied microstructural properties included various bulk and surface properties, including normalized areal Pt loading, porosity, PSD, surface crack density, surface crack aspect ratio, surface roughness, and surface chemistry. The developed platform was then used to investigate effects of key parameters involved in the CL fabrication, including substrate type, CL thickness, and hot-pressing, on the CL microstructure to understand any possible effects from the mentioned factors. This investigation was necessary to systematically confirm validity of the conductivity measurement procedures developed in this thesis, as the methods could use different substrate types, CL thicknesses, and hot-pressing.

Results showed that substrate type (among nonporous substrates), CL thickness (in the studied thickness range), and hot-pressing (up to 150 ˚C and 15 bar for 3 min) did not affect the microstructural properties. However, further studies showed that increasing the CL thickness beyond a certain limit would result in too much cracks in the CL, which would lead to loss of structural integrity of the CL and flaking off from the substrate, as also observed by Ref. [23]. Accordingly, the developed ex-situ measurement tools using different thicknesses of a CL are applicable for CL measurements provided that the CL thickness is changed in a controlled way to ensure the same amount of crack density as well as structural integrity of the CL. This condition was ensured for all the CLs of Table 2-1. The microstructural data of this chapter are tabulated in Appendix C.

Chapter 4.

Thermal Conductivity Measurements

Thermal properties measurement methods can be classified as: i) steady state, and ii) transient [41, 50, 51, 111-127]. The steady state methods have the advantage of simplicity of the analysis of the signal and the main disadvantage of long measurement times, whereas transient thermal properties tests are much quicker and more complex to analyze. In this thesis, first, efforts were made to initially evaluate through-plane thermal conductivity of a baseline CL (design #1 of Table 2-1) using a steady state and a transient method for cross-checking and comparison. Then, the steady state method was chosen for subsequent measurements, and the procedure for thermal conductivity tests was improved for CLs. Steady state measurements were conducted using a guarded heat flow (GHF) testbed, custom-made at Laboratory for Alternative Energy Conversion (LAEC) at SFU as per ASTM Standard E1530-11 [50]. Transient measurements were performed using a modified transient plane source (TPS) method for thin films [41], developed in this PhD program, on a Hot Disk TPS2500S Thermal Constants Analyser (Hot Disk AB, Gothenburg, Sweden and ThermTest Inc., Fredericton, Canada) at SFU LAEC.

4.1. Evaluation of the Thermal Conductivity Tools

Before conducting any measurements on the CLs, the tools were evaluated to understand their capabilities and limitations for thin films. In the following sections, principles of the tools are discussed, and then their performance is evaluated for different materials. As discussed later, in-plane thermal conductivity of a CL should play no role in heat transfer inside a fuel cell. Accordingly, only the through-plane testbeds are discussed in this thesis.

4.1.1. Steady State Measurements by the GHF Testbed

A schematic and a picture of the GHF testbed are shown in Figure 4-1. As shown in the figure, in the GHF test column, a sample is placed in between two fluxmeters, and the whole sandwich is then put in between a hot copper plate and a cold copper plate which act as the heat source and heat sink of the device, respectively. The hot plate is heated by an electrical element, whose power is controllable by a direct current (DC) power supply, and the cold plate is cooled by a water-cooled chiller, whose temperature can be adjusted. At first, the device had a hydraulic jack for adjusting contact pressure at the sample's cross section, which used to lose pressure over time. Accordingly, it was replaced afterwards with a pneumatic jack for better control over the pressure. As shown in Figure 4-1, the pneumatic jack is in contact with a small steel ball put on the hot plate, which serves two purposes: i) minimizing heat conduction from the hot plate to the jack, which is the major source of heat loss in the testbed, and ii) self-adjustment of the whole test column to achieve uniform contact pressure over the sample's cross section. The fluxmeters are made of Armco iron whose relationship of thermal conductivity versus temperature is known. The hot plate and the cold plate induce a temperature gradient across the sample, whose steady state value is used along with the value of the pumped heat to measure the total through-plane thermal resistance of the sample.

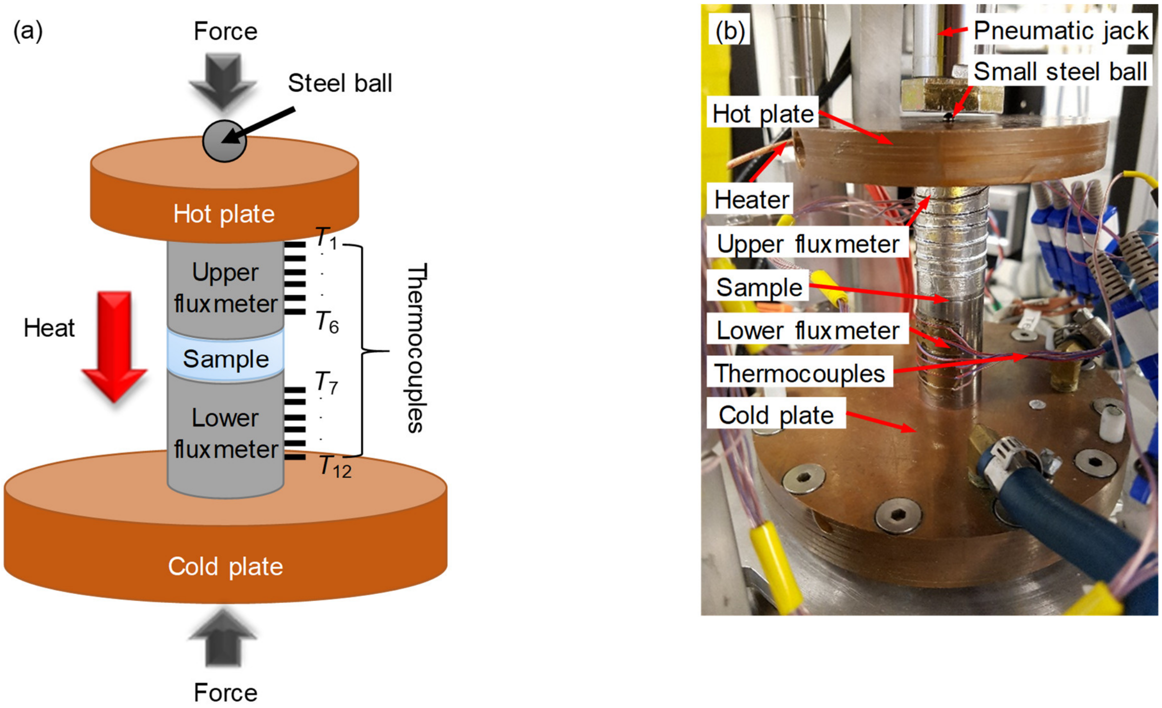

Figure 4-1. **GHF testbed: (a) a schematic, and (b) the real device at SFU LAEC**

Having measured the temperature difference across the sample and the passing heat, the total through-plane resistance of the sample can be calculated from:

$$R_{\mathrm{tot}} = \frac{\Delta T}{\dot{Q}_{\mathrm{ave}}} \tag{4.1}$$

where $\Delta T = T_{\mathrm{top}} - T_{\mathrm{bot}}$ is the temperature difference (T_{top}: temperature of the bottom surface of the upper fluxmeter; T_{bot}: temperature of the top surface of the lower fluxmeter), and $\dot{Q}_{\mathrm{ave}} = \left(\dot{Q}_{\mathrm{top}} + \dot{Q}_{\mathrm{bot}}\right)/2$ is the average heat passing through the sample ($\dot{Q}_{\mathrm{top}}$: heat entering from the top surface; $\dot{Q}_{\mathrm{bot}}$: heat exiting from the bottom surface). For each of the fluxmeters, the relation $\dot{Q} = k_{\mathrm{AI}} A_{\mathrm{sen}} (\partial T/\partial x)$ is used, in which k_{AI} is the thermal conductivity of Armco iron (calculated at average temperature of a fluxmeter), $A_{\mathrm{sen}} = 506.7\ \mathrm{mm}^2$ is area of the sensors (i.e., the sample's area), and x is the variable of location along a fluxmeter. The total resistance in Eq. (4.1) is summation of bulk thermal resistance of the sample and TCRs between the sample and the fluxmeters, as follows:

$$R_{\mathrm{tot}} = R_{\mathrm{b,s}} + TCR = \frac{h_{\mathrm{s}}}{k_{\mathrm{s}} A_{\mathrm{sen}}} + TCR \tag{4.2}$$

where $R_{\mathrm{b,s}} = h_{\mathrm{s}}/(k_{\mathrm{s}} A_{\mathrm{sen}})$ is the through-plane bulk resistance of the sample, TCR is summation of the TCRs between the sample and the fluxmeters, and h_{s} and k_{s} are thickness and through-plane conductivity of the sample, respectively. According to Eq. (4.2), there are two unknowns (k_{s} and TCR) for measurement of one thickness of a particular sample. Therefore, measurements of at least two thicknesses of the same sample, ideally with identical microstructure and surface features, are required to deconvolute the through-plane conductivity from the raw data. After conducting tests for two thicknesses of the same sample (h_1 and h_2), the through-plane conductivity can be deconvoluted from the total resistance data ($R_{\mathrm{tot,1}}$ and $R_{\mathrm{tot,2}}$) as:

$$k_{\mathrm{s}} = \frac{h_2 - h_1}{\left(R_{\mathrm{tot,2}} - R_{\mathrm{tot,1}}\right) A_{\mathrm{sen}}} \tag{4.3}$$

Alternatively, according to Eq.(4.2), since the total resistance (R_{tot}) is a linear function of the sample thickness (h_{s}), thermal conductivity of the sample (k_{s}) could be obtained by measuring at least two thicknesses of the sample and, then, fitting a line through the data of total resistance versus thickness; the slope of the line would be inversely proportional to the thermal conductivity of the sample, and the intercept would represent the TCR.

4.1.2. Transient Measurements by the TPS Testbed

Steady state methods are based on the simple Fourier law of heat conduction and, thus, do not have much variety. However, there are various transient methods based on sensor type, heat source, and data reduction method with different capabilities (see Table 4-1).

Table 4-1. Capabilities and limitations of available transient methods for thermal properties tests

Technique	Capabilities and limitations	Standard
Hot wire	• Suitable for liquids, powders, non-carbonaceous materials, and dielectric materials • Not suitable for anisotropic materials • Applicable for k<15 $W.m^{-1}.K^{-1}$ • Temperature range from room temperature to 1,500˚C • Long sensors and, consequently, long samples	ASTM C1113 / C1113M-09 [114]
Hot strip	• Capable of measuring thermal conductivity, thermal diffusivity, and specific heat [116] • Suitable for solids and fluids with low electrical conductivity [116] • Long sensors and, consequently, long samples	Not available
Transient plane source (TPS)	• Capable of measuring thermal conductivity, thermal diffusivity, and specific heat • Suitable for solids, liquids, and powders • Suitable for both isotropic and anisotropic materials • Compact sensors and, consequently, small samples	ISO22007-2 [120]
Laser flash	• Suitable for homogenous, isotropic, and opaque solids • Diffusivity values from 0.1-1,000 mm^2/s • Temperature range from 75-2,800 K	ASTM E1461-13 [122]
3ω	• For measurement of thermal conductivity [123] • Suitable for dielectric solids [123] • Temperature range from 30 to 750 K [123]	Not available
Differential photoacoustic	• For measurement of thermal conductivity of thin films [125]	Not available
Pulsed photothermal displacement	• For measurement of thermal diffusivity of solids [126]	Not available
Thermal-wave	• For measurement of thermal diffusivity of high temperature superconductors [127] • Temperature range from 10 to 300 K [127]	Not available

Schematics and pictures of the TPS device are shown in Figure 4-2. The TPS thin film sensor, shown in Figure 4-2 d, consists of a 10 μm thick double spiral nickel element, which is sandwiched between two 25 μm thick Kapton layers via some adhesive material [120]. According to the existing TPS method for thin films [120], the sensor should be sandwiched between two equivalent pieces of a sample supported by a background material, as shown in Figure 4-2 c. In this study, two stainless steel blocks (SIS2343) were used as the background material, as shown in Figure 4-2 a.

Conventional Data Reduction Method for TPS Thin Film Measurements

In the conventional TPS method for thin films as per ISO22007-2 [120], after obtaining temperature difference between the nickel sensor and the background material from TPS measurements, the full details of which can be found in Appendix D, effective thermal conductivity of the materials between the sensor and the background material can be found from the following relation:

$$k_{\text{eff}} = \frac{EPh_{\text{sen-bm}}}{2A_{\text{sen}}\,\Delta T_{\text{sen-bm}}} \tag{4.4}$$

where EP is the constant electric power of the sensor; $h_{\text{sen-bm}}$ is the thickness of the materials between the sensor and the background material (comprising the Kapton layer as well as the adhesive layer of the sensor), $A_{\text{sen}} = 727\ \text{mm}^2$ is the area of the sensor, and $\Delta T_{\text{sen-bm}}$ is the temperature difference between the nickel sensor and the background material (i.e., the temperature difference across all the materials in between).

As per ISO22007-2 [120], the following procedure should be taken for measuring the thermal conductivity of a thin film:

1. Determining the effective thermal conductivity of the Kapton layer together with the adhesive, $k_{\text{Kap\&adh}}$, by conducting a reference test with the thin film sensor alone between the slabs of the background material
2. Determining the effective thermal conductivity of a series combination of the adhesive layer, the Kapton layer, and the sample, k_{eff}, by performing an experiment with the sensor sandwiched between two identical pieces of the sample, supported by the slabs of the background material

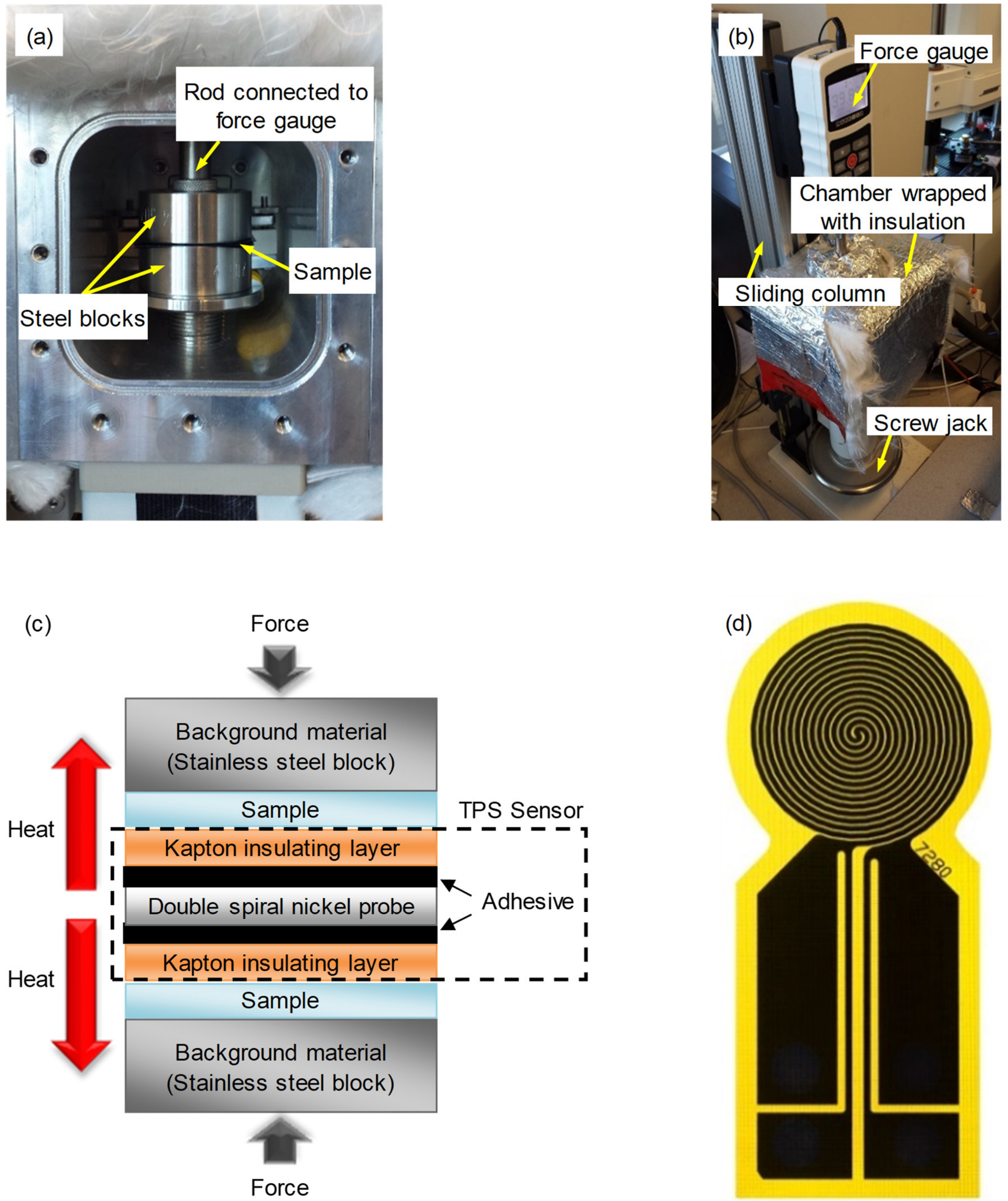

Figure 4-2. **TPS testbed at SFU LAEC: (a) inside of the test chamber, (b) the test chamber and the applying force mechanism, (c) a schematic of the TPS test column, and (d) the TPS thin film sensor (sensor #7280)**

Then, according to ISO22007-2 [120], effective thermal conductivity of the sample (k_s) should be found from [120]:

$$\frac{h_{\text{Kap\&adh}} + h_{\text{s}}}{k_{\text{eff}}} = \frac{h_{\text{s}}}{k_{\text{s}}} + \frac{h_{\text{Kap\&adh}}}{k_{\text{Kap\&adh}}} \tag{4.5}$$

which is, in fact, the simplified version of the following equations:

$$R_{\text{tot}} = R_{\text{b,s}} + R_{\text{b,Kap\&adh}} \quad \text{or} \quad \frac{h_{\text{Kap\&adh}} + h_{\text{s}}}{k_{\text{eff}} A_{\text{sen}}} = \frac{h_{\text{s}}}{k_{\text{s}} A_{\text{sen}}} + \frac{h_{\text{Kap\&adh}}}{k_{\text{Kap\&adh}} A_{\text{sen}}} \tag{4.6}$$

However, as also noted by the ISO22007-2 standard [120], tests on samples with different thicknesses or clamping pressures may be necessary to mathematically eliminate effects of TCRs present in the tests. At relatively low contact pressures, TCRs between contacting surfaces can be much higher than bulk resistance of a sample [128, 129]. Accordingly, a new data reduction method is developed and presented in this thesis for deconvoluting the effects of TCRs from TPS thin film measurements, which is necessary for obtaining accurate and noise-free values of bulk thermal conductivity for thin films.

A New Data Reduction Method for TPS Thin Film Measurements

Thermal resistance circuit of the TPS test column of Figure 4-2 c is shown in Figure 4-3. This circuit reveals that, instead of Eq. (4.6), the relationship between thermal resistances in a TPS test column should be expressed as:

$$\begin{aligned} R_{\text{tot}} &= R_{\text{c,bm-s}} + R_{\text{b,s}} + R_{\text{c,s-Kap}} + R_{\text{b,Kap\&adh}} + R_{\text{c,adh-sen}} \\ &= R_{\text{c,bm-s}} + \frac{h_{\text{s}}}{k_{\text{s}} A_{\text{sen}}} + R_{\text{c,s-Kap}} + \frac{h_{\text{Kap\&adh}}}{k_{\text{Kap\&adh}} A_{\text{sen}}} + R_{\text{c,adh-sen}} \\ &= \frac{h_{\text{s}}}{k_{\text{s}} A_{\text{sen}}} + \frac{h_{\text{Kap\&adh}}}{k_{\text{Kap\&adh}} A_{\text{sen}}} + TCR \end{aligned} \tag{4.7}$$

where $TCR = R_{\text{c,bm-s}} + R_{\text{c,s-Kap}} + R_{\text{c,adh-sen}}$ is defined as the total TCR of the test column. In Eq. (4.7), the term $R_{\text{b,Kap\&adh}}$ takes the effect of $R_{\text{c,Kap-adh}}$ into account. By comparing Eqs. (4.6) and (4.7), it is clear that the effective conductivity found for a sample by Eq. (4.6) may not be the true bulk conductivity of the sample if effects of the TCRs are significant because such an effective conductivity also includes the effects of the TCRs. In fact, it also includes effect of TCR between the Kapton layer and the background material induced by the reference tests; this may induce additional error in measurements by the standard method because such a TCR does not exist in measurements of a sample.

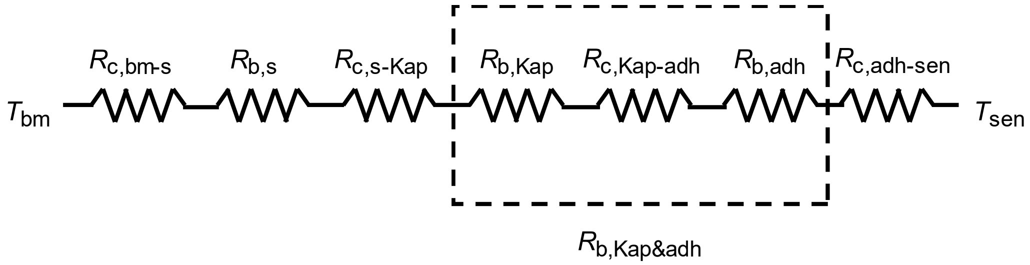

Figure 4-3. Thermal resistance circuit of the TPS test column

For convenience, Eq. (4.7) is rewritten as follows:

$$R_{\text{tot}} = \frac{h_{\text{s}}}{k_{\text{s}} A_{\text{sen}}} + R' \tag{4.8}$$

where $R' = \frac{h_{\text{Kap\&adh}}}{k_{\text{Kap\&adh}} A_{\text{sen}}} + TCR$ is constant for a specific sample. The total resistance in Eq. (4.8) can be back-calculated by plugging values of h_{s}, k_{s}, $h_{\text{Kap\&adh}}$, and $k_{\text{Kap\&adh}}$ into Eq. (4.6). For more clarification, Eq. (4.6) is rewritten as follows, and sequence of operations needed to back-calculate the total resistance is shown schematically in Figure 4-4:

$$R_{\text{tot}} = \frac{h_{\text{s}}}{k_{\text{s,app}} A_{\text{sen}}} + \frac{h_{\text{Kap\&adh}}}{k_{\text{Kap\&adh}} A_{\text{sen}}} \tag{4.9}$$

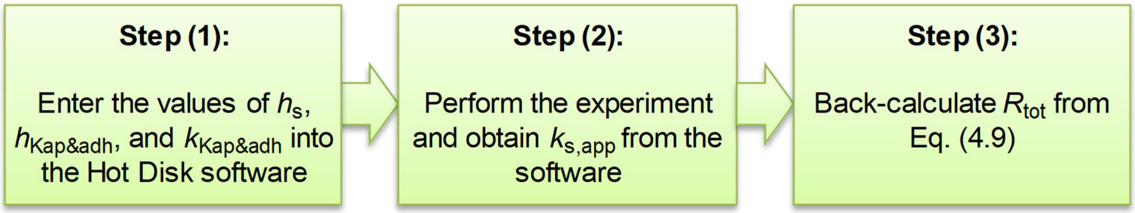

Figure 4-4. Back-calculating total thermal resistance from the Hot Disk software

Just like the GHF tests described in section 4.1.1, after performing measurements for at least two thicknesses of a sample, the bulk conductivity of the sample can be obtained by performing a linear regression analysis through the obtained data of total resistance versus thickness. As shown in Eq. (4.8), slope and intercept of such a line yield the bulk conductivity of the sample and the parasitic resistance, R', respectively. The developed method has the following advantages:

1. Accurate measurement of bulk thermal conductivity of thin films
2. Elimination of the previously needed reference tests and possibility of entering any values for h_s, $h_{\text{Kap\&adh}}$, and $k_{\text{Kap\&adh}}$ into the Hot Disk software due to usage of the same values in back-calculation of the total resistance
3. Elimination of the unwanted effect of the TCR between the Kapton layer and the background material, induced by the standard reference tests

The downside of the proposed method is the need for conducting tests on at least two thicknesses of the same sample, which may not be available.

4.1.3. Uncertainty Analysis

Uncertainty analysis of the steady state and transient methods was performed following the methods describe in Refs. [130] and [131] (see Appendix E).

4.1.4. Evaluation of the Thermal Conductivity Tools

In this section, the proposed procedure in section 4.1.2 for TPS thin film data reduction is validated by several case studies on ETFE, Nafion, and GDL using both TPS and GHF methods. The ETFE sheets were received from Asahi Glass Co. in thicknesses of 11, 24, 50, 105, and 204 µm, and the Nafion films were made in-house at AFCC in thicknesses of 10, 16, 26, and 48 µm. For GDL measurements, two commercial samples with the names of GDL 24BA and GDL 34BA, received from SIGRACET®, were used.

To compare the TPS tests with the GHF tests, both results are plotted next to each other throughout this section, where applicable. Moreover, since the TPS sensor and the GHF fluxmeters had different cross-sectional areas, the measured resistances per unit area, i.e., thermal insulance values [K·mm^2/W], are compared.

To ensure accurate TPS measurements, lack of temperature drift for the nickel sensor was ensured by allowing at least 5 min relaxation time prior to each measurement. Overall, each TPS measurement took ~ 3 min. For comparison, the first steady state test by the GHF testbed took about 5 hr, with subsequent tests at different pressures requiring ~ 2 hr.

ETFE Results

To show that the value of Kapton thermal conductivity can be chosen arbitrarily in the developed method, a sensitivity analysis was performed. For this purpose, raw data to be incorporated in the developed method was obtained in two ways: i) by entering arbitrary values of 25 μm and 0.06 W·m^{-1}·K^{-1} into the Hot Disk software for thickness and thermal conductivity of the Kapton film, respectively, and ii) by performing the conventional procedure for TPS thin film measurements as per the ISO standard [120], to enable comparison between the data reduction methods of the ISO standard and the developed method. The raw ETFE data obtained from the Hot Disk testbed are shown in Figure 4-5 for different thicknesses of ETFE. The values of k_{app}, shown in Figure 4-5 and introduced in Eq. (4.9), were outputted by the Hot Disk testbed and, thus, are outcomes of the ISO standard's data reduction method.

As shown in Figure 4-5, for the thickest sample (204 μm), the ISO standard yields almost the same results for both cases of arbitrary reference and measured reference; the obtained results in those cases are also pretty decent in the sense that they are very close to the nominal value, reported by the supplier. For lower thicknesses, deviations between the two cases start to become significant, and the values related to both methods start to deviate from the nominal value. The ISO standard with measuring the reference yields decent values (close to the nominal value) for thicknesses higher than (not including) 24 μm, but even the ISO standard with measuring the reference deviates significantly from the nominal value for the 24 and 11 μm thicknesses (i.e., thicknesses close to the range of CLs). Deviations between the values outputted by the ISO standard with measuring the reference and the nominal value goes up to 67% for the 11 μm thickness.

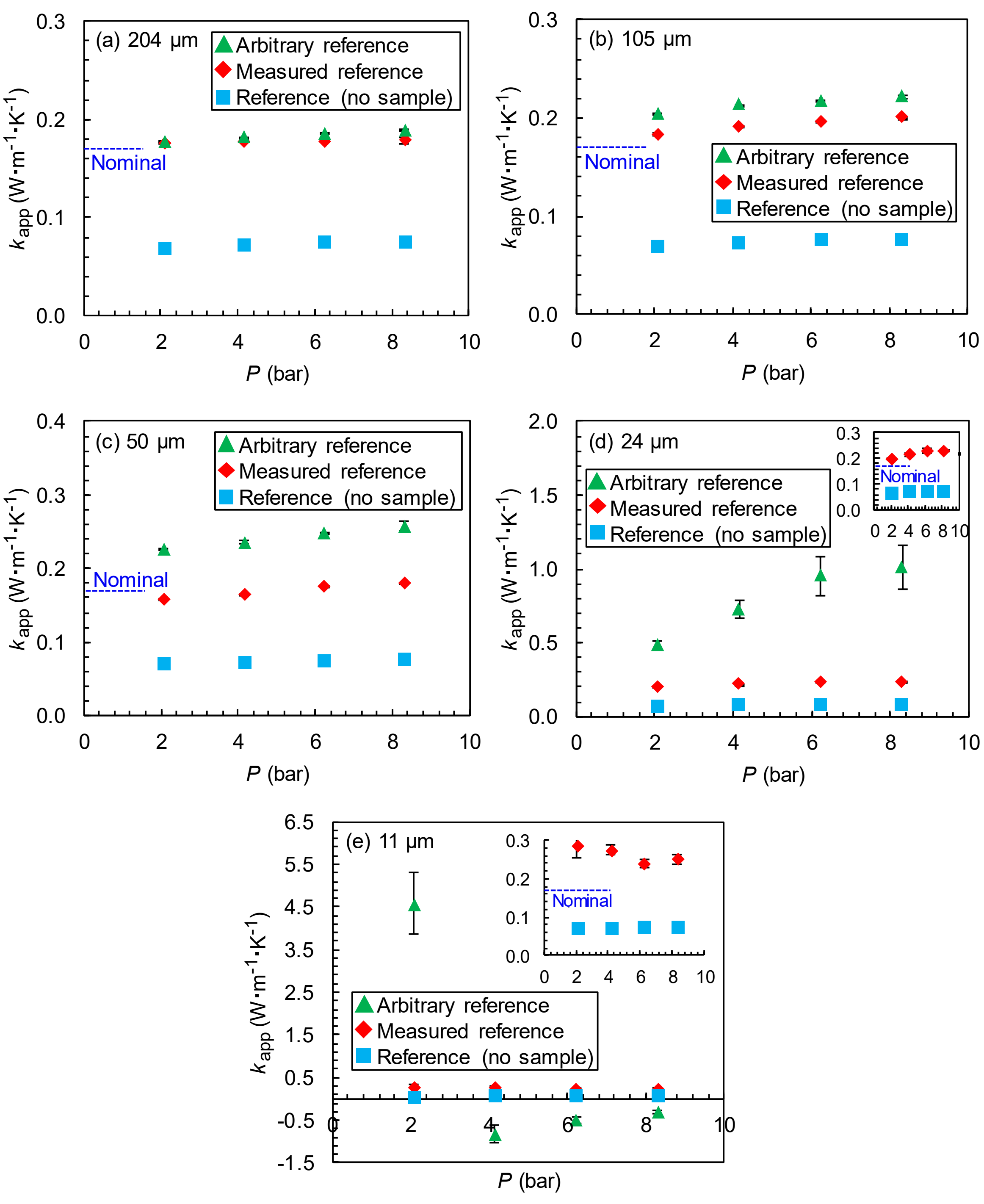

Figure 4-5. **Raw data obtained from the Hot Disk testbed vs. pressure at 29 °C for different thicknesses of ETFE (error bars: random errors)**

The values of k_{app} of Figure 4-5 contain the effects of TCRs of the TPS test column, which can be seen in the generally increasing trend of k_{app} with increasing the pressure. The

TCRs decrease with increasing the pressure, which leads to higher k_{app}'s, which could be misleading in the sense that it could make one believe in an increasing trend in the actual thermal conductivity. In fact, the TCRs, inherent in the measurements, result in deviation from the actual thermal conductivity of ETFE with increasing pressure; this issue will be discussed in more details later. For the 11 μm thickness, the deviations are even larger due to the higher share of the TCRs compared to the film bulk resistance.

The data of the different cases in Figure 4-5 were incorporated in the developed procedure to calculate the total resistance values. The results are shown in Figure 4-6 and show no noticeable difference between the results of the arbitrary reference and the measured reference, despite the significantly different k_{app}'s shown in Figure 4-5. The reason for this difference between the behaviors of R_{tot} and k_{app} is the different effects of TCRs on these parameters. The measured resistances have a maximum uncertainty (STD) of 1.3%.

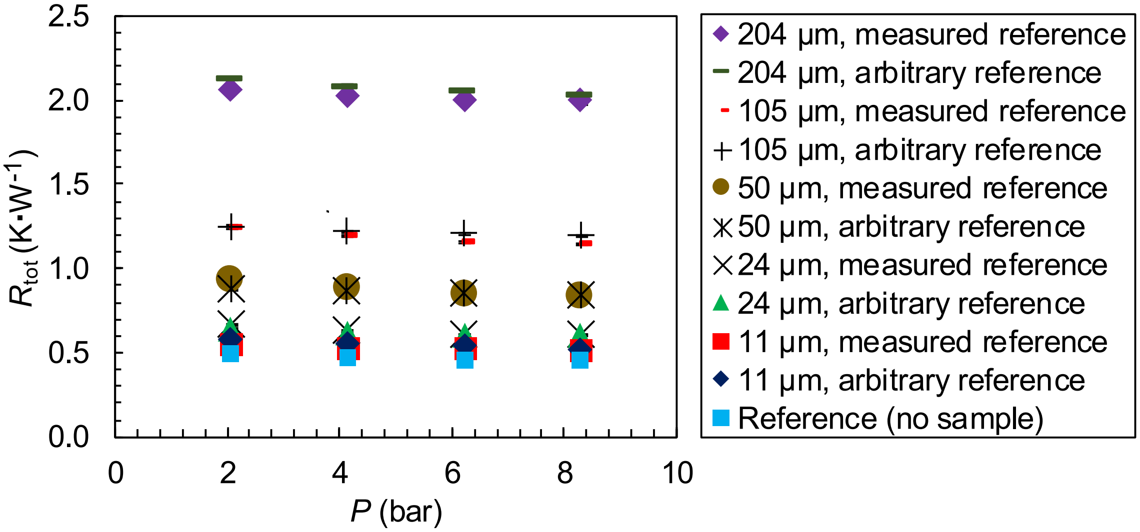

Figure 4-6. **Total thermal resistance vs. pressure at 29 °C from the modified TPS method for ETFE (error bars: random errors)**

Figure 4-7 shows total thermal insulance versus thickness for ETFE. As shown in the figure, the linear behavior of total thermal insulance versus thickness is well captured by both methods. Maximum uncertainty for $R_{\mathrm{tot}}A_{\mathrm{sen}}$ is 1.3% for the modified TPS method and 10.4% for the GHF method. $R_{\mathrm{tot}}A_{\mathrm{sen}}$ values measured by the GHF testbed are lower than the TPS testbed, which is mainly due to existence of the extra bulk resistance of the Kapton layer in the TPS test column.

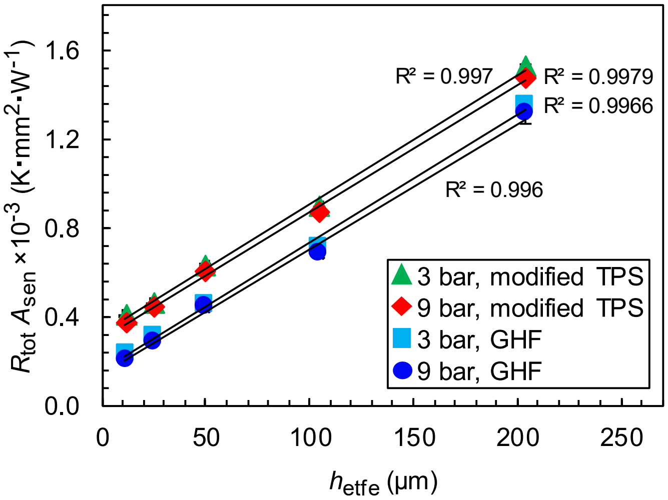

Figure 4-7. **Total thermal insulance vs. thickness for ETFE at 29 °C (error bars: STDs for thickness, random errors for insulance)**

Changes in $R'A_{\text{sen}}$ and $(TCR)A_{\text{sen}}$ values versus pressure are plotted in Figure 4-8. The decreasing trend of the data is due to reduction of the TCRs in the test columns of the testbeds with increasing the pressure. However, as can be inferred from the overlap of the error bars of each data set, the TCRs for each data set do not change much with pressure, which is expected considering the very low roughness of the ETFE films (see Figure 3-12).

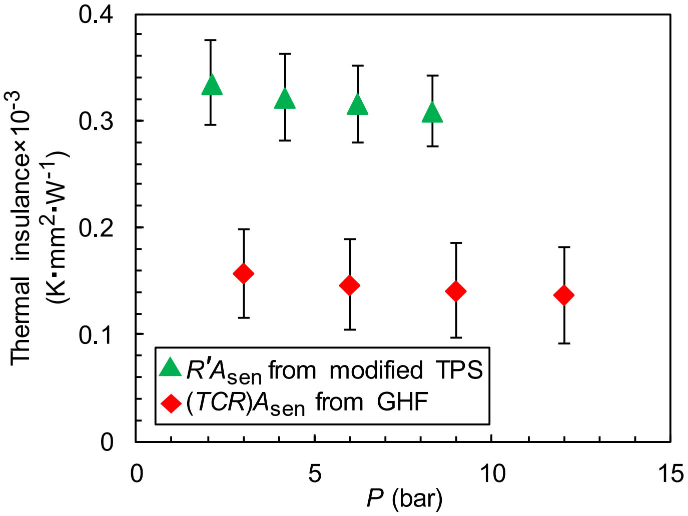

Figure 4-8. **$R'A_{sen}$ from TPS next to $(TCR)A_{sen}$ from GHF vs. pressure for ETFE at 29 °C (error bars: random errors)**

Maximum uncertainties of the data in Figure 4-8 are 12.7% for $R'A_{\text{sen}}$ and 32.5% for $(TCR)A_{\text{sen}}$. The main reason for higher $R'A_{\text{sen}}$ values than $(TCR)A_{\text{sen}}$ is existence of the

Kapton layer in the TPS test column. In addition, the GHF fluxmeters had flat metallic surfaces, whereas surfaces of the TPS sensor had patterns on them; this could result in higher TCRs in the TPS test column.

The measured conductivities at different pressures by the developed procedure are shown in Figure 4-9 next to the results of the conventional procedure. The results of the developed procedure show how well the raw data of the Hot Disk testbed, shown in Figure 4-5, collapse onto a consistent value of thermal conductivity when incorporated in the developed method. Figure 4-9 also shows a consistent measurement of thermal conductivity for ETFE by the developed method and the GHF method.

Comparing the obtained consistent conductivity values from the modified TPS method with the values from the conventional method further uncovers the significant effects of TCRs in the results of the conventional method, i.e., up to 67% relative difference between the two methods. As indicated by Figure 4-9, the TCR effects decrease as thickness of ETFE increases, the reason of which is reduction in the share of TCRs in the total resistance with increasing the thickness.

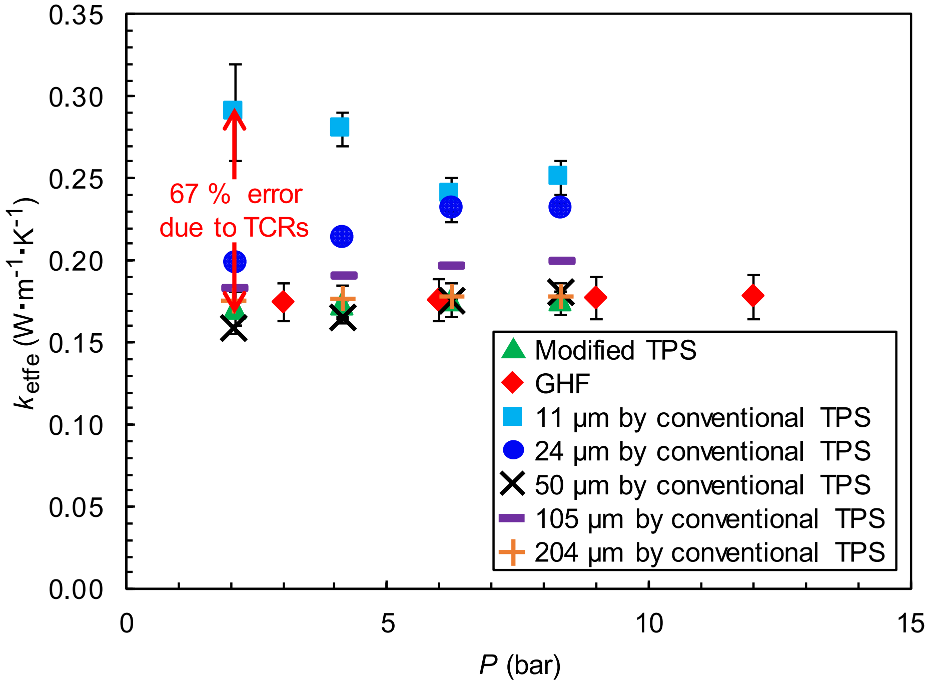

Figure 4-9. **Thermal conductivity of ETFE vs. pressure at 29 °C (error bars: random errors)**

Maximum uncertainties in Figure 4-9 are 6.7% for the developed method and 7.5% for the GHF method. Average value of thermal conductivity of ETFE is 0.174 ± 0.002 $W \cdot m^{-1} \cdot K^{-1}$ from the modified TPS method and 0.177 ± 0.002 $W \cdot m^{-1} \cdot K^{-1}$ from the GHF method.

Nafion Results

Results of Nafion are shown through Figures 4-10 to 4-12. Similar to Figure 4-7, both methods well capture the linear trend of total insulance versus thickness. Figure 4-11 shows lower $(TCR)A_{\mathrm{sen}}$ values for Nafion compared to that of ETFE shown in Figure 4-8, which could be due to the softer and more flexible nature of Nafion membranes, leading to more conformability of the membranes to the flat metallic surfaces of the GHF fluxmeters. In comparison with ETFE, the change in $R'A_{\mathrm{sen}}$ with pressure is significant for Nafion. Average relative difference between the conductivity results of the two methods, shown in Figure 4-12, is about 13.5%.

By averaging the data in Figure 4-12 over the whole pressure range, average thermal conductivity of Nafion measured by the modified TPS method is 0.243 ± 0.007 $W \cdot m^{-1} \cdot K^{-1}$, whereas the average value measured by the GHF method is 0.214 ± 0.003 $W \cdot m^{-1} \cdot K^{-1}$. Since share of bulk resistance of Nafion in the total resistance is larger in the GHF method, thermal conductivity results of GHF for Nafion are more accurate than the TPS method.

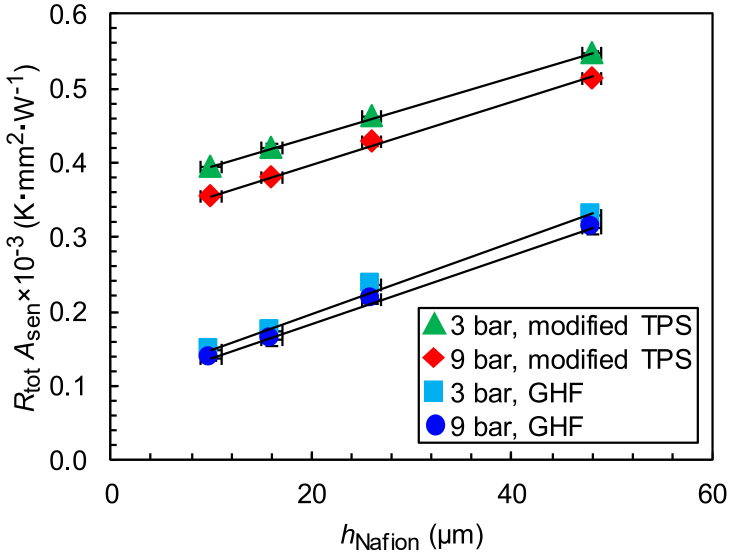

Figure 4-10. Total thermal insulance vs. thickness for Nafion at 29 °C (error bars: STDs for thickness, random errors for insulance)

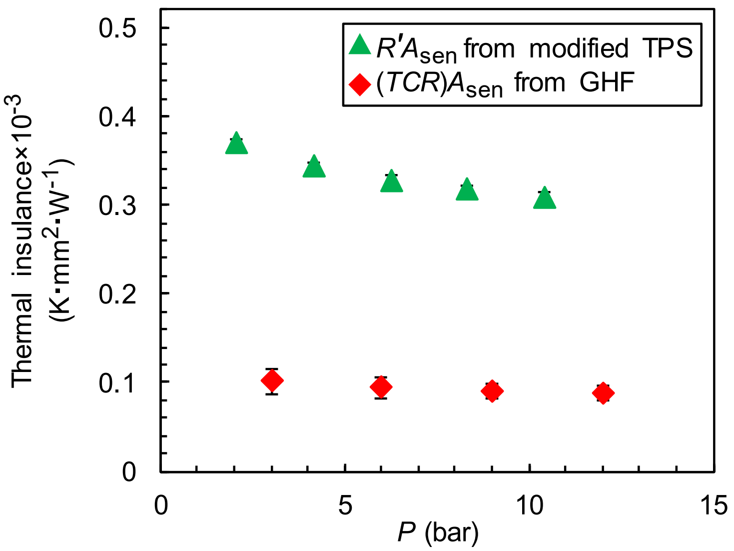

Figure 4-11. ***R′A*****$_{sen}$ from TPS next to (*****TCR*****)*****A*****$_{sen}$ from GHF vs. pressure for Nafion at 29 °C (error bars: random errors)**

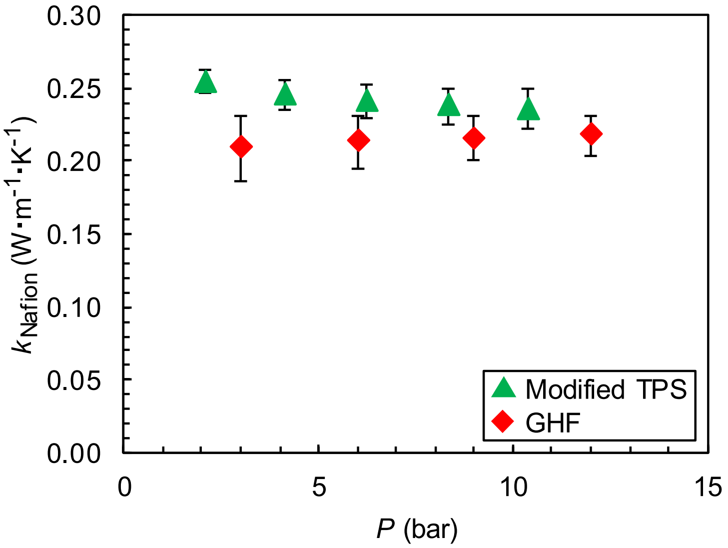

Figure 4-12. Thermal conductivity of Nafion vs. pressure at 29 °C (error bars: random errors)

GDL Results

Figure 4-13 shows a decreasing trend for total insulance versus compressive load. Figure 4-14, again, shows higher $R'A_{\mathrm{sen}}$ values than $(TCR)A_{\mathrm{sen}}$ values. Since the zero insulance is generally within the error ranges of the negative values in Figure 4-14, these values should be interpreted as small positive insulances which are very close to zero. Reasons behind the increasing trend of thermal conductivity of GDL with pressure in Figure 4-15 is given in several studies in literature [26, 28, 31]. In summary, by increasing the pressure, carbon fibers inside the GDL become more compressed against each other and, thus, sizes of contact points between them increase. This results in lower constriction/spreading resistances at the contact points and, thus, a higher thermal conductivity.

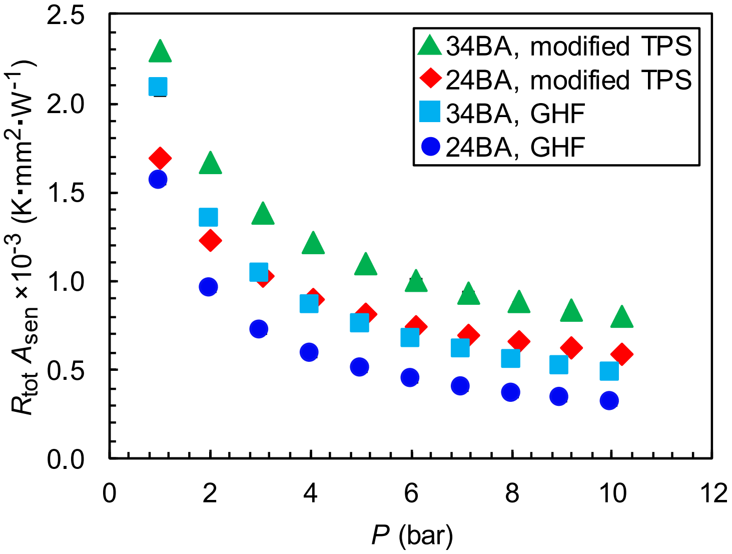

Figure 4-13. Total insulance of GDL from TPS and GHF vs. pressure at 29 °C (error bars: random errors)

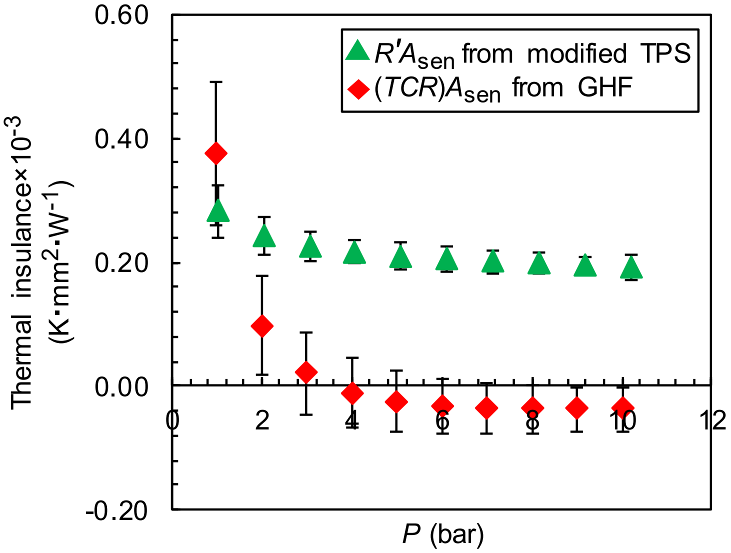

Figure 4-14. $R'A_{sen}$ from TPS next to $(TCR)A_{sen}$ from GHF vs. pressure for GDL at 29 °C (error bars: random errors)

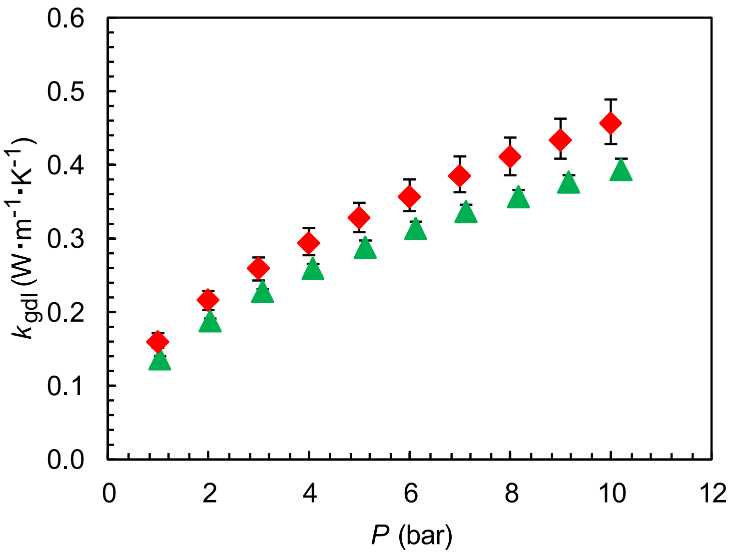

Figure 4-15. Thermal conductivity of GDL vs. pressure at 29 °C (error bars: random errors)

Thermal conductivity values of the GDL, measured by the two methods, are ~15.7% different from each other, which could mainly be attributed to hysteresis behavior of the GDL material under compressive load due to its fibrous porous structure, as explained in detail in Ref. [28]. In the GHF testbed, the fluxmeters undergo a series of thermal expansions and contractions until the device gets to steady state, whereas these effects are not present in the TPS testbed, due to its fast transient nature. Accordingly, the GDL samples could experience some hysteresis effects in the GHF testbed at each stage of pressure increment, whereas the TPS tests were free of such effects. Maximum uncertainties in the GDL conductivity data of Figure 4-15 are 3.4% for the modified TPS method and 6.6% for the GHF method.

Overall, when selecting a measurement method for measuring thermal conductivity of a thin film or coating, mechanical behaviors of the sample and the measurement device during the tests should be considered. The above GHF tests for ETFE, Nafion, and GDL were all conducted when a hydraulic jack was used in the GHF testbed. As mentioned before, the hydraulic jack used to lose pressure over time, and thus, minor pressure adjustments were necessary from time to time. This could exacerbate any hysteresis effects induced by the testbed on a sample. Accordingly, after finding out about the possible hysteresis effects which might have been imposed on the samples by the GHF fluxmeters, the hydraulic jack was replaced with a pneumatic jack, which did not lose pressure and had much more accurate control over the contact pressure. Further, a feedback control loop was designed for the testbed to accurately maintain the contact pressure during the tests (with an accuracy of 1 kPa). By performing these improvements, it was ensured that the testbed would not affect the CLs, and that any pressure-related and/or real hysteresis effects, if any, would be captured accurately during the tests.

4.2. CL Thermal Conductivity Measurements

4.2.1. Sample Configuration for CL Measurements

CLs have a highly fragile microstructure and a very small thickness (~2-8 um), which makes having a standalone CL impossible. For this reason, conductivity tests had to be performed on CCSs. In this study, to maintain a reasonable amount of catalyst in the test column and, also, to avoid any contact between the fragile catalyst and the hard surfaces of the TPS sensor or the GHF fluxmeters, two CCSs were made into a sandwich by contacting them from their catalyst sides. The resulting sandwich was considered as one sample/unit for the measurements. A schematic of the mentioned sandwich and its thermal resistance circuit are shown in Figure 4-16. It should be noted that, compared to a hypothetical standalone CL, the only differences resulted from stacking two CCSs in the test column are: i) addition of some constant resistances (substrates and TCRs) to the total resistance, and ii) doubling the bulk resistance of the CL in the total resistance. According to Figure 4-16, through-plane bulk resistance of a sandwich (or stack) can be expressed by the following relation:

$$\begin{aligned} R_{\mathrm{b,st}} &= R_{\mathrm{b,sub}} + R_{\mathrm{c,sub\text{-}cl}} + R_{\mathrm{b,cl(1)}} + R_{\mathrm{c,cl\text{-}cl}} + R_{\mathrm{b,cl(2)}} + R_{\mathrm{c,sub\text{-}cl}} + R_{\mathrm{b,sub}} \\ &= R_{\mathrm{b,cl(1)}} + R_{\mathrm{b,cl(2)}} + \left[2R_{\mathrm{b,sub}} + 2R_{\mathrm{c,sub\text{-}cl}} + R_{\mathrm{c,cl\text{-}cl}}\right] = \frac{h_{\mathrm{cl(1)}} + h_{\mathrm{cl(2)}}}{k_{\mathrm{cl,tp}} A_{\mathrm{sen}}} + R'' \\ &= \frac{h_{\mathrm{cl,tot}}}{k_{\mathrm{cl,tp}} A_{\mathrm{sen}}} + R'' \end{aligned} \tag{4.10}$$

where $h_{\text{cl,tot}} = h_{\text{cl}(1)} + h_{\text{cl}(2)}$ is the total thickness of the catalyst in the stack, and $R'' = 2R_{\text{b,sub}} + 2R_{\text{c,sub-cl}} + R_{\text{c,cl-cl}}$ is a share of the stack resistance which does not include the through-plane bulk resistances of the CLs. As it is clear from Eq. (4.10), when just the thicknesses of the CLs are changed in the stack, except for the through-plane bulk resistances of the CLs, the rest of the resistances remain constant, resulting in the resistances of two different stacks being just different in a constant, i.e., R''.

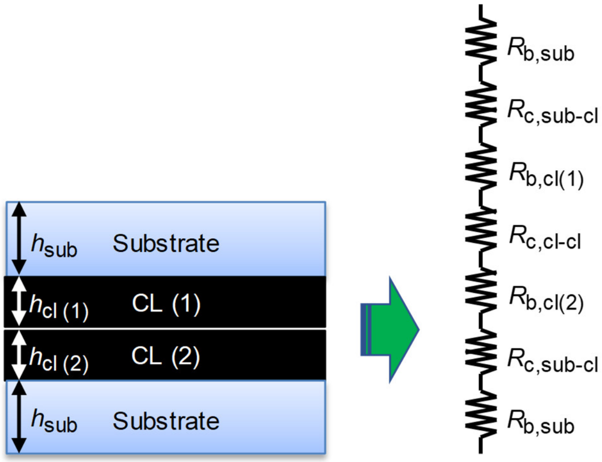

Figure 4-16. Schematics of a catalyst sandwich making one sample for the measurements and its through-plane thermal resistance circuit

On the other hand, based on the discussion of sections 4.1.1 and 4.1.2, total through-plane resistance of a sample measured by either of the GHF or TPS devices can be expressed by the following more general expression:

$$R_{\text{tot}} = R_{\text{b,s}} + R_{\text{res}} \tag{4.11}$$

where R_{res} is a residual (extra) resistance, which consists of either the TCRs between the sample and the GHF fluxmeters for GHF tests or the effects of through-plane resistance of the TPS sensor and the TCRs in the TPS test column for TPS tests. Thus, by combining Eqs. (4.10) and (4.11), in general, total resistance of a stack could be expressed by:

$$R_{\text{tot,st}} = R_{\text{b,st}} + R_{\text{res}} = \frac{h_{\text{cl,tot}}}{k_{\text{cl,tp}} A_{\text{sen}}} + R'' + R_{\text{res}} = \frac{h_{\text{cl,tot}}}{k_{\text{cl,tp}} A_{\text{sen}}} + R''' \tag{4.12}$$

where $R''' = R'' + R_{\mathrm{res}} = 2R_{\mathrm{b,sub}} + 2R_{\mathrm{c,sub\text{-}cl}} + R_{\mathrm{c,cl\text{-}cl}} + R_{\mathrm{res}}$ is a constant resistance including effects of the substrates, TCRs in the stack, and the residual resistance of the measurement device. Accordingly, total through-plane resistance of a stack measured by either the TPS or the GHF testbed is a linear function of total thickness of catalyst in the stack. Therefore, similar to measurements of standalone samples, discussed in sections 4.1.1 and 4.1.2, after measuring stacks with at least two different thicknesses of the same CL, $k_{\mathrm{cl,tp}}$ can be deconvoluted by Eq. (4.3) in case of two-thickness measurements. In case of multi-thickness measurements, $k_{\mathrm{cl,tp}}$ could be evaluated by performing a linear regression analysis through the data of $R_{\mathrm{tot,st}}$ vs. $h_{\mathrm{cl,tot}}$; according to Eq. (4.12), $k_{\mathrm{cl,tp}}$ would be related to inverse of the slope and R''' to intercept of the line.

4.2.2. Evaluation of the Thermal Conductivity Tools for CLs

The baseline CL (design #1 of Table 2-1) was measured using the GHF and the modified TPS methods to evaluate the tools for CL measurements. For this purpose, CLs were coated on (100 μm thick) ETFE with thicknesses of ~7 and 14 μm as well as on (50 μm thick) Al with thicknesses of ~4 and 12 μm. Total through-plane thermal insulance versus pressure for different total thicknesses of catalyst in the stack are shown in Figure 4-17. As shown in Figure 4-17, for each thickness of catalyst in a stack, the total insulance decreases with pressure due to reduction in the TCRs of the test column with increasing the pressure. In addition, the total insulance values measured by the modified TPS method are generally higher than the values measured by the GHF method due to: i) much higher resistance of the 100 μm thick ETFE substrates (thermal conductivity of ∼0.17 $\mathrm{W{\cdot}m^{-1}{\cdot}K^{-1}}$) used for the modified TPS tests compared to the 50 μm thick Al substrates (thermal conductivity of ∼205 $\mathrm{W{\cdot}m^{-1}{\cdot}K^{-1}}$) used for the GHF tests, and ii) extra bulk resistance of the Kapton layer in the TPS test column compared to the GHF test column. Maximum uncertainties for $R_{\mathrm{tot,st}}A_{\mathrm{sen}}$ are 0.4% for the modified TPS method and 4.6% for the GHF method. $R'''A_{\mathrm{sen}}$ versus pressure is plotted in Figure 4-18 for the modified TPS and GHF measurements. As expected, the observed decreasing trend of the data with increasing pressure is due to reduction in the TCRs of the test column as pressure increases. Maximum uncertainties of the data of Figure 4-18 are 2.7% for the modified TPS method and 17.3% for the GHF method. Reasons for having higher $R'''A_{\mathrm{sen}}$ values for the modified

TPS method compared to the GHF method are, again, the much higher bulk resistance of the ETFE substrates compared to the Al substrates and the extra resistance of the Kapton layer of the TPS sensor. In addition, as mentioned before, compared to the patterned surfaces of the TPS sensor, flatter and pattern-free metallic surfaces of the GHF fluxmeters result in lower contact insulances in the GHF test column.

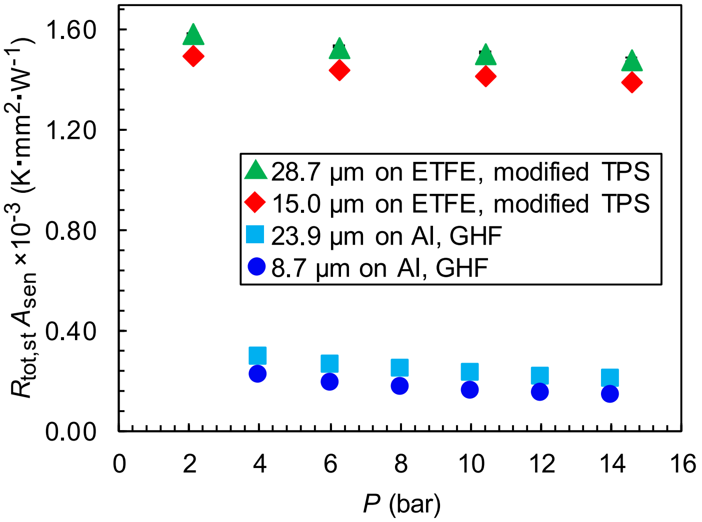

Figure 4-17. Total through-plane thermal insulance vs. pressure at 29 °C and room RH for different thicknesses of the baseline CL in a stack (error bars: random errors)

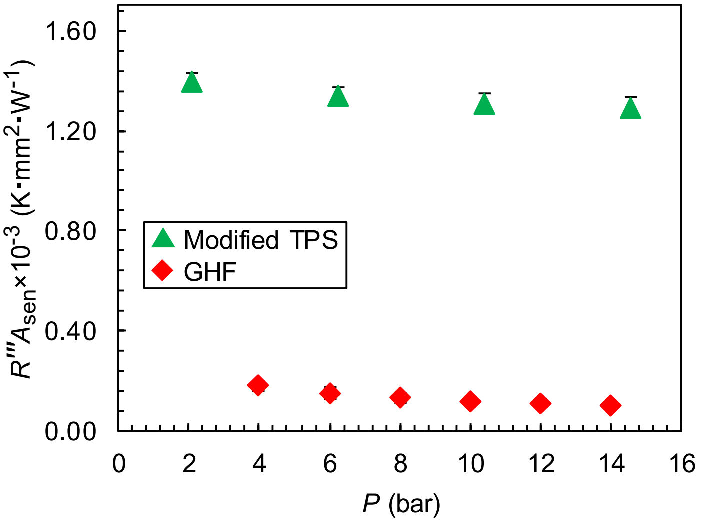

Figure 4-18. $R'''A_{\text{sen}}$ vs. pressure at 29 °C and room RH for the baseline CL by the modified TPS and GHF methods (error bars: random errors)

Modified TPS and GHF measurements of through-plane thermal conductivity are shown in Figure 4-19 for the baseline CL at different contact pressures. As shown in Figure 4-19, both methods agree well with each other throughout the whole pressure range. Moreover, changing the contact pressure did not affect the conductivity. As discussed in section 2.5, primary carbon particles are welded together in the aggregates by covalent bonding [77-80]; thus, the contact area between the particles in the aggregates is fixed and cannot change with pressure. One may argue that increasing the pressure may enhance the contact area between the aggregates adhered together by van der Waals forces; however, as discussed in later chapters, such effects should be very small because of presence of ionomer at through-plane contact regions between the aggregates. Based on this finding, the rest of the through-plane tests were conducted at 1,500 kPa, which is a typical pressure experienced by an MEA in a PEMFC. Maximum uncertainties of the data in Figure 4-19 are 8% for the modified TPS tests and 15% for the GHF tests. Through-plane thermal conductivity of the baseline CL averaged over the whole pressure range is 0.218 ± 0.005 $W \cdot m^{-1} \cdot K^{-1}$ for the modified TPS tests and 0.214 ± 0.005 $W \cdot m^{-1} \cdot K^{-1}$ for the GHF tests. The ± 0.005 $W \cdot m^{-1} \cdot K^{-1}$ value shows the STDs from the averages.

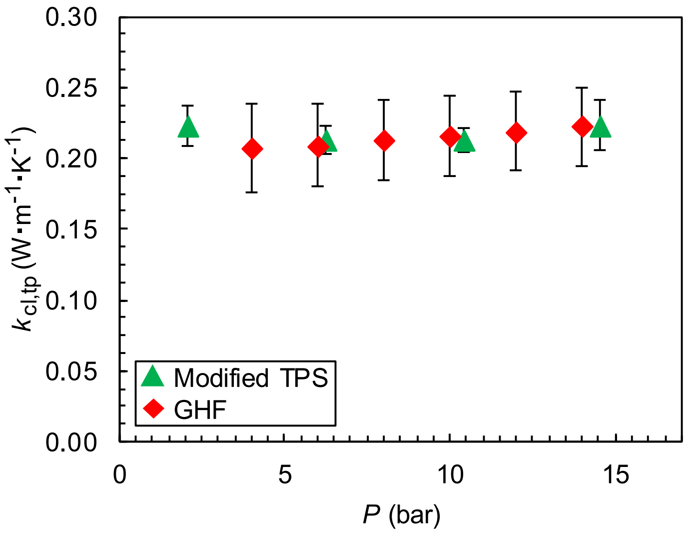

Figure 4-19. Through-plane thermal conductivity of the baseline CL vs. pressure at 29 °C and room RH (error bars: random errors)

As shown above, both GHF and modified TPS methods showed great capability for measuring the through-plane thermal conductivity of the CL. However, the hard surfaces of the insulating layer of the TPS sensor (i.e., the Kapton surfaces) were found to significantly imprint their patterns on the fragile CLs during the tests, although the TPS sensor was in contact with the substrates not with the CLs. This issue made a measured CL unusable for further investigations and repetitions of the TPS tests. Thus, repetitions of TPS tests were performed on fresh samples of the same batch (not on the same sample). Accordingly, the GHF method was chosen in this thesis for further measurements. Moreover, the 50 μm thick Al foil was chosen as the substrate for through-plane tests because it had a very low through-plane thermal resistance (~ 1/2,000th of a CL with the same thickness and area), which led to a much higher signal to noise ratio compared to other substrates like ETFE. It also had a very low through-plane electronic resistance (~ 1/340,000,000th of a CL with the same thickness and area), making the through-plane electronic resistance measurements possible. As measurements showed, through-plane thermal and electronic resistances of the Al foil were so small that the testbeds could not detect them.

4.2.3. Signal to Noise Ratio Enhancement

As indicated in section 4.2.1, using Eq. (4.12) for measuring the through-plane bulk conductivity of a CL requires that $k_{\text{cl,tp}}$ and R''' remain constant by changing $h_{\text{cl,tot}}$. On the other hand, as mentioned before, having constant $k_{\text{cl,tp}}$ and R''' for different $h_{\text{cl,tot}}$'s means having a linear relationship between $R_{\text{tot,st}}$ and $h_{\text{cl,tot}}$. In other words, if we measure $R_{\text{tot,st}}$ for different $h_{\text{cl,tot}}$'s and find out that the $(h_{\text{cl,tot}}, R_{\text{tot,st}})$ data points fall on a line, then according to Eq. (4.12), $k_{\text{cl,tp}}$ and R''' must have remained constant by changing $h_{\text{cl,tot}}$. However, since always a line could be passed through two points, measuring $R_{\text{tot,st}}$ for just two $h_{\text{cl,tot}}$'s cannot show this linearity effectively. Accordingly, measurements of $R_{\text{tot,st}}$ for stacks with more than two $h_{\text{cl,tot}}$'s should be performed to show this linearity, which will then prove that $k_{\text{cl,tp}}$ and R''' remain constant by changing $h_{\text{cl,tot}}$. A complication which may arise is that, in order to have the same microstructure, thickness of a CL could be increased to a certain limit. As mentioned in section 3.5, beyond that limit, too much cracks would be produced in the CL, and the CL could even flake off from its substrate. On the other hand, small increments in the CL thickness may result in $R_{\text{tot,st}}$'s for single stacks which are too close to each other to be captured by the testbeds effectively. Thus, in case of single-stack measurements, revealing the linear trend of $R_{\text{tot,st}}$ versus $h_{\text{cl,tot}}$ is compromised again. Figure 4-20 shows data points of single-stack measurements for the baseline CL logged by the TPS and GHF testbeds. As shown in Figure 4-20, the data of the single-stack measurements by both testbeds fall too close to and within the error range of one another. Based on the data points shown in Figure 4-20, the testbeds have a resolution of ~1-2 µm in terms of thickness of the baseline CL. The observed difference between the magnitudes of the TPS data and GHF data is again related to: i) the much higher resistance of the ETFE substrate used for the TPS tests than the Al substrate used for the GHF tests, and ii) extra resistance of the sensor insulation layer in TPS tests.

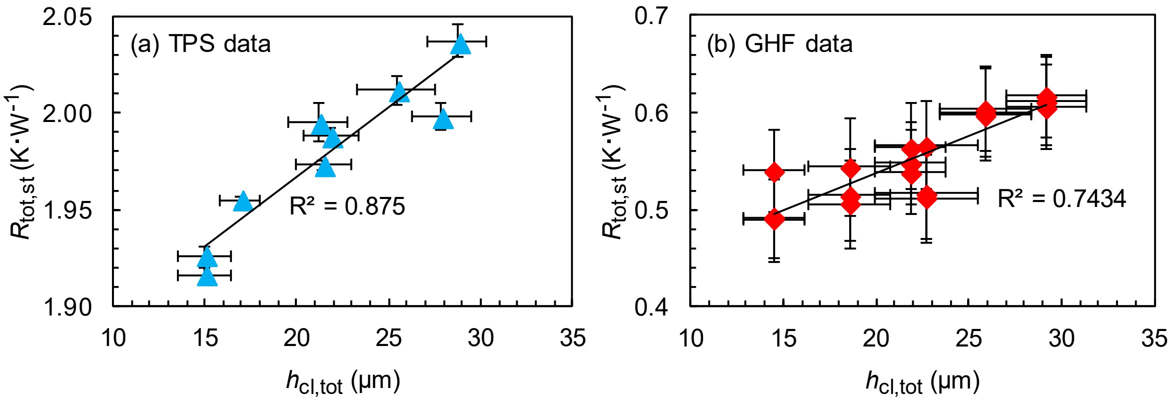

Figure 4-20. Single-stack measurements of total thermal resistance vs. total CL thickness for the baseline CL at 1,500 kPa, 29 °C, and room RH by: (a) modified TPS method, and (b) GHF method, showing a resolution of ~1-2 µm for resolving the CL resistance by the testbeds (error bars: STDs for thickness, random errors for resistance)

Thus, enhancing the signal to noise ratio is of paramount importance for two reasons: i) to effectively prove the linearity of $R_{\text{tot,st}}$ versus $h_{\text{cl,tot}}$, and ii) to enable measuring the CL conductivity where there are limitations to considerably change the CL thickness (due to issues with cracks and flaking). Enhancing the signal to noise ratio for measuring the through-plane thermal conductivity of CLs could be accomplished in two ways:

1. **A fixed number of stacks (n stacks) and different thicknesses:** In this method, signal from the CL bulk is enhanced by measuring more than one stack at a time (e.g., three stacks), where the number of stacks is fixed, and the bulk signal is changed by changing the thicknesses of the CLs in each stack to enable deconvolution of the bulk conductivity by linear regression. Figure 4-20 shows results for the

case of single stack (n=1) and different thicknesses. This method mathematically ensures complete deconvolution of all the parasitic resistances.

2. **Different numbers of stacks:** In this method, signal from the CL bulk is enhanced by adding more stacks in successive measurements, where stacks with the same or different CL thicknesses could be used. This method does not mathematically guarantee complete deconvolution of the parasitic resistances from the bulk conductivity. However, experiments show its promising capabilities not just for CLs but also for other materials like GDLs which may not be available in different thicknesses due to manufacturing limitations [29, 34, 37, 44].

In the following sections, justifications for the above methods are presented. Specifically, it is shown that by measuring more than one stack at a time instead of just one stack, a linear relationship holds between total resistance and total thickness of catalyst in the stacks, from which the CL bulk resistance (or conductivity) could be deconvoluted if the number of stacks is fixed and only the thickness of catalyst in the stacks is changed. Further, it is shown that additional resistances (other than the CL bulk) present in such measurements are not statistically different than those present in single-stack measurements, which will open the way for performing measurements by just adding more stacks (with the same or different thickness of catalyst) to enhance the signal from the CL bulk. Figure 4-21 shows a schematic of the various phases taken in this thesis to enhance the thermal resistance signal from the CL bulk. Phase 1 was already discussed above. In the following sections, the other two phases are explained.

A Fixed Number of Stacks (n Stacks) and Different Thicknesses

The relation for $R_{\text{tot,st}}$ remains the same as Eq. (4.12) for measuring n stacks of CCSs (fixed n, $n \geq 1$), with the exception that relations for $h_{\text{cl,tot}}$ and R''' become:

$$h_{\text{cl,tot}} = n\left(h_{\text{cl}(1)} + h_{\text{cl}(2)}\right) \tag{4.13}$$

$$R''' = n\left(2R_{\text{b,sub}} + 2R_{\text{c,sub-cl}} + R_{\text{c,cl-cl}}\right) + (n-1)R_{\text{c,sub-sub}} + R_{\text{res}} \tag{4.14}$$

where $R_{\text{c,sub-sub}}$ represents TCR between the substrates of two contacting stacks of CCSs. Therefore, similar to single-stack measurements, Eq. (4.12) shows that if $k_{\text{cl,tp}}$ and R'''

remain constant with changing $h_{\text{cl,tot}}$, then $R_{\text{tot,st}}$ will have a linear relationship with $h_{\text{cl,tot}}$; thus, again, the slope and intercept could be used to find $k_{\text{cl,tp}}$ and R''', respectively.

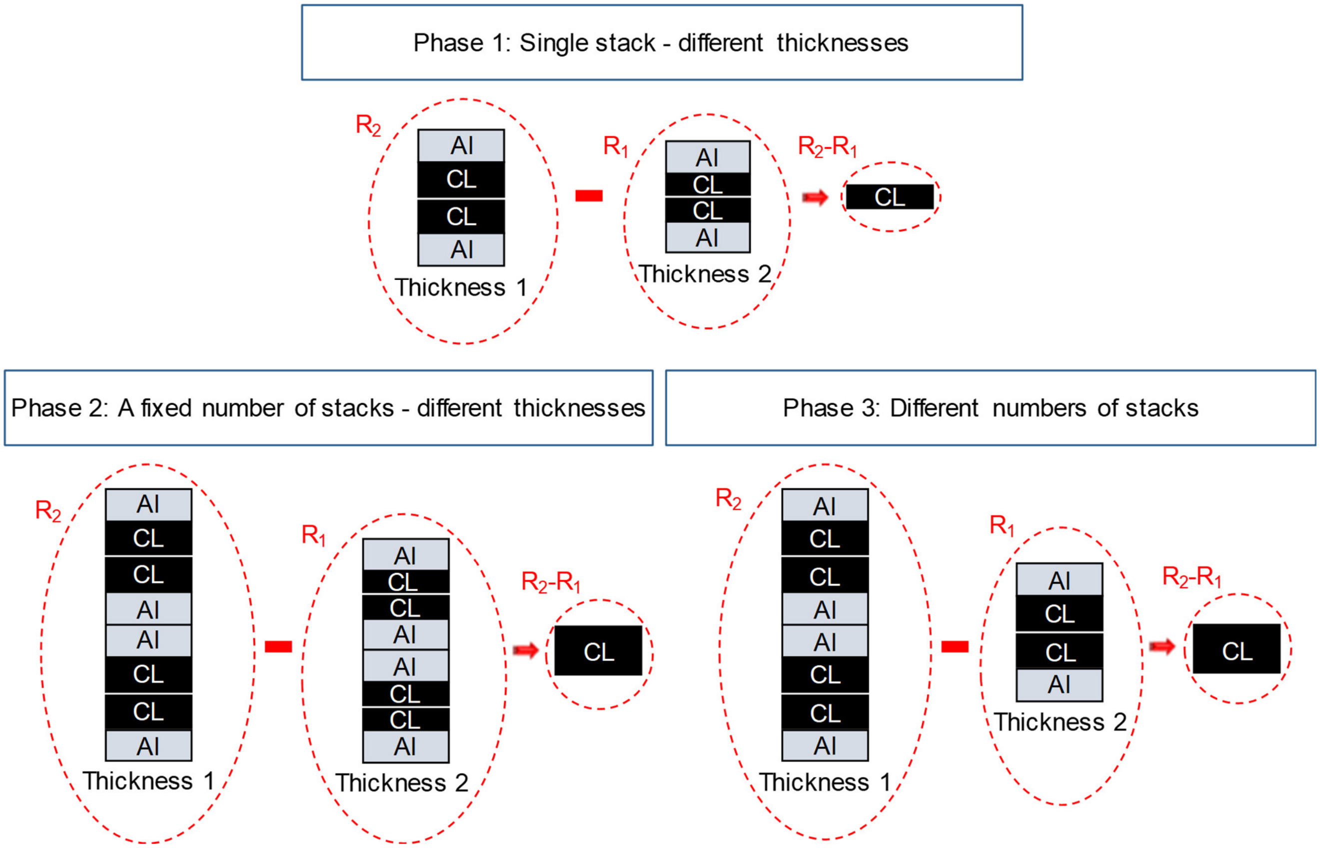

Figure 4-21. A schematic showing various phases of signal enhancement for measuring through-plane thermal resistance/conductivity of CL bulk

Accordingly, having a linear relationship between $R_{\text{tot,st}}$ and $h_{\text{cl,tot}}$ is still hinged on having a constant $k_{\text{cl,tp}}$ and R''' with changing $h_{\text{cl,tot}}$. In other words, if we measure $R_{\text{tot,st}}$ for a fixed number of stacks (fixed n) while changing $h_{\text{cl,tot}}$ and obtain a linear plot for $R_{\text{tot,st}}$ versus $h_{\text{cl,tot}}$, then $k_{\text{cl,tp}}$ and R''' must have remained constant for different $h_{\text{cl,tot}}$'s. The only difference in this case compared to single-stack measurements is that, here, we will have a higher signal from the CL bulk, i.e., $n\left(h_{\text{cl}(1)}+h_{\text{cl}(2)}\right)/\left(k_{\text{cl,tp}}A_{\text{sen}}\right)$ compared to $\left(h_{\text{cl}(1)}+h_{\text{cl}(2)}\right)/\left(k_{\text{cl,tp}}A_{\text{sen}}\right)$ for single-stack measurements. Figure 4-22 compares data of total resistance versus total thickness for n=1 and n=3, i.e., for 1-stack and 3-stacks tests of different stack thicknesses. As indicated by R-squared values in Figure 4-22, the 3-stacks measurements capture the linearity of the data significantly better than the

1-stack measurements. Figure 4-23 shows thermal conductivity values from the two methods. As shown in the figure, the 3-stacks method significantly reduces the measurement error.

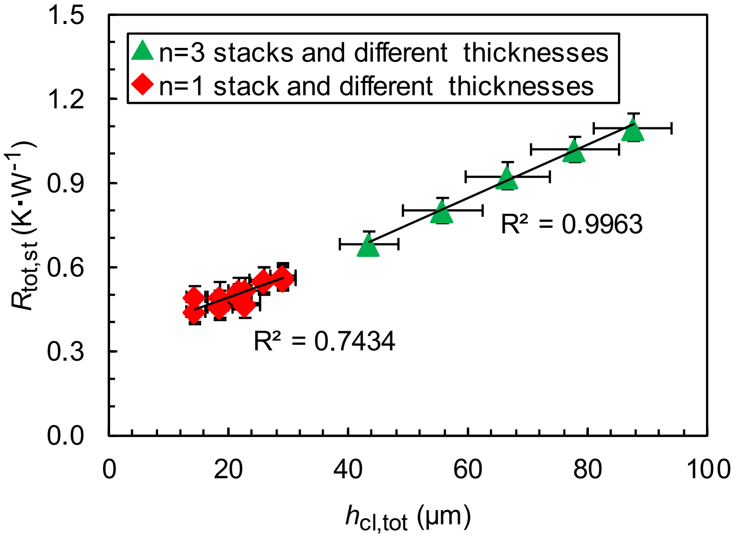

Figure 4-22. **Total thermal resistance vs. total CL thickness for the baseline CL at 1,500 kPa, 29 °C, and room RH, showing higher ability of 3-stacks tests compared to 1-stack tests in enhancing the bulk signal and capturing the linear trend in the data (error bars: STDs for thickness, random errors for resistance)**

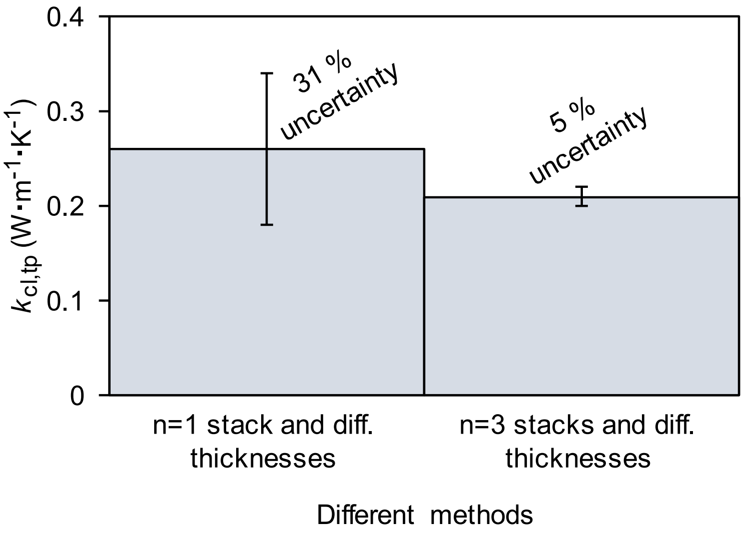

Figure 4-23. **Through-plane thermal conductivity of the baseline CL at 1,500 kPa, 29 °C, and room RH by different methods, showing lower uncertainty by measuring more stacks (error bars: random errors)**

According to Eq. (4.14), one would expect that the value of R''' goes up as the number of stacks (n) is increased. However, as shown in Figure 4-24, despite measuring two more stacks in the 3-stacks tests compared to the 1-stack tests, the value of R''' almost remains the same (within the error range) due to dominance of the last term in Eq. (4.14). This means that one could simply add more stacks to enhance the signal from the CL bulk instead of changing the CL thicknesses in the stacks. This gives way to the next method, i.e., measurements of different numbers of stacks.

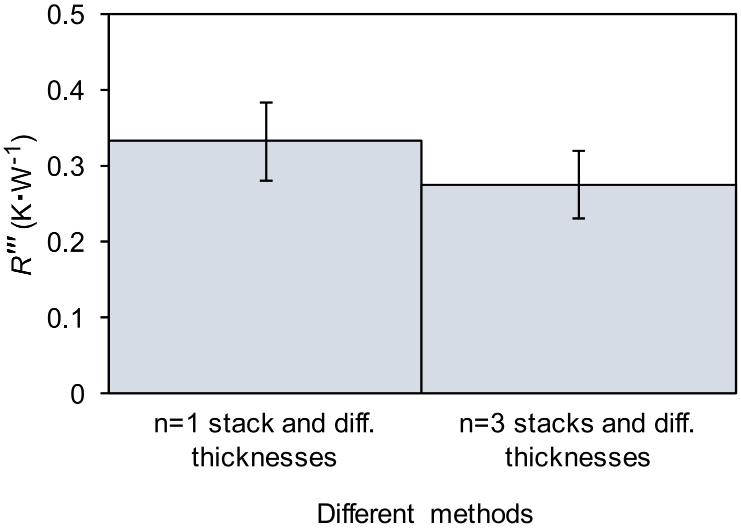

Figure 4-24. Parasitic thermal resistance in tests of the baseline CL at 1,500 kPa, 29 °C, and room RH, showing the same parasitic resistance (within the error range) by adding more stacks (error bars: random errors)

Different Numbers of Stacks

Relation for $R_{\mathrm{tot,st}}$ remains the same as Eq. (4.12) for measuring different numbers of stacks, and relations for $h_{\mathrm{cl,tot}}$ and R''' also remain the same as Eqs. (4.13) and (4.14), derived for n-stacks measurements. The only difference is that, previously, n was fixed and h_{cl}'s in each stack were changed to change the CL bulk signal in the method of "a fixed number of stacks (n stacks) and different thicknesses", whereas, here, h_{cl}'s of each stack are fixed (could also be changed) and n is changed to change the signal. Figure 4-25 shows the data measured by the method of "different numbers of stacks" (with the same CL thicknesses in the stacks and n up to 6) next to the data measured by the methods of "n=3 stacks and different thicknesses" and "n=1 stack and different thicknesses”. As shown in Figure 4-25, the methods of “different numbers of stacks” and “n=3 stacks and different thicknesses” are more capable of enhancing the signal from the CL bulk and capturing the linearity of the data.

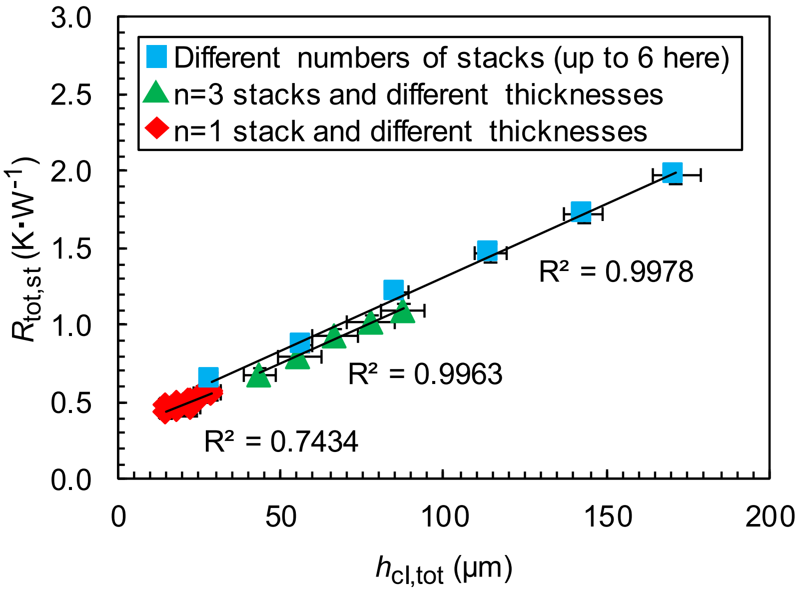

Figure 4-25. Total thermal resistance vs. total CL thickness for the baseline CL at 1,500 kPa, 29 °C, and room RH, showing different abilities of the methods in capturing the linear signal (error bars: STDs for thickness, random errors for resistance)

Figure 4-26 shows thermal conductivity values from the three methods, indicating progression of uncertainty minimization in various phases. The last two columns of Figure 4-26 also show that the CL thermal conductivity does not change with thickness (reminder: stacks with the same CL thicknesses were used in the method of “different numbers of stacks”). Further, the methods of “n=3 stacks and different thicknesses” and “different numbers of stacks” seem to be equally efficient according to the uncertainties shown in Figure 4-26. However, measurements of other CL designs showed that the latter method was generally more efficient. Appendix F contains similar measurements for designs #2 and #3 of Table 2-1, which further support this claim. In addition, the method of “different numbers of stacks” has the advantage of enabling measurements with just one thickness of the CL, which is useful where there are limitations for increasing the CL thickness, e.g., where structural integrity of a CL may be compromised by development of cracks and subsequent flaking.

It should be emphasized that the validity of the method of “different numbers of stacks” was confirmed here just for the 1,500 kPa contact pressure (and thus higher). Therefore, one should be cautious when using this method with lower pressures, as effects of TCRs may become significant at lower pressures. In this thesis, there was no need for confirming validity of the method for lower pressures, as the previous results of the method of “n=1 stack and different thicknesses” showed that thermal conductivity did not change with pressure (see Figure 4-19). Besides, this method is applicable for the whole ~15,00-3,000 kPa working pressure range of fuel cells.

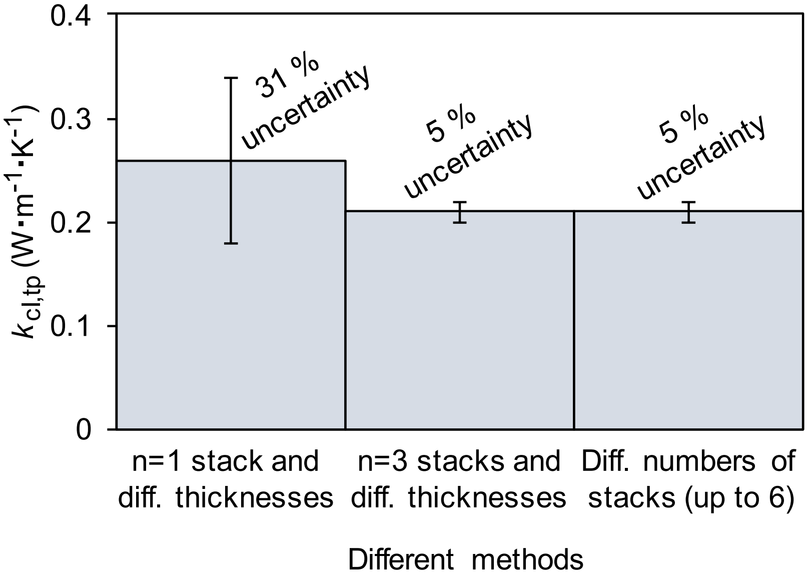

Figure 4-26. Through-plane thermal conductivity of the baseline CL by different methods at 1,500 kPa, 29 °C, and room RH showing progression of uncertainty minimzation (error bars: random errors)

Figure 4-27 shows parasitic resistances (i.e., R''' values) in different methods. As indicated by overlap of the error bars in the figure, the parasitic resistance does not change statistically by adding more stacks, which further supports the dominance of the TCRs between the stacks and the GHF fluxmeters in R''' (i.e., the last term in Eq. (4.14)). Similar observations were made by Ref. [29] for measuring thermal conductivity of GDLs by stacking.

Another supporting evidence regarding the dominance of the TCRs between the two end Al foils and the GHF fluxmeters is provided in Figure 4-28, where stacks of one and six

50 μm thick Al foil samples were measured. As shown in Figure 4-28, the Al foil samples were invisible to the device, and adding more Al foil samples to the stack did not change the measured total resistance. The total resistance of the stack of six Al foil samples comprises of five TCRs between the Al foil samples and two TCRs between the two end Al foil samples and the GHF fluxmeters. These TCRs are a part of the TCRs present in measurements of six Al-CL-CL-Al stacks (i.e., measurements by the method of "different numbers of stacks" shown above). The other part of TCRs in such tests consists of twelve Al-CL and six CL-CL TCRs. Figure 4-28 shows that the Al-Al TCRs were negligible compared to the TCRs between the Al foil samples and the GHF fluxmeters. On the other hand, the Al-CL and CL-CL TCRs should be much less than the Al-Al TCRs because: i) CLs are coated on (or bound onto) the Al foils, and ii) CLs have a lower surface roughness than Al foils, namely ~ 0.72 ± 0.04 μm vs. ~ 0.98 ± 0.04 μm (see Figure 3-12). Thus, the whole Al-Al, Al-CL, and CL-CL TCRs should be negligible compared to the TCRs between the apparatus and the samples, which is why the total resistances of Al foil stacks in Figure 4-28 are the same as the parasitic resistances of measurements of CCS stacks in Figure 4-27, within the error range.

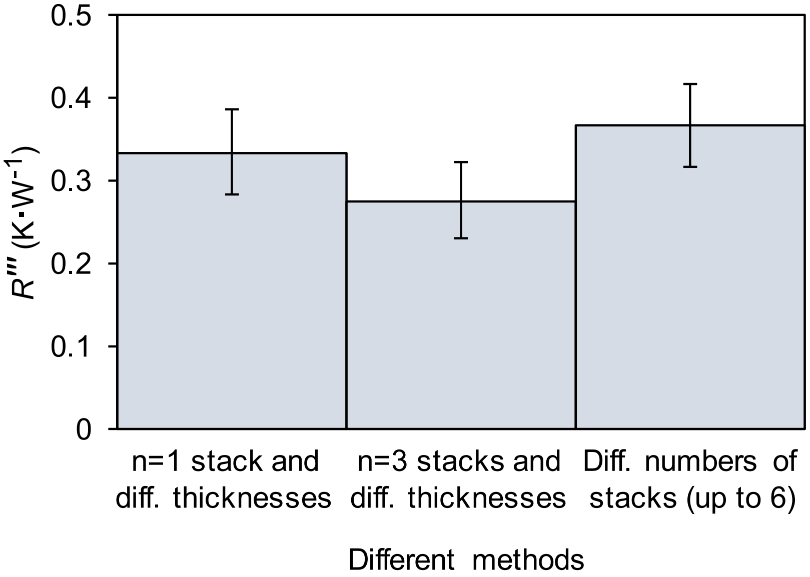

Figure 4-27. Parasitic thermal resistance in measurements of the baseline CL by different methods at 1,500 kPa, 29 °C, and room RH, showing the same parasitic resistance (within the error range) in different tests (error bars: random errors)

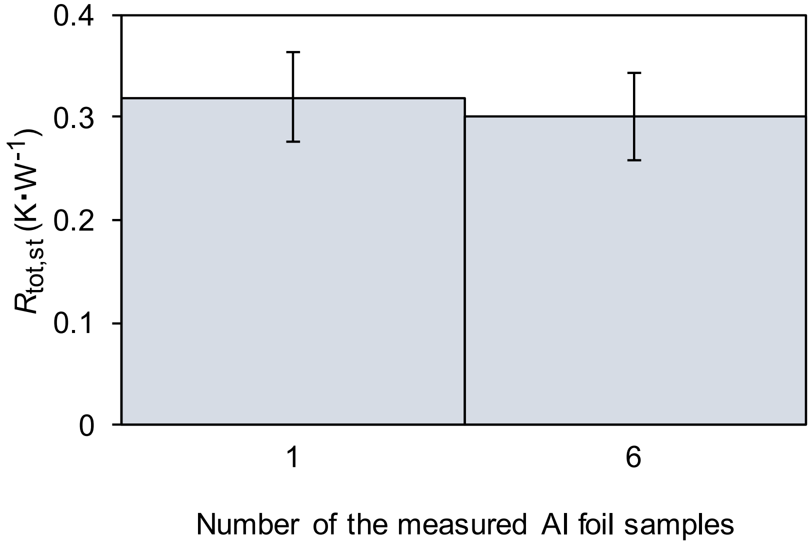

Figure 4-28. Total thermal resistance for stacks of one and six 50 µm thick Al foil samples at 1,500 kPa and 29 °C, showing negligibility of TCRs between the the Al foils as well as negligibility of resistance of the Al foil samples themeselves (error bars: random errors)

4.2.4. Feasibility of In-plane Thermal Conductivity Measurements

The author of this thesis is deeply doubtful about feasibility of measuring the in-plane thermal conductivity of CLs. Measuring this property requires measuring thermal resistance values for at least two lengths of a CL strip cut from the sample. Consider a CL strip with thickness of h_{cl}, width of Wid_{cl}, and length of Len_{cl}. The in-plane (along the length) bulk resistance of this strip could be expressed as:

$$R_{\mathrm{b,cl,ip}} = \frac{Len_{\mathrm{cl}}}{k_{\mathrm{cl,ip}} h_{\mathrm{cl}} Wid_{\mathrm{cl}}} \qquad (4.15)$$

Using Eq. (4.15) and assuming that in-plane thermal conductivity of a typical CL has the same order of magnitude as its through-plane conductivity, in-plane resistance of a hypothetical CL strip with thickness of 10 µm, width of 1 cm, length of 1 cm, and conductivity of 0.2 W·m^{-1}·K^{-1} would be calculated as 500,000 K·W^{-1}! This means that if 1 W heat were to pass through the 1 cm length of the strip, it would produce 500,000 K temperature difference across the length of the strip! Thus the 1 W heat, i.e., the ballpark amount of heat usually applied in thermal resistance tests, cannot pass through the strip.

Another way to look at the issue is to try calculating length of a CL strip with a typically measurable resistance of 1 K·W^{-1}. Using Eq. (4.15) and assuming a hypothetical CL strip with thickness of 10 μm, width of 1 cm, and conductivity of 0.2 W·m^{-1}·K^{-1}, a value of 20 nm is obtained for the strip length. Therefore, to measure such a typical resistance, one would have to cut a 20 nm long strip of the CL and fix it in between the jaws of the testbed's sample holder. Even if we assume thermal conductivity of graphene for in-plane direction of CLs, i.e., ~2000 W·m^{-1}·K^{-1}, which is highly unlikely, a length of 200 μm would be calculated for the strip which would still be impossible to cut accurately and fix in a conventional in-plane sample holder for the tests.

Therefore, measuring the in-plane thermal resistance of CLs may not be possible by any conventional method due to the extremely huge in-plane resistance of CLs, coming from the very small thickness of CLs. Due to such a huge resistance, any amount of heat applied to a CL strip by any in-plane testbed would either diffuse to a very short length through the sample and its substrate and then would totally diffuse to the ambient, or (optimistically) it would only pass through the CL substrate, whose much smaller resistance would be in parallel to the CL. The pessimistic view would be if the heat would not diffuse into the sample, the substrate, or the ambient, in which case, it would burn/melt the whole thing. Accordingly, the author of this thesis has great doubts about possibility of measuring the in-plane thermal conductivity of CLs. Based on the above discussion, reported values in the literature for this property would most likely represent the in-plane thermal conductivity of the substrate instead of the CL itself.

The above order of magnitude analysis of the in-plane thermal resistance shows that in-plane thermal conductivity of CLs should play no role in heat transfer inside PEMFCs. In this thesis, discussions of this property are limited to modeling this property jointly with the in-plane electronic conductivity (see Chapter 6).

4.2.5. Through-plane Thermal Conductivity Results for all the Designs

Figure 4-29 shows the measured thermal conductivities for all the CL designs. As shown in Figure 4-29, thermal conductivity decreases with increasing the I/C ratio and dry milling time but does not change with the drying temperature of the ink. Reasons behind the observed decreasing trends could be explained as follows:

i) The added ionomer (with increasing the I/C ratio) may affect contact points between carbon particles of neighboring agglomerates in the through-plane direction by penetrating between them and, thus, making the contact areas smaller. This will lead to higher spreading/constriction resistances at the contact areas. More justifications are provided in Chapter 5.

ii) As discussed in section 2.5, carbon particles go through a transition from a polyhedron shape to a spherical shape by dry milling [72]. This transition results in reduction in size of the contact areas between the particles from flat facets of the polyhedrons to point contacts between the spheres, leading to reduction in thermal conductivity.

Thermal conductivity did not change with the drying temperature of the ink because changing the drying temperature mainly changed the crack density and crack aspect ratio (see Figure 3-16), to which the through-plane conduction is not much sensitive. However, as discussed in Chapter 5, increasing the drying temperature of the ink enhanced the in-plane electronic conductivity by reducing the number and size of cracks.

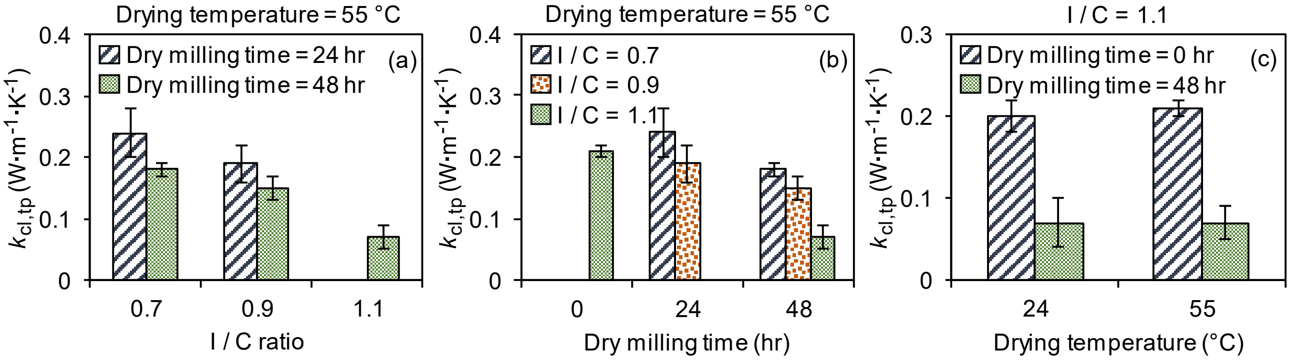

Figure 4-29. Through-plane thermal conductivity for different CL designs at 1,500 kPa, 29 °C, and room RH (error bars: random errors)

Results of Figure 4-29 show that design #4 with I/C=0.7, 24 hr dry milling time, and 55 °C drying temperature of the ink was the most conductive CL among all the designs. This CL was not among the least porous designs (see Figure 3-16). However, its specific composition and fabrication gave it a microstructure with the highest conductivity. The lowest conductivity belonged to designs #5 and #7 with I/C=1.1 and 48 hr dry milling time, which were the least porous designs as well (see Figure 3-16). The above results are very counterintuitive in the sense that one would normally expect a higher thermal conductivity for a less porous material. Thus, developing an in-depth understanding of the underlying structural effects is of paramount importance to fully understand heat transfer inside CLs, which is a topic for the modeling work presented in Chapter 6.

4.3. Conclusions

In this section, capabilities and limitations of two different through-plane thermal conductivity testbeds were investigated, and testing procedures were modified and developed to enhance the signal to noise ratio for CLs (and, thus, similar thin coatings). An order of magnitude analysis of in-plane thermal resistance of a typical CL showed that measuring the in-plane thermal conductivity was neither possible nor necessary due to the huge in-plane thermal resistance of CLs. Results showed that effects of TCRs between a transient or steady state apparatus and a sample (or stack of samples) were significant, which necessitated careful and accurate deconvolution of such effects. On the other hand, as steady state measurements of CLs on an Al substrate revealed, effects of TCRs within the layers of samples in a stack were not significant and could be neglected. Based on these findings, different procedures for signal to noise ratio enhancement were developed and tested with success. The procedures were then used to measure through-plane thermal conductivity of various CL designs with different compositions and microstructures. The through-plane thermal resistance/conductivity data of this chapter are tabulated in Appendix G.

Results showed that through-plane thermal conductivity of CLs did not change with contact pressure and drying temperature of the ink but significantly changed with I/C ratio and dry-milling time, all of which could be directly linked to the CL microstructure. Further, counterintuitive trends were observed in the data, which established the need for developing an in-depth understanding of structure-property correlations. In Chapter 5, electronic conductivity measurements are explained, which further shed light on the CL microstructure and reveal the significance of studies of structure-property correlations.

Chapter 5.

Electronic Conductivity Measurements

Electronic resistance measurements were performed by a Micro Junior 2 micro-ohm meter (Raytech, USA). The ohm meter measured a sample in a four-probe configuration by passing a DC current through the sample. Calibration of the device was checked with ±3% error using standard resistors in the range of 0.01-10^5 Ω. The data of Figure 5-1 were collected by directly attaching the voltage and current leads of the device to the resistors.

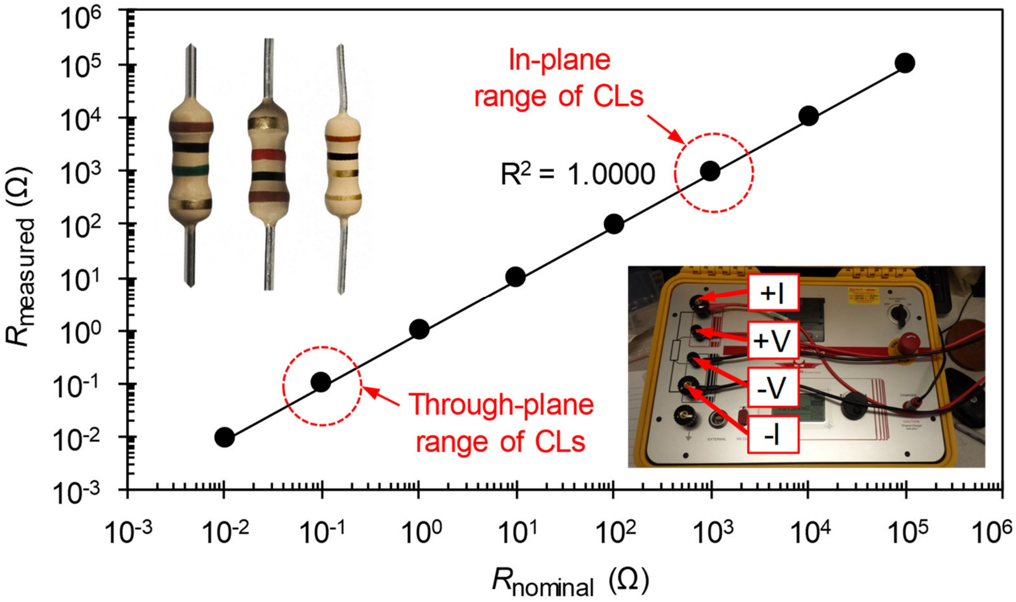

Figure 5-1. Calibration check of the micro-ohm meter using standard resistors

5.1. Through-plane Electronic Conductivity Measurements

To measure the through-plane electronic resistance of CLs, the same stacking method introduced in section 4.2.1 was used as a first trial. The prepared stack was then clamped between four custom-made gold-plated probes attached to corresponding current and voltage leads of the micro-ohm meter. The whole stacks-probes sandwich was put between the heat fluxmeters of the GHF testbed under pressure for mechanical pressure (P) and temperature (T) control (see Figure 5-2 a).

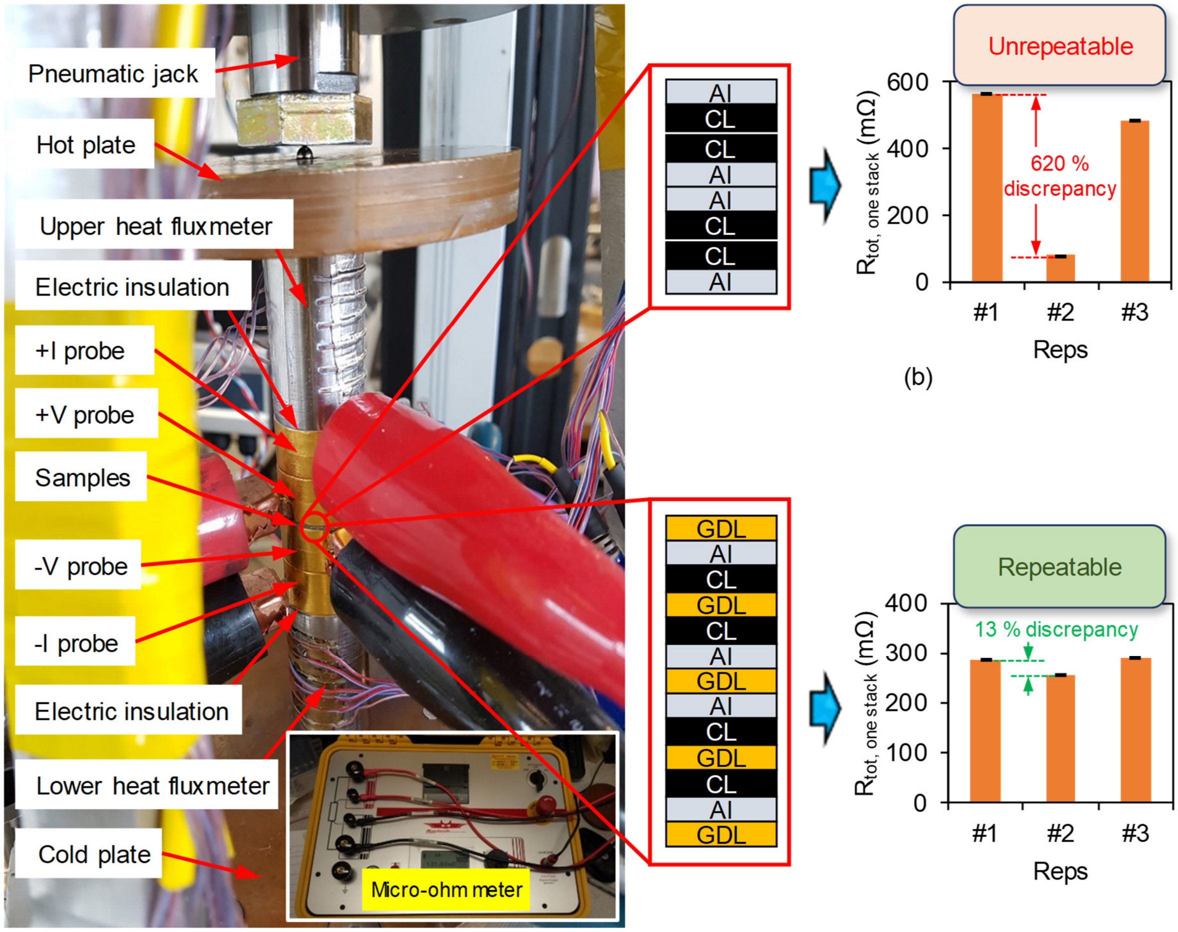

(a) (c)

Figure 5-2. Through-plane electronic conductivity testbed and sample configurations: (a) micro-ohm meter integrated with the GHF testbed for P and T control, (b) measurements of Al-CL-CL-Al stacks (error bars: systematic errors), and (c) measurements of catalyst-coated Al samples with GDLs in between (error bars: systematic errors)

Calibration of the through-plane testbed was ensured by measuring a GDL sample and obtaining a value which was in good agreement with measurements by the TUC_RUC device at AFCC (less than 2% discrepancy); the TUC_RUC device performed two-point measurements. Further, only a few μΩ was measured by the through-plane setup when no sample was mounted, which showed minimal contribution from the through-plane probes in the tests when compared to through-plane resistance of CLs which was in the order of a few Ω. The first trials on CLs using the same stacking method as used in the thermal tests were unrepeatable (see Figure 5-2 b). After conducting many tests on different materials with different mechanical properties, including thick and thin foils of Al and Cu, it was found that the reason for unrepeatability of the tests was the great role of electronic contact resistances (ECRs) originated from imperfect contact between the surfaces. For this reason, effort was made to find a material with high electronic conductivity which could reduce the ECRs at the interfaces by deforming plastically and filling the gaps at the interfaces. Among all the tested materials, GDLs proved to be the best option. Their through-plane resistance was two orders of magnitude lower than CCSs, and they could reduce the ECRs and make the measurements repeatable (see Figure 5-2 c). Different currents from 0.1 to 1 A yielded the same resistance, which confirmed applicability of Ohm's law for through-plane tests of CLs. Using the stacking method of Figure 5-2 c, total through-plane resistance measured for a stack consisting of n samples with GDLs at every interface could be expressed as:

$$R_{\mathrm{tot,st}} = R_{\mathrm{b,cl}} + R'''' = \frac{h_{\mathrm{cl,tot}}}{\sigma_{\mathrm{cl,tp}} A_{\mathrm{sen}}} + R'''' \tag{5.1}$$

where $R_{\mathrm{b,cl}}$ is through-plane bulk resistance of all the CLs in the stack, R'''' is summation of all the measured resistances except for the bulk of the CLs (i.e., Al substrates, GDLs, probes, and ECRs in between), $h_{\mathrm{cl,tot}} = nh_{\mathrm{cl}}$ is total thickness of the CLs in the stack, $\sigma_{\mathrm{cl,tp}}$ is through-plane electronic conductivity of the CL, and A_{sen} is area of the sensors covering the stack (the same as sample's area). As indicated by Eq. (5.1), $R_{\mathrm{tot,st}}$ is a linear function of $h_{\mathrm{cl,tot}}$. Accordingly, by measuring stacks with different $h_{\mathrm{cl,tot}}$'s, $\sigma_{\mathrm{cl,tp}}$ and R'''' could be deconvoluted from a linear regression analysis of the $R_{\mathrm{tot,st}}$ versus $h_{\mathrm{cl,tot}}$ plot ($\sigma_{\mathrm{cl,tp}}$ from the slope and R'''' from the intercept of the line). Thus, effects of all the substrates and interfaces are deconvoluted from the final conductivity results because those effects are bundled in R''''. For completeness, expression for R'''' is given as:

$$R'''' = n\left(R_{\mathrm{b,Al}} + R_{\mathrm{c,Al\text{-}cl}}\right) + (n+1)R_{\mathrm{b,gdl}} + nR_{\mathrm{c,cl\text{-}gdl}} + nR_{\mathrm{c,Al\text{-}gdl}} + 2R_{\mathrm{gdl\text{-}sen}} \tag{5.2}$$

where $R_{\mathrm{b,Al}}$ and $R_{\mathrm{b,gdl}}$ show through-plane bulk resistances of Al and GDL, respectively, $R_{\mathrm{c,Al\text{-}cl}}$ shows ECR between an Al foil and a CL, $R_{\mathrm{c,cl\text{-}gdl}}$ shows ECR between a CL and a

GDL, $R_{\text{c,Al-gdl}}$ shows ECR between an Al foil and a GDL, and $R_{\text{gdl-sen}}$ shows ECR between one of the end GDLs and one of the probes.

5.1.1. Signal to Noise Ratio Enhancement

CL thicknesses were very small, and resistances of different thicknesses were very close to each other. This led to high uncertainties for through-plane conductivity in case of measuring stacks of two samples ($n = 2$). Thus, similar to the through-plane thermal conductivity tests, there was a need to enhance the signal to noise ratio in order to have a satisfactory accuracy for through-plane electronic conductivity. Higher accuracy was achieved by increasing the number of samples in the stack. Figure 5-3 shows total resistance versus total CL thickness for design #2 of Table 2-1, when only two samples were stacked and measured. The high scatter of the data is due to measuring a few samples, leading to resistances which are too close to each other such that they would fall within the uncertainties of one another. Figure 5-4 shows total resistance data measured from stacks of two samples next to data measured from stacks of six samples. As indicated by R-squared values in Figure 5-4, the linearity of the data of total resistance versus thickness is captured considerably better by increasing the number of samples per stack. Figure 5-5 shows the through-plane conductivity values deconvoluted from the data and enhancement in accuracy by increasing the number of samples.

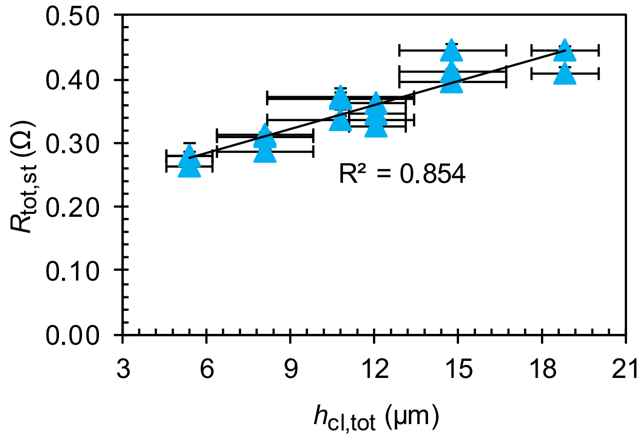

Figure 5-3. **Total through-plane electronic resistance vs. total CL thickness for two-samples tests of design #2 at 1,500 kPa, 21 °C, and room RH, showing high scatter of the data when measuring a few samples (error bars: STDs for thickness, random errors for resistance)**

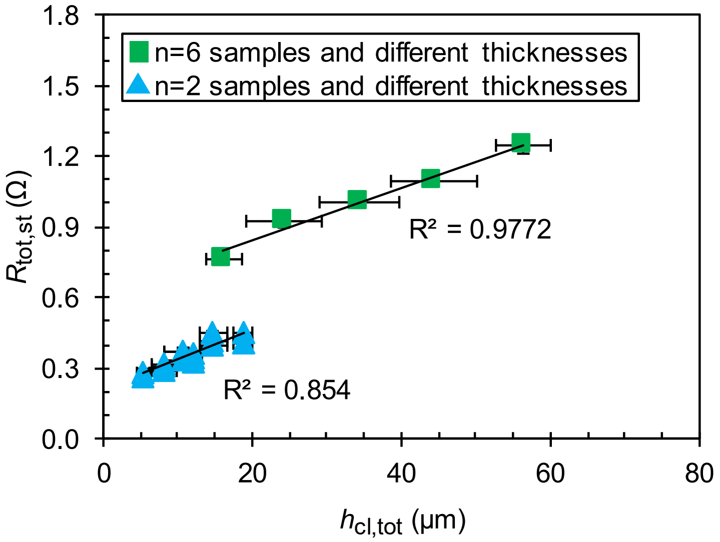

Figure 5-4. **Total through-plane electronic resistance vs. total CL thickness for two-samples and six-samples tests of design #2 at 1,500 kPa, 21 °C, and room RH, showing lower scatter of the data by measuring more samples (error bars: STDs for thickness, random errors for resistance)**

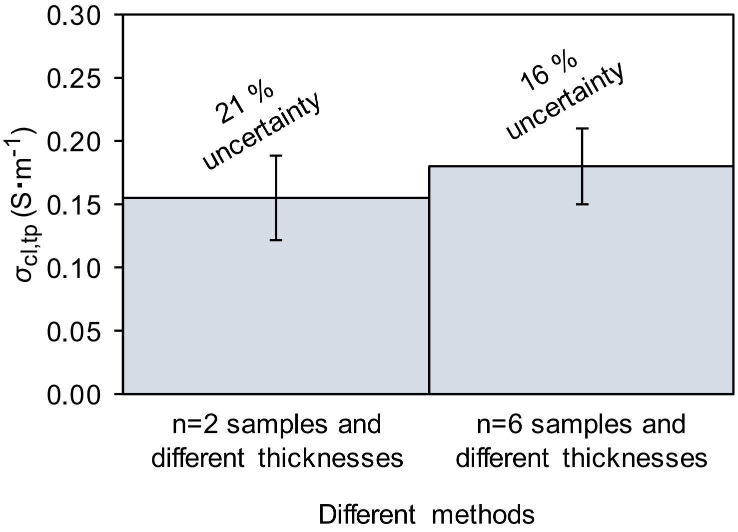

Figure 5-5. **Through-plane electronic conductivity of design #2 at 1,500 kPa, 21 °C, and room RH, showing enhancement of measurement accuracy by increasing the number of samples per stack (error bars: random errors)**

However, as shown in Figure 5-6, unlike the thermal tests discussed in section 4.2.3, the parasitic through-plane electronic resistance substantially increases by adding more samples, making it impossible to measure the CL bulk by measuring different numbers of samples in the electrical tests. The reason behind this difference between the thermal and electrical tests is that the gas at the interfaces has a very small effective thickness and a finite thermal conductivity, which give it a very small thermal resistance, but it is completely electronically insulating. This leads to small TCRs but considerable ECRs at the interfaces.

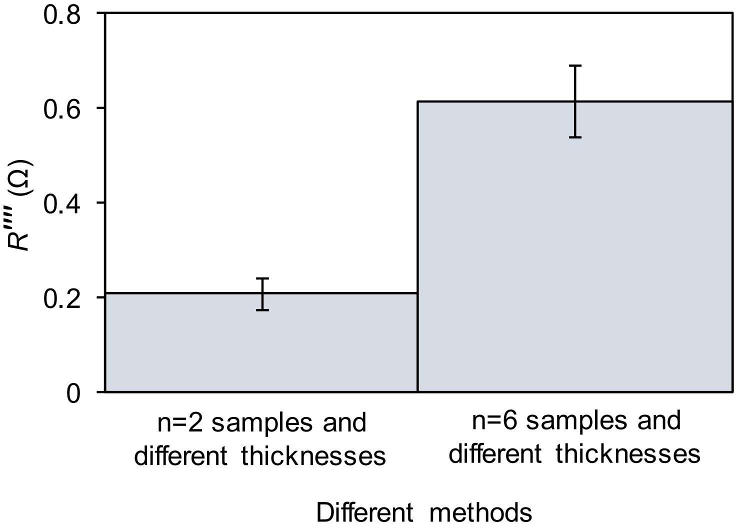

Figure 5-6. Parasitic through-plane electronic resistance in measurements of design #2 at 1,500 kPa, 21 °C, and room RH, showing a higher parasitic resistance by measuring more samples (error bars: random errors)

5.2. In-plane Electronic Conductivity Measurements

In-plane electronic resistance tests were performed using a custom-made in-plane sample holder, shown in Figure 5-7, integrated with the micro-ohm meter. The sample holder consisted of two metallic jaws, for clamping strips of samples, and four sliding plastic frames, enabling adjustment of the sample length between the probes. After clamping a desired length of the sample, current and voltage leads of the ohm meter were connected in a four-probe configuration to the clamps. GDLs were used between the clamps and the sample to protect the CL surfaces from the metallic jaws and reduce ECRs in the clamps. In-plane resistance of the GDLs used in the clamps was orders of magnitude lower than the CLs, which would fall into the error range of the tests and could be neglected. Accordingly, total in-plane resistance measured for a sample could be expressed as:

$$R_{\mathrm{tot,ip}} = R_{\mathrm{b,cl,ip}} + ECR = \frac{Len_{\mathrm{cl}}}{\sigma_{\mathrm{cl,ip}} h_{\mathrm{cl}} Wid_{\mathrm{cl}}} + ECR \tag{5.3}$$

where $\sigma_{\mathrm{cl,ip}}$ is in-plane conductivity of the CL, Len_{cl} is probed length (length of the sample between the clamps), and Wid_{cl} is width of the CL strip. Similar to Eq. (5.1), measuring at least two lengths of a sample would enable deconvolution of $\sigma_{\mathrm{cl,ip}}$ and ECR by a linear regression analysis of the $R_{\mathrm{tot,ip}} - Len_{\mathrm{cl}}$ data points.

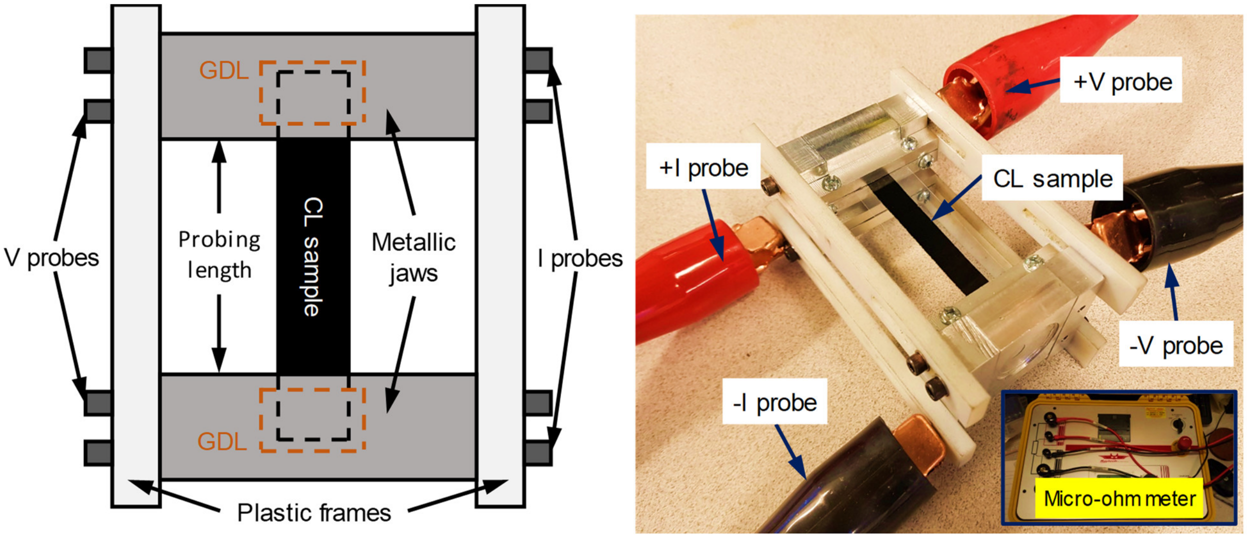

(a) (b)

Figure 5-7. In-plane electronic conductivity testbed and sample holder: (a) a schematic of the in-plane sample holder, and (b) the in-plane sample holder integrated with the micro-ohm meter

5.2.1. Signal to Noise Ratio Enhancement

High signal to noise ratio for the in-plane tests was ensured by designing the in-plane sample holder such that the metallic jaws would have no movable parts other than the clamps, to minimize ECRs in the jaws. The clamps could be fastened tightly using bolts. Further, the design of the in-plane sample holder allowed changing the probing length in a wide range, ensuring highly linear $R_{\mathrm{tot,ip}} - Len_{\mathrm{cl}}$ curves with R-squared values more than 0.99 for the CLs. Calibration of the in-plane sample holder was ensured by clamping and measuring standard resistors in the range of 0.01-10^5 Ω as well as strips of 50 μm thick Al foil. The standard resistor measurements completely overlapped with the data in Figure 5-1 and had only ±3% discrepancy with the nominal values, as if the voltage and current leads were directly attached to the resistors. The Al measurements, shown in Figure 5-8, yielded a value of (34 ± 4) × 10^6 S·m^{-1} which was in good agreement with the range of 35 – 37 × 10^6 S·m^{-1} found in the literature for Al at 20 °C (~3-9% discrepancy). Figure 5-9 shows a highly linear $R_{\mathrm{tot,ip}} - Len_{\mathrm{cl}}$ plot measured for design #1 of Table 2-1, which led to deconvolution of 526 ± 36 S·m^{-1} for in-plane conductivity of the CL (~7% uncertainty). The deconvoluted ECR was an ideal close-to-zero value of ~ 0.01 ± 0.02 kΩ.

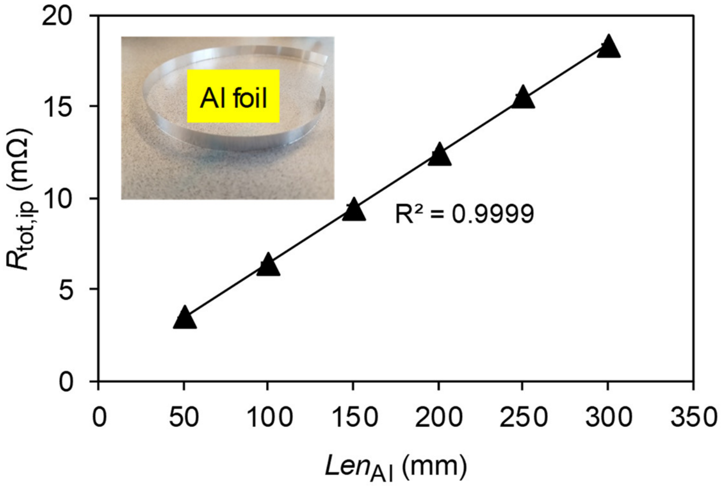

Figure 5-8. Total in-plane electronic resistance of 50 µm thick Al strips, showing a highly linear signal (errors: random errors)

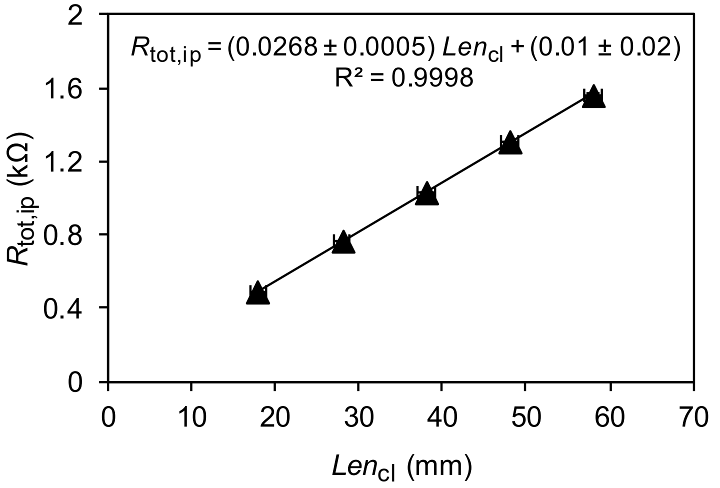

Figure 5-9. Total in-plane electronic resistance of CL strips (design #1) at 21 °C and room RH, showing a highly linear signal (errors: random errors)

5.3. Through-plane vs. In-plane Electronic Conductivity for all the CL Designs

Figure 5-10 shows through-plane vs. in-plane electronic conductivity for all the designs. As shown in the figure, through-plane values are generally three orders of magnitude lower than the in-plane values, which indicates anisotropy of the CLs. This anisotropy is discussed in the next section. Through-plane electronic conductivity tests at different contact pressures showed that the conductivity did not change with pressure. This may be explained based on having a fixed contact area between covalently-bonded carbon particles in the aggregates [77-80], which would not change by changing the pressure. Similar observations were made for through-plane thermal conductivity (see Figure 4-19).

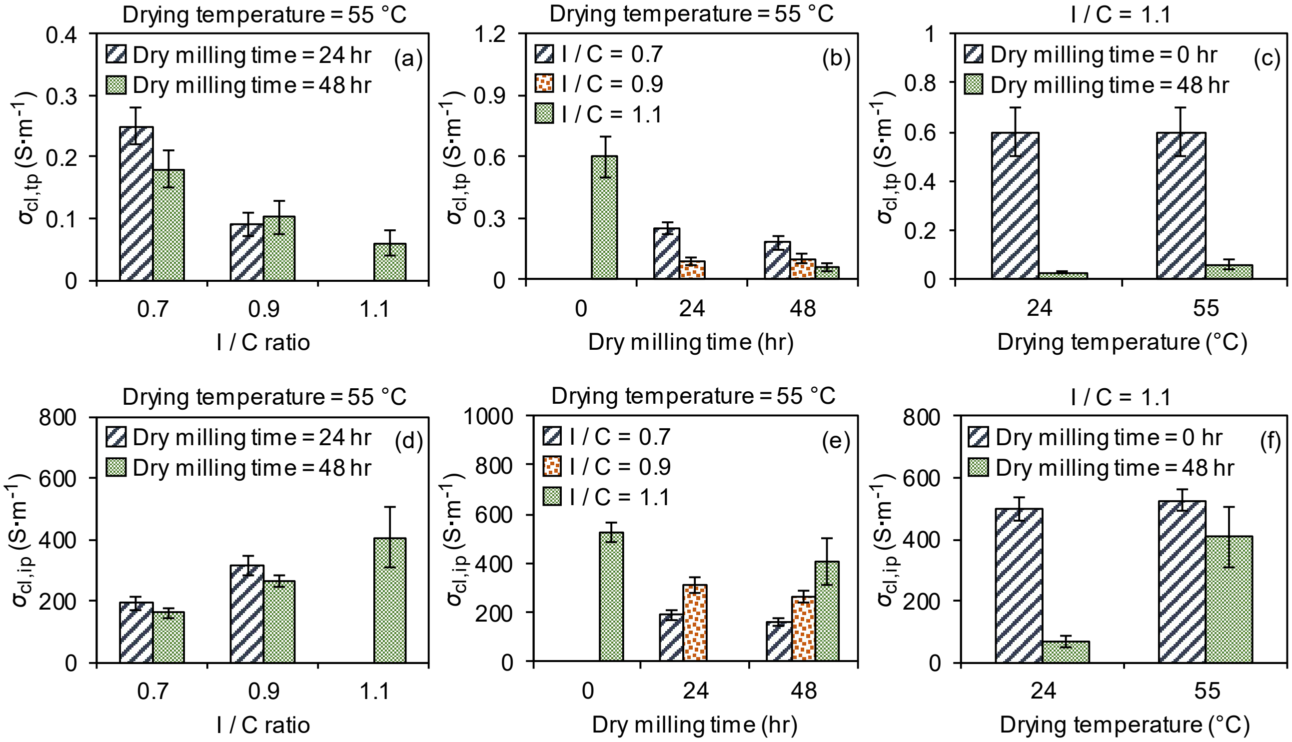

Figure 5-10. Electronic conductivity of different CL designs at 21 °C and room RH (error bars: random errors): (a-c) through-plane vs. (d-f) in-plane

Figure 5-10 a and b show that, similar to the through-plane thermal conductivity results of section 4.2.5, through-plane electronic conductivity decreases with increasing the I/C ratio and dry milling time. Possible reasons behind these decreasing trends are the same as the ones mentioned for through-plane thermal conductivity, namely: i) reduction in the number of carbon-carbon contacts between neighboring agglomerates by increasing the I/C ratio, and ii) reduction in the size of carbon-carbon contacts between neighboring agglomerates by increasing the dry milling time. The decreasing trends are relatively steeper for through-plane electronic (compared to through-plane thermal) conductivity because ionomer and gas at the contact points completely block the electrons but finitely conduct the heat. Figure 5-10 c shows that increasing the drying temperature increases the through-plane conductivity for dry milling time of 48 hr but does not change the conductivity for 0 hr dry milling time. This could be explained based on the very different structure of the CL with I/C=1.1, 48 hr dry milling time, and 24 °C drying temperature. SEM surface images of different CLs with different drying temperatures are shown in Figure 5-11. As shown in Figure 5-11, changing the drying temperature from 55 to 24 °C did not change the structure in a significant way from design #1 to design #8 but significantly changed the structure from design #5 to design #7, such that design #7 has a noticeably lower CL area compared to design #5. Hence, design #7 should have a noticeably lower through-plane electronic conductivity than design #5. Further, free spots left from detachment of big chunks of catalyst in design #7 increase electronic constriction resistances through the CL. However, as discussed in section 4.2.5, this structural change did not affect the through-plane thermal conductivity in a significant way because the air in the gaps would still be thermally conductive with a conductivity of the same order of magnitude as the CLs in those cases.

In Figure 5-10 d, a different trend with I/C ratio is observed for in-plane conductivity; unlike the through-plane conductivity, it increases with increasing the I/C ratio because of reduction in the surface crack density and crack aspect ratio with increasing the I/C ratio (see Figure 3-16 for comparing values of crack density and crack aspect ratio). Addition of more ionomer results in better structural integrity of the CL in the in-plane direction (hence fewer and smaller cracks and more carbon-carbon contacts). As discussed later in section 5.4, experiments show that ionomer must not penetrate much in between the in-plane connections of the aggregates. Thus, unlike the through-plane electronic connections, there should be no negative effect from ionomer on the in-plane electronic connections. Figure 5-10 e and f show the same trends observed for effects of dry milling time and drying temperature on the through-plane conductivity. In addition to the reasons mentioned for these trends for the through-plane conductivity, the following factors may negatively affect the in-plane conductivity: i) augmentation of crack density and crack aspect ratio by increasing the dry milling time (see Figure 3-16), in addition to increasing sphericity of the particles, and ii) significant augmentation of crack aspect ratio (in addition to crack density) by decreasing the drying temperature for 48 hr dry milling time (see Figure 3-16).

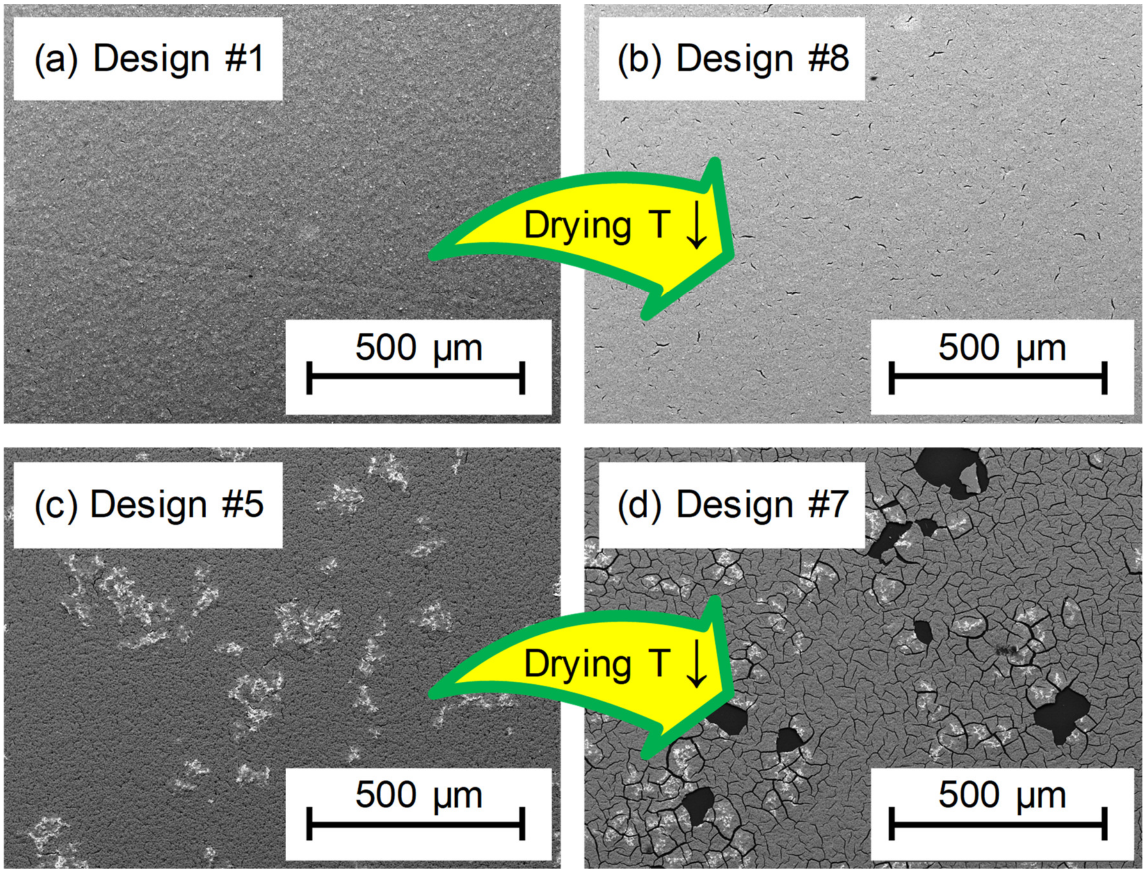

Figure 5-11. SEM surface images of CLs with different drying temperatures: (a) and (b) with the same I/C (1.1) and dry milling time (0 hr) with (a) dried at 55 °C and (b) dried at 24 °C; (c) and (d) also with the same I/C (1.1) and dry milling time (48 hr) with (c) dried at 55 °C and (d) dried at 24 °C, showing the very different structure of the latter CL

Results of Figure 5-10 show that designs #1 and #8 with I/C=1.1 and 0 hr dry milling time were the most conductive CLs among all the designs, which is counterintuitive considering that these CLs had the highest I/C ratio (i.e., the highest ionomer content) and porosities among all the designs (see Figure 3-16 for comparing the porosity values). The highest conductivities of these CLs are results of their specific microstructure dictated by their specific composition and fabrication, as discussed above. This further shows that a simple intuitive relationship between the conductivity and porosity or ionomer content of CLs does not exist and clarifies the need for developing an in-depth understanding of structure-property correlations, which is a topic for Chapter 6.

5.4. Anisotropy of Electronic Conductivity

To explain the anisotropy, a discussion is needed first regarding the limiting factor of electron conduction in CLs. The only components of a CL which could conduct electrons are carbon (C) and platinum (Pt) particles. The Pt particles, however, have a very small volume fraction compared to the C particles; the ratio between the volume of Pt and C could be obtained as $(m_{\mathrm{Pt}}/m_{\mathrm{C}}) \times (\rho_{\mathrm{C}}/\rho_{\mathrm{Pt}})$ which is calculated to be ~7%, considering the 1:1 mass ratio of Pt to C in the used Pt/C catalyst and densities of ~1,600 $\mathrm{kg{\cdot}m^{-3}}$ for porous C particles and ~21,450 $\mathrm{kg{\cdot}m^{-3}}$ for Pt particles. Further, the current trend in literature for optimizing CLs is to reduce their cost by decreasing their Pt loading, meaning that share of Pt particles in the volume of CLs could go way below 7%. Thus, Pt particles do not contribute much in conduction of electrons as they do not occupy much volume in CLs. Micrographs of Pt/C aggregates available in the literature also confirm this claim by showing Pt particles as tiny particles sparsely covering the surface of C aggregates (for example see Ref. [53]). Therefore, electron conduction in CLs should be determined by the properties of the carbon phase. On the other hand, as discussed in section 2.5, C particles are strongly fused together inside the aggregates [77-80], which means that bulk conductivity of the aggregates should be fairly high. Accordingly, conduction of electrons in CLs should be limited by carbon-carbon contacts of neighboring aggregates. Thus, the only way to explain the anisotropy in CLs is if the Pt/C aggregates were connected together considerably better in the in-plane direction than the through-plane direction. To test this hypothesis on a CL, effort was made to weaken the connections between the aggregates by hydrating the CL ex-situ and examining its effects on the through-plane and in-plane electronic conductivities. Hydration was expected to weaken the connections as a consequence of ionomer swelling. For this purpose, samples of design #1 (i.e., the CL with the highest electronic conductivity in both directions) were kept under 80 °C DI water for 1 hr to allow penetration of water into the pores and ionomer. The 80 °C temperature was used to reduce the surface tension of water and allow its penetration into the pores. The same strategy was used by Gostick et al. [132] for hydrating GDLs. Experiments showed that CLs almost completely lost their through-plane electronic conductivity at ~16-20% water uptake in an irreversible way when hydrated in the way explained, whereas the loss in the in-plane conductivity was only ~ 50%. This showed that as hydration occurred, ionomer swelled and took adjacent Pt/C aggregates apart from each other, thereby weakening the contacts between them. Observing a nearly complete loss in the through-plane electronic conductivity of the hydrated CLs revealed that adjacent Pt/C aggregates must have had very weak through-plane connections, which completely broke as the CLs were hydrated, but much stronger in-plane connections, of which only ~50% broke by hydration. However, in real operation of a fuel cell, all the cells are under ~1.5-3.0 MPa compression when hydration occurs in-situ as a result of the electrochemical reaction, and we can speculate that these high contact pressures would hold the structural integrity of the CLs and prevent the collapse of CL through-plane electronic conductivity observed during our ex-situ hydration tests. Thus, the results of the ex-situ hydration tests conducted in this thesis should strictly be regarded as proofs for different contacts of Pt/C aggregates in the in-plane and through-plane directions, and the conductivity results for the hydrated CLs are not relevant for fuel cell performance. Morris et al. [48] conducted electronic conductivity tests on CLs at elevated RH; they also observed reduction in electronic conductivity by increasing the gas RH and attributed the losses to ionomer swelling. Electronic conductivity values reported by Morris et al. [48] ranged from ~60-300 $S \cdot m^{-1}$ for dry CLs, which is in the same range of in-plane measurements of this thesis despite the very different measurement method and CLs used by this reference. The values of Ref. [48] are, however, in the lower range of the measurements of this thesis, perhaps due to using the VDP method [52] by Ref. [48], which only gives an average conductivity, as also noted by Refs. [48, 133].

The very different contacts of Pt/C aggregates in the through-plane and in-plane directions may be explained based on the used coating method in this thesis and behavior of ionomer in the catalyst ink under shear. As discussed in Chapter 2, Mayer-bar coating was used in this thesis for producing CLs due to its high resemblance to the roll-coating process used in industry for mass production of CLs. In this process, a coating rod would move with a speed of ~0.1 $\mathrm{m \cdot s^{-1}}$ over the catalyst ink to spread it on the substrate. In this thesis, viscosity of the ink was not measured. However, taking the viscosity value of 2.75 Pa·s from Ref. [134], approximating the applied shear by the coating rod on the ink as $vis_{\mathrm{ink}} v_{\mathrm{rod}} / h_{\mathrm{ink}}$ where the terms respectively represent viscosity of the catalyst ink, speed of the coating rod, and thickness of the ink, and assuming a thickness of ~ 20 μm for the ink (higher than dried CL thicknesses), a shear force of ~14,000 $\mathrm{N \cdot m^{-2}}$ is calculated which is a considerable value. On the other hand, ionomer, as a polymer electrolyte, has a fibrillar structure which could be aligned in presence of shear forces along the shear direction [135-141]. Further, hydration of ionomer nanofibers in the catalyst ink could produce a one-dimensional paracrystalline lattice, separated by polymer layers, as showed by Ref. [142] for hydrated Nafion; this could further help alignment of ionomer nanofibers along the shear by straightening the hydrated nanofibers like hoses filled with water. Several researchers have reported effects of this alignment in ionomers on physical properties. For instance, Ref. [141] showed highly anisotropic proton conduction in block copolymer electrolyte membranes aligned by applying electric field and shear. Ref. [143] showed highly anisotropic ionic conductivity of block copolymer membranes aligned in presence of magnetic field. Accordingly, it is speculated that alignment of hydrated ionomer nanofibers in presence of high shear forces during Mayer-bar coating may be the main reason for having weak through-plane connections between the aggregates. It is also speculated that alignment of ionomer nanofibers in the in-plane direction (i.e., the shear direction) leads to penetration of ionomer into the through-plane contacts between the aggregates, thereby weakening the contacts and increasing their chance of breakage by ionomer swelling. This may further explain the observed almost total loss of through-plane conduction by hydrating the CLs; as hydration occurred, it is possible that the ionomer at the through-plane contact regions between the aggregates swelled and disconnected the through-plane electronic connections. The in-plane electronic connections, though, were not affected as much as the through-plane connections, perhaps due to the much lower amount of ionomer at the in-plane contact regions. As noted by Refs. [136, 140], ionomer fibrillar structures have a diameter of 3-4 nm and a length on the order of ~100 nm which is well comparable with the aggregate size of 100-300 nm. This suggests another speculation for effect of hydration on the in-plane electronic conductivity. It is possible that each fibrillar structure, after getting aligned in the in-plane direction (still a speculation), adheres to two neighboring aggregates in the in-plane direction and binds them together, thereby providing structural integrity for the CL in the in-plane direction, as shown schematically in Figure 5-12. After the ink dries, these nanofibers may contract in length and enhance the in-plane contacts between the aggregates. Thus, a probable mechanism for reduction of the in-plane conductivity by hydration could be loosening the long ionomer strands holding the aggregates in the in-plane direction.

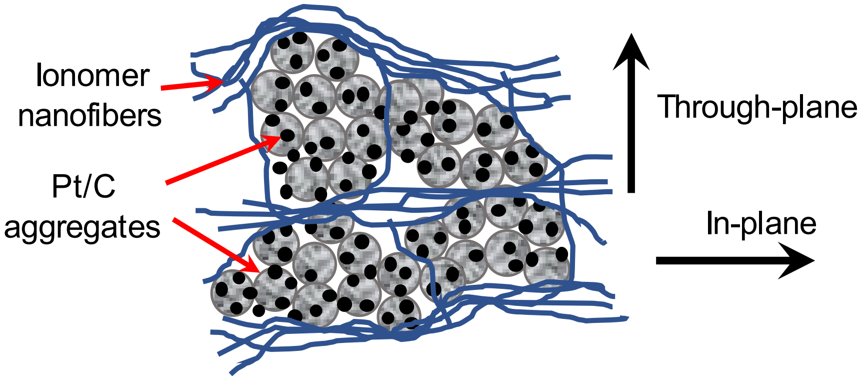

Figure 5-12. The proposed model for arrangement of ionomer nanofibers around the Pt/C aggregates in a CL (small black spheres: Pt; larger spheres: C), suggesting existence of more ionomer nanofibers along the in-plane direction due to alignment by shear during coating

One argument regarding the proposed model in Figure 5-12 is that the proposed structural anisotropy of the ionomer phase should also be seen in protonic conductivity. However, measurements of protonic conductivity of CLs in different directions have not been reported in the literature yet, and the existing protonic conductivity measurements have assumed negligibility of the electronic resistance of the CLs in their analyses [24, 144-146]. The through-plane electronic conductivity measurements of this thesis show that such an assumption may not be valid. The measurements of this thesis could be served as a first step toward development of more accurate techniques for protonic conductivity measurements in different directions, which can further be used to examine the validity of the proposed model in Figure 5-12 by investigating the anisotropy for protonic conductivity. Another aspect is that such anisotropy in protonic conductivity is speculated to be detrimental to fuel cell performance because, according to the model proposed in Figure

5-12, most of the ionomer nanofibers would be aligned in the in-plane direction. It is probably more beneficial to have ionomer nanofibers aligned in the through-plane direction to transfer protons between the membrane and the catalyst sites inside the CLs. Investigation of these issues is beyond the scope of this thesis and is only suggested here as a future work.

Another argument is that since Mayer bar coating is a directional method, which performs the coating in only one direction, one may expect to see difference between in-plane electronic conductivity/resistance values along the machine (or coating) direction and measurements along the direction perpendicular to the coating direction. However, experiments with CL strips of design #1 showed no difference between the two directions, which is counterintuitive and demands a more in-depth analysis of the CL microstructure. This shows that the proposed model in Figure 5-12 needs to be further confirmed/improved/modified through advanced ionomer visualization techniques, such as soft X-ray spectro-tomography introduced in Ref. [147]. This will help better understand the true 3D distribution of ionomer within the CL. The electronic conductivity measurements of this thesis provide a motivation for such more in-depth investigations.

5.5. Anisotropy Trends

Anisotropy trends are revealed by plotting the ratio of in-plane (IP) to through-plane (TP) electronic conductivity for various designs, as shown in Figure 5-13. The graph shows that increasing the ionomer content leads to an increase in the IP/TP anisotropy. This seems to make sense if we consider the ionomer as the lubricant and insulating material between the particles. More ionomer may lead to less particle-to-particle contact points in the TP direction after coating, perhaps due to shear/separation effect (see Figure 5-12). Dry milling generally increases the anisotropy; for I/C=1.1 (and 55 °C drying temperature), the increase is almost a factor of 8. Higher dry milling time may lead to smaller and rounder particles with less particle-to-particle contact points in the TP direction after coating, leading to an increase in anisotropy. The graph further shows that only for the dry-milled powder, the drying temperature has an effect. Higher drying temperature means faster drying, which "freezes" the after-coating structure. Thus, it appears that faster drying could better conserve/freeze the anisotropy for the dry-milled case. The reason for this observation is the much more significant augmentation in crack density and crack aspect ratio with slow drying for the dry-milled case (see Figure 3-16 f and i), which makes the IP conductivity significantly worse and closer to the TP conductivity (see Figure 5-10 c and f), thereby reducing the anisotropy in this case.

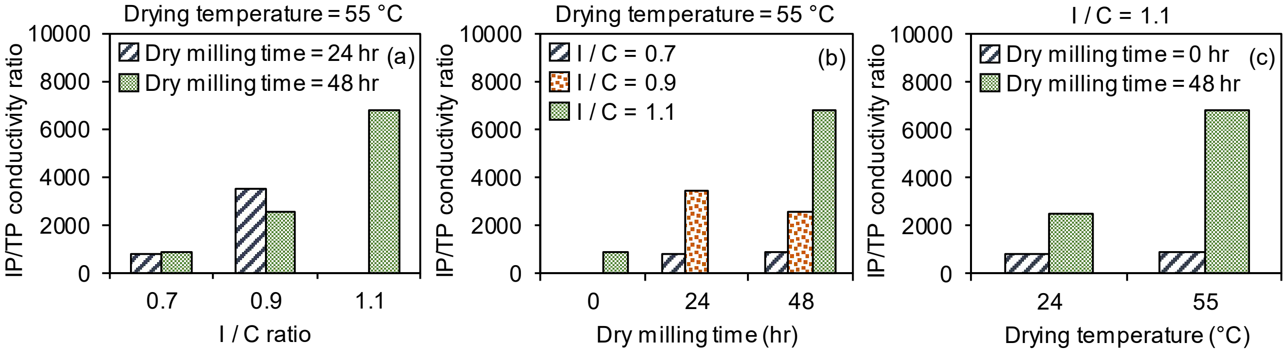

Figure 5-13. In-plane (IP) to through-plane (TP) electronic conductivity ratio for different CL designs, showing a three orders of magnitude anisotropy in electronic conductivity and higher anisotropy with larger I/C ratio, dry milling time, and drying temperature

5.6. Significance of Having a Low Through-plane Electronic Conductivity for CLs

Low magnitude of through-plane electronic conductivity of CLs could have significant impacts on the performance of PEMFCs. A simple order of magnitude analysis of possible voltage drop across a CL clarifies the issue. In practice, only a fraction of the CL thickness may be utilized in the electrochemical reaction due to mass transport limitations and other factors [1, 99, 148, 149]. The utilized fraction of the CL thickness depends on operating conditions, CL composition, and balance between transport of species through the CL [1, 99]. Accordingly, order of magnitude of the voltage drop across a CL could be obtained as O$(R_{\text{cl,tp}}I)$~O$\left(\{\mathcal{E}h_{\text{cl}}/\left(\sigma_{\text{cl,tp}}A_{\text{cell}}\right)\}I\right)$ in [V], where $R_{\text{cl,tp}}$ is the CL through-plane resistance in [Ω], I the current in [A], $\mathcal{E}$ the utilized fraction of the CL thickness (O$(\mathcal{E})\sim 0.1$ [99]), h_{cl} the CL thickness (O$(h_{\text{cl}})\sim 10^{-4}$ cm), $\sigma_{\text{cl,tp}}$ the CL through-plane conductivity (O$\left(\sigma_{\text{cl,tp}}\right)\sim 10^{-3}$ S·cm^{-1}), and A_{cell} the cell area in [cm^2]. For a typical cell with $A_{\text{cell}} = 1$ cm^2, output voltage of 700 mV, and current density of 1 A·cm^{-2}, this means having O$(R_{\text{cl,tp}}I)$~O$(10$ mV$)$. In practice, this voltage drop could also be influenced by nonuniform distribution of the current density through the CL thickness [1, 99, 148, 149]; for instance, similar calculations considering a linear distribution for current density across the thickness (as suggested by Ref. [1]) yields $\mathrm{O}(R_{\mathrm{cl,tp}}I){\sim}\mathrm{O}(5\ \mathrm{mV})$.

Accordingly, the exact value of voltage drop across the CLs could be significant. Based on the order of magnitude analysis of shares of different losses in section 1.2, the relative share of CLs in ohmic loss of a cell may be of the order of $\sim\mathrm{O}(5-10\ \%)$, meaning that CLs could have a significant contribution in the total ohmic loss. This indicates a motivation to enhance the CL through-plane electronic conductivity; one way could be developing coating methods which would not prefer one direction to another. The exact value of share of CLs in the performance loss, however, should be obtained through a rigorous modeling of the performance, while considering precise values for other resistances, namely, protonic resistances of the electrolyte and CLs as well as resistances of the interconnects and contacts [1]. Unfortunately, such a detailed breakdown of different resistances is not available at the moment. Further, there are two other complications regarding such a rigorous analysis:

i) As mentioned before, measurements of protonic conductivity of CLs in the literature have been under the assumption of negligible electronic resistance for the CLs [24, 144-146], which was questioned in this thesis.

ii) In this thesis, electronic conductivity was measured for fresh CLs, whereas in practice, CLs are conditioned before a fuel cell is made operational [144, 145, 150]. This could further change the morphology of the CLs and could affect their conductivity in operation.

Accordingly, more research is still needed in the above-mentioned areas to fill the existing knowledge gaps and enable a precise analysis of the different modes of ohmic loss.

5.7. Conclusions

In this chapter, a procedure for measuring the through-plane electronic conductivity of CLs was developed for the first time, which could make the through-plane tests repeatable and, thus, could enable deconvolution of signal from the CL bulk in such tests. Further, a new accurate method was proposed for measuring the in-plane electronic conductivity of

CLs. The through-plane and in-plane procedures/testbeds were further improved to enhance the signal to noise ratio in the tests. The developed tools enabled separate measurements of the through-plane and in-plane electronic conductivities for the first time, which uncovered new insights into the CL microstructure, including its anisotropy. The through-plane conductivity was found to be three orders of magnitude lower than the in-plane conductivity because of the anisotropy. Employing the tools for measuring different CL designs revealed additional insights into the microstructure, including possibilities of: i) bending effects of dry milling on carbon particles, ii) contact/separation effects of ionomer, and iii) structure-freezing effects of drying temperature of the ink. An order of magnitude analysis of voltage drop across a CL revealed the significance of the low through-plane electronic conductivity of CLs for performance of PEMFCs and clarified the need for developing more efficient isotropic coating methods for CLs. The electronic resistance/conductivity data of this chapter are tabulated in Appendix H. In the next chapter, insights from the microstructural study and thermal and electronic conductivity measurements, discussed in the previous chapters, are employed to develop structure-property correlations which could precisely link the conductivities to the microstructure.

Chapter 6.

Modeling the Thermal and Electronic Conductivities

Before presenting the models, it is beneficial to briefly explain the path which was taken in this PhD program to develop the presented models. Thermal conductivity was the first property to model, and cracks were not initially considered in the model because they would contribute minimally to the through-plane conduction under dry conditions. Carbon particles were considered as separate particles, and particle-particle contacts were modeled using the Hertzian contact theory [151]. Aggregates of particles were modeled using micro-mechanics models [152], considering the possibility of relative displacement of particles under pressure, determined by inter-particle interactions under the assumption of completely rough/smooth particles [153]. A random packing [154] was considered for the particles inside the aggregates. A portion of the aggregates was assumed to be fully covered/isolated by ionomer all over, and the remaining portion was assumed to be in contact with each other with an unknown overlap angle and full ionomer coverage elsewhere. As one could imagine, this initial model contained many physical and geometrical properties, most of which could not even be estimated, such as the portion of completely rough particles, the portion of isolated aggregates, and the overlap angle, not to mention that some of the assumptions such as completely rough/smooth particles could be very far from the actual physics. The unknown parameters in this initial model were basically used as handles to fit the model to experimental data. Aside from the significant amount of guesswork for fitting the tweaking parameters, comparing the modeling results with the data of Ref. [13] showed that the model would significantly overpredict the effects of contact pressure between the particles.

In the next step, it was assumed that the particles were arranged in an SC pattern inside the agglomerates, and relative displacement of the particles was neglected to remove some of the tweaking parameters from the model. In this approach, particle-particle contacts were assumed to be Hertzian contacts [151], whose sizes were determined solely from the contact pressure. Further, the particles inside each agglomerate were treated discretely to construct a circuit of particle resistances inside the agglomerate, which was then used to find the aggregate resistance. In this circuit, there were several rows of particles in an aggregate, each of which was made of a parallel configuration of particle resistances, and the effective row resistances were in series with each other. However, the resistance circuit of the aggregate was significantly dominated by the two end rows at the overlap regions, which had the highest resistances due to having the smallest sizes (i.e., the fewest parallel particle resistances). This led to a significant instability of the modeling results, when particles would be removed/added to the aggregate by changing a parameter such as radii of the aggregate and carbon particles or overlap angle between the neighboring aggregates. It also yielded a conductivity of zero at zero contact pressure due to not predicting any contact area between the carbon particles at zero contact pressure.

In the next step, to remove the numerical instability, an integration scheme was developed to find the resistance of the aggregate. Effective conductivity of the aggregate was found through a unit cell approach, and the aggregate resistance was obtained by integrating over the resistance of an infinitesimally small element of the aggregate (a differential element of the row resistance). Further, adhesion force between the particles [155] was taken into account to correct the model for zero contact pressure. This modeling approach mitigated the instability issue and could reasonably predict the through-plane thermal conductivity at different contact pressures, including the zero pressure. The results of this model were published in Refs. [60, 156]. However, the model still lacked effects of factors such as cracks, temperature, and hydration, and it would significantly overpredict the electronic conductivities due to considering pure carbon-carbon contacts between the neighboring aggregates. Further, it considered the carbon particles inside the aggregates as separate particles, whereas the actual physics was having covalent bonding between the particles [77-80]. This meant that modeling approaches such as Hertzian theory [151] would be inconsistent with the actual physics. This also explained the negligible changes observed in the experimental data of the through-plane conductivities versus pressure because contact area between particles, welded together by covalent bonding, should not change with pressure. The Hertzian theory, although inconsistent with the actual physics, also predicted a negligible change in the through-plane thermal conductivity with increasing the pressure [60, 156]. Thus, another aspect, revealed by this modeling exercise, was that contact pressure was not a significant factor in the model and could safely be removed. Removing the negligible effect of contact pressure also meant further simplification of the model by removing the need to calculate the parameters associated with the Hertzian theory [151] and the adhesion effects [155]. Another inconsistency in this model was that, still, an SC arrangement was assumed for the carbon particles inside the aggregates, whereas high-resolution electron microscope images showed a dense packing of particles inside the aggregates. The above-mentioned inconsistencies and deficiencies provided enough motivation to improve the model and turn it into the forms presented in this chapter.

6.1. Assumptions

The experience gained through the model development exercises, explained above, led to the following list of assumptions to mitigate the inconsistencies and include the required level of microstructural details for modeling the conductivities:

i) An agglomerate-like structure for the CL (see the discussions of sections 3.1 and 3.3.6);

ii) An orderly structure which could be dissected into geometric units (unit cells) to simplify the analytical modeling;

iii) A cracked structure with cracks in form of high aspect ratio ellipsoidal particles randomly oriented within the CL, backed by the crack characterizations of section 3.4;

iv) Negligible contribution of Pt particles to heat and electron conduction due to occupying less than ~2% of the volume of the CL (explained later);

v) A continuous, dense structure for the fused carbon particles in an aggregate, sparsely populated by nanopores between the particles (explained later), backed up by high-resolution electron microscope images of aggregates;

vi) An orderly, dense FCC arrangement for the carbon particles inside an aggregate to simplify the analytical modeling;

vii) Existence of ionomer at contact areas (overlap regions) between neighboring aggregates, indicated by the conductivity data of sections 4.2.5 and 5.3 and the analyses provided in sections 5.4 and 5.5;

viii) Anisotropic structure of carbon particles, with graphitic layers covering an amorphous core, in accordance with carbon black and CL literature (for example see Refs. [55, 56, 80]);

ix) An SC arrangement for the agglomerates to simplify the analytical modeling;

x) Spread of ionomer around the aggregate in form of a thin film;

xi) Possibility of having a partial coverage for the ionomer film on the surface of an aggregate (i.e., ionomer coverage), in accordance with CL literature (for example see Ref. [157]);

xii) Steady state heat/electron conduction through the CL;

xiii) Possibility of using the physical properties of Nafion for Aquivion, and the physical properties of PTFE (i.e., the backbone of ionomers such as Nafion and Aquivion) instead of the physical properties of the dry ionomer, which is a common practice in literature (for example see Refs. [158, 159]);

xiv) Possibility of using the physical properties of single crystals of graphite for modeling the carbon particles, due to the graphitic structure of the partially graphitized carbon particles used in this study; and

xv) Negligible effects of contact pressure on the bulk conductivities, backed up by the experimental data of sections 4.2.2 and 5.3.

6.2. Modeling Approach

A multi-scale unit cell approach is adopted to derive closed-form expressions for the thermal and electronic conductivities. In this context, a unit cell in a certain scale refers to a geometric unit of the material which could be representative of the whole material at that scale. The proposed geometrical model, shown in Figure 3-1, dictates the chain of unit cells shown in Figure 6-1, featuring four scales of unit cells:

i) A macroscale unit cell for the cracked structure, consisting of a dispersion of cracks in the catalyst bulk;

ii) A microscale unit cell in which agglomerates are clustered around a micropore at the middle of the cell;

iii) A mesoscale unit cell which is the unit cell of an agglomerate cluster around the micropore; and

iv) A nanoscale unit cell which represents the unit cell of a Pt/C aggregate inside an agglomerate.

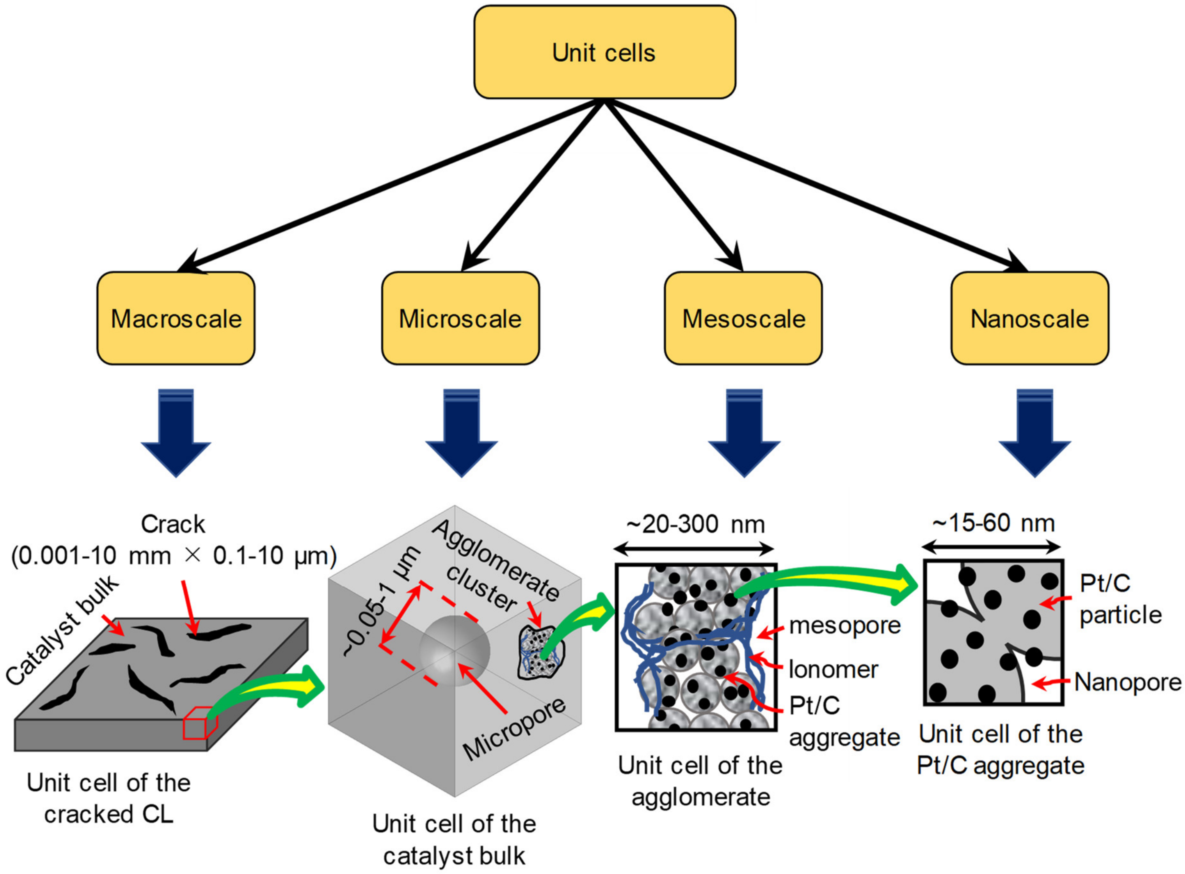

Figure 6-1. The proposed multi-scale unit cell model for modeling the thermal and electronic conductivities of CLs

The micropore between the agglomerate clusters is considered as a spherical pore in the middle of the microscale unit cell. Further, as mentioned before, for simplicity, an SC arrangement is considered for the overlapping agglomerates in the mesoscale unit cell, and an FCC arrangement is considered for the Pt/C particles in the nanoscale unit cell due to their compact arrangement in the agglomerates (observed in TEM images).

Monitoring weight change of CLs by a Thermogravimetric Sorption Analyzer (IGA-002, Hiden Isochema) from ~ 0-90% RH showed less than 5% water uptake per mass of dry CL. In addition, monitoring thermal resistance of CLs at different RH values did not show any meaningful change in the thermal resistance. Accordingly, in this thesis, only the extreme cases of dry and fully-flooded with liquid water are modeled.

In the following subsections, the conductivities are modeled at different scales using the developed unit cells, and the developed models are then coupled to yield the effective conductivities.

6.3. Modeling the Conductivities at Macroscale

6.3.1. Through-plane Conduction at Macroscale

Through-plane conductivity of a CL has the following relationship with its thickness and resistance:

$$\Lambda_{\mathrm{cl,tp}} = \frac{h_{\mathrm{cl}}}{R_{\mathrm{cl,tp}} A_{\mathrm{cl,tot}}} \tag{6.1}$$

where $\Lambda_{\mathrm{cl,tp}}$ is the through-plane thermal or electronic conductivity of the CL, $R_{\mathrm{cl,tp}}$ is the through-plane thermal or electronic resistance of the CL, h_{cl} is the CL thickness, and $A_{\mathrm{cl,tot}}$ is total geometric area of the CL including area of cracks. To consider effects of cracks on the through-plane conduction at macroscale, we consider a cracked CL to be made of islands of catalyst bulk separated by the cracks. The island-like structure is reconciled with the much higher in-plane electronic conductivity by considering that the CL is anisotropic in each island, with the through-plane electronic conductivity being much less than the in-plane electronic conductivity. The cracks just reduce the in-plane electronic conductivity from the value of each island to that of the cracked CL. Using such an assumption (i.e., the island-like structure), resistances of those catalyst bulk islands and the cracks would all be in parallel to each other in the through-plane conduction, the combination of which would yield $R_{\mathrm{cl,tp}}$. Thus $R_{\mathrm{cl,tp}}$ could be expressed as:

$$R_{\mathrm{cl,tp}} = \left(\sum_i \frac{1}{\left(R_{\mathrm{b,cl,tp}}\right)_i} + \sum_e \frac{1}{\left(R_{\mathrm{cr,tp}}\right)_e} \right)^{-1} \tag{6.2}$$

where $\left(R_{\mathrm{b,cl,tp}}\right)_i$ and $\left(R_{\mathrm{cr,tp}}\right)_e$ are through-plane resistances of the i'th catalyst bulk island and the e'th crack, respectively, expressed as:

$$\left(R_{\mathrm{b,cl,tp}}\right)_i = \frac{h_{\mathrm{cl}}}{\Lambda_{\mathrm{b,cl,tp}}\left(A_{\mathrm{b,cl}}\right)_i} \tag{6.3}$$

$$\left(R_{\mathrm{cr,tp}}\right)_e = \frac{h_{\mathrm{cl}}}{\Lambda_{\mathrm{cr}}\left(A_{\mathrm{cr}}\right)_e} \tag{6.4}$$

where $\Lambda_{\mathrm{b,cl,tp}}$ and Λ_{cr} are conductivities of the CL bulk (in the through-plane direction) and cracks, respectively, and $\left(A_{\mathrm{b,cl}}\right)_i$ and $\left(A_{\mathrm{cr}}\right)_e$ are areas of the i'th CL bulk island and the e'th crack, respectively. Combining Eqs. (6.1)-(6.4) and simplifying the result would yield the following relation for $\Lambda_{\mathrm{cl,tp}}$:

$$\Lambda_{\mathrm{cl,tp}} = \Lambda_{\mathrm{b,cl,tp}} \frac{\sum_i \left(A_{\mathrm{b,cl}}\right)_i}{A_{\mathrm{cl,tot}}} + \Lambda_{\mathrm{cr}} \frac{\sum_e \left(A_{\mathrm{cr}}\right)_e}{A_{\mathrm{cl,tot}}} \tag{6.5}$$

On the other hand, from the definition of crack density, we have:

$$CD = \frac{\sum_e \left(A_{\mathrm{cr}}\right)_e}{A_{\mathrm{cl,tot}}} = 1 - \frac{\sum_i \left(A_{\mathrm{b,cl}}\right)_i}{A_{\mathrm{cl,tot}}} \tag{6.6}$$

where CD represents crack density of the CL. Thus, using the above definition in Eq. (6.5) yields the following relation for $\Lambda_{\mathrm{cl,tp}}$ in terms of $\Lambda_{\mathrm{b,cl,tp}}$, Λ_{cr}, and CD:

$$\Lambda_{\mathrm{cl,tp}} = (1 - CD)\Lambda_{\mathrm{b,cl,tp}} + (CD)\Lambda_{\mathrm{cr}} \tag{6.7}$$

Cracks are either filled with gas in dry CLs or water in flooded CLs. Thus, Λ_{cr} is zero for electronic conduction and bulk thermal conductivity of the gas or water for thermal conduction. Since dimensions of cracks are generally one to six orders of magnitude higher than molecular mean free path of air ($\sim 0.07\ \mu\mathrm{m}$) and three to eight orders of magnitude higher than molecular mean free path of liquid water (~ 2.4 Å), size effects could be neglected for cracks, and bulk thermal conductivity of the fluid is directly applicable for use in Eq. (6.7). More discussions will be provided later in this chapter regarding calculation of the mean free paths. To account for temperature effects, the following relations are used for thermal conductivity of air [160] and water [161]:

$$k_{\mathrm{a}} = 5.75 \times 10^{-5}(1 + 0.00317T - 0.0000021T^2)[\times 418.68] \tag{6.8}$$

$$k_{\mathrm{w}} = a + bT + cT^{1.5} + dT^2 + eT^{0.5} \tag{6.9}$$

where T's are in [°C]; k's are calculated in $[\mathrm{W{\cdot}m^{-1}{\cdot}K^{-1}}]$; $a = 0.5650285$, $b = 0.0026363895$, $c = -0.00012516934$, $d = -1.5154918 \times 10^{-6}$, and $e = -0.0009412945$.

6.3.2. In-plane Conduction at Macroscale

Fricke [162] derived a closed-form analytical expression for effective electronic conductivity of a suspension of randomly oriented ellipsoidal particles. This reference used the developed model to predict the conductivity of a blood suspension containing red ellipsoidal corpuscles, which, when compared to experimental data, showed excellent agreement in a wide range of concentrations from 10-90%. This model could easily be turned into a model for a cracked CL by estimating cracks as large aspect ratio ellipsoidal particles dispersed in the catalyst bulk. Following the Fricke's model [162], the in-plane conductivity could be expressed as the following after some mathematical manipulations:

$$\begin{aligned}\Lambda_{\mathrm{cl,ip}} = {} & \frac{(1 - CD)\left(\frac{\Lambda_{\mathrm{cr}}}{\Lambda_{\mathrm{b,cl,ip}}} - 1\right)}{(1 - CD)\left(\frac{\Lambda_{\mathrm{cr}}}{\Lambda_{\mathrm{b,cl,ip}}} - 1\right) + \zeta(CD)} \Lambda_{\mathrm{b,cl,ip}} \\ & + \frac{\zeta(CD)}{(1 - CD)\left(\frac{\Lambda_{\mathrm{cr}}}{\Lambda_{\mathrm{b,cl,ip}}} - 1\right) + \zeta(CD)} \Lambda_{\mathrm{cr}}\end{aligned} \tag{6.10}$$

where $\Lambda_{\mathrm{b,cl,ip}}$ is in-plane conductivity of the CL bulk, and ζ is a dimensionless parameter defined as:

$$\zeta=\frac{1}{3}\left[\frac{2}{1+\frac{1}{2}\left(\frac{\Lambda_{\mathrm{cr}}}{\Lambda_{\mathrm{b,cl,ip}}}-1\right)p}+\frac{1}{1+\left(\frac{\Lambda_{\mathrm{cr}}}{\Lambda_{\mathrm{b,cl,ip}}}-1\right)(1-p)}\right]\left(\frac{\Lambda_{\mathrm{cr}}}{\Lambda_{\mathrm{b,cl,ip}}}-1\right) \tag{6.11}$$

where p is another dimensionless parameter which has the following relation with crack aspect ratio:

$$p=\frac{\left(\varphi-\frac{1}{2}\sin(2\varphi)\right)}{\sin^3(\varphi)}\cos(\varphi) \tag{6.12}$$

where $\cos(\varphi)=1/AR$, and AR is the crack aspect ratio. In applying the Fricke's model to write Eq. (6.10) for CLs, it was assumed that volume fraction of cracks was the same as their areal crack density, denoted by CD, because as discussed in section 3.2.8, cracks were found to penetrate through the whole CL thickness. Further, as shown in section 3.4, cracks were found to have generally high aspect ratios; in such cases, as also shown by Hasselman [163], the relation for p could be simplified as $p\cong\pi/(2AR)$. For in-plane electronic conductivity, Eq. (6.10) is simplified by putting $\Lambda_{\mathrm{cr}}=0$, which is also approximately true for in-plane thermal conductivity of dry CLs due to the much smaller conductivity of the gas phase (~ 0.03 W·m^{-1}·K^{-1}) compared to the bulk catalyst. In such cases, Eq. (6.10) could be simplified to the following form:

$$\Lambda_{\mathrm{cl,ip}}=\frac{\Lambda_{\mathrm{b,cl,ip}}}{1+\frac{CD}{3(1-CD)}\left(\frac{8}{4AR-\pi}+\frac{2}{\pi}\right)AR} \tag{6.13}$$

where the approximation of $p\cong\pi/(2AR)$ was used. For in-plane thermal conductivity of CLs whose thermal conductivities are in the same order of magnitude of the gas conductivity (e.g., designs #5 and #7 in Table 2-1) or for hydrated CLs where the water in the cracks may be much more conductive than the CLs themselves, Eq. (6.10) should be used instead of the simplified form in Eq. (6.13). However, as discussed in section 4.2.4, in-plane heat conduction should play no role in heat transfer inside CLs due to the very high in-plane resistance resulted from the very small thickness of the CLs. Thus, the discussion of this section regarding the in-plane thermal conductivity was just provided for the sake of completeness and continuity of the discussion.

6.4. Modeling the Conductivities at Microscale

The only unknown in Eqs. (6.7) and (6.10) is $\Lambda_{\mathrm{b,cl,tp/ip}}$, i.e., the through-plane/in-plane conductivity of the catalyst bulk at microscale. Maxwell [164] derived a closed-form analytical model for effective conductivity of a composite material consisting of sparsely distributed spherical particles in another medium. Following the Maxwell's model [164] and assuming that the entire microscale unit cells can be treated like a composite medium consisting of sparsely distributed micropores (the inclusions) in clusters of agglomerates (the host medium), the effective through-plane/in-plane thermal/electronic conductivity of a CL at microscale can be found from:

$$\Lambda_{\mathrm{b,cl,tp/ip}} = \frac{3\Lambda_{\mathrm{ac,tp/ip}}\Lambda_{\mathrm{mip}}\chi + \left(2\Lambda_{\mathrm{ac,tp/ip}} + \Lambda_{\mathrm{mip}}\right)\Lambda_{\mathrm{ac,tp/ip}}(1-\chi)}{3\Lambda_{\mathrm{ac,tp/ip}}\chi + \left(2\Lambda_{\mathrm{ac,tp/ip}} + \Lambda_{\mathrm{mip}}\right)(1-\chi)} \tag{6.14}$$

where $\Lambda_{\mathrm{ac,tp/ip}}$ is through-plane/in-plane effective conductivity of the agglomerate clusters, Λ_{mip} is effective conductivity of the micropores, and χ is volume fraction of micropores.

6.4.1. Effective Conductivity of Micropores

For electron conduction, $\Lambda_{\mathrm{mip}} = \sigma_{\mathrm{mip}} = 0$, and Eq. (6.14) is simplified to:

$$\sigma_{\mathrm{b,cl,tp/ip}} = \frac{2(1-\chi)}{\chi+2}\sigma_{\mathrm{ac,tp/ip}} \tag{6.15}$$

For thermal conduction, $\Lambda_{\mathrm{mip}} = k_{\mathrm{mip}}$ is found by correcting the fluid conductivity (k_{f}) for size effects in micropores as [165, 166]:

$$k_{\mathrm{mip}} = \frac{k_{\mathrm{f}}}{1 + \alpha\beta MFP_{\mathrm{f}}/\bar{d}_{\mathrm{mip}}} \tag{6.16}$$

where k_f is determined from Eq. (6.8) or (6.9) depending on the type of fluid in the micropore, α is an accommodation parameter, β is a fluid parameter, MFP_f is molecular mean free path of the fluid, and $\bar{d}_\mathrm{mip}$ is the mean diameter of micropores whose relation is derived later in this chapter. The expression $MFP_\mathrm{f}/\bar{d}_\mathrm{mip}$ in the denominator of Eq. (6.16) is, in fact, the Knudsen number for micropores, which takes the size effects into account. Refs. [128, 167] nicely bundled/defined the terms $\alpha\beta MFP_\mathrm{f}$ as a single fluid parameter M when they derived their models for gas-filled gaps. Following their approach to make the model more compact and its interpretation easier, Eq. (6.16) is written as:

$$k_\mathrm{mip} = \frac{k_\mathrm{f}}{1 + M/\bar{d}_\mathrm{mip}} \tag{6.17}$$

where the fluid parameter, M, is defined as [128, 167]:

$$M = \left[\frac{2-\alpha_{T_1}}{\alpha_{T_1}} + \frac{2-\alpha_{T_2}}{\alpha_{T_2}}\right]\left[\frac{2\gamma}{1+\gamma}\right]\left(\frac{1}{\mathrm{Pr}}\right) MFP_\mathrm{f} \tag{6.18}$$

where α_{T_1} and α_{T_2} are thermal accommodation coefficients for surfaces of agglomerates at temperatures of T_1 and T_2, with T_1 being temperature of the bottom surface of a micropore and T_2 being temperature of the upper surface if heat transfers from bottom to top or vice versa, γ is ratio of specific heats of the fluid ($\gamma = 1.4$ for air and 1 for liquid water), and Pr is the Prandtl number of the fluid. For air-filled pores, $\mathrm{Pr_a} \cong 0.7$ in the temperature range of 0-100 °C [168]. However, for water-filled pores, $\mathrm{Pr_w}$ changes quite a bit in that temperature range [168]. Accordingly, in the case of water-filled pores, $\mathrm{Pr_w}$ was found from [161]:

$$\mathrm{Pr_w} = \frac{1}{a + bT + cT^2 + dT^3} \tag{6.19}$$

where $a = 0.074763403,\ b = 0.0029020983,\ c = 2.8606181 \times 10^{-5},\ d = -8.1395537 \times 10^{-8}$, and T is in [°C].

α_T's in Eq. (6.18) are calculated from [128]:

$$\alpha_T = \left(\frac{MW_\mathrm{f}^*}{6.8 + MW_\mathrm{f}^*}\right)\exp\left[-0.57\left(\frac{T-273}{273}\right)\right] + \frac{2.4\mu}{(1+\mu)^2}\left\{1 - \exp\left[-0.57\left(\frac{T-273}{273}\right)\right]\right\} \tag{6.20}$$

where $MW_\mathrm{f}^* = MW_\mathrm{f}$ for monatomic gases and $MW_\mathrm{f}^* = 1.4MW_\mathrm{f}$ for diatomic/polyatomic gases (like air or with some approximation water), MW_f is molecular weight of the fluid (air or water) in [kg/kmol], T is surface temperature in [K], $\mu = MW_\mathrm{f}/MW_\mathrm{surf}$, and MW_surf is molecular weight of the surface material in [kg/kmol]. Since micropores are surrounded by agglomerates, MW_surf would be molecular weight of the agglomerate surface for micropores. Since only parts of the agglomerates are covered by ionomer, a plausible way to calculate M for micropores would be to perform the calculation once based on the ionomer surface properties and then based on the carbon black surface properties and then take the average. However, calculations showed that M was not much sensitive to the choice of surface; typical values were $0.3225\ \mu\mathrm{m}$ for calculations based on the carbon black surface and $0.3061\ \mu\mathrm{m}$ for calculations based on the ionomer surface, which were only ~5% different. Thus, for convenience, M was calculated only based on the carbon black surface. Further, temperature difference across CLs is small. Experiments showed that temperature difference across a CL of design #1 was less than ~5 °C for different amounts of heat passing through the CL, while the CL bulk temperature was maintained within the range of ~0-100 °C. On the other hand, α_T does not change much within such a narrow range. Accordingly, α_T's in Eq. (6.18) were calculated at the CL bulk temperature.

For gas-filled pores, relation for MFP_g in Eq. (6.18) is given as [128]:

$$MFP_\mathrm{g} = \left(\frac{P_0}{P_\mathrm{g}}\right)\left(\frac{T_\mathrm{g}}{T_0}\right)MFP_0 \tag{6.21}$$

where MFP_0 is molecular mean free path at some reference temperature and pressure of T_0 and P_0. Reference conditions were arbitrarily taken as $P_0 = 101.3\ \mathrm{kPa}$ and $T_0 = 298\ \mathrm{K}$, at which $MFP_{0,\mathrm{a}} = 0.07\ \mu\mathrm{m}$ [169]. In case of having liquid water in the pores, mean free path of water molecules should be known in liquid phase to be able to find M from Eq.

(6.18). Water molecules are packed more closely than gas molecules and do not have much room for movement. They are also under the influence of intermolecular hydrogen bonding which further limits their movement. For these reasons, accurate estimation or measurement of their mean free path in liquid form is very difficult and, to the author's best knowledge, not reported yet in the literature. Accordingly, a simple estimation of the mean free path of water molecules in liquid phase is given here, which will serve the purposes of this thesis. Mean free path of a particle, MFP, is related to the particle number density, n, and collision cross section between two molecules, A_{col}, through $MFP = 1/(nA_{\mathrm{col}})$ [170], where n is the number of molecules per unit volume. Since the molecular weight of water is $18\ \mathrm{g{\cdot}mol^{-1}}$ and the density of water is $1\ \mathrm{g{\cdot}cm^{-3}}$, it follows that volumetric molar density of water is $(1/18)\ \mathrm{mol{\cdot}cm^{-3}}$, or in other words, $n = (N_{\mathrm{A}}/18)\ \mathrm{cm^{-3}} \approx 3.35 \times 10^{22}\ \mathrm{cm^{-3}}$, where $N_{\mathrm{A}} = 6.022 \times 10^{23}$ is the Avogadro's number. On the other hand, if we approximate geometric cross section of each water molecule as $\sim\pi Len_{\mathrm{H\text{-}O}}^2$, where $Len_{\mathrm{H\text{-}O}} \approx 1\ \mathrm{Å}$ is the OH bond length in a water molecule [171], then the collision cross section between each two molecules may be approximated as about four times as large or $A_{\mathrm{col}} \approx 4\pi Len_{\mathrm{H\text{-}O}}^2 \approx 1.26 \times 10^{-15}\ \mathrm{cm^2}$. The mean free path of a water molecule is thus calculated as $MFP_{\mathrm{H_2O}} \approx 2.4\ \mathrm{Å}$, which is ~300 times less than the mean free path of air molecules. This value agrees well with the 2.7-3.00 $\mathrm{Å}$ intermolecular distance between the water molecules in liquid form [172], which was expected considering the close packing order of water molecules in liquid form. Since density of water does not change much with temperature (less than 5% in 0-100 °C temperature range [168]), the value of $MFP_{\mathrm{H_2O}} \approx 2.4\ \mathrm{Å}$ should be an accurate enough approximation for the operating temperature range of PEMFCs.

6.4.2. Mean Diameter and Volume Fraction of Micropores

The volume fraction of micropores was estimated from TEM images of CLs. TEM imaging for measuring χ was performed for designs #1-4 and #7 in Table 2-1. These designs were expected to yield the entire range of χ values, as they covered the whole I/C ratios and dry milling times of the CLs studied in this thesis. Based on the total porosity results shown in Figure 3-16, χ was expected to decrease considerably with dry milling time and I/C ratio but remain invariant with drying temperature of the ink. TEM sample preparation, imaging, and image processing were performed as described in sections 3.2.7 and 3.3.3. When analyzing the images, χ was taken to be the volume fraction of pores whose areas were larger than average area of pores between the agglomerates. Average size of agglomerates was estimated to be ~100 nm from high-resolution electron microscopy; the data was gathered by Dr. Jasna Jankovic at AFCC. Figure 6-2 shows sample raw TEM images of the CLs, indicating different volume fractions of micropores (large pores in the images) for different designs. Measured values of average micropore diameter, denoted by $\bar{d}_{\mathrm{mip}}$, and χ are shown in Table 6-1 for the different designs. Values of $\bar{d}_{\mathrm{mip}}$ show reduction with dry milling time and weak correlation with I/C ratio, whereas values of χ show reduction with both I/C ratio and dry milling time.

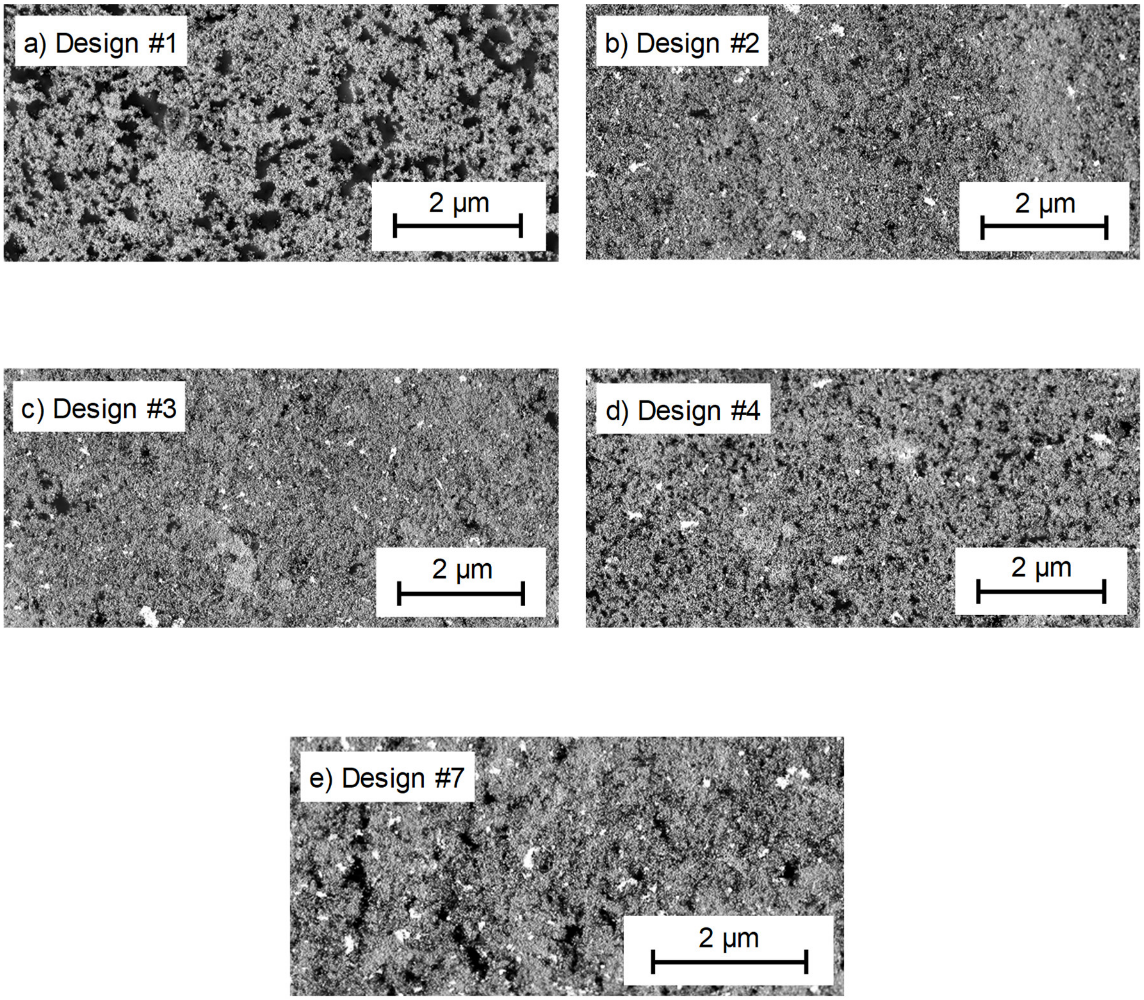

Figure 6-2. Sample raw TEM images of different CL designs with different I/C ratios and dry milling times, showing different volume fractions of micropores (large pores in the images) for different designs

Table 6-1. Mean diameter and volume fraction of micropores for designs #1-4,7

Design #	I/C ratio	Dry milling time (hr)	$\bar{d}_{\text{mip}}$ (nm)	χ
1	1.1	0 (None)	141	0.47
2	0.7	48	82	0.1
3	0.9	48	88	0.08
4	0.7	24	95	0.2
7	1.1	48	94	0.07

To be able to derive $\bar{d}_{\text{mip}}$ and χ for all the designs, correlations were found between these structural parameters and the fabrication parameters. As shown in Table 6-1, increasing the dry milling time led to considerable reduction in $\bar{d}_{\text{mip}}$, and increasing the I/C ratio or the dry milling time led to considerable reduction in χ. Such steep decreasing trends may well be approximated by exponential and power law functions. It turned out that a power law function for $\bar{d}_{\text{mip}}$ in form of $a(1+t_{\text{dm}})^b$ and an exponential function for χ in form of $a\exp(\text{b}l_{\text{I/C}}+ct_{\text{dm}})$ would well predict the data of Table 6-1, where t_{dm} denotes the dry milling time in [hr], and $l_{\text{I/C}}$ denotes the I/C ratio. The functionality of $\bar{d}_{\text{mip}}$ with t_{dm} was considered as $(1+t_{\text{dm}})^b$ instead of t_{dm}^b to account for cases with 0 hr dry milling time. The unknown coefficients of these functions were found from least-square analysis of the data of Table 6-1 with R^2=0.9476 for $\bar{d}_{\text{mip}}$ and R^2=0.9892 for χ. The final correlations are given below ($\bar{d}_{\text{mip}}$ is in [nm]):

$$\bar{d}_{\text{mip}} = 141(1+t_{\text{dm}})^{-0.1216} \tag{6.22}$$

$$\chi = 0.7809\exp\left(-0.5080 l_{\text{I/C}} - 0.0377 t_{\text{dm}}\right) \tag{6.23}$$

6.4.3. Structural Relationship between the Volume Fraction of Micropores and CL Porosity

By defining porosity of agglomerate clusters around the micropores (ε_{ac}) as volume fraction of pores in the clusters and porosity of a CL (ε_{cl}) as volume fraction of all the pores in the CL including the micropores, the following relation holds between ε_{ac}, ε_{cl}, and χ:

$$\chi = 1 - \frac{1-\varepsilon_{\mathrm{cl}}}{1-\varepsilon_{\mathrm{ac}}} \tag{6.24}$$

where $\varepsilon_{\mathrm{ac}}$ is found from the following relation (see Appendix I for the derivation of $\varepsilon_{\mathrm{ac}}$):

$$\varepsilon_{\mathrm{ac}} = 1 - \sqrt{2}\pi^2(1-\varepsilon_{\mathrm{C}})\left[1 + l_{\mathrm{Pt/C}}\frac{\rho_{\mathrm{C}}}{\rho_{\mathrm{Pt}}} + \frac{\rho_{\mathrm{C}} l_{\mathrm{ion}}\left(1 + l_{\mathrm{Pt/C}}\right)}{\rho_{\mathrm{ion,dry}}\left(1 - l_{\mathrm{ion}}\right)}\right] \times \frac{\left\{\frac{4}{3} - \left[1-\cos\left(\frac{\theta_{\mathrm{agg}}}{2}\right)\right]\left(3\sin^2\left(\frac{\theta_{\mathrm{agg}}}{2}\right) + \left[1-\cos\left(\frac{\theta_{\mathrm{agg}}}{2}\right)\right]^2\right)\right\}}{48\cos^3\left(\frac{\theta_{\mathrm{agg}}}{2}\right)} \tag{6.25}$$

where ε_{C} is porosity of a carbon particle, $l_{\mathrm{Pt/C}}$ is Pt loading, defined as mass of Pt over mass of carbon, l_{ion} is ionomer loading, defined as mass of ionomer over total mass of the CL, ρ_{C}, ρ_{Pt}, and $\rho_{\mathrm{ion,dry}}$ are volumetric mass densities of carbon, Pt, and dry ionomer, respectively, and θ_{agg} is overlap angle between two neighboring Pt/C aggregates. l_{ion} can be expressed in terms of I/C ratio ($l_{\mathrm{I/C}}$) and $l_{\mathrm{Pt/C}}$ as:

$$l_{\mathrm{ion}} = \frac{l_{\mathrm{I/C}}}{l_{\mathrm{I/C}} + l_{\mathrm{Pt/C}} + 1} \tag{6.26}$$

The overlap angle, θ_{agg}, is illustrated in Figure 6-3 along with other geometrical parameters of the aggregates and agglomerates. Definitions of the geometrical parameters, shown in Figure 6-3, are given in Table 6-2. Ionomer coverage on the surface of aggregates, denoted by ψ, is defined as the fraction of surface of the aggregates covered by ionomer and is expressed as:

$$\psi = \frac{A_{\mathrm{ion}}}{2\pi r_{\mathrm{agg}}^2} \tag{6.27}$$

where A_{ion} is the surface area of ionomer on half of an aggregate, and $2\pi r_{\mathrm{agg}}^2$ is the surface area of half of the aggregate.

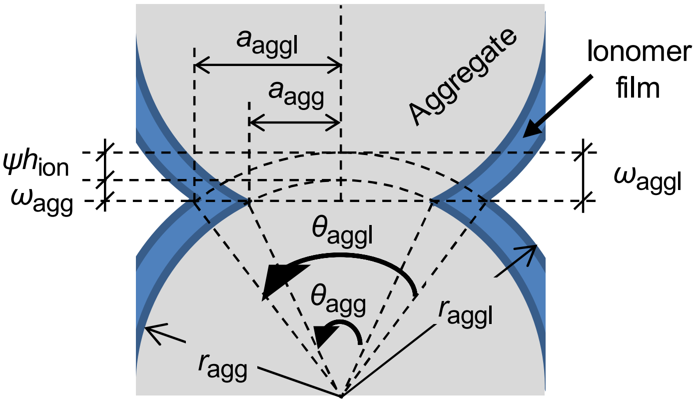

Figure 6-3. **Geometrical parameters of agglomerates and Pt/C aggregates, shown in a mesoscale unit cell (Ionomer strands at the overlap regions between the aggregates are not shown for clarity of the schematic.)**

Table 6-2. **Definitions of geometrical parameters of aggregates and agglomerates**

Parameter	Definition	Parameter	Definition
$r_{\rm agg}$	Radius of aggregates	$r_{\rm aggl}$	Radius of agglomerates
$a_{\rm agg}$	Overlap radius of neighboring aggregates	$a_{\rm aggl}$	Overlap radius of neighboring agglomerates
$\omega_{\rm agg}$	Overlap depth of neighboring aggregates	$\omega_{\rm aggl}$	Overlap depth of neighboring agglomerates
$\theta_{\rm agg}$	Overlap angle of neighboring aggregates	$\theta_{\rm aggl}$	Overlap angle of neighboring agglomerates
$h_{\rm ion}$	Thickness of ionomer covering the aggregates	ψ	Ionomer coverage on the surface of aggregates

Eqs. (6.24) and (6.25) show that, for a certain composition of a CL (fixed $\varepsilon_{\rm C}$, $l_{\rm Pt/C}$, and $l_{\rm ion}$), $\varepsilon_{\rm cl}$ is a function of χ and $\theta_{\rm agg}$. Therefore, by having $\varepsilon_{\rm cl}$ and χ, $\theta_{\rm agg}$ could be determined from Eqs. (6.24) and (6.25).

6.5. Modeling the Conductivities at Mesoscale

The unknown effective conductivity of the agglomerate clusters in Eq. (6.14), i.e., $\Lambda_{\rm ac,tp/ip}$, is obtained from resistance of the mesoscale unit cell as follows:

$$\Lambda_{\mathrm{ac,tp/ip}} = \frac{h_{\mathrm{meu}}}{R_{\mathrm{meu,tp/ip}} A_{\mathrm{meu}}} \tag{6.28}$$

where h_{meu} is thickness of the mesoscale unit cell across which the heat/electron transfer occurs, $R_{\mathrm{meu,tp/ip}}$ is the through-plane/in-plane thermal/electronic resistance of the mesoscale unit cell, and A_{meu} is cross-sectional area of the mesoscale unit cell through which heat/electrons transfer. The parameters h_{meu} and A_{meu} are simply obtained from the geometry of the mesoscale unit cell (see Figure 6-3):

$$h_{\mathrm{meu}} = 2\left(r_{\mathrm{agg}} - \omega_{\mathrm{agg}}\right) \tag{6.29}$$

$$A_{\mathrm{meu}} = h_{\mathrm{meu}}^2 \tag{6.30}$$

Preliminary modeling results showed that conductance of the Pt/C aggregate in the mesoscale unit cell was much higher than: i) conductance of the ionomer around the aggregate, and ii) conductance of the gas/water in the mesopore. For thermal conduction, typical effective thermal conductivity values (including size effects) were ~16 $\mathrm{W \cdot m^{-1} \cdot K^{-1}}$ for the aggregate, ~0.006 $\mathrm{W \cdot m^{-1} \cdot K^{-1}}$ for an air-filled mesopore, ~0.6 $\mathrm{W \cdot m^{-1} \cdot K^{-1}}$ for a water-filled mesopore, and ~0.21 $\mathrm{W \cdot m^{-1} \cdot K^{-1}}$ for ionomer. Clearly, for electron conduction, aggregate is the only conductive part. Thus, for both heat and electron conduction, surface of the aggregate could be treated as an equipotential surface with respect to the ionomer and the mesopore, which dictates two parallel paths for conduction inside the mesoscale unit cell: i) through the Pt/C aggregate, and ii) through the series configuration of ionomer and mesopore. Thus, $R_{\mathrm{meu,tp/ip}}$ in Eq. (6.28) could be expressed as:

$$R_{\mathrm{meu,tp/ip}} = \left[\frac{1}{R_{\mathrm{agg,tp/ip}}} + \frac{1}{R_{\mathrm{mep}} + 2R_{\mathrm{ion}}}\right]^{-1} \tag{6.31}$$

where $R_{\mathrm{agg,tp/ip}}$, R_{mep}, and $2R_{\mathrm{ion}}$ are resistances of the aggregate (in the through-plane/in-plane direction), mesopore, and ionomer, respectively, and R_{ion} represents the ionomer resistance on half of the aggregate.

6.5.1. Modeling the Aggregate Resistance

Chan and Tien [173] solved the Laplace equation analytically through a solid sphere subjected to uniform wall heat flux at two poles of the sphere, covering the poles up to an arbitrary central angle, and zero heat flux on the rest of the sphere to obtain its resistance to heat transfer in a packed bed of spheres in vacuum. The geometry and boundary conditions they modeled very much resemble the problem of conduction through an aggregate in this thesis, except that their geometry was a complete sphere as opposed to the aggregate geometry which lacks six spherical caps due to overlap between the aggregates. However, two main reasons justified usage of their solution to obtain the aggregate resistance in this thesis:

i) As modeling results showed, all the CLs had overlap angles around ~ 40°, which resulted in less than ~6% loss of volume (due to the cut spherical caps) compared to a whole sphere. Thus, aggregates had more than ~94% of the volume of a whole sphere, which justified their approximation by whole spheres.

ii) As classical problems of conduction through solids show, heat/electron flow lines would mostly pass through the middle part of a sphere rather than bending toward the surface of the sphere, in order to take paths of least resistance. Thus, even in a complete sphere, regions close to the surface, including the side caps, would not contribute much in conduction through the sphere.

Accordingly, the aggregate resistance was found using the model developed by Ref. [173] for solid spheres, which is expressed as follows in terms of the aggregate parameters:

$$\tilde{R}_{\mathrm{agg,tp/ip}} = \frac{2r_{\mathrm{agg}}}{\Lambda_{\mathrm{agg}}\pi a_{\mathrm{agg}}^2\left(1-\cos\left(\frac{\theta_{\mathrm{agg}}}{2}\right)\right)}\sum_{i=1}^{\infty}\frac{1}{(2i-1)(4i-1)}\left\{P_{2i-2}\left[\cos\left(\frac{\theta_{\mathrm{agg}}}{2}\right)\right] - P_{2i}\left[\cos\left(\frac{\theta_{\mathrm{agg}}}{2}\right)\right]\right\}^2 \tag{6.32}$$

where Λ_{agg} is the aggregate conductivity, and P_i is a Legendre polynomial of degree i. The resistance $\tilde{R}_{\mathrm{agg,tp/ip}}$ still needs to be corrected for: i) effects of ionomer at the contact region between two neighboring aggregates, and ii) sphericity of the contacting particles at the contact region, which is determined by the initial polyhedron shape of the carbon particles as well as the dry milling effects. Since these effects mainly affect the contact area between the aggregates, we can correct Eq. (6.32) by multiplying the area (πa_{agg}^2 in the denominator) by a function $\xi = \xi\left(l_{\mathrm{I/C}}, t_{\mathrm{dm}}\right)$ to account for these effects; we call this function “contact effectiveness factor”. Thus, the aggregate resistance is expressed as:

$$R_{\mathrm{agg,tp/ip}} = \frac{2r_{\mathrm{agg}}}{\Lambda_{\mathrm{agg}}\pi a_{\mathrm{agg}}^2\xi\left(1-\cos\left(\frac{\theta_{\mathrm{agg}}}{2}\right)\right)}\sum_{i=1}^{\infty}\frac{1}{(2i-1)(4i-1)}\left\{P_{2i-2}\left[\cos\left(\frac{\theta_{\mathrm{agg}}}{2}\right)\right] - P_{2i}\left[\cos\left(\frac{\theta_{\mathrm{agg}}}{2}\right)\right]\right\}^2 \tag{6.33}$$

As discussed later in this chapter, we will derive the function $\xi\left(l_{\mathrm{I/C}}, t_{\mathrm{dm}}\right)$ from a few experiments. In this thesis, a tolerance of 0.1% change was considered to calculate the infinite series in Eq. (6.33). Computing the series for all the CL designs showed that it converged very fast such that it would change less than 0.1% after the ~10th term.

6.5.2. Modeling the Mesopore Resistance

For electron conduction, since only the Pt/C aggregate is the conductive part, R_{mep} becomes ∞, and the term containing R_{mep} in Eq. (6.31) vanishes. However, for heat conduction, this term should be modeled. Bahrami et al. [167] modeled thermal resistance of a gas filling the space between nonconforming surfaces by integrating infinitesimally small gap resistances between the surfaces. Ref. [167] developed their model for a half-sphere contacting a perfectly flat surface, following an effective surface approach for the purpose of contact mechanics modeling. In this thesis, a similar model was developed for mesopore resistance between overlapping agglomerates, following the same approach of Ref. [167]. The developed model for the mesopore resistance is expressed as:

$$R_{\mathrm{mep}} = \frac{1}{\pi k_{\mathrm{f}}\left\{S\ln\left[\frac{S-B}{S-K}\right] + B - K\right\}} \tag{6.34}$$

where k_f is the bulk thermal conductivity of the fluid in the mesopore (gas or liquid water), $K=\sqrt{r_\mathrm{aggl}^2-a_\mathrm{aggl}^2}=r_\mathrm{aggl}-\omega_\mathrm{aggl}$, $B=\sqrt{r_\mathrm{aggl}^2-\left(r_\mathrm{aggl}-\omega_\mathrm{aggl}\right)^2}=a_\mathrm{aggl}$, and $S=r_\mathrm{aggl}-\omega_\mathrm{aggl}+0.5M$. In this model, size effects are accounted for by the fluid parameter M, which was defined in Eq. (6.18). Thus, k_f should be calculated from Eq. (6.8) or (6.9).

6.5.3. Modeling the Ionomer Resistance

For electron conduction, similar to the mesopore resistance, ionomer resistance goes to ∞; thus, the term containing R_ion in Eq. (6.31) vanishes again, which we concluded in the previous section as well. For thermal conduction, since the ionomer thickness is relatively low in comparison with radius of the aggregate that it covers, the ionomer film around the aggregate can be modeled as a thin spherical shell. Therefore, thermal resistance of ionomer in Eq. (6.31) (half of the total ionomer resistance) can simply be obtained from the slab formula, as:

$$R_\mathrm{ion}=\frac{h_\mathrm{ion}}{k_\mathrm{eff,ion}A_\mathrm{ion}} \tag{6.35}$$

where h_ion is the thickness of the ionomer film, A_ion is the surface area of the ionomer on half of the aggregate, and $k_\mathrm{eff,ion}$ is ionomer thermal conductivity corrected for size effects. Since ionomer is resistant to flow of electrons, there is no free valence electrons in ionomer to contribute to heat conduction, and thus, thermal energy is conducted only by phonons (lattice waves) inside the ionomer [174]. Thus, thermal conductivity of ionomer could be corrected by mean free path of phonons as [174]:

$$k_\mathrm{eff,ion}=\frac{k_\mathrm{ion}}{1+\mathrm{Kn}_\mathrm{ion}} \tag{6.36}$$

where $\mathrm{Kn}_\mathrm{ion}=MFP_\mathrm{ph,ion}/h_\mathrm{ion}$ is the Knudsen number for the ionomer film, where $MFP_\mathrm{ph,ion}$ is the phonon mean free path of the bulk ionomer. Experimental data for k_ion is not available at different water contents of the ionomer. However, by performing a volumetric averaging, k_ion for a humidified membrane could be expressed as [5, 158]:

$$k_{\mathrm{ion}} = \frac{(EW_{\mathrm{ion}}\rho_{\mathrm{w}})k_{\mathrm{dry,ion}} + \left(MW_{\mathrm{w}}\lambda\rho_{\mathrm{dry,ion}}\right)k_{\mathrm{w}}}{(EW_{\mathrm{ion}}\rho_{\mathrm{w}}) + \left(MW_{\mathrm{w}}\lambda\rho_{\mathrm{dry,ion}}\right)} \tag{6.37}$$

where EW_{ion} is equivalent weight of the ionomer defined as mass of the dry ionomer per mole of sulfonic acid groups ($\mathrm{SO_3}^-$), $\rho_{\mathrm{w}} = 1{,}000\ \mathrm{kg{\cdot}m^{-3}}$ is volumetric density of water, $k_{\mathrm{dry,ion}}$ is thermal conductivity of the dry ionomer, $MW_{\mathrm{w}} = 18\ \mathrm{kg{\cdot}kmol^{-1}}$ is molecular weight of water, λ is water content of the ionomer defined as mole of water per mole of $\mathrm{SO_3}^-$, $\rho_{\mathrm{dry,ion}}$ is volumetric density of the dry ionomer, and k_{w} is thermal conductivity of water obtained from Eq. (6.9). For the Aquivion ionomer, $EW_{\mathrm{ion}} \approx 790\ \mathrm{g/mol\ of\ SO_3}^-$ from the manufacturer's specification sheet. However, physical properties of the Aquivion ionomer at different temperatures are not readily available. For this reason, physical properties of Nafion are used for ionomer, and wherever a property is not available for dry Nafion, property of its PTFE backbone is used. PTFE has roughly the same lattice structure of dry Nafion [175], and using its properties instead of dry Nafion is a common practice in the literature (for example see Refs. [158, 159]).

By definition, the value of λ is taken to be 0 for dry conditions. For a fully-hydrated bulk Nafion, λ could change from ~14 for a vapor-saturated ionomer to ~22 for a liquid-saturated ionomer [176, 177]. However, in case of having a very thin film of ionomer, which is the case for the ionomer film around the agglomerates, the value of λ is much lower than the bulk value. In such small thicknesses of ionomer, the ability of ionomer to retain water becomes much less than the bulk ionomer due to the very different microstructure of thin films of ionomer compared to bulk ionomer [23, 178-185]. Data of Refs. [23, 185] suggest that for fully-hydrated ionomer in CLs, $\lambda \approx 4$. PTFE data of Ref. [186] showed that density of PTFE changes less than ~4% from 0-100 °C; accordingly, a constant value of $\rho_{\mathrm{dry,ion}} = 1{,}980\ \mathrm{kg{\cdot}m^{-3}}$ was considered from the Nafion data of Ref. [176]. $k_{\mathrm{dry,ion}}$ was obtained by fitting the following curve through the Nafion data of Ref. [39] from 35-80 °C with $R^2=0.9349$ (average discrepancy of ~3%):

$$k_{\mathrm{dry,ion}} = 3.6131 \times 10^{-5}\, T^2 - 5.4290 \times 10^{-3}\, T + 0.3396 \tag{6.38}$$

where T is in [°C], and $k_{\mathrm{dry,ion}}$ is in $[\mathrm{W{\cdot}m^{-1}{\cdot}K^{-1}}]$. The above relation yields a value of ~0.21 W·m^{-1}·K^{-1} for Nafion at 29°C which agrees well with the value of 0.214 ± 0.003 W·m^{-1}·K^{-1} measured at 29°C by the GHF testbed in this thesis (see Figure 4-12).

To the author's best knowledge, no experimental work is available in literature for the mean free path of phonons in Nafion or other ionomeric polymers, yet this property is an input for Eq. (6.36). Kinetic theory predicts bulk thermal conductivity of a material as $k = (1/3)\rho c v MFP$, where ρ, c, v, and MFP are volumetric mass density, specific heat, speed, and mean free path of thermal energy carriers, respectively [174]. This relation could be rearranged as follows to obtain the mean free path of phonons in the ionomer from other physical properties of the ionomer:

$$MFP_{\mathrm{ph,ion}} = \frac{3k_{\mathrm{ion}}}{\rho_{\mathrm{ion}} c_{\mathrm{ion}} v_{\mathrm{ph,ion}}} \tag{6.39}$$

where ρ_{ion} is $1{,}980\ \mathrm{kg{\cdot}m^{-3}}$ for dry conditions and is calculated to be $1{,}675\ \mathrm{kg{\cdot}m^{-3}}$ by entering $\lambda = 4$ into the relation provided in Ref. [176], $v_{\mathrm{ph,ion}}$ is given by Ref. [187] as $1{,}735\ \mathrm{m{\cdot}s^{-1}}$ for dry Nafion and $\sim 1{,}345\ \mathrm{m{\cdot}s^{-1}}$ for a fully hydrated Nafion, and c_{ion} is the specific heat capacity of ionomer, which could change with temperature and is obtained by a mass averaging as [158]:

$$c_{\mathrm{ion}} = \frac{c_{\mathrm{w}}}{1 + \frac{1}{\eta_{\mathrm{w}} MW_{\mathrm{w}}}} + \frac{c_{\mathrm{dry,ion}}}{1 + \eta_{\mathrm{w}} MW_{\mathrm{w}}} \tag{6.40}$$

where $\eta_{\mathrm{w}} = \lambda / EW_{\mathrm{ion}}$ is molality of water in kmol of water per kmol of dry Nafion, which is 0 for dry conditions and is ~0.005 for full hydration, $c_{\mathrm{w}} = 4{,}217\ \mathrm{J{\cdot}kg^{-1}{\cdot}K^{-1}}$ (less than 1% change within 0-100 °C) [168], and $c_{\mathrm{dry,ion}}$ is obtained by fitting a line through the PTFE data of Ref. [186] from 0-100 °C with R^2=0.9788 (less than 1% discrepancy) as:

$$c_{\mathrm{dry,ion}} = 1.5858\, T + 995 \tag{6.41}$$

where T is in [°C] and $c_{\mathrm{dry,ion}}$ is in $[\mathrm{J{\cdot}kg^{-1}{\cdot}K^{-1}}]$.

A_{ion} in Eq. (6.35) should be found from Eq. (6.27). As shown in Appendix J, relation for the ionomer thickness, h_{ion} in Eq. (6.35), is derived as:

$$h_{\mathrm{ion}} = \frac{4\pi\rho_{\mathrm{C}} n_{\mathrm{C}} r_{\mathrm{C}}^3 l_{\mathrm{ion}}\left(1 + l_{\mathrm{Pt/C}}\right)(1 - \varepsilon_{\mathrm{C}})}{3\rho_{\mathrm{ion}}(2A_{\mathrm{ion}})(1 - l_{\mathrm{ion}})} \tag{6.42}$$

where n_{C} is the number of carbon particles in an aggregate, which is obtained from (see Appendix J for the derivation):

$$n_{\mathrm{C}} = \frac{\frac{4}{3}\pi r_{\mathrm{agg}}^3 - \frac{\pi}{6}\omega_{\mathrm{agg}}\left(3a_{\mathrm{agg}}^2 + \omega_{\mathrm{agg}}^2\right) \times 6}{\left(2r_{\mathrm{C}}/\sqrt{2}\right)^3} \times \frac{1}{2} \tag{6.43}$$

6.5.4. Modeling the Aggregate Conductivity

Efforts were made to simplify the complex microstructure of the Pt/C aggregate for analytical modeling of its conductivity, Λ_{agg}, by considering the Pt/C particles as an effective medium. Accordingly, various effective properties (e.g., thermal conductivity and Young's modulus) were found for the effective aggregate using bounds and models provided for these properties in Ref. [188]. However, less than ~3% change in the effective properties versus Pt loading was predicted in the practical range of Pt loading, meaning that an effective aggregate could simply be taken as an aggregate only made of the carbon phase for modeling the conductivities. The reason behind such a small contribution from Pt particles is the small volume fraction of Pt particles in: i) the Pt/C aggregates (less than ~7%), and ii) the whole CL (less than ~2%), in the practical range of Pt loading (i.e., $l_{\mathrm{Pt/C}} = 0 - 50\%$). This small volume fraction is originated from the much higher density of Pt particles (21.45 g·cm^{-3}) compared to that of porous carbon particles (1.6 g·cm^{-3}).

As discussed in section 2.5, carbon particles are fused together by covalent bonds in the aggregates [77-80]. Thus, contact mechanics theories such as Hertzian theory [151] would not hold for contact regions between the particles, as such theories would consider the particles as elastic spheres whose contact could change as a function of the applied mechanical load. Further, as discussed in sections 4.2 and 5.3, thermal and electronic conductivity of the CLs did not change with pressure as a result of the fixed contact area between the fused particles. Thus, a better approach for modeling the porous aggregates would be to find an effective aggregate conductivity for the continuous structure of the aggregates, sparsely populated with nanopores between the fused carbon particles. The physics of this problem is again the same as the effective medium problem of Maxwell [164], and therefore, the same formulation of Eq. (6.14) would be applicable. Rewriting the Maxwell's model for the aggregates would yield the aggregate conductivity as:

$$\Lambda_{\mathrm{agg}} = \frac{3\Lambda_{\mathrm{eff,C}}\Lambda_{\mathrm{np}}\varepsilon_{\mathrm{agg}} + \left(2\Lambda_{\mathrm{eff,C}} + \Lambda_{\mathrm{np}}\right)\Lambda_{\mathrm{eff,C}}\left(1 - \varepsilon_{\mathrm{agg}}\right)}{3\Lambda_{\mathrm{eff,C}}\varepsilon_{\mathrm{agg}} + \left(2\Lambda_{\mathrm{eff,C}} + \Lambda_{\mathrm{np}}\right)\left(1 - \varepsilon_{\mathrm{agg}}\right)} \qquad (6.44)$$

where $\Lambda_{\mathrm{eff,C}}$ is effective conductivity of the carbon phase (the host medium), Λ_{np} is effective conductivity of the nanopores (the inclusions), and $\varepsilon_{\mathrm{agg}}$ is aggregate porosity. For electron conduction, $\Lambda_{\mathrm{np}} = \sigma_{\mathrm{np}} = 0$, and Eq. (6.44) is simplified to:

$$\sigma_{\mathrm{agg}} = \frac{2\left(1 - \varepsilon_{\mathrm{agg}}\right)}{\varepsilon_{\mathrm{agg}} + 2}\sigma_{\mathrm{eff,C}} \qquad (6.45)$$

Similar to Eq. (6.17), for heat conduction, $\Lambda_{\mathrm{np}} = k_{\mathrm{np}}$ is found by correcting the fluid conductivity for size effects in nanopores as:

$$k_{\mathrm{np}} = \frac{k_{\mathrm{f}}}{1 + M/\bar{d}_{\mathrm{np}}} \qquad (6.46)$$

where k_{f} is again determined from Eq. (6.8) or (6.9) depending on the type of fluid in the nanopore, M is the fluid parameter determined from Eq. (6.18), and $\bar{d}_{\mathrm{np}}$ is the mean diameter of nanopores determined from the assumed FCC arrangement of carbon particles in the aggregates as (see Figure 6-4):

$$\bar{d}_{\mathrm{np}} \approx 2r_{\mathrm{C}}\left(\sqrt{2} - 1\right) \qquad (6.47)$$

where r_C is the mean radius of carbon particles, which was determined to be ~15 nm from high-resolution electron microscopy data gathered by Dr. Jasna Jankovic at AFCC.

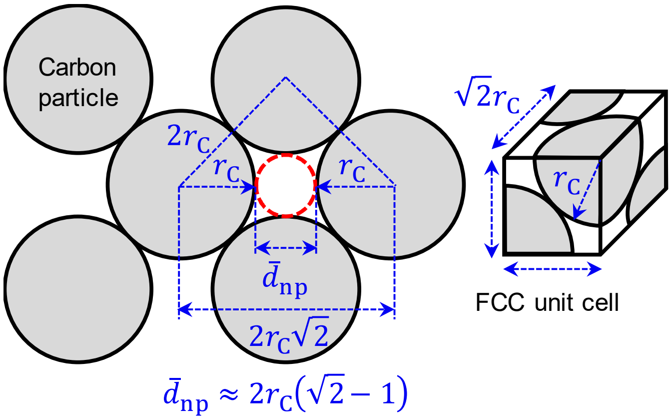

Figure 6-4. **Mean diameter of nanopores between FCC-arranged carbon particles in the aggregates**

ε_{agg} is obtained from the FCC arrangement of carbon particles as well as porosity of each particle, ε_C. As shown in Figure 6-4, in each FCC unit cell, there are four one-eighth particles, adding up to half a particle; thus, ε_{agg} could be obtained as one minus volume fraction of the solid part in a nanoscale unit cell as:

$$\varepsilon_{agg} = 1 - \frac{\frac{1}{2} \times \frac{4}{3}\pi r_C^3(1-\varepsilon_C)}{\left(\sqrt{2}r_C\right)^3} = 1 - \frac{\pi\sqrt{2}}{6}(1-\varepsilon_C) \tag{6.48}$$

6.6. Modeling the Conductivities at Nanoscale

To find the unknown $\Lambda_{eff,C}$ in Eq. (6.44), two structural characteristics of carbon particles should be addressed:

i) Graphitic structure of carbon particles, leading to high anisotropy of their thermal and electronic conductivities (typical conductivity values for graphite at room temperature: ~8 W·m^{-1}·K^{-1} [189] and 100 S·m^{-1} [190] for through-plane direction and ~1700 W·m^{-1}·K^{-1} [189] and ~10^{6} S·m^{-1} [190] for in-plane direction)

ii) Their nanoscale size, leading to significant size effects due to scattering of phonons (i.e., lattice vibrations acting as thermal energy carriers) and conduction electrons (i.e., free valence electrons acting as charge carriers) [174]

6.6.1. Anisotropy of the Carbon Particles

As pointed out by several studies in literature [191-197], the issue of anisotropy could be addressed accurately by taking the geometric mean of the conductivities in different directions. Refs. [194, 196] solved the heat conduction equation analytically and showed that thermal conductivity of the effective isotropic material is simply the geometric mean of the conductivities in different directions. Accordingly, the effective conductivity of the carbon particles was taken as the geometric mean of the conductivities of the graphitic structure in different directions. Considering that through-plane conductivity represents conduction in one direction while in-plane conductivity represents conduction in two directions, the effective bulk conductivity of the carbon particles could be expressed as:

$$\widetilde{\Lambda}_{\mathrm{eff,C}} = \sqrt[3]{\Lambda_{\mathrm{C,tp}}\Lambda_{\mathrm{C,ip}}^{2}} \tag{6.49}$$

where $\Lambda_{\mathrm{C,tp}}$ and $\Lambda_{\mathrm{C,ip}}$ are effective bulk conductivities of the graphitic structure of carbon particles in the through-plane and in-plane directions, respectively. $\widetilde{\Lambda}_{\mathrm{eff,C}}$ will be corrected later for size effects. $\Lambda_{\mathrm{C,tp}}$ and $\Lambda_{\mathrm{C,ip}}$ should be obtained from the properties of single crystals of graphite or, alternatively, highly-oriented, stress-annealed pyrolytic graphite whose properties approach those of single-crystal graphite [189, 198-205]. This particular type of graphite with a high degree of crystallinity was mainly developed to simulate the structure of single crystals of graphite due to difficulties associated with production and handling of single crystals. Accordingly, the thermal conductivities ($k_{\mathrm{C,tp}}$ and $k_{\mathrm{C,ip}}$) were taken from Ref. [189], which measured the conductivities for pyrolytic graphite in a broad temperature range of 100-900 K. Ref. [189] provided their data in form of graphs; thus, to use their data in the models, parts of their graphs between ~200-400 K (applicable for fuel cells) were digitized, and the following curves were fitted through their data with R^2=0.9934 for the through-plane conductivity (average discrepancy of ~2%) and R^2=0.9758 for the in-plane conductivity (average discrepancy of ~4%):

$$k_{\mathrm{C,tp}} = 5{,}313\, T^{-1.1505} \tag{6.50}$$

$$k_{\mathrm{C,ip}} = 3{,}416{,}509\, T^{-1.3387} \tag{6.51}$$

where T's are in $[\mathrm{K}]$, and k's are in $[\mathrm{W{\cdot}m^{-1}{\cdot}K^{-1}}]$. The electronic conductivities ($\sigma_{\mathrm{C,tp}}$ and $\sigma_{\mathrm{C,ip}}$) were taken from Ref. [190], which measured the conductivities of single crystals of graphite in a temperature range of 80-470 K. Ref. [190] tabulated their data; thus, to use their data in the models, the following curves were fitted through parts of their data between 260-400 K (applicable for fuel cells) with $R^2=0.9413$ for the through-plane conductivity (less than 1% discrepancy) and $R^2=0.9914$ for the in-plane conductivity (less than 1% discrepancy):

$$\sigma_{\mathrm{C,tp}} = 0.046607\, T + 85.13 \tag{6.52}$$

$$\sigma_{\mathrm{C,ip}} = 5.022 \times 10^{6}\, T^{-0.2816} \tag{6.53}$$

where T's are in $[\mathrm{K}]$, and σ's are in $[\mathrm{S{\cdot}m^{-1}}]$.

6.6.2. Size Effect Considerations for Modeling the Carbon Particles

In solids, conduction electrons can contribute in thermal conduction in addition to their specific role as charge carriers, which is especially significant for metals that have abundant free electrons [174]. However, in solids like graphite, which do not have as many free electrons as metals, phonons are the dominant carriers of thermal energy [107, 189, 198, 206, 207]. Thus, size effects could be addressed by correcting the effective bulk conductivity of Eq. (6.49) with mean free path of phonons for thermal conduction and conduction electrons for electronic conduction, as follows [174]:

$$\Lambda_{\mathrm{eff,C}} = \frac{\widetilde{\Lambda}_{\mathrm{eff,C}}}{1 + \mathrm{Kn}} \tag{6.54}$$

where $\mathrm{Kn} = MFP/d_\mathrm{C}$ is the Knudsen number of the thermal energy/charge carriers, where MFP is intrinsic or bulk mean free path of phonons for thermal conduction and conduction electrons for electronic conduction, and $d_\mathrm{C} = 2r_\mathrm{C}$ is the (mean) diameter of carbon particles. The intrinsic mean free path, MFP, is related to scattering of phonons or electrons in an infinite bulk material ignoring the effects of boundaries. Scattering from the boundaries of a carbon particle is taken into account in Eq. (6.54) by the Knudsen number, which becomes significant as the particle diameter gets smaller with respect to the intrinsic mean free path. Due to its anisotropic conductivities, graphite has anisotropic mean free paths as well [189, 208-210]. Thus, it is necessary to plug the effective mean free paths into Eq. (6.54). Considering that both thermal and electronic conductivities are proportional to the mean free path of their respective carriers [174], the same strategy of taking the geometric mean will work for obtaining the effective mean free paths. In addition, experimental data of mean free path gathered using methods based on isotropy assumption would also provide accurate determination of the effective mean free paths. In this thesis, based on the availability of applicable data in the literature, the effective mean free path of phonons was determined by taking the geometric mean of the phonon mean free paths in different directions, and the effective mean free path of conduction electrons was obtained from a reference in literature [211], which directly gathered the effective mean free path of conduction electrons. In the process, care was taken to just extract the intrinsic mean free path from this reference by ignoring the terms related to scattering by the crystal boundaries, which is very specific to the production process of a material and is not intrinsic to the material. Besides, as mentioned before, boundary scattering effects were accounted for by the Knudsen number in Eq. (6.54).

Thus, the effective mean free path of phonons could be expressed as:

$$MFP_\mathrm{ph,C} = \sqrt[3]{MFP_\mathrm{ph,C,tp} MFP_\mathrm{ph,C,ip}^2} \tag{6.55}$$

where $MFP_\mathrm{ph,C,tp}$ and $MFP_\mathrm{ph,C,ip}$ are mean free paths of phonons in single-crystal or highly-oriented pyrolytic graphite in the through-plane and in-plane directions, respectively. $MFP_\mathrm{ph,C,ip}$ was directly obtained from Ref. [189] as:

$$MFP_{\mathrm{ph,C,ip}} = 9.0 \times 10^{-9} \exp\left(2{,}480/(2.20\,T)\right) \tag{6.56}$$

where T is in $[\mathrm{K}]$, and $MFP_{\mathrm{ph,C,ip}}$ is in $[\mathrm{m}]$.

Ref. [208] measured thermal conductivity of thin films of graphite with different thicknesses from 200-300 K but extracted the c-axis phonon mean free path only for 300 K. In this thesis, using their extraction methodology, the rest of their data was processed, and the c-axis mean free path of phonons was obtained at other temperatures. Then, the following curve was fitted through their data with R^2=0.9846:

$$MFP_{\mathrm{ph,C,tp}} = 103 \times 10^{-9} \exp(207/T) \tag{6.57}$$

where T is in $[\mathrm{K}]$ and $MFP_{\mathrm{ph,C,tp}}$ is in $[\mathrm{m}]$. The above relation yields a value of 205 nm at 300 K which agrees well with the value of 204 nm reported by Ref. [208]. As temperature increases, lattice vibrations increase, or in other words, more phonons will contribute to conduction of heat; hence, the probability of collision between the phonons increases, leading to reduction in their mean free path, which is indicated by Eqs. (6.56) and (6.57).

Ref. [211] used the VDP method [52] in their electronic resistance measurements to determine mean free path of conduction electrons in a highly-oriented pyrolytic graphite. As also mentioned before, VDP method only gives an average conductivity, which has been noted by several references including Refs. [48, 133] as well as Ref. [211] itself. Accordingly, mean free path values reported by Ref. [211] are also average values, as also mentioned by this reference, making them directly applicable in Eq. (6.54) for electronic conduction. Thus, using the correlation provided by Ref. [211], intrinsic mean free path of conduction electrons in graphite could be expressed as:

$$MFP_{\mathrm{e,C}} = 5.63 \times 10^{-3}\, T^{-2} \tag{6.58}$$

where T is in $[\mathrm{K}]$ and $MFP_{\mathrm{e,C}}$ is in $[\mathrm{m}]$.

6.7. Determining the Contact Effectiveness Factor

As explained in section 6.5.1, $\xi\left(l_{\mathrm{I/C}}, t_{\mathrm{dm}}\right)$ is a complex function of ionomer content at the contact regions between the aggregates as well as shape of carbon particles which may change between a polyhedron for no dry milling to a sphere for long dry milling. In general, modeling this function needs detailed knowledge of placement of ionomer nanofibers at the contact regions, chemical interactions between the ionomer structure (i.e., its backbone and side chains) and Pt/C particles, and the shape transition of carbon particles from polyhedron to sphere by dry milling. For the purpose of this thesis, we could avoid these complexities by obtaining ξ for the conductivities from a few designs and confirming the model predictions for all the designs. Using designs #1 and #3-5, which cover the entire range of I/C ratios and dry milling times in this thesis, and assuming a power law in form of $a\left(l_{\mathrm{I/C}}\right)^{b}(1+t_{\mathrm{dm}})^{c}$, the function ξ was obtained as shown in Table 6-3 for different conductivities. $\xi\left(l_{\mathrm{I/C}}, t_{\mathrm{dm}}\right)$ is different for different conductivities in different directions due to: i) different ionomer content at the in-plane and through-plane contacts (refer to the discussions of section 5.4), and ii) different nature of ionomer in thermal and electronic conduction (i.e., electronically insulating but thermally conductive).

Table 6-3. Contact effectiveness factor for different conductivities

Functional relationship	$\xi(l_{\mathrm{I/C}}, t_{\mathrm{dm}}) = a(l_{\mathrm{I/C}})^{b}(1+t_{\mathrm{dm}})^{c}$			
Conductivity	**Coefficients**			
	a	b	c	R^2
Through-plane thermal	2.4019×10^{-1}	-2.9386	-4.9300×10^{-1}	0.9814
Through-plane electronic	1.1396×10^{-3}	-2.89622	-8.29130×10^{-1}	0.9997
In-plane electronic	7.8056×10^{-1}	-1.4475×10^{-1}	-2.6005×10^{-1}	0.9508

Since in-plane thermal tests were not possible, relation for ξ to describe the in-plane thermal contact points could not be determined. However, as shown in Table 6-3, through-plane thermal contacts were much better than the through-plane electronic contacts due to the different nature of ionomer in heat and electron conduction. On the other hand, ξ for in-plane electronic contacts was $\sim \mathrm{O}(0.1)$, and, by definition, its upper limit is equal to 1. Thus, using a similar analogy, one could take $\xi \approx 1$ for an order of magnitude analysis of the in-plane thermal conductivity.

6.8. Multi-scale Coupling

The developed conductivity models for different scales are coupled, as shown in Figure 6-5, to yield the conductivities for a CL. To sum it up, after coupling the models by following the steps in Figure 6-5 and simplifying the results as much as possible, closed-form expressions were obtained for the conductivities, as shown in Table 6-4.

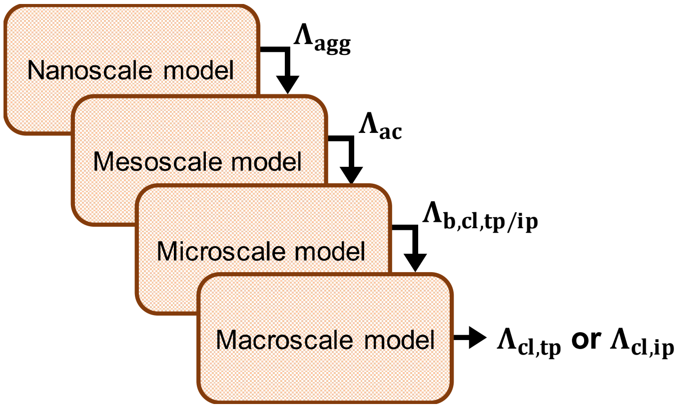

Figure 6-5. A block diagram showing the multi-scale coupling

Table 6-4. Closed-form expressions for the conductivities

Through-plane electronic conductivity: $\sigma_{\mathrm{cl,tp}} = (1-CD)\frac{2(1-\chi)}{\chi+2}\left\{\frac{4\cot\left(\frac{\theta_{\mathrm{agg}}}{2}\right)}{\sigma_{\mathrm{agg}}\pi\xi\left(1-\cos\left(\frac{\theta_{\mathrm{agg}}}{2}\right)\right)\sin\left(\frac{\theta_{\mathrm{agg}}}{2}\right)}\sum_{i=1}^{\infty}\frac{\left\{P_{2i-2}\left[\cos\left(\frac{\theta_{\mathrm{agg}}}{2}\right)\right]-P_{2i}\left[\cos\left(\frac{\theta_{\mathrm{agg}}}{2}\right)\right]\right\}^2}{(2i-1)(4i-1)}\right\}^{-1}$
Through-plane thermal conductivity: $k_{\mathrm{cl,tp}} = (1-CD)k_{\mathrm{b,cl}} + (CD)k_{\mathrm{f}}$
In-plane electronic conductivity: $\sigma_{\mathrm{cl,ip}} = \frac{2(1-\chi)}{\chi+2}\left\{\frac{4\left[1+\frac{CD}{3(1-CD)}\left(\frac{8}{4AR-\pi}+\frac{2}{\pi}\right)AR\right]\cot\left(\frac{\theta_{\mathrm{agg}}}{2}\right)}{\sigma_{\mathrm{agg}}\pi\xi\left(1-\cos\left(\frac{\theta_{\mathrm{agg}}}{2}\right)\right)\sin\left(\frac{\theta_{\mathrm{agg}}}{2}\right)}\sum_{i=1}^{\infty}\frac{\left\{P_{2i-2}\left[\cos\left(\frac{\theta_{\mathrm{agg}}}{2}\right)\right]-P_{2i}\left[\cos\left(\frac{\theta_{\mathrm{agg}}}{2}\right)\right]\right\}^2}{(2i-1)(4i-1)}\right\}^{-1}$
In-plane thermal conductivity: $k_{\mathrm{cl,ip}} = \frac{(1-CD)\left(\frac{k_{\mathrm{f}}}{k_{\mathrm{b,cl}}}-1\right)}{(1-CD)\left(\frac{k_{\mathrm{f}}}{k_{\mathrm{b,cl}}}-1\right)+\zeta(CD)}k_{\mathrm{b,cl}} + \frac{\zeta(CD)}{(1-CD)\left(\frac{k_{\mathrm{f}}}{k_{\mathrm{b,cl}}}-1\right)+\zeta(CD)}k_{\mathrm{f}}$

The unknown coefficients/conductivities/functions in the expressions of Table 6-4 should be obtained from the expressions provided in Table 6-5.

Table 6-5. Expressions for the unknown terms in the models

Conductivities:

$$k_{\mathrm{b,cl}} = \frac{\frac{\left(\chi+\frac{1}{2}\right)k_{\mathrm{f}}}{1+M/\bar{d}_{\mathrm{mip}}}+\frac{(1-\chi)}{2R_{\mathrm{meu,th}}r_{\mathrm{agg}}\cos\left(\frac{\theta_{\mathrm{agg}}}{2}\right)}}{1+\left(\frac{1}{2}\right)\chi+\frac{k_{\mathrm{f}}}{1+M/\bar{d}_{\mathrm{mip}}}(1-\chi)R_{\mathrm{meu,th}}r_{\mathrm{agg}}\cos\left(\frac{\theta_{\mathrm{agg}}}{2}\right)}, \quad \sigma_{\mathrm{agg}} = \frac{2\pi\sqrt{2}(1-\varepsilon_{\mathrm{C}})\sqrt[3]{\sigma_{\mathrm{C,tp}}\sigma_{\mathrm{C,ip}}^{2}}}{\left[18-\pi\sqrt{2}(1-\varepsilon_{\mathrm{C}})\right]\left(1+\frac{MFP_{\mathrm{e,C}}}{2r_{\mathrm{C}}}\right)}$$

$$k_{\mathrm{agg}} = \frac{\frac{\left(6-\frac{2\pi\sqrt{2}}{3}(1-\varepsilon_{\mathrm{C}})\right)r_{\mathrm{C}}k_{\mathrm{f}}}{1+\frac{M}{2r_{\mathrm{C}}(\sqrt{2}-1)}}+\frac{8\left(r_{\mathrm{C}}^{2}\right)\sqrt[3]{k_{\mathrm{C,tp}}k_{\mathrm{C,ip}}^{2}}}{2r_{\mathrm{C}}+\sqrt[3]{MFP_{\mathrm{ph,C,tp}}MFP_{\mathrm{ph,C,ip}}^{2}}}}{2r_{\mathrm{C}}\left(3-\frac{\pi\sqrt{2}}{6}(1-\varepsilon_{\mathrm{C}})\right)+\frac{\pi\sqrt{2}(1-\varepsilon_{\mathrm{C}})k_{\mathrm{f}}\left(2r_{\mathrm{C}}+\sqrt[3]{MFP_{\mathrm{ph,C,tp}}MFP_{\mathrm{ph,C,ip}}^{2}}\right)}{6\left(1+\frac{M}{2r_{\mathrm{C}}(\sqrt{2}-1)}\right)\sqrt[3]{k_{\mathrm{C,tp}}k_{\mathrm{C,ip}}^{2}}}}$$

Thermal resistance of mesopores:

$$R_{\mathrm{meu,th}} = \left\{\left[\frac{2\sum_{i=1}^{\infty}\frac{\left\{P_{2i-2}\left[\cos\left(\frac{\theta_{\mathrm{agg}}}{2}\right)\right]-P_{2i}\left[\cos\left(\frac{\theta_{\mathrm{agg}}}{2}\right)\right]\right\}^{2}}{(2i-1)(4i-1)}}{k_{\mathrm{agg}}\pi r_{\mathrm{agg}}\xi\left(1-\cos\left(\frac{\theta_{\mathrm{agg}}}{2}\right)\right)\sin^{2}\left(\frac{\theta_{\mathrm{agg}}}{2}\right)}\right]^{-1} + \left[\left[\pi k_{\mathrm{f}}\left(r_{\mathrm{agg}}\cos\left(\frac{\theta_{\mathrm{agg}}}{2}\right)+0.5M\right)\right]^{-1}\times\right.\right.$$

$$\left\{\ln\left[\frac{r_{\mathrm{agg}}\left[\cos\left(\frac{\theta_{\mathrm{agg}}}{2}\right)-\sin\left(\frac{\theta_{\mathrm{agg}}}{2}\right)\right]+0.5M}{0.5M}\right]+\frac{r_{\mathrm{agg}}\left[\sin\left(\frac{\theta_{\mathrm{agg}}}{2}\right)-\cos\left(\frac{\theta_{\mathrm{agg}}}{2}\right)\right]}{\left(r_{\mathrm{agg}}\cos\left(\frac{\theta_{\mathrm{agg}}}{2}\right)+0.5M\right)}\right\}^{-1} +$$

$$\left.\left.\frac{\left[(EW_{\mathrm{ion}}\rho_{\mathrm{w}})+(MW_{\mathrm{w}}\lambda\rho_{\mathrm{dry,ion}})\right]\left(h_{\mathrm{ion}}+\frac{3k_{\mathrm{ion}}}{\rho_{\mathrm{ion}}c_{\mathrm{ion}}v_{\mathrm{ph,ion}}}\right)}{\pi r_{\mathrm{agg}}^{2}\psi\left[(EW_{\mathrm{ion}}\rho_{\mathrm{w}})k_{\mathrm{dry,ion}}+(MW_{\mathrm{w}}\lambda\rho_{\mathrm{dry,ion}})k_{\mathrm{w}}\right]}\right]^{-1}\right\}^{-1}$$

Coefficients / Geometric parameters:

$$\zeta = \left[\frac{\frac{2}{3}\left(\frac{k_{\mathrm{f}}}{k_{\mathrm{b,cl}}}-1\right)}{1+\frac{1}{2}\left(\frac{k_{\mathrm{f}}}{k_{\mathrm{b,cl}}}-1\right)\frac{\pi}{2AR}}+\frac{\frac{1}{3}\left(\frac{k_{\mathrm{f}}}{k_{\mathrm{b,cl}}}-1\right)}{1+\left(\frac{k_{\mathrm{f}}}{k_{\mathrm{b,cl}}}-1\right)\left(1-\frac{\pi}{2AR}\right)}\right]$$

$$h_{\mathrm{ion}} = \frac{4\pi\rho_{\mathrm{C}}n_{\mathrm{C}}r_{\mathrm{C}}^{3}l_{\mathrm{ion}}(1+l_{\mathrm{Pt/C}})(1-\varepsilon_{\mathrm{C}})}{3\rho_{\mathrm{ion}}(2A_{\mathrm{ion}})(1-l_{\mathrm{ion}})}, \quad n_{\mathrm{C}} = \frac{\frac{4}{3}\pi r_{\mathrm{agg}}^{3}-\frac{\pi}{6}\omega_{\mathrm{agg}}(3a_{\mathrm{agg}}^{2}+\omega_{\mathrm{agg}}^{2})\times 6}{\left(2r_{\mathrm{C}}/\sqrt{2}\right)^{3}}\times\frac{1}{2}$$

Physical/geometrical properties in the expressions of Table 6-4 and Table 6-5 should be found from the relations provided in Table 6-6. As indicated in Table 6-6, two extreme cases of dry CLs (air in the pores) and fully hydrated CLs (liquid water in the pores and ionomer) are considered. Python codes were developed to find the conductivities from the models presented in Tables 6-4 and 6-5, using the physical/geometrical properties presented in Table 6-6. In the next section, different validations of the models are presented and discussed.

Table 6-6. Physical/geometrical properties used in the models

Conductivities:

$k_{\mathrm{a}}[\mathrm{W{\cdot}m^{-1}{\cdot}K^{-1}}] = 5.75 \times 10^{-5}(1 + 0.00317T[^\circ\mathrm{C}] - 0.0000021T[^\circ\mathrm{C}]^2)(\times 418.68)$ [160]

$k_{\mathrm{w}}[\mathrm{W{\cdot}m^{-1}{\cdot}K^{-1}}] = 0.5650285 + 0.0026363895T[^\circ\mathrm{C}] - 0.00012516934T[^\circ\mathrm{C}]^{1.5} - 1.5154918 \times 10^{-6}T[^\circ\mathrm{C}]^2 - 0.0009412945T[^\circ\mathrm{C}]^{0.5}$ [161]

$k_{\mathrm{dry,ion}}[\mathrm{W{\cdot}m^{-1}{\cdot}K^{-1}}] = 3.6131 \times 10^{-5}\, T[^\circ\mathrm{C}]^2 - 5.4290 \times 10^{-3}\, T[^\circ\mathrm{C}] + 0.3396$ by fitting the data of Ref. [39]

$k_{\mathrm{C,tp}}[\mathrm{W{\cdot}m^{-1}{\cdot}K^{-1}}] = 5{,}313\, T[\mathrm{K}]^{-1.1505}$ by fitting the data of Ref. [189]

$k_{\mathrm{C,ip}}[\mathrm{W{\cdot}m^{-1}{\cdot}K^{-1}}] = 3{,}416{,}509\, T[\mathrm{K}]^{-1.3387}$ by fitting the data of Ref. [189]

$\sigma_{\mathrm{C,tp}}[\mathrm{S{\cdot}m^{-1}}] = 0.046607\, T[\mathrm{K}] + 85.13$ by fitting the data of Ref. [190]

$\sigma_{\mathrm{C,ip}}[\mathrm{S{\cdot}m^{-1}}] = 5.022 \times 10^{6}\, T[\mathrm{K}]^{-0.2816}$ by fitting the data of Ref. [190]

Volumetric mass densities:

$\rho_{\mathrm{Pt}} = 21{,}450\ \mathrm{kg{\cdot}m^{-3}}$, $\rho_{\mathrm{C}} = 2{,}260\ \mathrm{kg{\cdot}m^{-3}}$ [107], $\rho_{\mathrm{dry,ion}} = \begin{cases} 1{,}980\ \mathrm{kg{\cdot}m^{-3}}, & \text{dry} \\ 1{,}675\ \mathrm{kg{\cdot}m^{-3}}, & \text{fully hydrated} \end{cases}$ [176], $\rho_{\mathrm{w}} = 1{,}000\ \mathrm{kg{\cdot}m^{-3}}$

Mean free paths:

$MFP_{\mathrm{g}} = \left(\frac{P_0}{P_{\mathrm{g}}}\right)\left(\frac{T_{\mathrm{g}}}{T_0}\right) MFP_0$ [128], $P_0 = 101.3\ \mathrm{kPa}$, $T_0 = 298\ \mathrm{K}$, $MFP_{0,\mathrm{a}} = 0.07\ \mu\mathrm{m}$ [169], $MFP_{\mathrm{w}} \approx 2.4\ \text{Å}$

$MFP_{\mathrm{ph,C,ip}}[\mathrm{m}] = 9.0 \times 10^{-9} \exp\left(2480/(2.20\, T[\mathrm{K}])\right)$ by fitting the data of Ref. [189]

$MFP_{\mathrm{ph,C,tp}}[\mathrm{m}] = 103 \times 10^{-9} \exp(207/T[\mathrm{K}])$ by fitting the data of Ref. [208]

$MFP_{\mathrm{e,C}}[\mathrm{m}] = 5.63 \times 10^{-3}\, T[\mathrm{K}]^{-2}$ by fitting the data of Ref. [211]

Ionomer:

$EW_{\mathrm{ion}} = 790\ \mathrm{g/mol\ of\ SO_3^-}$, $\lambda = \begin{cases} 0, & \text{dry} \\ 4, & \text{fully hydrated} \end{cases}$ [23, 185], $v_{\mathrm{ph,ion}} = \begin{cases} 1{,}735\ \mathrm{m{\cdot}s^{-1}}, & \text{dry} \\ 1{,}345\ \mathrm{m{\cdot}s^{-1}}, & \text{fully hydrated} \end{cases}$ [187]

$c_{\mathrm{ion}} = \frac{c_{\mathrm{w}}}{1+\frac{1}{\eta_{\mathrm{w}} MW_{\mathrm{w}}}} + \frac{c_{\mathrm{dry,ion}}}{1+\eta_{\mathrm{w}} MW_{\mathrm{w}}}$ [158], $c_{\mathrm{w}} = 4{,}217\ \mathrm{J{\cdot}kg^{-1}{\cdot}K^{-1}}$ [168], $\eta_{\mathrm{w}} = \begin{cases} 0, & \text{dry} \\ 0.005, & \text{fully hydrated} \end{cases}$

$c_{\mathrm{dry,ion}}[\mathrm{J{\cdot}kg^{-1}{\cdot}K^{-1}}] = 1.5858\, T[^\circ\mathrm{C}] + 995$ by fitting the data of Ref. [186]

Fluid parameter M:

$$M = \left[\frac{2-\alpha_{T_1}}{\alpha_{T_1}} + \frac{2-\alpha_{T_2}}{\alpha_{T_2}}\right]\left[\frac{2\gamma}{1+\gamma}\right]\left(\frac{1}{\mathrm{Pr}}\right) MFP_{\mathrm{f}} \text{ [128]}, \quad \gamma = \begin{cases} 1.4, & \text{air} \\ 1.0, & \text{water} \end{cases} \text{ [212]}, \quad \mathrm{Pr}_{\mathrm{a}} \cong 0.7 \text{ [168]}$$

$$\mathrm{Pr}_{\mathrm{w}} = \frac{1}{0.074763403+0.0029020983T+2.8606181\times10^{-5}T^2-8.1395537\times10^{-8}T^3} \text{ [161]}$$

$$\alpha_T = \left(\frac{MW_{\mathrm{f}}^{*}}{6.8+MW_{\mathrm{f}}^{*}}\right)\exp\left[-0.57\left(\frac{T-273}{273}\right)\right] + \frac{2.4(MW_{\mathrm{f}}/12)}{[1+(MW_{\mathrm{f}}/12)]^2}\left\{1 - \exp\left[-0.57\left(\frac{T-273}{273}\right)\right]\right\} \text{ [128]}$$

$$MW_{\mathrm{f}}^{*} = \begin{cases} MW_{\mathrm{f}}, & \text{monoatomic gasses} \\ 1.4MW_{\mathrm{f}}, & \text{diatomic/polyatomic gases (like air) and water} \end{cases} \text{ [128]}, \quad MW_{\mathrm{f}} = \begin{cases} 29\ \mathrm{kg{\cdot}kmol^{-1}}, & \text{air} \\ 18\ \mathrm{kg{\cdot}kmol^{-1}}, & \text{water} \end{cases}$$

Geometrical properties:

$$f(\theta_{\mathrm{agg}}) = -\frac{\sqrt{2}\pi^2(1-\varepsilon_{\mathrm{C}})\left[1+l_{\mathrm{Pt/C}}\frac{\rho_{\mathrm{C}}}{\rho_{\mathrm{Pt}}}+\frac{\rho_{\mathrm{C}} l_{\mathrm{ion}}(1+l_{\mathrm{Pt/C}})}{\rho_{\mathrm{ion,dry}}(1-l_{\mathrm{ion}})}\right]\left\{\frac{4}{3}-\left[1-\cos\left(\frac{\theta_{\mathrm{agg}}}{2}\right)\right]\left(3\sin^2\left(\frac{\theta_{\mathrm{agg}}}{2}\right)+\left[1-\cos\left(\frac{\theta_{\mathrm{agg}}}{2}\right)\right]^2\right)\right\}}{48\cos^3\left(\frac{\theta_{\mathrm{agg}}}{2}\right)} + \frac{1-\varepsilon_{\mathrm{cl}}}{1-\chi} = 0$$

$\varepsilon_{\mathrm{C}} = 0.287$ [108], $\bar{d}_{\mathrm{mip}}[\mathrm{nm}] = 141(1 + t_{\mathrm{dm}}[\mathrm{hr}])^{-0.1216}$, $\chi = 0.7809\exp(-0.5080 l_{\mathrm{I/C}} - 0.0377 t_{\mathrm{dm}}[\mathrm{hr}])$

$r_{\mathrm{C}} = 15\ \mathrm{nm}$ (measured), $r_{\mathrm{agg}} = 50\ \mathrm{nm}$ (measured), $\psi \approx 0.5$ [157] (Only wet thermal conductivity is sensitive to ψ.)

$$l_{\mathrm{ion}} = \frac{l_{\mathrm{I/C}}}{l_{\mathrm{I/C}}+l_{\mathrm{Pt/C}}+1}, \quad \xi = \begin{cases} 0.24019(l_{\mathrm{I/C}})^{-2.9386}(1 + t_{\mathrm{dm}}[\mathrm{hr}])^{-0.49300}, & \text{for through-plane thermal conduction} \\ 1.1396 \times 10^{-3}(l_{\mathrm{I/C}})^{-2.89622}(1 + t_{\mathrm{dm}}[\mathrm{hr}])^{-0.829130}, & \text{for through-plane electronic conduction} \\ 0.78056(l_{\mathrm{I/C}})^{-0.14475}(1 + t_{\mathrm{dm}}[\mathrm{hr}])^{-0.26005}, & \text{for in-plane electronic conduction} \\ 1, & \text{for an order of magnitude analysis of in-plane thermal conductivity} \end{cases}$$

6.9. Results and Discussion

6.9.1. Model Validation

Modeling results are compared to the experimental data in Figure 6-6 and Figure 6-7. As shown in Figure 6-6, the models agree well with the experimental data and can predict the structural trends (defined here as differences between the conductivities of different designs due to the different microstructures).

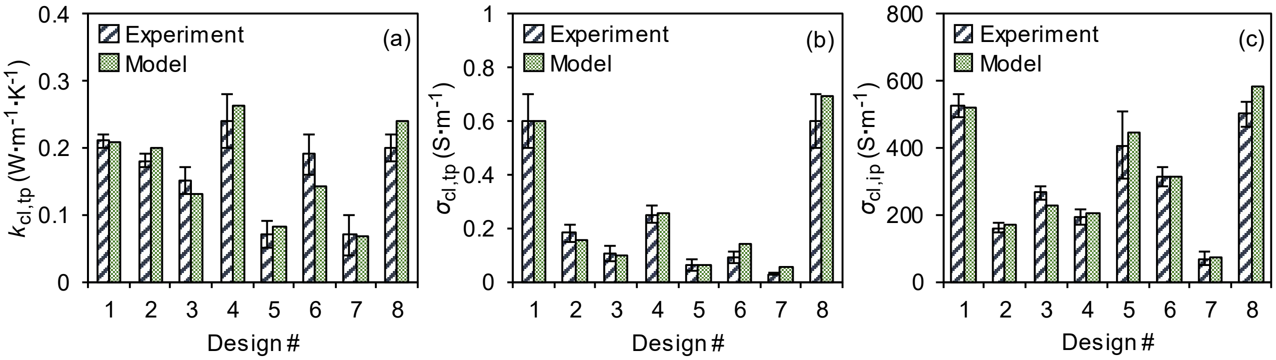

Figure 6-6. **Model vs. experiment for different CL designs at room temperature and RH (error bars: random errors): (a) through-plane thermal conductivity, (b) through-plane electronic conductivity, and (c) in-plane electronic conductivity**

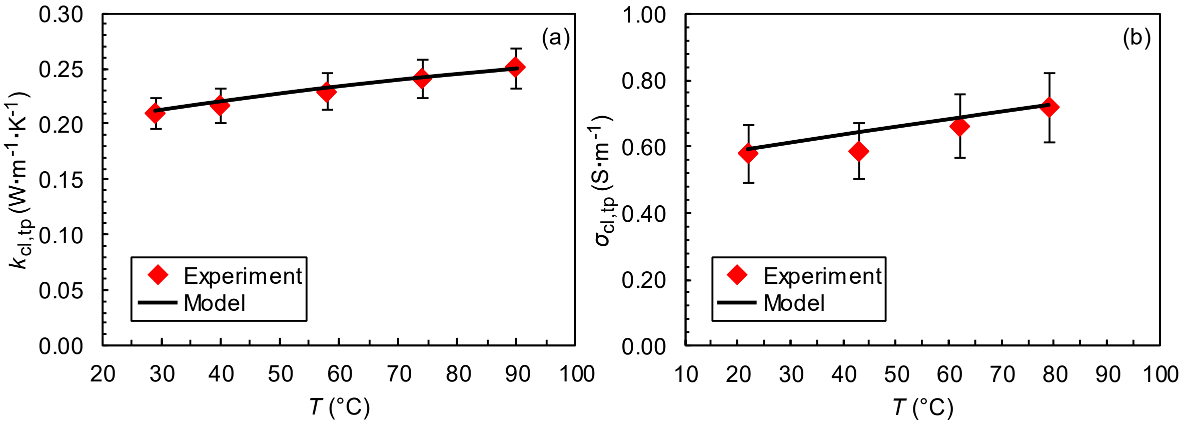

Figure 6-7. **Model vs. experiment for design #1 at different temperatures at 1,500 kPa (RH: not controlled, error bars: random errors): (a) through-plane thermal conductivity, and (b) through-plane electronic conductivity**

Figure 6-7 shows that the models are also capable of predicting the conductivities at different temperatures. As shown later, the increasing trends with increasing the temperature are due to reduction in the mean free paths of heat and charge carriers; this leads to smaller size effects, which are detrimental to both conductivities.

In an effort, the through-plane thermal and electronic conductivity data were tested to find correlations between the conductivities, but no correlation was found, perhaps because of having ionomer in contact areas between the particles in CLs. The ionomer in the contact areas is finitely thermally conductive but completely electronically insulating. Thus, narrowing the conduction pathway by the ionomer in the contact points, in different ways for heat and electron conduction, may disturb any relationship between the conductivities.

6.9.2. Predictions for Fully Wet Conditions

As explained in section 5.4, ex-situ hydration of CLs led to structural collapse of the CLs. For this reason, no reliable experimental data could be collected for the conductivities of the CLs hydrated ex-situ. However, the model was used to perform an order of magnitude analysis in wet conditions. Considering that hydration occurs in-situ in fuel cells while the MEA is under ~1.5-3.0 MPa compression, it is speculated that through-plane contact effectiveness factors (ξ's) may not change much with hydration. Thus, through-plane electronic conductivity of a wet CL is speculated to be similar to that of the dry CL. However, since hydration replaces the gas in the pores with high-thermal-conductivity water and leads to swelling of the ionomer, changes in thermal conductivity should certainly occur, as also noted by Ref. [13]. Model predictions for through-plane thermal conductivity in dry and wet conditions are compared in Figure 6-8 and show possibility of achieving a ~3-8 times higher thermal conductivity in fully wet conditions compared to dry conditions. Further, model predictions show that structural trends in the conductivity for wet conditions almost remain the same as those for dry conditions. Reasons for the significant enhancement in thermal conductivity with hydration are discussed in the next sections.

On the other hand, CLs are supported on the membrane in fuel cells, and membranes swell and deform by hydration. The through-plane swelling of the membrane increases the pressure, which may counteract the effect from through-plane swelling of ionomer in the CL (trying to separate the particles) and may keep the through-plane ξ's almost the same as in dry conditions. However, since no in-plane clamping force is applied to the MEA, it is speculated that the in-plane deformation of the membrane may have a significant effect on the CL and, thus, on the in-plane ξ's. This issue may not matter for in-plane thermal conductivity of the CL because, as shown in section 4.2.4, this property should play no role in heat transfer inside PEMFCs. For the in-plane electronic conductivity, one could simply obtain the in-plane ξ's by performing ex-situ tests of in-plane electronic conductivity under different RH. However, such ex-situ tests may not be a good representative of the changes in an actual MEA, as the membrane may undergo a much more complicated deformation due to: i) nonuniform clamping pressure, induced by the land-channel pattern of the bipolar plates, and ii) different hydration of different parts of the membrane due to nonuniform distribution of the reactions. Thus, understanding the effects of hydration and RH on the in-plane electronic conductivity of an operating CL requires a much more in-depth investigation, which is not in the scope of this thesis and is suggested here as a future work.

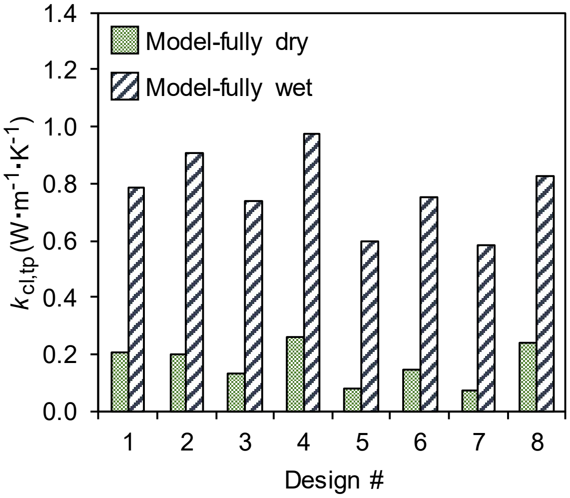

Figure 6-8. **Model predictions for through-plane thermal conductivity at 25°C: fully dry vs. fully wet conditions**

6.9.3. Heat and Electron Conduction Regimes inside CLs

The conduction regimes in different conditions, predicted by mean free path calculations, are summarized in Table 6-7. Calculations of mean free paths of electrons at 25 °C yielded a value of ~60 nm which is above the size of the conducting carbon particles (~15-60 nm).

Thus, electron conduction in the carbon particles is ballistic. Calculations of mean free paths of thermal energy carriers in dry conditions at 25 °C yielded: i) ~70 nm for molecular mean free path of the gas, ii) ~300 nm for mean free path of phonons inside the carbon particles, and iii) ~0.2 nm for mean free path of phonons inside the ionomer. The ~70 nm molecular mean free path of the gas is well above the sizes of nanopores inside the aggregates (~5-25 nm) and mesopores between the agglomerates (~8-50 nm) and below the sizes of most micropores between the agglomerate clusters (~50-1000 nm) and cracks (~100-10^7 nm). The ~300 nm mean free path of phonons inside the carbon particles is well above the size of carbon particles (~15-60 nm), and the ~0.2 nm mean free path of phonons inside the ionomer is well below the thickness of the ionomer around the aggregates (~14-22 nm). Accordingly, heat conduction regime in dry state is ballistic inside the nanopores, mesopores, and carbon particles and diffusive inside the micropores, cracks, and ionomer.

Table 6-7. Model predictions for heat and electron conduction regimes inside CLs in fully dry and fully wet conditions

Conduction phenomenon	CL component	Hydration state of the CL	Conduction regime
Electronic	Carbon particles	Dry or Wet	Ballistic
Thermal	Nanopores	Dry	Ballistic
		Wet	Diffusive
	Mesopores	Dry	Ballistic
		Wet	Diffusive
	Micropores	Dry	Diffusive
		Wet	Diffusive
	Cracks	Dry	Diffusive
		Wet	Diffusive
	Ionomer	Dry	Diffusive
		Wet	Diffusive
	Carbon particles	Dry or Wet	Ballistic

Similar calculations for wet conditions yielded: i) ~0.24 nm for molecular mean free path of liquid water in the pores, which is considerably smaller than sizes of fluid-filled pores and cracks inside CLs, ii) ~300 nm for mean free path of phonons inside the carbon particles (does not change with hydration), and iii) ~0.4 nm for mean free path of phonons inside the ionomer, which is still considerably smaller than thickness of the hydrated ionomer film around the aggregates (~16-26 nm). Thus, hydration only changes heat conduction regime of nanopores and mesopores from ballistic to diffusive but maintains the ballistic conduction regime of carbon particles and the diffusive conduction regime of micropores, cracks, and ionomer. This change of conduction regime in nanopores and mesopores from ballistic to diffusive is the main reason behind the predicted significant enhancement in thermal conductivity by hydration, as shown in Figure 6-8. More clarifications are given in the next section where shares of different resistances in different conditions are discussed.

6.9.4. Shares of Different Resistances inside CLs

To understand the dominant conduction pathways inside CLs, shares of different resistances inside CLs are compared at the agglomerate scale for dry and wet conditions.

Shares of Resistances in Fully Dry CLs

Table 6-8 shows model predictions for shares of different resistances inside the baseline CL (design #1 in Table 2-1) for two extreme temperatures of 20 and 90 °C in dry conditions. $R_{\mathrm{ion,tot}}$ in Table 6-8 represents the total ionomer resistance on an aggregate.

Table 6-8. Shares of different resistances in the baseline CL in dry conditions

Conduction phenomenon	Resistance	T (°C)	Magnitude
Thermal	$\boldsymbol{R}_{\mathbf{agg}}\ (\mathrm{GK{\cdot}W^{-1}})$	20	0.0233
		90	0.0189
	$\boldsymbol{R}_{\mathbf{mep}}\ (\mathrm{GK{\cdot}W^{-1}})$	20	4.50
		90	5.10
	$\boldsymbol{R}_{\mathbf{ion,tot}}\ (\mathrm{GK{\cdot}W^{-1}})$	20	0.0229
		90	0.0390
Electronic	$\boldsymbol{R}_{\mathbf{agg}}\ (\mathrm{M\Omega})$	20	7.83
		90	6.13

As shown in Table 6-8, for thermal conduction, gas resistance has the largest share. Further, the ionomer resistance is comparable with the aggregate resistance, but the series configuration of the ionomer resistance and the mesopore gas resistance makes a highly resistant pathway for heat and leads most of the heat to the much smaller parallel resistance of the aggregate. Overall, the aggregate-aggregate contacts make the dominant pathways for heat conduction inside dry CLs, just like electron conduction. The aggregate resistance decreases with temperature, while the gas and ionomer resistances increase with temperature. These trends could be explained based on the heat conduction regimes in these components. Molecular mean free path of the gas increases from ~66 nm at 20 °C to ~82 nm at 90 °C; this leads to a more ballistic heat conduction regime inside the nanopores and mesopores and, thus, increases the gas resistance. However, for ionomer which has a completely diffusive heat conduction regime, it is the reduction in the bulk conductivity from ~0.24 $W \cdot m^{-1} \cdot K^{-1}$ at 20 °C to ~0.14 $W \cdot m^{-1} \cdot K^{-1}$ at 90 °C that leads to the increase in the ionomer resistance with temperature. On the other hand, mean free path of phonons in carbon particles decreases from ~333 nm at 20 °C to ~195 nm at 90 °C. This leads to a less ballistic (more diffusive) heat conduction regime inside the carbon particles and, thus, reduction in the aggregate resistance with temperature. Similarly, mean free path of electrons in carbon particles decreases from ~66 nm at 20 °C to ~43 nm at 90 °C, which leads to a less ballistic (more diffusive) electron transport inside the carbon particles and, hence, reduction in the aggregate electronic resistance with increasing the temperature. Clearly, aggregate-aggregate contacts are the only electron conduction pathway inside CLs.

Shares of Resistances in Fully Wet CLs

Based on the discussions of section 6.9.2, it is speculated that through-plane electronic resistance of the aggregates in wet conditions be the same as dry conditions. However, no speculation could be made at this point regarding the in-plane electronic resistance of the wet aggregates due to the indirect effects of the membrane, as explained in section 6.9.2. Table 6-9 shows shares of through-plane thermal resistances inside the baseline CL for two extreme temperatures of 20 and 90 °C in wet (fully hydrated) conditions.

Table 6-9. Shares of through-plane thermal resistances in the baseline CL in fully wet conditions

Resistance	T (°C)	Magnitude $(\mathrm{GK \cdot W^{-1}})$
R_{agg}	20	0.0224
	90	0.0182
R_{mep}	20	0.0024
	90	0.0029
$R_{\text{ion,tot}}$	20	0.0188
	90	0.0216

As indicated by the values in Table 6-9, aggregate-aggregate contacts are no longer the dominant pathways for heat conduction in wet conditions. In wet conditions: i) the mesopore resistance becomes much smaller than other resistances due to the change in its heat conduction regime from ballistic to diffusive, and ii) ionomer resistance remains comparable to the aggregate resistance. Thus, the series combination of mesopore and ionomer makes an alternative pathway for heat conduction through the agglomerate, whose resistance is comparable to the aggregate resistance. The overall effect is a considerably smaller agglomerate resistance and, hence, a considerably higher thermal conductivity in wet conditions, as shown in Figure 6-8. As shown in Table 6-9 for the baseline CL, increasing the temperature reduces the aggregate resistance and increases the mesopore and ionomer resistances, just like the dry conditions. Model predictions for effects of temperature on thermal conductivity in fully wet conditions is compared to completely dry conditions in Figure 6-9 for the baseline CL and show the same trend as the dry conditions. The slight increasing trend with temperature in wet conditions is again governed by the subsequent reduction in the aggregate resistance.

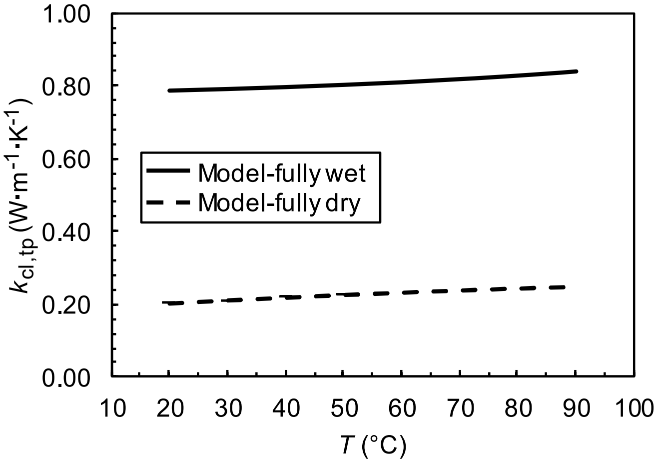

Figure 6-9. **Model predictions for effects of temperature on through-plane thermal conductivity of the baseline CL: fully dry vs. fully wet**

6.9.5. Order of Magnitude Analysis of In-plane Thermal Conductivity

As explained in section 4.2.4, measurement of in-plane thermal conductivity was neither possible due to the huge in-plane thermal resistance of CLs nor necessary due to the expected negligible role of in-plane thermal conduction in CLs. On the other hand, the in-plane contact effectiveness factor (ξ) could not be determined due to impossibility of such tests. Thus, we only perform an order of magnitude analysis on this property for the sake of completeness. By arbitrarily choosing $\xi \approx 1$ to predict the order of magnitude of in-plane thermal conductivity of different CL designs, the model yields values of ~0.7-2.6 $W{\cdot}m^{-1}{\cdot}K^{-1}$ for the CLs in fully dry conditions and ~1.8-3.4 $W{\cdot}m^{-1}{\cdot}K^{-1}$ for the CLs in fully wet conditions. These values are well above the through-plane values due to the much better effectiveness of in-plane contacts (backed up by the electrical tests). Thus, based on the model, thermal conductivity is also expected to be anisotropic, just like the electronic conductivity. The predicted in-plane values are ~4-32 times the through-plane values for dry conditions and ~2-6 times the through-plane values for wet conditions. Thus, hydration by liquid water is expected to reduce the degree of anisotropy in thermal conductivity.

6.9.6. Sensitivity of the Models to Other Structural Parameters

So far, we have studied effects of different structural and compositional parameters. This section is dedicated to analyzing sensitivity of the models to ionomer coverage, radius of aggregates, radius of carbon particles, and platinum loading in fully dry and fully wet conditions. To facilitate analysis of the numerical results, the baseline CL (i.e., design #1 in Table 2-1) is selected as a reference, and results are reported relative to this reference at 25 °C. Moreover, when a parameter is changed, for the sake of parametric study, the rest of the parameters are kept constant. Figure 6-10 shows results of the sensitivity analyses for different conductivities.

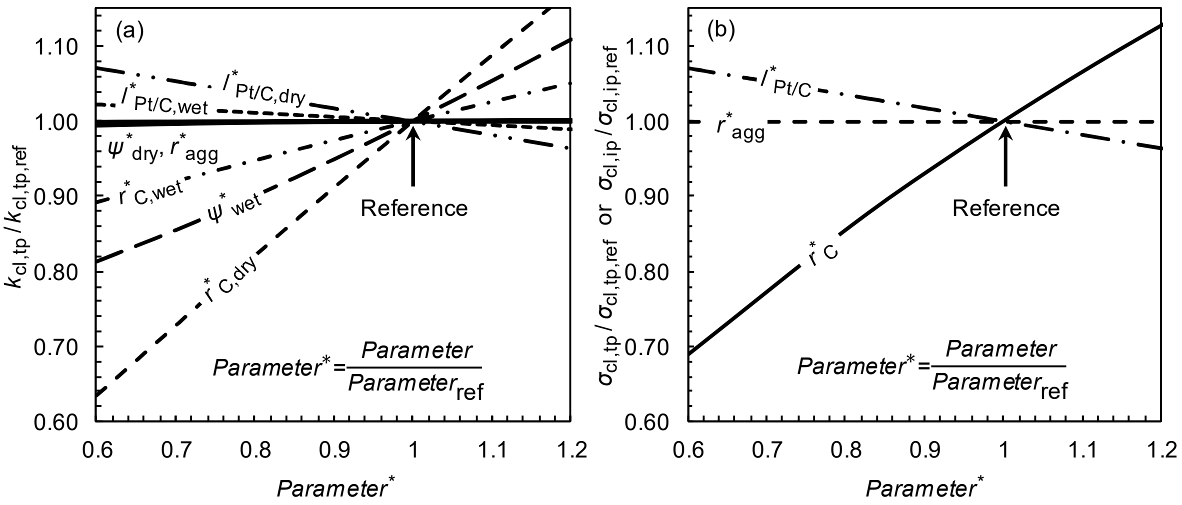

Figure 6-10. Sensitivity analyses of the models: (a) through-plane thermal conductivity, (b) through-plane or in-plane electronic conductivity

As shown in Figure 6-10, none of the conductivities are sensitive to the radius of the aggregates (in any of the dry or wet conditions). The reason for this behavior could be explained by the interplay between the resultant changes in the values of resistance per unit area (also known as insulance) of the agglomerates (i.e., $R_{\mathrm{meu,tp/ip}}A_{\mathrm{meu}}$) and length of the heat transfer pathway inside the agglomerates (i.e., h_{meu}). As modeling results showed, increasing the aggregate radius resulted in more material (or resistance) per unit area of the agglomerate by almost the same factor as lengthening the heat transfer pathway inside the agglomerate. Thus, scaling the agglomerate insulance and the heat transfer length by more or less the same factor leads to a very negligible change in the conductivities.

The amount of ionomer at the contact regions between the aggregates is a function of I/C ratio and dry milling time and, therefore, does not change with how the ionomer covers the rest of an aggregate. Thus, the electronic conductivities would not depend on ionomer coverage. However, changing the ionomer coverage could change the thickness of the ionomer film around the aggregates and, therefore, could change the thermal conductivity. Modeling results for thermal conduction showed that ionomer resistance decreased as ionomer coverage increased because of the resultant wider spread of the same amount of ionomer on the outer surface of the aggregates, which results in both a higher heat transfer area for the ionomer and a shorter heat transfer pathway through the ionomer (due to smaller thickness). As shown in Figure 6-10 a, thermal conductivity is highly insensitive to ionomer coverage in dry conditions, due to placement of the ionomer resistance in a series configuration with the large resistance of the gas in the mesopores. Thus, the reduction in the ionomer resistance with increasing the ionomer coverage does not affect the thermal conductivity in dry conditions. However, in wet (fully hydrated) conditions, thermal conductivity is highly dependent on ionomer coverage and could increase up to ~37% by increasing the dimensionless ionomer coverage in the range shown in the figure. The reason behind this trend is placement of the ionomer resistance in a series configuration with the small resistance of liquid water in the mesopore, which provides an alternative pathway for heat conduction through the agglomerate; the result is enhancement in thermal conductivity due to reduction in the ionomer resistance with increasing the ionomer coverage.

Figure 6-10 further shows that all the conductivities are enhanced by increasing the radius of carbon particles. The reason behind this trend is reduction in ballistic transport and, thus, enhancement of diffusive transport of heat/electrons inside the carbon particles by increasing the radius. Results show that increasing the dimensionless radius of carbon particles in the range shown in the figure could increase the through-plane thermal conductivity up to ~138% in fully dry conditions and up to ~28% in fully wet conditions. The reason behind the much larger enhancement in dry conditions is the much more significant share of carbon particles in heat conduction in dry conditions. In wet conditions, the liquid-filled mesopores and hydrated ionomer also contribute significantly to heat conduction through the agglomerates, and thus, effect of enhancing the effective conductivity of carbon particles on the CL conductivity is less. In case of electron conduction, increasing the dimensionless radius in the range shown in the figure could increase the electronic conductivities up to ~94%. In this case, carbon-carbon contacts are the only conductive pathways. The magnitude of enhancement in electronic conductivity is less than the enhancement in thermal conductivity due to different mean free paths of phonons and electrons inside the carbon particles. Heat conduction through the carbon particles has a higher degree of ballistic transport than electron conduction through the particles; the reason is the much larger mean free path of phonons (~300 nm) compared to electrons (~60 nm). This leads to a more significant impact of mitigating the size effects for carbon particles (e.g., through increasing their radius) on the overall conductivity in the case of heat conduction.

As shown in Figure 6-10, the conductivities decrease by increasing the Pt loading. Although effects of Pt particles are negligible in thermal/electronic resistance at nanoscale due to their small size and volume fraction, they still contribute to geometry of the aggregates (~4-9% volume of the aggregates for Pt loading of 0.6-1.2). Modeling results showed that by increasing the Pt loading (at constant CL porosity and volume fraction of micropores), the overlap (or compactness) of the aggregates had to decrease to maintain the constant porosity of the CL (as assumed in the parametric study). This led to an increase in spreading/constriction resistance of the aggregates and, consequently, reduction in the conductivities. Figure 6-10 further shows that the reduction in through-plane thermal conductivity is more in dry conditions compared to wet conditions. This, again, is a result of having an alternative heat transfer pathway through the hydrated ionomer and water-filled pores and, thus, less share/impact of the aggregate resistance in wet conditions. However, it should be noted that the observed reduction in the conductivities with increasing the Pt loading is a direct result of keeping the other parameters (e.g., CL porosity and volume fraction of micropores) constant, which may not be the case in real world. In fact, due to interactions between the Pt particles and ionomer [57, 213, 214], correlations may exist between porosity of a CL and its Pt loading and/or between volume fraction of micropores and Pt loading. In case of existence of such correlations, porosity of the CL and/or volume fraction of micropores will not be independent from the Pt loading, and such correlations should also be fed into the models to have a sound prediction of the conductivities. Overall, the performed sensitivity analysis shows that changing the Pt loading within 0.6-1.2 could change the through-plane thermal conductivity up to ~10% in fully dry conditions and up to ~3% in fully wet conditions and could also change the electronic conductivities up to ~10%. Measurements of Ref. [13] showed no significant change in the through-plane thermal conductivity of CLs by changing the Pt loading.

6.10. Significance of Heat Transfer through CLs

In this section, a simple order of magnitude analysis is preformed to understand shares of different heat transfer modes inside CLs and, thus, the significance of heat transfer through CLs. In general, four different modes may be identified for transfer of heat between two media: i) radiation, ii) conduction, iii) convection, and iv) advection. Since radiation heat transfer is dependent on difference between two temperatures, each to the fourth power, it only becomes significant in case of having a high temperature difference between the two media or in case of heat transfer in vacuum [168]. Thus, radiation effects are negligible for the MEA layers where temperature difference across the layers is in the order of a few degrees [14, 215]. Thus, the problem of finding shares of different heat transfer modes in CLs boils down to finding the shares of conduction through the solid matrix and advection/convection by the fluids in the pores. In general, these heat transfer modes are coupled and may affect each other. For instance, if one of these modes does not transfer the generated heat as effectively as the others, then most of the burden will be on the other modes. Thus, the heat transfer problem in CLs (and other layers of the MEA) is in general a conjugate heat transfer problem through the solid matrix and the fluids in the pores. As a preliminary modeling exercise by the author showed, modeling of such conjugate heat transfer problem would require additional information, such as saturation and permeability of the porous medium, velocity and partial pressures of the fluids in the pores, and internal convective heat transfer coefficient between the fluids and the solid matrix. Such information was not available for this project. Accordingly, instead, a simple order of magnitude analysis of the conduction and advection/convection shares are performed here.

Ref. [14] developed a model to simulate effects of through-plane thermal conductivities of different layers of the MEA on internal temperature profiles across the layers. In this work, portions of their temperature profiles related to a CCL were digitized to find the order of magnitude of temperature difference across a CL. The found temperature difference was then divided by the CCL thickness used in their study to find the order of magnitude of temperature gradient in the CL. Then, using the through-plane thermal conductivity value chosen in Ref. [14] for the CCL, share of conduction heat transfer per unit area through the CL was calculated as $-k_{\mathrm{cl,tp}} dT/dx \sim 0.18\ \mathrm{W/cm^2}$, where x is the variable of location across the MEA. On the other hand, total heat generation per unit area of an MEA could be expressed as $j(E_{\mathrm{th}} - E_{\mathrm{cell}})$[1], where j is current density (current per unit area of the MEA), $E_{\mathrm{th}} \approx 1.3\ \mathrm{V}$ [1] is thermal voltage, assuming all the potential chemical energy from the overall electrochemical reaction would go to electric work, and E_{cell} is the cell operating voltage which was taken to be $\sim 0.7\ \mathrm{V}$ at a current density of $1\ \mathrm{A/cm^2}$ in accordance with Ref. [14]. As shown in Refs. [14, 215], temperature profiles in PEMFCs are pretty symmetrical with respect to the membrane, if hydrogen and oxygen streams have the same inlet temperature. Thus, total heat flux through half of the MEA could be approximated as $\sim j(E_{\mathrm{th}} - E_{\mathrm{cell}})/2$, which is calculated to be $\sim 0.3\ \mathrm{W/cm^2}$. This energy clearly contains not only heat generation inside the CL but also Joule heating in other components of the MEA. A quick comparison between the conduction share of the CL ($\sim 0.18\ \mathrm{W/cm^2}$) and the total heat flux through half of the MEA ($\sim 0.3\ \mathrm{W/cm^2}$), reveals the significance of conduction heat transfer across the CL ($\sim 60\%$ of the total heat transfer). As discussed in section 1.2, heat generation in other fuel cell components occurs mainly by Joule heating, whose flux could be calculated from $j^2RA = j^2h/\sigma_{\mathrm{tp}}$. Using this relation and taking through-plane proton conductivity of $\sim 10\ \mathrm{S/m}$ for a fully hydrated Nafion membrane [216], through-plane electronic conductivity of $\sim 300\ \mathrm{S/m}$ for a GDL (as measured in this thesis), half-thickness of $25\ \mu\mathrm{m}$ for the membrane, and thickness of $250\ \mu\mathrm{m}$ for the GDL in accordance with Ref. [14], Joule heating in the membrane and GDL could be approximated as ~ 0.025 and $\sim 0.008\ \mathrm{W/cm^2}$, respectively. Thus, heat generation in the rest of the half-MEA components (other than the CL) could be obtained by adding these values as $\sim 0.033\ \mathrm{W/cm^2}$. Taking this value away from the total value of $\sim 0.3\ \mathrm{W/cm^2}$, total heat generation in the CL could be approximated as $\sim 0.27\ \mathrm{W/cm^2}$. As mentioned before, $\sim 0.18\ \mathrm{W/cm^2}$ of this amount is related to the conduction share. Thus, the rest of the generated heat (i.e., $\sim 0.09\ \mathrm{W/cm^2}$) should be related to the advection/convection share in the CL. Thus, conduction heat transfer accounts for $\sim 67\%$ of the total heat transfer in the CL, while advection/convection account for the rest ($\sim 33\%$). This reveals the more significant share of conduction heat transfer through CLs compared to advection/convection.

The above analysis was performed assuming a through-plane thermal conductivity of $\sim 0.09\ \mathrm{W \cdot m^{-1} \cdot K^{-1}}$ in accordance with Ref. [14]. As shown in Figure 6-6 a, this is a relatively small value for the through-plane thermal conductivity, and by engineering the CL microstructure, values as large as $\sim 0.24\ \mathrm{W \cdot m^{-1} \cdot K^{-1}}$ could be achieved. Thus, conduction heat transfer through the CL could even be more significant. References [13, 14] further elaborated on significant effects of thermal conductivity of different MEA layers, including the CLs, on temperature profiles across an MEA.

6.11. Conclusions and Design Guidelines

Throughout this chapter, multi-scale models were developed for thermal and electronic conductivities of CLs in different directions, by building on insights gained through the literature and the previous chapters on the CL microstructure. Great care was taken to closely follow the physics of the transport phenomena at different scales to enable modeling of the complex porous composite thin coating. It was found that the transport phenomena were closely linked to microstructural details of CLs at different scales.

Specifically, the transport phenomena were found to be governed by: i) size-dependence of various physical properties at nanoscale, ii) agglomerate geometry at mesoscale, iii) geometry of the matrix of agglomerate clusters and large pores at microscale, and iv) cracked structure of the coating at macroscale. Operating conditions (dry/wet, temperature) were found to significantly influence the results at different scales. Since partially graphitized carbon black was used for fabricating the CLs studied in this thesis, the models were developed and validated for this type of carbon by considering the physical properties of single crystals of graphite (or highly-oriented, stress-annealed pyrolytic graphite) when modeling the carbon particles. One may use the models for CLs having other carbon types by using the structure and properties of the desired type of carbon in the models. Further, microstructural properties of those CLs (e.g., porosity, crack density, crack aspect ratio, and carbon particle size) should be characterized and used in the models to obtain sound predictions of the conductivities. However, more in-depth analyses and measurements are still needed for CLs with different carbon types. Overall, engineering the conductivities showed that heat and electron conduction through a CL could be enhanced through:

1. **Using Pt/C catalyst powders whose shape of carbon particles are far from a complete sphere:** This is necessary to increase the contact area between the particles. This may be achieved by reducing the pre-processing steps/time needed to prepare the powders, e.g., by decreasing the dry milling time. To explain more, carbon blacks are generally shipped and placed on the market in form of pellets which are, in fact, compressed agglomerates [79]. Thus, to make a catalyst ink, it may be necessary to convert the as-shipped carbon black pellets into carbon black powder by dry milling the pellets. According to the experimental and modeling results of this thesis, the dry milling time for such pre-processing should be decreased to enhance the thermal and electronic conductivities. Decreasing the dry milling time would also ensure lower loss of porosity for the coating, which is necessary to reduce mass transport resistances inside the coating.

2. **Decreasing the I/C ratio, without compromising the structural integrity of the CL:** As experimental and modeling results showed, both of the through-plane thermal and electronic conductivities decreased significantly with increasing the I/C ratio, whereas the in-plane electronic conductivity was significantly enhanced. Since, the overall direction of heat, mass, and charge transfer in the MEA is in the through-plane direction, the through-plane conductivities are expected to affect the fuel cell performance more significantly than the in-plane

conductivities. Further, increasing the I/C ratio led to a significant reduction in porosity, which is a concern for enhancing mass transport through CLs. Thus, reducing the I/C ratio, without compromising the structural integrity, may seem desirable to reduce the through-plane thermal, electronic, and mass transport resistances. However, protonic conductivity may be compromised by decreasing the I/C ratio, which in turn could negatively affect the performance [217, 218]. Thus, more in-depth investigations and optimizations of the mentioned trade-offs are still needed to understand the optimum composition of the CL.

3. **Freezing the after-coating structure by drying the CL at high temperatures after coating:** Results showed that such freezing could significantly reduce the density and aspect ratio of cracks (depending on the dry milling time of the catalyst powder) and, thus, could significantly enhance the in-plane electronic conductivity.

4. **Using catalyst powders whose (fused) primary carbon particles are large in diameter:** This is necessary to reduce the detrimental effects of phonon/electron scattering inside the carbon particles on the conductivities and may also lead to less mass transport resistances inside the agglomerates. Nanopores between the carbon particles inside the agglomerates may get larger in size by increasing the size of the carbon particles, thereby providing wider channels for transport of species inside the agglomerates.

5. **Keeping the CL at an optimal level of hydration to increase the through-plane thermal conductivity:** An optimal level of hydration for the CLs would ensure maintaining the balance between benefits from the increased conductivity and losses from the reduced mass transport by hydration. Hydrating the CLs is also necessary to increase their protonic conductivity and may also enhance the membrane hydration, which is necessary to have sufficient protonic conductivity through the membrane. The observed enhancements in thermal and electronic conductivities with increasing the temperature versus drying effect of high temperatures is one instance of trade-offs which should be optimized for water management through the layers.

6. **Developing new coating methods for CLs which would not be directionally biased:** Developing such new coating methods may be necessary to prevent possible alignment of ionomer nanofibers in the in-plane direction by high shear forces during coating. It is speculated that such phenomenon (if exists) would lead to low through-plane electronic and protonic conductivities, which would be detrimental to fuel cell performance. The very low through-plane electronic conductivities, measured in this thesis, are speculated to be results of this phenomenon. However, confirming and understanding this phenomenon and its consequent effects still needs more in-depth investigations.

It is necessary to clarify that the above guidelines only state possible ways to enhance the thermal and electronic conductivities and do not set ultimate guidelines to optimize the fuel cell performance, as such an optimization was not in the scope of this thesis and, therefore, was not followed here. However, as discussed throughout the above points, trade-offs exist between different phenomena, which necessitates performing an in-depth optimization of the performance using the conductivity data/models provided in this thesis. Another point to be considered in this regard is that a high thermal conductivity may not be desirable where decreased performance due to flooding is a concern; a high thermal conductivity may, in fact, substantially decrease the evaporation rates that, in turn, could lead to flooding and decreased performance [219].

The above discussions open several areas of research and development regarding improving the CL microstructure and its conductivities/other transport properties as well as performance modeling and optimization. In the next chapter, a brief overview is given on the challenges faced during the experimental and modeling work of this thesis together with attractive areas for future research.

Chapter 7.

Future Research and Development

As discussed in the previous chapters, challenges were faced at every measurement and modeling step of the research. Many of those challenges were resolved successfully in this program, which led to pushing the boundaries of research on those areas. A part of the challenges, however, remained unresolved, which opens opportunities for future research and development (R&D). In the following, a brief overview of the faced challenges is provided together with recommendations for future studies.

7.1. CL Fabrication

Several challenges were faced for coating uniform thicknesses of CLs at a high speed, needed for different characterizations. Three different tools were evaluated: two printers (Fujifilm Inkjet and Microfab Inkjet printers) and a Mayer bar coater.

7.1.1. Challenges

The printers yielded CLs with nonuniform thicknesses at a very low yield rate. Besides, maintenance and troubleshooting of the printers needed to be done several times during a printing process, and the resolutions were found to be time-consuming, difficult, and costly. The Fujifilm Inkjet printer had a major issue with clogging of its cartridge nozzles, which, if happened, needed to be taken care of by cleaning/replacing the cartridge during a multi-step time-consuming process. This issue was even worse for the Microfab Inkjet printer due to having a single nozzle which, if clogged, would terminate the whole coating process. Another major issue with the Microfab Inkjet printer was significant fluctuations of its pneumatic system, used to make vacuum on its platen and inject the ink at the same time. Those fluctuations were found to result in very unrepeatable/nonuniform coatings in terms of thickness, areal Pt loading, and even visual appearance (light reflection properties). Another issue which compromised the repeatability was the clogging issue; whenever the clogging happened, one needed to pause/stop the printing, clean/replace the printing head, and then try to find the exact location where the printing was left off to continue from that point. However, finding the exact location was not an easy task (often entailed trials and errors), especially if extra printing bands were going to be added to an already printed coating to increase the coating thickness; most of the times, one needed to settle for some overlap between the old and the new printing bands. Another issue with repeatability was nonuniform deposition of the ink from the printing heads of the printers, which required the operator to rotate the substrate inside the printers once in a while to ensure a uniform deposition. All the above factors led to production of nonuniform unrepeatable coatings at a very slow rate by the printers. Accordingly, the printers were deemed unsuitable for the project, and all the samples made by them finally went to waste and were recovered for their Pt catalyst.

The Mayer bar coater, on the other hand, produced highly uniform CLs at a high yield rate. Its maintenance was easy and quick; each time, after using a rod for coating, one had to clean the rod using tissue paper, brush, a soap-water solution, tap water, DI water, and IPA, in a multi-step process to prevent contamination of future coatings by ink leftovers on the rod. More importantly, this coater resembled the same roll-coating process used in industry for mass production of CLs and, thus, could ensure direct applicability of the measurements for state-of-the-art PEMFCs. The only issue with this coater was the possible directional biasedness of the coater; high shear forces applied by the coating rod on the ink during coating could align the ionomer nanofibers in the shear direction (in-plane direction), which could be the reason for the very low through-plane electronic conductivity of the coatings.

7.1.2. Future Opportunities

1. **Developing specifically designed surfactants to prevent agglomeration of particles in catalyst inks during coating without affecting the after-coating microstructure:** Such surfactants may resolve the issue of clogging in printers. Despite their drawbacks, printers are still viewed as attractive tools for R&D purposes due to the possibility of fine-tuning the microstructure, e.g., by patterning.

2. **Improving the speed/reliability of printers by improving their hardware:** The same justifications as the previous point may be made here.

3. **Modifying the operation/hardware of Mayer bar coaters to make them directionally unbiased:** This may lead to production of CLs with high through-plane electronic/protonic conductivity, which may potentially improve the fuel cell performance.

4. **Developing new materials for the ionomer component of CLs, with a more isotropic structure:** This may result in isotropic coatings and may potentially resolve the problem of low through-plane electronic conductivity of CLs produced by roll-coating. On the other hand, considering that the state-of-the-art ionomers have gone through decades of development, the idea of developing new ionomers with new structures may not seem attractive or feasible. However, preliminary feasibility studies on this idea seem to be beneficial.

7.2. Thickness Measurements

Several methods were examined for measurement of thickness of CLs, including: i) SEM on cross sections of samples embedded in epoxy, ii) SEM on samples freeze-fractured in liquid nitrogen, and iii) the buoyancy method (i.e., the densitometer).

7.2.1. Challenges

Among the sample preparation methods for SEM imaging, epoxy-embedding was inferior to freeze-fracture due to smearing the samples' cross sections during several steps of polishing by a lapping machine (see Appendix B). The sample preparation time was also very long and could take days due to the several steps involved, such as sample-stacking, epoxy-embedding, curing, polishing, and carbon coating. Aside from these drawbacks, one had to work in a fume hood while casting the epoxy to prevent inhaling harmful vapors of the epoxy and the release agent, hence adding even more cost to the process.

The SEM sample preparation method of freeze-fracture was easier and faster in the sense that it only needed cutting samples under liquid nitrogen and mounting them on a vertical sample holder. The only drawbacks of this method were: i) requiring a high level of skill for the experimenter to cut a sample under liquid nitrogen by a one-time action of the cutter, and ii) limitations in the number and dimensions of samples which could be mounted on the sample holder for imaging.

The buoyancy method proved to be very accurate. Another advantage of this method was the possibility of directly measuring the porosity at the same time by adding a few more steps. The drawbacks of this method were: i) the need for a highly skilled experimenter able to remove air bubbles in water measurements from the CL surface while being careful not to damage the surface/microstructure during bubble removal and handling the samples, and ii) long measurement time. Time had to be allocated (~30 min) for relaxation of the microbalance after changing the fluid between the steps; one reason was to allow the fluid vapor inside the chamber of the microbalance to reach to equilibrium with the fluid, at the rate of leakage of the vapor from the chamber, in order to have a steady reading by the microbalance. Post-processing the raw data was also time-consuming.

7.2.2. Future Opportunities

1. **Improving the epoxy material to decrease the cure time and prevent the smearing effects during polishing:** Despite its drawbacks, there is one advantage for the sample preparation method of epoxy-embedding, which may motivate future research for its improvement. Despite sample preparation by freeze-fracture and measurements by the densitometer, many more samples could be stacked and measured by epoxy-embedding. Fast or mass thickness measurements is critical for the fast-paced environments of fuel cell research labs and companies, which are still experimenting in the field and need fast R&D capabilities. Thus, one attractive area of improvement would be developing new bubble-phobic epoxy materials with low cure time, with a highly brittle structure such that, during polishing, it would not transfer shear forces to layers of epoxy below the imaging surface.
2. **Automating the “cutting” and “bubble removal” steps in the methods of freeze-fracture and densitometer:** As mentioned before, a major issue with sample preparation by freeze-fracture and measurements by the densitometer was the skill level of the experimenter to cut samples or remove air bubbles. For this reason, automation of these steps or the whole procedures would help improve the methods for higher repeatability and accuracy.

7.3. Sample Preparation for Ex-situ Tests

As discussed in Chapter 3, one major concern with the coated samples for the ex-situ tests was to confirm if their microstructure was the same as the CLs used in a real fuel cell product. Further, microstructural data were needed as geometrical inputs for the models.

7.3.1. Challenges

A vast set of experimental tools had to be employed in a very costly and time-consuming process to ensure similarity of the coatings made for the tests to CLs in a real fuel cell product. This study entailed coating different thicknesses of CLs on different substrates as well as performing hot-pressing steps. The microstructural study, performed in this thesis, satisfied the research needs of the project and led to a fundamental understanding of the microstructure of state-of-the-art CLs. However, there is still a need to enable using the same CLs made during normal MEA production processes for ex-situ measurements of the conductivities (and other properties of CLs). This would be extremely beneficial in R&D of new CLs, where there may not be enough time to do such a comprehensive study on the microstructure for newly developed coatings/materials.

7.3.2. Future Opportunities

1. **Devising new decal-transfer techniques with less limitations on the target substrate:** Current decal-transfer techniques require a balance between surface energies of the original and target substrates to enable the transfer. Thus, considering that the original substrate is usually ETFE, choices of the target substrate are limited. For example, experiments by the author showed that a CL coated on ETFE could not be transferred onto Al, graphite, or ETFE. For this reason, samples had to be coated directly on the substrates suitable for the tests, which gave rise to the concerns regarding the microstructure. Thus, techniques enabling such transfers would be beneficial in the sense that samples needed for the tests could directly be taken from the normal processes of MEA construction, eliminating the concerns about the microstructure. This is particularly advantageous for development of new CLs. One idea is to change surface properties of the target substrate to make it suitable for the transfer. Such surface modification should not deposit any materials on the substrate, as any extra layer of a material would act as a source of noise in the tests.

2. **Developing conductive tapes to peel of CLs from their normal (ETFE) substrate for the ex-situ through-plane tests:** Such tapes should have the minimum possible adhesive thickness/resistance for minimal noise, as experimenting with existing tapes was not successful.

7.4. Effects of Operating Conditions

7.4.1. Challenges

A typical PEMFC constantly goes under hygrothermal stresses due to changes of temperature and moisture during normal operation of the PEMFC in an automotive duty cycle [220-224]. In addition, swelling of ionomer due to water absorption in the membrane and CLs leads to different compression of the layers when the water content of ionomer changes [220, 222, 224, 225]. Accordingly, effects of mechanical pressure, temperature, and moisture content (humidity or hydration) on the conductivities should be understood. In this thesis, it was shown that mechanical pressure did not have any significant effect on the conductivities, and effects of temperature were also studied in-depth. However, due to collapse of the microstructure in ex-situ hydration tests, studies on effects of hydration were limited to modeling heat conduction through hydrated CLs.

7.4.2. Future Opportunities

1. **Understanding effects of in-situ hydration on the microstructure as well as the conductivities:** It is particularly interesting to somehow take high-resolution images of a CL in an operating fuel cell while hydration occurs in-situ, to capture changes made in the microstructure by in-situ hydration. Studies of such effects on the conductivities (and other properties of CLs) would also be an attractive area of research.

2. **Understanding effects of cycling the operating conditions on the microstructure and the conductivities:** As discussed above, CLs undergo constant changes of pressure, temperature, and relative humidity/hydration in an automotive duty cycle. This necessitates understanding such cyclic effects on the properties of CLs.

7.5. Degradation

7.5.1. Challenges

As discussed in Chapter 1, different degradation mechanisms may occur in CLs, such as carbon corrosion [21, 22] and operational degradations [23-25], which may significantly affect the performance and lifetime of fuel cells.

7.5.2. Future Opportunities

1. **Including microstructural changes from different degradation mechanisms in the developed models in this thesis:** This will help understand effects of those mechanisms on the conductivities.
2. **Performing conductivity measurements on degraded samples, using the tools developed in this thesis:** This will help better understand degradation mechanisms and the underlying effects on the microstructure. It will also be beneficial for development of conductivity databases for degraded CLs (and even other layers of the MEA).

7.6. Microstructural Characterizations

7.6.1. Challenges

As discussed in section 3.3.3, the PSD results of this thesis for the baseline CL, acquired by analysis of TEM images, yielded a range of pore sizes which was different than the range reported in the literature [56, 64], acquired by N_2 adsorption porosimetry for similar CLs, yet the peak sizes were around the same value.

Further, the electronic conductivity measurements of Chapter 5 together with a literature review on microstructure of ionomer and its behavior under shear led to derivation of a model for distribution of ionomer around the Pt/C aggregates in CLs, which was introduced in Figure 5-12. However, this model was not concretely verified in this thesis.

7.6.2. Future Opportunities

1. **Conducting and comparing PSD measurements on CLs using different tools:** Such investigation should entail an in-depth analysis of the principles and underlying assumptions of the different measurement techniques, as well as determining applicability of each technique for different modeling/analysis purposes. Ideally, it would be beneficial to develop a unified/standard platform for PSD measurements to have consistency between data and analysis from different sources.
2. **Visualizing the ionomer in CLs and developing tools for such visualization:** This is a necessary step to determine the validity of the model proposed in Figure 5-12 and will help better understand the true

3D distribution of ionomer in CLs. A good starting point would be using soft X-ray spectro-tomography introduced in Ref. [147]. However, since the delicate structure of ionomer is very susceptible to be changed/damaged by high energy beams/irradiation during ex-situ characterizations, care should be taken to use/develop techniques which would not damage/change the ionomer in the CL.

7.7. Modeling and Optimization

7.7.1. Challenges

In this thesis, while modeling the conductivities, it was revealed through literature review that experimental data on various physical properties of Nafion were scarce or unavailable. Among the scarce/unavailable properties were: thermal conductivity, phonon mean free path, and phonon speed (sound speed) at different hydration levels and temperatures. Further, various physical properties of Aquivion were close to non-existent.

Modeling the carbon black particles revealed that, due to the very small size of the particles and experimental limitations, various physical properties of carbon blacks were also scarce in literature, which led to using graphite properties for the partially graphitized particles.

A preliminary modeling exercise by the author to solve the conjugate heat transfer problem in CLs showed that many physical properties needed for such studies were scarce or unavailable in the literature, including: permeability and internal convective heat transfer coefficient between the fluids and the solid matrix. Among the other unknown properties were volumetric distributions of hydrophobic/hydrophilic porosity and contact angle of water in CLs.

In this thesis, an order of magnitude analysis showed significance of low through-plane electronic conductivity of CLs for fuel cell performance. However, a detailed performance analysis was not performed. To enable a rigorous analysis, several knowledge gaps remain to be addressed, including measuring/modeling: i) protonic conductivity of CLs considering that their electronic conductivity may not be negligible in such measurements (as shown in this thesis), ii) thermal and electronic conductivities of CLs in operation (after the CLs undergo possible morphological changes induced by conditioning and in-situ hydration), iii) resistances of interconnects, and iv) contact resistances between the different layers. On the topic of contact resistances, specifically, the XPS measurements of this thesis showed a much higher I/C ratio (and, thus, a much higher ionomer coverage) on the decal side of a CL compared to its normal side, which means potentially different protonic/electronic contact resistances at the membrane-CL and CL-GDL interfaces in the actual fuel cell. This may have significant implications for the performance, as the normal side is the surface in contact with the membrane (after decal-transferring the CL onto the membrane), while the decal side is the surface in contact with the GDL. Ideally, it is probably more beneficial to have a more ionomer coverage on the normal side and less coverage on the decal side to have a lower protonic contact resistance at the membrane-CL interface and a lower electronic contact resistance at the CL-GDL interface. The XPS measurements of this thesis showed the opposite. Accordingly, measuring and modeling these protonic/electronic contact resistances is necessary for a rigorous analysis of the performance.

The measured conductivities in this thesis showed a great deal of variety in terms of orders of magnitude of the data and their relationships to different structural parameters of the CLs. The measured microstructural properties also varied significantly between the different CL designs. Further, trade-offs could be observed/predicted between the effects of different parameters on the transport properties, yet no performance modeling/optimization of a PEMFC was performed here.

The conductivity models of this thesis were developed and validated for CLs having partially graphitized carbon black particles. However, other types/structures of carbon support were not studied here.

7.7.2. Future Opportunities

1. **Characterizing various physical properties of state-of-the-art ionomers including Nafion and Aquivion:** As mentioned above, such data are needed for modeling purposes.
2. **Characterizing various physical properties of individual particles of carbon blacks:** As mentioned above, such data are needed for modeling purposes. Most of the data in the literature on carbon blacks

belong to powders of carbon blacks, and studies on individual particles are scarce.

3. **Characterizing internal convective heat transfer coefficient, permeability, and volumetric distributions of contact angle and hydrophilic porosity inside CLs:** As mentioned above, such data are needed for modeling the conjugate heat transfer inside CLs.

4. **Characterizing thermal and electronic conductivities of CLs after conditioning and in-situ hydration, protonic conductivity of CLs without neglecting their electronic resistance, and resistances of interconnects and contacts:** As mentioned above, such data are needed for a rigorous modeling of the fuel cell performance.

5. **Modeling effects of low through-plane electronic conductivity of CLs on fuel cell performance:** This could lead to a better understanding of the precise magnitude of the resultant voltage loss across the CLs. Assuming the CLs as interfaces or the classical/ballpark assumption of having a uniform current density through the CLs may fail for such modeling. Thus, a more sophisticated 3D modeling of the transport phenomena in the 3D structure of the CLs is needed here.

6. **Modeling the fuel cell performance while incorporating the conductivity models developed in this thesis for CLs:** Such a modeling will better reveal effects of different structural, compositional, and fabrication-related parameters of CLs on the performance. It will also enable further engineering/fine-tuning the CL microstructure for optimizing the performance.

7. **Extending the capability of the conductivity models developed in this thesis to include other types/structures of carbon support:** As new types/structures of carbon support (e.g., non-graphitized carbon blacks, carbon nanofibers, and carbon nanotubes) get developed for use in CLs, the conductivity models need to be adjusted for the new carbon types by modeling their specific structures. Two areas which would need adjustment/development would be the aggregate conductivity and the effective conductivity of the carbon support (see sections 6.5.4 and 6.6). Further adjustments may be necessary on other parts of the models, such as the shape/definition of catalyst bulk units (e.g., agglomerates) or even geometrical model of the whole CL. Clearly, in case of adjusting any part of the geometrical model, the relevant analytical expressions should be adjusted as well.

References

[1] M. M. Mench, *Fuel cell engines*. Hoboken: John Wiley & Sons, Inc., 2008.

[2] Y. Wang, K. S. Chen, J. Mishler, S. C. Cho, and X. C. Adroher, "A review of polymer electrolyte membrane fuel cells: technology, applications, and needs on fundamental research," *Applied Energy,* vol. 88, no. 4, pp. 981-1007, 2011.

[3] M. J. Lampinen and M. Fomino, "Analysis of free energy and entropy changes for half-cell reactions," *Journal of The Electrochemical Society,* vol. 140, no. 12, pp. 3537-3546, 1993.

[4] S. G. Kandlikar and Z. Lu, "Thermal management issues in a PEMFC stack–A brief review of current status," *Applied Thermal Engineering,* vol. 29, no. 7, pp. 1276-1280, 2009.

[5] M. Khandelwal and M. Mench, "Direct measurement of through-plane thermal conductivity and contact resistance in fuel cell materials," *Journal of Power Sources,* vol. 161, no. 2, pp. 1106-1115, 2006.

[6] M. Bhaiya, A. Putz, and M. Secanell, "Analysis of non-isothermal effects on polymer electrolyte fuel cell electrode assemblies," *Electrochimica Acta,* vol. 147, pp. 294-309, 2014.

[7] J. Wu *et al.*, "A review of PEM fuel cell durability: Degradation mechanisms and mitigation strategies," *Journal of Power Sources,* vol. 184, no. 1, pp. 104-119, 2008.

[8] K. Jiao and X. Li, "Cold start analysis of polymer electrolyte membrane fuel cells," *International Journal of Hydrogen Energy,* vol. 35, no. 10, pp. 5077-5094, 2010.

[9] K. Jiao and X. Li, "Effects of various operating and initial conditions on cold start performance of polymer electrolyte membrane fuel cells," *International Journal of Hydrogen Energy,* vol. 34, no. 19, pp. 8171-8184, 2009.

[10] K. Jiao and X. Li, "Three-dimensional multiphase modeling of cold start processes in polymer electrolyte membrane fuel cells," *Electrochimica Acta,* vol. 54, no. 27, pp. 6876-6891, 2009.

[11] M. Khandelwal, S. Lee, and M. Mench, "One-dimensional thermal model of cold-start in a polymer electrolyte fuel cell stack," *Journal of Power Sources,* vol. 172, no. 2, pp. 816-830, 2007.

[12] J. Yuan and B. Sundén, "On continuum models for heat transfer in micro/nano-scale porous structures relevant for fuel cells," *International Journal of Heat and Mass Transfer,* vol. 58, no. 1, pp. 441-456, 2013.

[13] O. S. Burheim, H. Su, H. H. Hauge, S. Pasupathi, and B. G. Pollet, "Study of thermal conductivity of PEM fuel cell catalyst layers," *International Journal of Hydrogen Energy,* vol. 39, no. 17, pp. 9397-9408, 2014.

[14] O. S. Burheim, "Review: PEMFC Materials' Thermal Conductivity and Influence on Internal Temperature Profiles," *ECS Transactions,* vol. 80, no. 8, pp. 509-525, 2017.

[15] V. Stanic, J. Braun, and M. Hoberecht, "Durability of membrane electrode assemblies (MEAs) in PEM fuel cells operated on pure hydrogen and oxygen," in *1st International Energy Conversion Engineering Conference (IECEC)*, 2003, p. 5965.

[16] W. H. J. Hogarth and J. B. Benziger, "Operation of polymer electrolyte membrane fuel cells with dry feeds: Design and operating strategies," *Journal of Power Sources,* vol. 159, no. 2, pp. 968-978, 2006.

[17] P. Rama, R. Chen, and J. Andrews, "A review of performance degradation and failure modes for hydrogen-fuelled polymer electrolyte fuel cells," *Proceedings of the Institution of Mechanical Engineers, Part A: Journal of Power and Energy,* vol. 222, no. 5, pp. 421-441, 2008.

[18] A. Tavassoli Kakhki, "Investigating the Local Membrane Degradation Mechanisms in PEM Fuel Cells," Master of Applied Science, Mechatronic Systems Engineering, Simon Fraser University, Simon Fraser University, 2014.

[19] J. Zhang *et al.*, "High temperature PEM fuel cells," *Journal of Power Sources,* vol. 160, no. 2, pp. 872-891, 2006.

[20] H. Wang, H. Li, and X.-Z. Yuan, *PEM fuel cell failure mode analysis*. Boca Raton: CRC Press, 2012.

[21] M. Baghalha, J. Stumper, D. Harvey, and M. Eikerling, "Modeling the effect of low carbon conductivity of the cathode catalyst layer on PEM fuel cell performance," *ECS Transactions,* vol. 28, no. 23, pp. 113-123, 2010.

[22] R. Sharma and S. M. Andersen, "Quantification on Degradation Mechanisms of Polymer Electrolyte Membrane Fuel Cell Catalyst Layers during an Accelerated Stress Test," *ACS Catalysis,* vol. 8, no. 4, pp. 3424-3434, 2018.

[23] A. Kusoglu, A. Kwong, K. T. Clark, H. P. Gunterman, and A. Z. Weber, "Water uptake of fuel-cell catalyst layers," *Journal of The Electrochemical Society,* vol. 159, no. 9, pp. F530-F535, 2012.

[24] T. Suzuki, H. Murata, T. Hatanaka, and Y. Morimoto, "Analysis of the catalyst layer of polymer electrolyte fuel cells," *R&D Rev. Toyota CRDL,* vol. 39, no. 3, pp. 33-38, 2003.

[25] S. Kundu, M. Fowler, L. Simon, and S. Grot, "Morphological features (defects) in fuel cell membrane electrode assemblies," *Journal of Power Sources,* vol. 157, no. 2, pp. 650-656, 2006.

[26] E. Sadeghi, M. Bahrami, and N. Djilali, "Analytic determination of the effective thermal conductivity of PEM fuel cell gas diffusion layers," *Journal of Power Sources,* vol. 179, no. 1, pp. 200-208, 2008.

[27] J. Ramousse, S. Didierjean, O. Lottin, and D. Maillet, "Estimation of the effective thermal conductivity of carbon felts used as PEMFC Gas Diffusion Layers," *International Journal of Thermal Sciences,* vol. 47, no. 1, pp. 1-6, 2008.

[28] E. Sadeghi, N. Djilali, and M. Bahrami, "Effective thermal conductivity and thermal contact resistance of gas diffusion layers in proton exchange membrane fuel cells. Part 2: Hysteresis effect under cyclic compressive load," *Journal of Power Sources,* vol. 195, no. 24, pp. 8104-8109, 2010.

[29] O. Burheim, P. Vie, J. Pharoah, and S. Kjelstrup, "Ex situ measurements of through-plane thermal conductivities in a polymer electrolyte fuel cell," *Journal of Power Sources,* vol. 195, no. 1, pp. 249-256, 2010.

[30] G. Karimi, X. Li, and P. Teertstra, "Measurement of through-plane effective thermal conductivity and contact resistance in PEM fuel cell diffusion media," *Electrochimica Acta,* vol. 55, no. 5, pp. 1619-1625, 2010.

[31] E. Sadeghi, N. Djilali, and M. Bahrami, "Effective thermal conductivity and thermal contact resistance of gas diffusion layers in proton exchange membrane fuel cells. Part 1: Effect of compressive load," *Journal of Power Sources,* vol. 196, no. 1, pp. 246-254, 2011.

[32] E. Sadeghi, N. Djilali, and M. Bahrami, "A novel approach to determine the in-plane thermal conductivity of gas diffusion layers in proton exchange membrane fuel cells," *Journal of Power Sources,* vol. 196, no. 7, pp. 3565-3571, 2011.

[33] N. Zamel, E. Litovsky, S. Shakhshir, X. Li, and J. Kleiman, "Measurement of in-plane thermal conductivity of carbon paper diffusion media in the temperature range of− 20° C to+ 120° C," *Applied Energy,* vol. 88, no. 9, pp. 3042-3050, 2011.

[34] O. S. Burheim, J. G. Pharoah, H. Lampert, P. J. Vie, and S. Kjelstrup, "Through-plane thermal conductivity of PEMFC porous transport layers," *Journal of Fuel Cell Science and Technology,* vol. 8, no. 2, p. 021013, 2011.

[35] H. Sadeghifar, M. Bahrami, and N. Djilali, "A statistically-based thermal conductivity model for fuel cell gas diffusion layers," *Journal of Power Sources,* vol. 233, pp. 369-379, 2013.

[36] N. Zamel and X. Li, "Effective transport properties for polymer electrolyte membrane fuel cells–with a focus on the gas diffusion layer," *Progress in Energy and Combustion Science,* vol. 39, no. 1, pp. 111-146, 2013.

[37] O. Burheim, G. Ellila, J. Fairweather, A. Labouriau, S. Kjelstrup, and J. Pharoah, "Ageing and thermal conductivity of porous transport layers used for PEM fuel cells," *Journal of Power Sources,* vol. 221, pp. 356-365, 2013.

[38] N. Alhazmi, M. Ismail, D. Ingham, K. Hughes, L. Ma, and M. Pourkashanian, "The in-plane thermal conductivity and the contact resistance of the components of the membrane electrode assembly in proton exchange membrane fuel cells," *Journal of Power Sources,* vol. 241, pp. 136-145, 2013.

[39] N. Alhazmi, D. Ingham, M. Ismail, K. Hughes, L. Ma, and M. Pourkashanian, "The through-plane thermal conductivity and the contact resistance of the components of the membrane electrode assembly and gas diffusion layer in proton exchange membrane fuel cells," *Journal of Power Sources,* vol. 270, pp. 59-67, 2014.

[40] H. Sadeghifar, N. Djilali, and M. Bahrami, "Effect of polytetrafluoroethylene (PTFE) and micro porous layer (MPL) on thermal conductivity of fuel cell gas diffusion layers: modeling and experiments," *Journal of Power Sources,* vol. 248, pp. 632-641, 2014.

[41] M. Ahadi, M. Andisheh-Tadbir, M. Tam, and M. Bahrami, "An improved transient plane source method for measuring thermal conductivity of thin films: Deconvoluting thermal contact resistance," *International Journal of Heat and Mass Transfer,* vol. 96, pp. 371-380, 2016.

[42] N. Zamel, J. Becker, and A. Wiegmann, "Estimating the thermal conductivity and diffusion coefficient of the microporous layer of polymer electrolyte membrane fuel cells," *Journal of Power Sources,* vol. 207, pp. 70-80, 2012.

[43] G. Unsworth, N. Zamel, and X. Li, "Through-plane thermal conductivity of the microporous layer in a polymer electrolyte membrane fuel cell," *International Journal of Hydrogen Energy,* vol. 37, no. 6, pp. 5161-5169, 2012.

[44] O. S. Burheim, H. Su, S. Pasupathi, J. G. Pharoah, and B. G. Pollet, "Thermal conductivity and temperature profiles of the micro porous layers used for the polymer electrolyte membrane fuel cell," *International Journal of Hydrogen Energy,* vol. 38, no. 20, pp. 8437-8447, 2013.

[45] A. Thomas, G. Maranzana, S. Didierjean, J. Dillet, and O. Lottin, "Thermal and water transfer in PEMFCs: Investigating the role of the microporous layer," *International Journal of Hydrogen Energy,* vol. 39, no. 6, pp. 2649-2658, 2014.

[46] M. Andisheh-Tadbir, E. Kjeang, and M. Bahrami, "Thermal conductivity of microporous layers: Analytical modeling and experimental validation," *Journal of Power Sources,* vol. 296, pp. 344-351, 2015.

[47] P. Gode, F. Jaouen, G. Lindbergh, A. Lundblad, and G. Sundholm, "Influence of the composition on the structure and electrochemical characteristics of the PEFC cathode," *Electrochimica Acta,* vol. 48, no. 28, pp. 4175-4187, 2003.

[48] D. R. Morris, S. P. Liu, D. Villegas Gonzalez, and J. T. Gostick, "Effect of water sorption on the electronic conductivity of porous polymer electrolyte membrane fuel cell catalyst layers," *ACS Applied Materials & Interfaces,* vol. 6, no. 21, pp. 18609-18618, 2014.

[49] C. Du, P. Shi, X. Cheng, and G. Yin, "Effective protonic and electronic conductivity of the catalyst layers in proton exchange membrane fuel cells," *Electrochemistry Communications,* vol. 6, no. 5, pp. 435-440, 2004.

[50] *ASTM E1530-11, " Standard test method for evaluating the resistance to thermal transmission of materials by the guarded heat flow meter technique"*, ASTM International, West Conshohocken, PA, 2011, www.astm.org.

[51] B. M. Zawilski, R. T. Littleton IV, and T. M. Tritt, "Description of the parallel thermal conductance technique for the measurement of the thermal conductivity of small diameter samples," *Review of Scientific Instruments,* vol. 72, no. 3, pp. 1770-1774, 2001.

[52] L. J. van der PAUW, "A method of measuring specific resistivity and Hall effect of discs of arbitrary shape," *Philips Research Reports,* vol. 13, pp. 1-9, 1958.

[53] K. More, R. Borup, and K. Reeves, "Identifying contributing degradation phenomena in PEM fuel cell membrane electrode assemblies via electron microscopy," *ECS Transactions,* vol. 3, no. 1, pp. 717-733, 2006.

[54] K. Malek, M. Eikerling, Q. Wang, T. Navessin, and Z. Liu, "Self-organization in catalyst layers of polymer electrolyte fuel cells," *The Journal of Physical Chemistry C,* vol. 111, no. 36, pp. 13627-13634, 2007.

[55] T. Sobolyeva, "On the microstructure of PEM fuel cell catalyst layers," PhD, Science: Department of Chemistry, Simon Fraser University, Vancouver, Canada, 2010.

[56] T. Soboleva, X. Zhao, K. Malek, Z. Xie, T. Navessin, and S. Holdcroft, "On the micro-, meso-, and macroporous structures of polymer electrolyte membrane fuel cell catalyst layers," *ACS Applied Materials & Interfaces,* vol. 2, no. 2, pp. 375-384, 2010.

[57] S. Holdcroft, "Fuel cell catalyst layers: a polymer science perspective," *Chemistry of Materials,* vol. 26, no. 1, pp. 381-393, 2013.

[58] D. Pantea, H. Darmstadt, S. Kaliaguine, L. Sümmchen, and C. Roy, "Electrical conductivity of thermal carbon blacks: Influence of surface chemistry," *Carbon,* vol. 39, no. 8, pp. 1147-1158, 2001.

[59] B. G. Pollet and J. T. E. Goh, "The importance of ultrasonic parameters in the preparation of fuel cell catalyst inks," *Electrochimica Acta,* vol. 128, pp. 292-303, 2014.

[60] M. Ahadi, M. Tam, M. S. Saha, J. Stumper, and M. Bahrami, "Thermal conductivity of catalyst layer of polymer electrolyte membrane fuel cells: Part 1–Experimental study," *Journal of Power Sources,* vol. 354, pp. 207-214, 2017.

[61] M. Sudan Saha, D. K. Paul, B. A. Peppley, and K. Karan, "Fabrication of catalyst-coated membrane by modified decal transfer technique," *Electrochemistry Communications,* vol. 12, pp. 410-413, 2010.

[62] C.-Y. Jung, W.-J. Kim, and S.-C. Yi, "Optimization of catalyst ink composition for the preparation of a membrane electrode assembly in a proton exchange membrane fuel cell using the decal transfer," *International Journal of Hydrogen Energy,* vol. 37, pp. 18446-18454, 2012.

[63] H. J. Cho *et al.*, "Development of a novel decal transfer process for fabrication of high-performance and reliable membrane electrode assemblies for PEMFCs," *International Journal of Hydrogen Energy,* vol. 36, pp. 12465-12473, 2011.

[64] T. Suzuki, S. Tsushima, and S. Hirai, "Effects of Nafion® ionomer and carbon particles on structure formation in a proton-exchange membrane fuel cell catalyst layer fabricated by the decal-transfer method," *International Journal of Hydrogen Energy,* vol. 36, pp. 12361-12369, 2011.

[65] J. A. Elliott, S. Hanna, A. M. S. Elliott, and G. E. Cooley, "The swelling behaviour of perfluorinated ionomer membranes in ethanol/water mixtures," *Polymer,* vol. 42, no. 5, pp. 2251-2253, 2001.

[66] A. Chertovich, P. G. Khalatur, and A. R. Khokhlov, "Computer Simulation Study of Model Nafion Membrane in Water/Methanol Solvent," *Composite Interfaces,* vol. 16, no. 4-6, pp. 547-577, 2009.

[67] J. Y. Huang, H. Yasuda, and H. Mori, "Highly curved carbon nanostructures produced by ball-milling," *Chemical Physics Letters,* vol. 303, pp. 130-134, 1999.

[68] Y. Chen, J. F. Gerald, L. T. Chadderton, and L. Chaffron, "Nanoporous carbon produced by ball milling," *Applied Physics Letters,* vol. 74, pp. 2782-2784, 1999.

[69] X. H. Chen *et al.*, "Generation of curved or closed-shell carbon nanostructures by ball-milling of graphite," *Journal of Crystal Growth,* vol. 218, pp. 57-61, 2000.

[70] Z. Q. Li, C. J. Lu, Z. P. Xia, Y. Zhou, and Z. Luo, "X-ray diffraction patterns of graphite and turbostratic carbon," *Carbon,* vol. 45, pp. 1686-1695, 2007.

[71] J. M. Yusof, M. A. M. Salleh, S. A. Rashid, I. Ismail, and S. N. Adam, "Characterisation of carbon particles (CPs) derived from dry milled kenaf biochar," *Journal of Engineering Science and Technology,* pp. 125-131, 2014.

[72] S. Zhang *et al.*, "Control of graphitization degree and defects of carbon blacks through ball-milling," *RSC Advances,* vol. 4, pp. 505-509, 2014.

[73] S. Li, S. Liu, Z. Fu, Q. Li, C. Wu, and W. Guo, "Surface modification and characterization of carbon black by sodium lignosulphonate," *Surface and Interface Analysis,* vol. 49, pp. 197-204, 2017.

[74] N. Hamran and A. A. Rashid, "Effect of combination ultrasonic and ball milling techniques of commercial fillers dispersion on mechanical properties of natural rubber (NR) latex films," in *AIP Conference Proceedings*, 2017, vol. 1865, p. 040011.

[75] D. Leistenschneider *et al.*, "Mechanochemical Functionalization of Carbon Black at Room Temperature," *C,* vol. 4, no. 1, p. 14, 2018.

[76] J.-L. Do and T. Friščić, "Mechanochemistry: A Force of Synthesis," *ACS Central Science,* vol. 3, no. 1, pp. 13-19, 2016.

[77] C. M. Long, M. A. Nascarella, and P. A. Valberg, "Carbon black vs. black carbon and other airborne materials containing elemental carbon: Physical and chemical distinctions," *Environmental Pollution,* vol. 181, pp. 271-286, 2013.

[78] C. A. Gray and H. Muranko, "Studies of robustness of industrial aciniform aggregates and agglomerates—carbon black and amorphous silicas: a review amplified by new data," *Journal of Occupational and Environmental Medicine,* vol. 48, pp. 1279-1290, 2006.

[79] *Carbon Black User's Guide: Safety, Health, & Environmental Information*. International Carbon Black Association (ICBA), 2006 (www.carbon-black.org).

[80] J. B. Donnet, R. C. Bansal, and M. J. Wang, *Carbon black: science and technology*, Second ed. New York: CRC Press, 1993.

[81] M. Uchida, Y. Aoyama, N. Eda, and A. Ohta, "Investigation of the microstructure in the catalyst layer and effects of both perfluorosulfonate ionomer and PTFE-loaded carbon on the catalyst layer of polymer electrolyte fuel cells," *Journal of The Electrochemical Society,* vol. 142, pp. 4143-4149, 1995.

[82] M. Uchida, Y. Fukuoka, Y. Sugawara, N. Eda, and A. Ohta, "Effects of microstructure of carbon support in the catalyst layer on the performance of polymer-electrolyte fuel cells," *Journal of The Electrochemical Society,* vol. 143, pp. 2245-2252, 1996.

[83] R. Fernandez, P. Ferreira-Aparicio, and L. Daza, "PEMFC electrode preparation: influence of the solvent composition and evaporation rate on the catalytic layer microstructure," *Journal of Power Sources,* vol. 151, pp. 18-24, 2005.

[84] H. M. Yu, C. Ziegler, M. Oszcipok, M. Zobel, and C. Hebling, "Hydrophilicity and hydrophobicity study of catalyst layers in proton exchange membrane fuel cells," *Electrochimica Acta,* vol. 51, pp. 1199-1207, 2006.

[85] P. P. Mukherjee and C. Y. Wang, "Stochastic microstructure reconstruction and direct numerical simulation of the PEFC catalyst layer," *Journal of The Electrochemical Society,* vol. 153, pp. A840-A849, 2006.

[86] Z. Yu and R. N. Carter, "Measurements of effective oxygen diffusivity, pore size distribution, and porosity in pem fuel cell electrodes," *ECS Transactions,* vol. 19, pp. 1-15, 2009.

[87] K. Malek, T. Mashio, and M. Eikerling, "Microstructure of catalyst layers in PEM fuel cells redefined: A computational approach," *Electrocatalysis,* vol. 2, pp. 141-157, 2011.

[88] H. Schulenburg *et al.*, "3D imaging of catalyst support corrosion in polymer electrolyte fuel cells," *Journal of Physical Chemistry C,* vol. 115, pp. 14236-14243, 2011.

[89] P. Dobson, C. Lei, T. Navessin, and M. Secanell, "Characterization of the PEM fuel cell catalyst layer microstructure by nonlinear least-squares parameter estimation," *Journal of The Electrochemical Society,* vol. 159, pp. B514-B523, 2012.

[90] Z. Yu, R. N. Carter, and J. Zhang, "Measurements of pore size distribution, porosity, effective oxygen diffusivity, and tortuosity of pem fuel cell electrodes," *Fuel Cells,* vol. 12, pp. 557-565, 2012.

[91] S. Ghosh, H. Ohashi, H. Tabata, Y. Hashimasa, and T. Yamaguchi, "Microstructural pore analysis of the catalyst layer in a polymer electrolyte membrane fuel cell: A combination of resin pore-filling and FIB/SEM," *International Journal of Hydrogen Energy,* vol. 40, pp. 15663-15671, 2015.

[92] M. Sabharwal, L. M. Pant, A. Putz, D. Susac, J. Jankovic, and M. Secanell, "Analysis of catalyst layer microstructures: from imaging to performance," *Fuel Cells,* vol. 16, pp. 734-753, 2016.

[93] M. S. Wilson and S. Gottesfeld, "High performance catalyzed membranes of ultra-low Pt loadings for polymer electrolyte fuel cells," *Journal of The Electrochemical Society,* vol. 139, pp. L28-L30, 1992.

[94] T. A. Zawodzinski, T. E. Springer, F. Uribe, and S. Gottesfeld, "Characterization of polymer electrolytes for fuel cell applications," *Solid State Ionics,* vol. 60, pp. 199-211, 1993.

[95] H. Tang, S. Wang, S. P. Jiang, and M. Pan, "A comparative study of CCM and hot-pressed MEAs for PEM fuel cells," *Journal of Power Sources,* vol. 170, pp. 140-144, 2007.

[96] M. Yazdanpour, A. Esmaeilifar, and S. Rowshanzamir, "Effects of hot pressing conditions on the performance of Nafion membranes coated by ink-jet printing of Pt/MWCNTs electrocatalyst for PEMFCs," *International Journal of Hydrogen Energy,* vol. 37, pp. 11290-11298, 2012.

[97] T. E. Springer, T. Zawodzinski, and S. Gottesfeld, "Polymer electrolyte fuel cell model," *Journal of The Electrochemical Society,* vol. 138, no. 8, pp. 2334-2342, 1991.

[98] T. E. Springer, M. S. Wilson, and S. Gottesfeld, "Modeling and experimental diagnostics in polymer electrolyte fuel cells," *Journal of The Electrochemical Society,* vol. 140, no. 12, pp. 3513-3526, 1993.

[99] C. Marr and X. Li, "Composition and performance modelling of catalyst layer in a proton exchange membrane fuel cell," *Journal of Power Sources,* vol. 77, no. 1, pp. 17-27, 1999.

[100] W. Sun, B. A. Peppley, and K. Karan, "An improved two-dimensional agglomerate cathode model to study the influence of catalyst layer structural parameters," *Electrochimica Acta,* vol. 50, no. 16, pp. 3359-3374, 2005.

[101] M. Srinivasarao, D. Bhattacharyya, R. Rengaswamy, and S. Narasimhan, "Performance analysis of a PEM fuel cell cathode with multiple catalyst layers," *International Journal of Hydrogen Energy,* vol. 35, no. 12, pp. 6356-6365, 2010.

[102] E. Sadeghi, A. Putz, and M. Eikerling, "Hierarchical model of reaction rate distributions and effectiveness factors in catalyst layers of polymer electrolyte fuel cells," *Journal of The Electrochemical Society,* vol. 160, no. 10, pp. F1159-F1169, 2013.

[103] M. Moore *et al.*, "Understanding the effect of kinetic and mass transport processes in cathode agglomerates," *Journal of The Electrochemical Society,* vol. 161, no. 8, pp. E3125-E3137, 2014.

[104] K. J. Lange, P.-C. Sui, and N. Djilali, "Pore scale simulation of transport and electrochemical reactions in reconstructed PEMFC catalyst layers," *Journal of The Electrochemical Society,* vol. 157, no. 10, pp. B1434-B1442, 2010.

[105] N. Siddique and F. Liu, "Process based reconstruction and simulation of a three-dimensional fuel cell catalyst layer," *Electrochimica Acta,* vol. 55, no. 19, pp. 5357-5366, 2010.

[106] C. Ziegler, S. Thiele, and R. Zengerle, "Direct three-dimensional reconstruction of a nanoporous catalyst layer for a polymer electrolyte fuel cell," *Journal of Power Sources,* vol. 196, no. 4, pp. 2094-2097, 2011.

[107] H. O. Pierson, *Handbook of carbon, graphite, diamonds and fullerenes: properties, processing and applications*. Noyes Publications, 1993.

[108] A. Voet and P. Aboytes, "Porosity of carbon blacks," *Carbon,* vol. 9, no. 2, pp. 135-138, 1971.

[109] J. Chen, D. J. Weidner, L. Wang, M. T. Vaughan, and C. E. Young, "Density measurements of molten materials at high pressure using synchrotron X-ray radiography: Melting volume of FeS," in *Advances in high-pressure technology for geophysical applications*: Elsevier, 2005, pp. 185-194.

[110] N. Stojilovic, "Why Can’t We See Hydrogen in X-ray Photoelectron Spectroscopy? ," *Journal of Chemical Education,* vol. 89, p. 1331−1332, 2012.

[111] *ASTM C177-13, " Standard test method for steady-state heat flux measurements and thermal transmission properties by means of the guarded-hot-plate apparatus"*, ASTM International, West Conshohocken, PA, 2013, www.astm.org.

[112] R. F. Speyer, *Thermal analysis of materials*. New York: Marcel Dekker, Inc., 1994.

[113] T. M. Tritt, *Thermal conductivity: theory, properties, and applications*. New York: Kluwer Academic / Plenum Publishers, 2004.

[114] *ASTM C1113 / C1113M-09, " Standard test method for thermal conductivity of refractories by hot wire (platinum resistance thermometer technique)"*, ASTM International, West Conshohocken, PA, 2013, www.astm.org.

[115] S. E. Gustafsson, "A non-steady-state method of measuring the thermal conductivity of transparent liquids," *Zeitschrift für Naturforschung A-A Journal of Physical Sciences,* vol. 22, no. 7, pp. 1005-1011, 1967.

[116] S. E. Gustafsson, E. Karawacki, and M. N. Khan, "Transient hot-strip method for simultaneously measuring thermal conductivity and thermal diffusivity of solids and fluids," *Journal of Physics D: Applied Physics,* vol. 12, no. 9, p. 1411, 1979.

[117] S. E. Gustafsson, E. Karawacki, and M. A. Chohan, "Thermal transport studies of electrically conducting materials using the transient hot-strip technique," *Journal of Physics D: Applied Physics,* vol. 19, no. 5, p. 727, 1986.

[118] S. E. Gustafsson, "Transient plane source techniques for thermal conductivity and thermal diffusivity measurements of solid materials," *Review of Scientific Instruments,* vol. 62, no. 3, pp. 797-804, 1991.

[119] M. Gustavsson, E. Karawacki, and S. E. Gustafsson, "Thermal conductivity, thermal diffusivity, and specific heat of thin samples from transient measurements with hot disk sensors," *Review of Scientific Instruments,* vol. 65, no. 12, pp. 3856-3859, 1994.

[120] *ISO22007-2, " Plastics-Determination of thermal conductivity and thermal diffusivity-Part 2: Transient plane heat source (hot disc) method"*, 2008, pp. 1-16.

[121] J. Gustavsson, M. Gustavsson, and S. Gustafsson, "On the use of the hot disk thermal constants analyser for measuring the thermal conductivity of thin samples of electrically insulating materials," in *24th International Thermal Conductivity Conference*, Lancaster, PA, 1999, vol. 24, pp. 116-122: Technomic Publishing Company, Inc.

[122] *ASTM E1461-13, " Standard test method for thermal diffusivity by the flash method"*, ASTM International, West Conshohocken, PA, 2013, www.astm.org.

[123] D. G. Cahill, "Thermal conductivity measurement from 30 to 750 K: the 3ω method," *Review of Scientific Instruments,* vol. 61, no. 2, pp. 802-808, 1990.

[124] D. G. Cahill, M. Katiyar, and J. Abelson, "Thermal conductivity of a-Si: H thin films," *Physical Review B,* vol. 50, no. 9, p. 6077, 1994.

[125] S. Govorkov, W. Ruderman, M. Horn, R. Goodman, and M. Rothschild, "A new method for measuring thermal conductivity of thin films," *Review of Scientific Instruments,* vol. 68, no. 10, pp. 3828-3834, 1997.

[126] G. Bennis, R. Vyas, R. Gupta, S. Ang, and W. Brown, "Thermal diffusivity measurement of solid materials by the pulsed photothermal displacement technique," *Journal of Applied Physics,* vol. 84, no. 7, pp. 3602-3610, 1998.

[127] V. Calzona, M. Cimberle, C. Ferdeghini, M. Putti, and A. Siri, "Fully automated apparatus for thermal diffusivity measurements on HTSC in high magnetic field," *Review of Scientific Instruments,* vol. 64, no. 3, pp. 766-773, 1993.

[128] M. Bahrami, M. Yovanovich, and J. Culham, "Thermal joint resistances of conforming rough surfaces with gas-filled gaps," *Journal of Thermophysics and Heat Transfer,* vol. 18, no. 3, pp. 318-325, 2004.

[129] M. Bahrami, J. Culham, and M. Yovanovich, "Modeling thermal contact resistance: a scale analysis approach," *Journal of Heat Transfer,* vol. 126, no. 6, pp. 896-905, 2004.

[130] J. Taylor, *Introduction to error analysis, the study of uncertainties in physical measurements*, Second ed. Sausalito: University Science Books, 1997.

[131] D. C. Montgomery and G. C. Runger, *Applied statistics and probability for engineers*, Third ed. New York: John Wiley & Sons, Inc., 2003.

[132] J. T. Gostick, M. W. Fowler, M. A. Ioannidis, M. D. Pritzker, Y. M. Volfkovich, and A. Sakars, "Capillary pressure and hydrophilic porosity in gas diffusion layers for polymer electrolyte fuel cells," *Journal of Power Sources,* vol. 156, pp. 375-387, 2006.

[133] D. W. Koon and C. J. Knickerbocker, "What do you measure when you measure resistivity?," *Review of Scientific Instruments,* vol. 63, no. 1, pp. 207-210, 1992.

[134] R. N. Bonifácio, J. O. A. Paschoal, M. Linardi, and R. Cuenca, "Catalyst layer optimization by surface tension control during ink formulation of membrane electrode assemblies in proton exchange membrane fuel cell," *Journal of Power Sources,* vol. 196, no. 10, pp. 4680-4685, 2011.

[135] L. Rubatat and O. Diat, "Stretching effect on Nafion fibrillar nanostructure," *Macromolecules,* vol. 40, pp. 9455-9462, 2007.

[136] P. C. Van der Heijden, L. Rubatat, and O. Diat, "Orientation of drawn Nafion at molecular and mesoscopic scales," *Macromolecules,* vol. 37, pp. 5327-5336, 2004.

[137] J. Li, K. G. Wilmsmeyer, and L. A. Madsen, "Hydrophilic channel alignment modes in perfluorosulfonate ionomers: Implications for proton transport," *Macromolecules,* vol. 41, pp. 4555-4557, 2008.

[138] N. Metatla, S. Palato, and A. Soldera, "Change in morphology of fuel cell membranes under shearing," *Soft Matter,* vol. 9, pp. 11093-11097, 2013.

[139] C. J. Jacobs, "Influence of catalyst ink mixing procedures on catalyst layer properties and in-situ PEMFC performance," Master of Science in Engineering, Department of Chemical Engineering, University of Cape Town, Cape Town, South Africa, 2016.

[140] L. Rubatat, G. Gebel, and O. Diat, "Fibrillar structure of Nafion: Matching Fourier and real space studies of corresponding films and solutions," *Macromolecules,* vol. 37, pp. 7772-7783, 2004.

[141] M. J. Park and N. P. Balsara, "Anisotropic proton conduction in aligned block copolymer electrolyte membranes at equilibrium with humid air," *Macromolecules,* vol. 43, no. 1, pp. 292-298, 2010.

[142] K. Schmidt-Rohr and Q. Chen, "Parallel cylindrical water nanochannels in Nafion fuel-cell membranes," *Nature Materials,* vol. 7, pp. 75-83, 2008.

[143] P. W. Majewski, M. Gopinadhan, W.-S. Jang, J. L. Lutkenhaus, and C. O. Osuji, "Anisotropic ionic conductivity in block copolymer membranes by magnetic field alignment," *Journal of the American Chemical Society,* vol. 132, no. 49, pp. 17516-17522, 2010.

[144] L. Li, "A characterization study on catalyst layers in proton exchange membrane fuel cells," PhD, Chemical Engineering, The University of Tennessee, Knoxville, 2016.

[145] M. Cimenti, D. Bessarabov, M. Tam, and J. Stumper, "Investigation of proton transport in the catalyst layer of PEM fuel cells by electrochemical impedance spectroscopy," *ECS transactions,* vol. 28, no. 23, pp. 147-157, 2010.

[146] M. C. Lefebvre, R. B. Martin, and P. G. Pickup, "Characterization of ionic conductivity profiles within proton exchange membrane fuel cell gas diffusion electrodes by impedance spectroscopy," *Electrochemical and Solid-State Letters,* vol. 2, no. 6, pp. 259-261, 1999.

[147] J. Wu *et al.*, "4D imaging of polymer electrolyte membrane fuel cell catalyst layers by soft X-ray spectro-tomography," *Journal of Power Sources,* vol. 381, pp. 72-83, 2018.

[148] D. M. Bernardi and M. W. Verbrugge, "A mathematical model of the solid-polymer-electrolyte fuel cell," *Journal of the Electrochemical Society,* vol. 139, no. 9, pp. 2477-2491, 1992.

[149] S. Um, C. Y. Wang, and K. S. Chen, "Computational fluid dynamics modeling of proton exchange membrane fuel cells," *Journal of the Electrochemical society,* vol. 147, no. 12, pp. 4485-4493, 2000.

[150] C. Boyer, S. Gamburzev, O. Velev, S. Srinivasan, and A. J. Appleby, "Measurements of proton conductivity in the active layer of PEM fuel cell gas diffusion electrodes," *Electrochimica Acta,* vol. 43, no. 24, pp. 3703-3709, 1998.

[151] K. Johnson, *Contact mechanics*. Cambridge: Cambridge University Press, 1985.

[152] R. M. Christensen, "A critical evaluation for a class of micro-mechanics models," *Journal of the Mechanics and Physics of Solids,* vol. 38, no. 3, pp. 379-404, 1990.

[153] K. Walton, "The effective elastic moduli of a random packing of spheres," *Journal of the Mechanics and Physics of Solids,* vol. 35, no. 2, pp. 213-226, 1987.

[154] W. Huang and L. Yu, "Serial symmetrical relocation algorithm for the equal sphere packing problem," 2012.

[155] B. V. Derjaguin, V. M. Muller, and Y. P. Toporov, "Effect of contact deformations on the adhesion of particles," *Journal of Colloid and Interface Science,* vol. 53, no. 2, pp. 314-326, 1975.

[156] M. Ahadi, A. Putz, J. Stumper, and M. Bahrami, "Thermal conductivity of catalyst layer of polymer electrolyte membrane fuel cells: Part 2–Analytical modeling," *Journal of Power Sources,* vol. 354, pp. 215–228, 2017.

[157] E. Sadeghi, A. Putz, and M. Eikerling, "Effects of ionomer coverage on agglomerate effectiveness in catalyst layers of polymer electrolyte fuel cells," *Journal of Solid State Electrochemistry,* vol. 18, no. 5, pp. 1271-1279, 2014.

[158] T. J. Silverman, J. P. Meyers, and J. J. Beaman, "Dynamic thermal, transport and mechanical model of fuel cell membrane swelling," *Fuel Cells,* vol. 11, no. 6, pp. 875-887, 2011.

[159] H. Wu, P. Berg, and X. Li, "Non-isothermal transient modeling of water transport in PEM fuel cells," *Journal of Power Sources,* vol. 165, no. 1, pp. 232-243, 2007.

[160] W. G. Kannuluik and E. H. Carman, "The temperature dependence of the thermal conductivity of air," *Australian Journal of Chemistry,* vol. 4, no. 3, pp. 305-314, 1951.

[161] C. O. Popiel and J. Wojtkowiak, "Simple Formulas for Thermophysical Properties of Liquid Water for Heat Transfer Calculations (from 0°C to 150°C)," *Heat Transfer Engineering,* vol. 19, no. 3, pp. 87-101, 1998.

[162] H. Fricke, "A mathematical treatment of the electric conductivity and capacity of disperse systems-I. The electric conductivity of a suspension of homogeneous spheroids," *Physical Review,* vol. 24, pp. 575-587, 1924.

[163] D. P. H. Hasselman, "Effect of cracks on thermal conductivity," *Journal of Composite Materials,* vol. 12, pp. 403-407, 1978.

[164] H. Carslaw and J. Jaeger, *Conduction of heat in solids*, Second ed. Oxford: Clarendon Press, 1959.

[165] Y. Ogniewicz and M. Yovanovich, "Effective conductivity of regularly packed spheres: basic cell model with constriction," *Heat Transfer and Thermal Control Systems, Progress in Astronautics and Aeronautics,* vol. 60, 1978.

[166] M. M. Yovanovich, "Thermal contact correlations," in *AIAA 16th Thermophysics Conference*, Palo Alto, Calif., 1981, vol. 83, pp. 83-95, New York: American institute of Aeronautics and Astronautics, Inc., 1982.

[167] M. Bahrami, M. Yovanovich, and J. Culham, "Thermal joint resistances of nonconforming rough surfaces with gas-filled gaps," *Journal of Thermophysics and Heat Transfer,* vol. 18, no. 3, pp. 326-332, 2004.

[168] T. L. Bergman, F. P. Incropera, D. P. DeWitt, and A. S. Lavine, *Fundamentals of heat and mass transfer*, 7th ed. John Wiley & Sons, 2011.

[169] S. G. Jennings, "The mean free path in air," *Journal of Aerosol Science,* vol. 19, pp. 159-166, 1988.

[170] G. Röpke and G. Rpke, *Nonequilibrium Statistical Physics*. Somerset, GERMANY: John Wiley & Sons, Incorporated, 2013.

[171] F. H. Stillinger, "Theory and molecular models for water," *Advances in Chemical Physics: Non-Simple Liquids,* vol. 31, pp. 1-101, 1975.

[172] Y. Huang *et al.*, "Size, separation, structural order, and mass density of molecules packing in water and ice," *Scientific Reports,* vol. 3, p. 3005, 2013.

[173] C. K. Chan and C. L. Tien, "Conductance of packed spheres in vacuum," *Journal of Heat Transfer,* vol. 95, no. 3, pp. 302-308, 1973.

[174] Z. M. Zhang, *Nano/microscale Heat Transfer*, First ed. (McGraw-Hill Nanoscience and Technology Series). New York, NY: McGraw-Hill, 2007.

[175] K. A. Mauritz and R. B. Moore, "State of understanding of Nafion," *Chemical Reviews,* vol. 104, no. 10, pp. 4535-4585, 2004.

[176] T. F. Fuller, "Solid-polymer-electrolyte fuel cells," Ph.D., Department of Chemical Engineering, University of California, Berkeley, California, 1992.

[177] G. S. Hwang, D. Y. Parkinson, A. Kusoglu, A. A. MacDowell, and A. Z. Weber, "Understanding water uptake and transport in nafion using x-ray microtomography," *ACS Macro Letters,* vol. 2, no. 4, pp. 288-291, 2013.

[178] Z. Siroma, R. Kakitsubo, N. Fujiwara, T. Ioroi, S.-i. Yamazaki, and K. Yasuda, "Depression of proton conductivity in recast Nafion® film measured on flat substrate," *Journal of Power Sources,* vol. 189, no. 2, pp. 994-998, 2009.

[179] D. K. Paul, A. Fraser, and K. Karan, "Towards the understanding of proton conduction mechanism in PEMFC catalyst layer: Conductivity of adsorbed Nafion films," *Electrochemistry Communications,* vol. 13, no. 8, pp. 774-777, 2011.

[180] D. K. Paul, K. Karan, A. Docoslis, J. B. Giorgi, and J. Pearce, "Characteristics of self-assembled ultrathin Nafion films," *Macromolecules,* vol. 46, no. 9, pp. 3461-3475, 2013.

[181] Q. He, N. S. Suraweera, D. C. Joy, and D. J. Keffer, "Structure of the ionomer film in catalyst layers of proton exchange membrane fuel cells," *The Journal of Physical Chemistry C,* vol. 117, no. 48, pp. 25305-25316, 2013.

[182] M. J. Park *et al.*, "Increased water retention in polymer electrolyte membranes at elevated temperatures assisted by capillary condensation," *Nano Letters,* vol. 7, no. 11, pp. 3547-3552, 2007.

[183] Q. He, D. C. Joy, and D. J. Keffer, "Impact of oxidation on nanoparticle adhesion to carbon substrates," *RSC Advances,* vol. 3, no. 36, pp. 15792-15804, 2013.

[184] Q. He, D. C. Joy, and D. J. Keffer, "Nanoparticle adhesion in proton exchange membrane fuel cell electrodes," *Journal of Power Sources,* vol. 241, pp. 634-646, 2013.

[185] A. Kusoglu, T. J. Dursch, and A. Z. Weber, "Nanostructure/Swelling Relationships of Bulk and Thin-Film PFSA Ionomers," *Advanced Functional Materials,* vol. 26, no. 27, pp. 4961-4975, 2016.

[186] J. Blumm, A. Lindemann, M. Meyer, and C. Strasser, "Characterization of PTFE using advanced thermal analysis techniques," *International Journal of Thermophysics,* vol. 31, no. 10, pp. 1919-1927, 2010.

[187] M. Plazanet, P. Bartolini, R. Torre, C. Petrillo, and F. Sacchetti, "Structure and acoustic properties of hydrated nafion membranes," *The Journal of Physical Chemistry B,* vol. 113, no. 30, pp. 10121-10127, 2009.

[188] M. Wang and N. Pan, "Predictions of effective physical properties of complex multiphase materials," *Materials Science and Engineering: R: Reports,* vol. 63, no. 1, pp. 1-30, 2008.

[189] R. Taylor, "The thermal conductivity of pyrolytic graphite," *Philosophical Magazine,* vol. 13, no. 121, pp. 157-166, 1966.

[190] A. K. Dutta, "Electrical conductivity of single crystals of graphite," *Physical Review,* vol. 90, no. 2, pp. 187-192, 1953.

[191] D. Deming, "Estimation of the thermal conductivity anisotropy of rock with application to the determination of terrestrial heat flow," *Journal of Geophysical Research: Solid Earth,* vol. 99, no. B11, pp. 22087-22091, 1994.

[192] D. Pribnow and T. Umsonst, "Estimation of thermal conductivity from the mineral composition: Influence of fabric and anisotropy," *Geophysical Research Letters,* vol. 20, no. 20, pp. 2199-2202, 1993.

[193] S. Fuchs, F. Schütz, H.-J. Förster, and A. Förster, "Evaluation of common mixing models for calculating bulk thermal conductivity of sedimentary rocks: correction charts and new conversion equations," *Geothermics,* vol. 47, pp. 40-52, 2013.

[194] D. Fournier, M. Marangolo, M. Eddrief, N. Kolesnikov, and C. Fretigny, "Straightforward measurement of thermal properties of anisotropic materials: the case of Bi2Se3 single crystal," *arXiv:1710.09456 [cond-mat.mtrl-sci],* pp. 1-10, 2017.

[195] K. Midttømme, E. Roaldset, and P. Aagaard, "Thermal conductivity of selected claystones and mudstones from England," *Clay Minerals,* vol. 33, no. 1, pp. 131-145, 1998.

[196] T. Ohmura, M. Tsuboi, and T. Tomimura, "Estimation of the mean thermal conductivity of anisotropic materials," *International Journal of Thermophysics,* vol. 23, no. 3, pp. 843-853, 2002.

[197] L. Ray, H.-J. Förster, A. Förster, S. Fuchs, R. Naumann, and O. Appelt, "Tracking the thermal properties of the lower continental crust: Measured versus calculated thermal conductivity of high-grade metamorphic rocks (Southern Granulite Province, India)," *Geothermics,* vol. 55, pp. 138-149, 2015.

[198] G. A. Slack, "Anisotropic thermal conductivity of pyrolytic graphite," *Physical Review,* vol. 127, no. 3, pp. 694-701, 1962.

[199] C. A. Klein, "Electrical properties of pyrolytic graphites," *Reviews of Modern Physics,* vol. 34, no. 1, pp. 56-79, 1962.

[200] C. N. Hooker, A. R. Ubbelohde, and D. A. Young, "Anisotropy of thermal conductance in near-ideal graphite," *Proceedings of the Royal Society of London. Series A,* vol. 284, no. 1396, pp. 17-31, 1965.

[201] M. G. Holland, C. A. Klein, and W. D. Straub, "The lorenz number of graphite at very low temperatures," *Journal of Physics and Chemistry of Solids,* vol. 27, no. 5, pp. 903-906, 1966.

[202] J. Pappis and S. L. Blum, "Properties of pyrolytic graphite," *Journal of the American Ceramic Society,* vol. 44, no. 12, pp. 592-597, 1961.

[203] A. W. Moore, A. R. Ubbelohde, and D. A. Young, "Stress recrystallization of pyrolytic graphite," *Proceedings of the Royal Society of London. Series A,* vol. 280, no. 1381, pp. 153-169, 1964.

[204] M. R. Null, W. W. Lozier, and A. W. Moore, "Thermal diffusivity and thermal conductivity of pyrolytic graphite from 300 to 2700 K," *Carbon,* vol. 11, no. 2, pp. 81-87, 1973.

[205] C. A. Klein and M. G. Holland, "Thermal conductivity of pyrolytic graphite at low temperatures. I. Turbostratic structures," *Physical Review,* vol. 136, no. 2A, pp. A575-A590, 1964.

[206] A. W. Smith and N. S. Rasor, "Observed dependence of the low-temperature thermal and electrical conductivity of graphite on temperature, type, neutron irradiation, and bromination," *Physical Review,* vol. 104, no. 4, pp. 885-891, 1956.

[207] P. Wagner, J. A. O'rourke, and P. E. Armstrong, "Porosity effects in polycrystalline graphite," *Journal of the American Ceramic Society,* vol. 55, no. 4, pp. 214-219, 1972.

[208] Q. Fu, J. Yang, Y. Chen, D. Li, and D. Xu, "Experimental evidence of very long intrinsic phonon mean free path along the c-axis of graphite," *Applied Physics Letters,* vol. 106, no. 3, p. 031905, 2015.

[209] Z. Wei, J. Yang, W. Chen, K. Bi, D. Li, and Y. Chen, "Phonon mean free path of graphite along the c-axis," *Applied Physics Letters,* vol. 104, no. 8, p. 081903, 2014.

[210] H. Zhang, X. Chen, Y.-D. Jho, and A. J. Minnich, "Temperature-dependent mean free path spectra of thermal phonons along the c-axis of graphite," *Nano Letters,* vol. 16, no. 3, pp. 1643-1649, 2016.

[211] N. García, P. Esquinazi, J. Barzola-Quiquia, B. Ming, and D. Spoddig, "Transition from ohmic to ballistic transport in oriented graphite: Measurements and numerical simulations," *Physical Review B,* vol. 78, no. 3, p. 035413, 2008.

[212] C. Borgnakke and R. E. Sonntag, *Fundamentals of thermodynamics*, 7th ed. Hoboken: John Wiley & Sons, Inc., 2009.

[213] D. Malevich, V. Zamlynny, S.-G. Sun, and J. Lipkowski, "In situ infrared reflection absorption spectroscopy studies of the interaction of Nafion® with the Pt electrode surface," *Zeitschrift für Physikalische Chemie,* vol. 217, no. 5, pp. 513-526, 2003.

[214] R. Subbaraman, D. Strmcnik, V. Stamenkovic, and N. M. Markovic, "Three phase interfaces at electrified metal− solid electrolyte systems 1. Study of the Pt (hkl)− Nafion interface," *Journal of Physical Chemistry C,* vol. 114, no. 18, pp. 8414-8422, 2010.

[215] S. K. Das and A. S. Bansode, "Heat and mass transport in proton exchange membrane fuel cells—a review," *Heat Transfer Engineering,* vol. 30, no. 9, pp. 691-719, 2009.

[216] Y. Sone, P. Ekdunge, and D. Simonsson, "Proton conductivity of Nafion 117 as measured by a four-electrode AC impedance method," *Journal of The Electrochemical Society,* vol. 143, no. 4, pp. 1254-1259, 1996.

[217] Q. Wang *et al.*, "Functionally graded cathode catalyst layers for polymer electrolyte fuel cells I. theoretical modeling," *Journal of the Electrochemical Society,* vol. 151, no. 7, pp. A950-A957, 2004.

[218] D. Song, Q. Wang, Z. Liu, T. Navessin, M. Eikerling, and S. Holdcroft, "Numerical optimization study of the catalyst layer of PEM fuel cell cathode," *Journal of Power Sources,* vol. 126, no. 1-2, pp. 104-111, 2004.

[219] O. S. Burheim and J. G. Pharoah, "A review of the curious case of heat transport in polymer electrolyte fuel cells and the need for more characterisation," *Current Opinion in Electrochemistry,* vol. 5, no. 1, pp. 36-42, 2017.

[220] Y. Tang, M. H. Santare, A. M. Karlsson, S. Cleghorn, and W. B. Johnson, "Stresses in proton exchange membranes due to hygro-thermal loading," *Journal of Fuel Cell Science and Technology,* vol. 3, no. 2, pp. 119-124, 2006.

[221] R. Solasi, Y. Zou, X. Huang, K. Reifsnider, and D. Condit, "On mechanical behavior and in-plane modeling of constrained PEM fuel cell membranes subjected to hydration and temperature cycles," *Journal of Power Sources,* vol. 167, no. 2, pp. 366-377, 2007.

[222] A. Kusoglu, A. M. Karlsson, M. H. Santare, S. Cleghorn, and W. B. Johnson, "Mechanical response of fuel cell membranes subjected to a hygro-thermal cycle," *Journal of Power Sources,* vol. 161, no. 2, pp. 987-996, 2006.

[223] M. A. R. S. Al-Baghdadi, "A CFD study of hygro–thermal stresses distribution in PEM fuel cell during regular cell operation," *Renewable Energy,* vol. 34, no. 3, pp. 674-682, 2009.

[224] A. Kusoglu, A. M. Karlsson, M. H. Santare, S. Cleghorn, and W. B. Johnson, "Mechanical behavior of fuel cell membranes under humidity cycles and effect of swelling anisotropy on the fatigue stresses," *Journal of Power Sources,* vol. 170, no. 2, pp. 345-358, 2007.

[225] Y. Tang, A. M. Karlsson, M. H. Santare, M. Gilbert, S. Cleghorn, and W. B. Johnson, "An experimental investigation of humidity and temperature effects on the mechanical properties of perfluorosulfonic acid membrane," *Materials Science and Engineering: A,* vol. 425, no. 1-2, pp. 297-304, 2006.

Appendix A.

Geometrical Relations for Agglomerates and Pt/C Aggregates inside the Agglomerates

The following relations hold for geometrical parameters of the agglomerates and Pt/C aggregates (see Figure A-1):

$$a_{\mathrm{agg}} = r_{\mathrm{agg}} \sin\left(\theta_{\mathrm{agg}}/2\right) \tag{A.1}$$

$$\omega_{\mathrm{agg}} = r_{\mathrm{agg}} \left(1 - \cos\left(\theta_{\mathrm{agg}}/2\right)\right) \tag{A.2}$$

$$r_{\mathrm{aggl}} = r_{\mathrm{agg}} + \psi h_{\mathrm{ion}} \tag{A.3}$$

$$\omega_{\mathrm{aggl}} = \omega_{\mathrm{agg}} + \psi h_{\mathrm{ion}} \tag{A.4}$$

$$a_{\mathrm{aggl}} = \sqrt{r_{\mathrm{aggl}}^2 - \left(r_{\mathrm{aggl}} - \omega_{\mathrm{aggl}}\right)^2} \tag{A.5}$$

$$\theta_{\mathrm{aggl}} = 2\sin^{-1}\left(a_{\mathrm{aggl}}/r_{\mathrm{aggl}}\right) \tag{A.6}$$

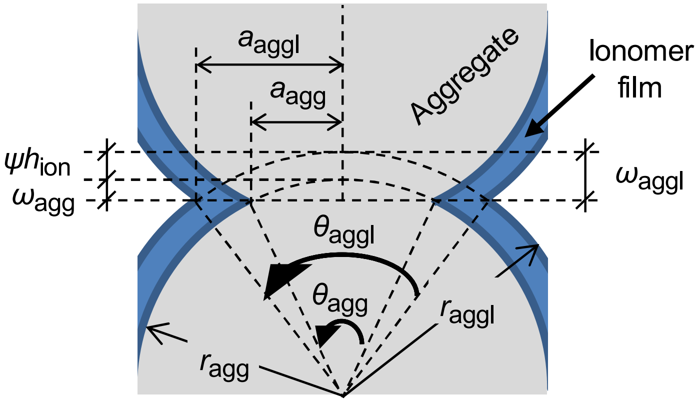

Figure A-1. Geometrical parameters of the agglomerates and Pt/C aggregates, shown in a mesoscale unit cell

It should be noted that because surface of an aggregate may not be fully covered by ionomer, ψ is used in Eqs. (A.3) and (A.4) to scale h_{ion} and find the effective values of r_{aggl} and ω_{aggl}, as if $\psi = 1$ and the surface of the aggregate was fully covered by ionomer (see Eqs. (6.27) and (6.42)).

Appendix B.

Challenges Faced in Measurements of CL Thickness by SEM

Standard Sample Preparation Procedure at AFCC for Thickness Measurements by SEM

The standard sample preparation procedure at AFCC for measuring the CL thickness by SEM was epoxy embedding. In this method, samples were first stacked together with some GDLs and plastic films in between to give the stack mechanical stability. The stack was then clamped using plastic or metal clamps to prevent the samples from movement during handling, and the clamped stack was then placed inside a mold, whose inside surfaces were covered by a release agent. Then, the mixture of epoxy and epoxy-hardener was poured into the mold to fill the gaps within the stack and between the stack and the mold. To ensure uniformity and clarity of the epoxy, which was necessary for taking high quality images, the mold was placed inside a desiccator chamber attached to a vacuum pump to remove air bubbles from the epoxy before curing. Air bubble removal was performed in the following successive steps:

i) The pump was turned on and left on for ~3 min to extract the large air bubbles form the epoxy, which would then gather as a layer of foam on the surface of the epoxy, and then turned off while letting air get into the chamber to burst the large bubbles on the surface.

ii) The pump was turned on and left on for ~1 min to remove the small air bubbles from the epoxy and then turned off while letting air get into the chamber to burst the small bubbles.

iii) Step (ii) was repeated as many times as needed to ensure complete removal of the air bubbles from the epoxy.

The mold was then removed from the chamber and placed and kept inside a fume hood for at least ~12 hr to cure the epoxy. Afterwards, the cured epoxy was removed from the mold and polished in successive steps. First, both surfaces of the epoxy puck were polished by a lapping machine using a coarse-grit polishing pad to ensure evenness of the surfaces for placement inside the SEM device. Then, the samples' cross-section side was polished several times by the lapping machine using polishing pads with different grit sizes, from coarse grits to very soft grits, to remove the thick layer of epoxy above the samples' cross sections, which would hinder their detection by the SEM electron beam. At the end, the polished surface was rubbed on a polishing cloth covered by a mixture of water and fine-grit diamond paste for optimal polishing and exposure of the samples' cross sections to the electron beam, which was repeated until the polished surface acquired a highly glassy appearance such that the samples' cross sections could be observed clearly under a typical low-mag optical microscope. Water was applied on the polishing pads/cloth during all steps of polishing to remove the generated heat and chips and facilitate polishing by reducing the friction. In the next step, the polished surface was carbon-coated using a sputtering device, and then both surfaces of the epoxy (i.e., the polished top surface and the bottom surface sitting on the sample holder inside the SEM device) were attached together by a copper tape to provide an electron conduction path from the imaging surface to the SEM device. This was necessary to prevent charging effects by the electron beam, which would deteriorate the image quality. The electron conduction path was completed by applying small amounts of carbon paste at two points on the tape and epoxy along the connection of the tape to the carbon-coated surface of the epoxy. An SEM sample puck, made in this way, is shown in Figure B-1. As shown later in this section, this standard method, however, proved to be very tricky and prone to systematic errors, depending on the type of substrate used for the CLs, because of the several polishing steps involved.

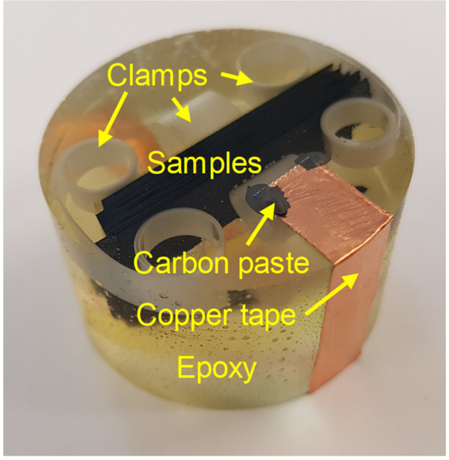

Figure B-1. A polished carbon-coated epoxy puck containing samples

Calibration of the SEM Device

Before doing any measurements, calibration of the ESEM device at AFCC was checked by measuring a standard SEM calibration sample. This calibration sample was a silicon wafer chip having an array of rectangles cut onto its surface, whose horizontal and vertical pitch had to be measured at 10 μm for a prefect calibration. SEM images, taken from the calibration sample by the secondary electron (SE) and backscattered electron (BSE) detectors of the ESEM device at different beam energies, are shown in Figure B-2; the images indicate a perfect calibration of the device.

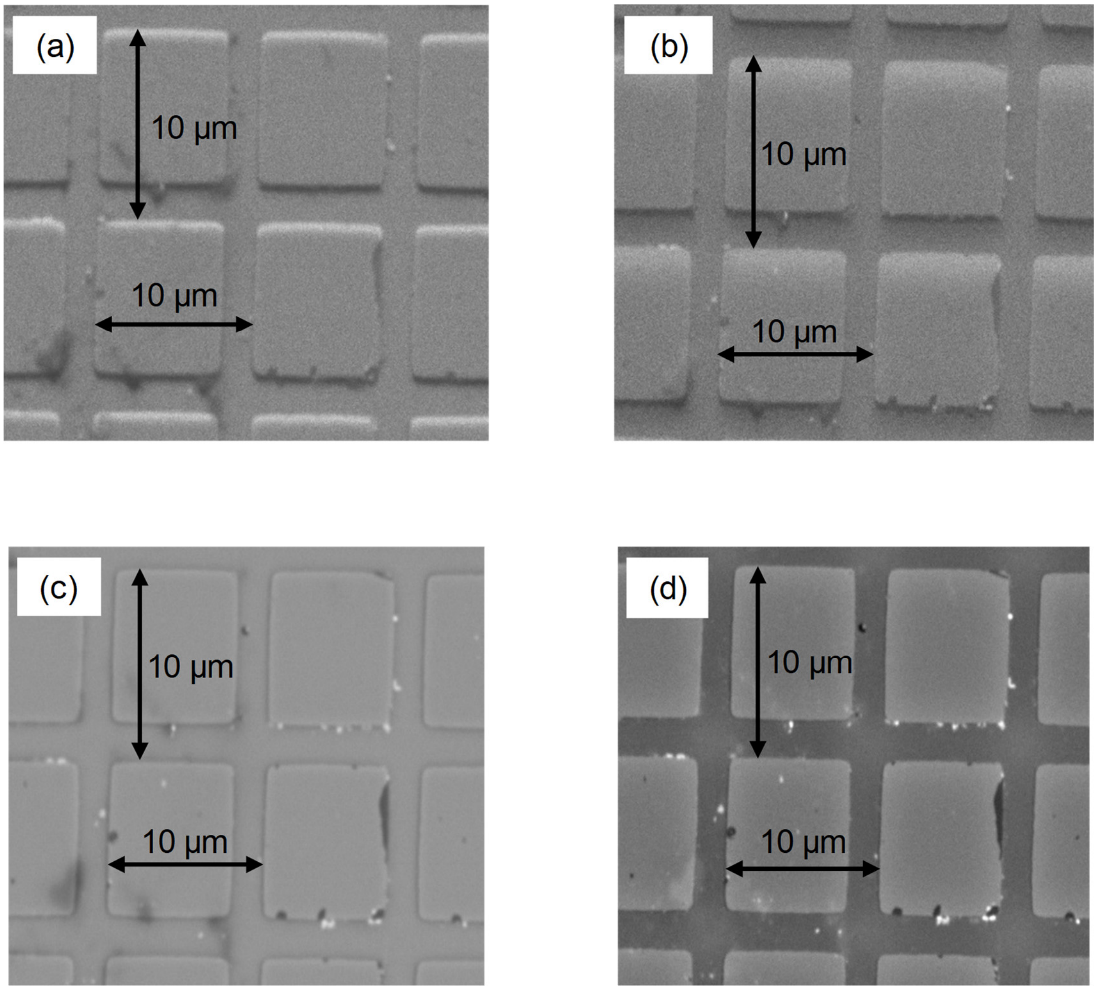

Figure B-2. SEM images of the SEM standard calibration sample by: (a) SE mode at 5 keV, (b) SE mode at 20 keV, (c) BSE mode at 5 keV, and (d) BSE mode at 20 keV, showing perfect calibration of the ESEM device at different SEM imaging parameters

Sensitivity of Thickness Measurements to SEM Imaging Parameters

Before measuring thickness of CLs, which could not be made as standalone layers and had to be coated on substrates, effort was made first to measure thicknesses of standalone layers of other materials by SEM and confirm those measurements by the known nominal thicknesses provided by the suppliers. For this purpose, thicknesses of Nafion films, made in-house at AFCC in nominal thicknesses of 10, 15, 25, and 50 µm, and ETFE sheets, received from Asahi Glass Co. in nominal thicknesses of 10, 25, and 100 µm, were measured by the ESEM device at AFCC using the standard epoxy-embedding sample preparation procedure described above. As shown in Table B-1, consistently higher thicknesses were measured compared to the nominal thicknesses such that the differences between the measured thicknesses and the nominal thicknesses were considerable when compared to the µm scale of CL thickness (could be as large as thickness of a CL). For this reason, two paths were taken to investigate the reasons:

i) Measuring the materials' thicknesses under different SEM imaging parameters, including different beam energies and different numbers of carbon layers coated on the epoxy sample puck, to understand the effects of the imaging parameters on the measurements;

ii) Measuring the materials' thicknesses, including aluminum (Al) foils, by various instruments, including the TUC_RUC device at AFCC performing the thickness measurements mechanically, two other SEM devices at SFU 4D LABS with the names of Explorer (an ESEM device) and Helios (a high-resolution SEM), and a high resolution optical microscope at SFU 4D LABS, to understand the effects of using different instruments and thickness measurement techniques.

Sample images taken from the 25 µm thick Nafion membrane by the different devices are shown in Figure B-3 and indicate measurements of higher thicknesses than the nominal thickness as well as harder detection of the sample's cross section by the optical microscope compared to SEM due to the carbon coating on top. Results of different SEM imaging parameters and measurement devices/techniques are shown in Table B-2 and Table B-3, respectively. The empty cells for some samples in Table B-3 are due to inability of the optical microscope in detecting cross sections of those samples, which were buried under three layers of carbon coating. As shown in Table B-2, SEM imaging parameters had no effect on the SEM thicknesses. Further, Table B-3 shows that except for the TUC_RUC device, whose measurements were in good agreement with the nominal thicknesses, measurements by the other methods were all considerably off from the nominal thicknesses but in good agreement with themselves. Considering that no sample preparation was used for the TUC_RUC measurements while the epoxy-embedding sample preparation was used for other methods, the epoxy-embedding sample preparation method was recognized as the main source of difference and discrepancy between the different measurements. Accordingly, a hypothesis was formed to explain possible effects of the epoxy-embedding sample preparation process on the thickness measurements. In the next section, this hypothesis is explained.

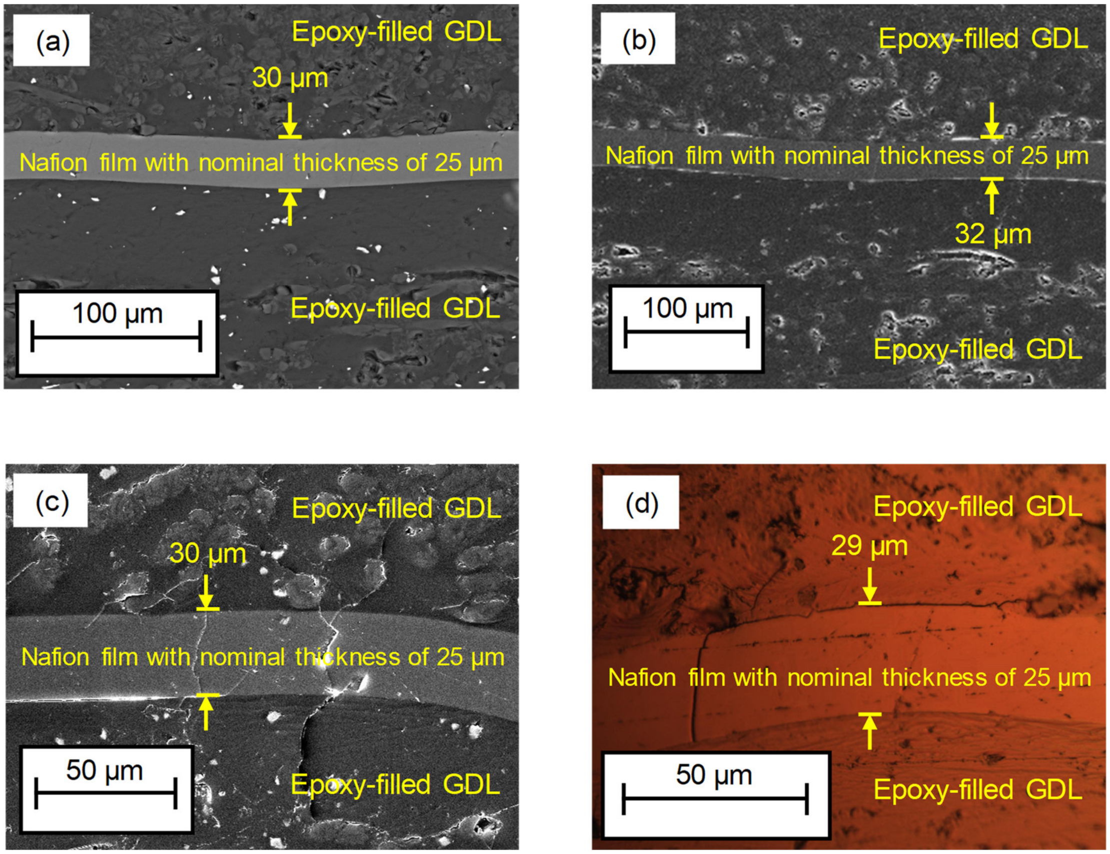

Figure B-3. Sample images of a Nafion membrane with a nominal thickness of 25 µm taken by various instruments, showing measurements of higher thicknesses than the nominal value by different instruments and techniques: (a) ESEM device at AFCC, (b) Explorer ESEM device at SFU 4D LABS, (c) Helios high resolution SEM device at SFU 4D LABS, and (d) a high resolution optical microscope at SFU 4D LABS

Table B-1. **Thickness measurements by the ESEM device at AFCC for Nafion and ETFE films with different nominal thicknesses (errors: STDs)**

Sample / Nominal thickness	Measured thickness (µm)	Difference between the thicknesses (µm)	% difference between the thicknesses
Nafion / 10 µm	12 ± 2	~ 2	~ 20 %
Nafion / 15 µm	18.4 ± 0.4	~ 3	~ 20 %
Nafion / 25 µm	30 ± 1	~ 5	~ 20 %
Nafion / 50 µm	52 ± 1	~ 2	~ 4 %
ETFE / 12 µm	17.0 ± 0.6	~ 5	~ 42 %
ETFE / 25 µm	29.7 ± 0.7	~ 5	~ 20 %
ETFE / 100 µm	106.6 ± 0.6	~ 7	~ 7 %

Table B-2. **Thickness measurements by the ESEM device at AFCC for Nafion and ETFE films with different nominal thicknesses using different SEM imaging parameters (errors: STDs)**

Sample / Nominal thickness	Measured thickness (µm)			
	1 layer of carbon coating, 20 keV	3 layers of carbon coating		
		10 keV	15 keV	20 keV
Nafion / 10 µm	12 ± 2	11 ± 1	11 ± 1	11 ± 2
Nafion / 15 µm	18.4 ± 0.4	18 ± 1	19 ± 1	18 ± 1
Nafion / 25 µm	30 ± 1	29 ± 1	29.9 ± 0.6	29.2 ± 0.5
Nafion / 50 µm	52 ± 1	51.8 ± 0.7	51.3 ± 0.6	51.8 ± 0.8
ETFE / 12 µm	17.0 ± 0.6	17.2 ± 0.8	16.8 ± 0.5	16.6 ± 0.4
ETFE / 25 µm	29.7 ± 0.7	29.9 ± 0.4	30.0 ± 0.8	30.1 ± 0.5
ETFE / 100 µm	106.6 ± 0.6	107 ± 1	108 ± 1	107.0 ± 0.7

Table B-3. **Thickness measurements by different devices/methods for Nafion, ETFE, and Al with different nominal thicknesses (errors: STDs)**

Sample / Nominal thickness	Thickness measured by different devices (µm)				
	TUC_RUC at AFCC	ESEM at AFCC	Explorer at 4D LABS	Helios at 4D LABS	Optical microscope at 4D LABS
Nafion / 10 µm	10 ± 1	12 ± 2	12.5 ± 0.2	11.2 ± 0.2	11.7 ± 0.1
Nafion / 15 µm	16 ± 1	18.4 ± 0.4	19.7 ± 0.8	18.8 ± 0.4	17.2 ± 0.5
Nafion / 25 µm	26 ± 1	30 ± 1	32.4 ± 0.8	30 ± 1	29.0 ± 0.3
Nafion / 50 µm	49 ± 1	52 ± 1	55.5 ± 0.8	52.2 ± 0.3	50.7 ± 0.3
ETFE / 12 µm	11 ± 1	17.0 ± 0.6	18.0 ± 0.6	15.8 ± 0.5	—
ETFE / 25 µm	24 ± 1	29.7 ± 0.7	32.8 ± 0.1	29.3 ± 0.2	—
ETFE / 100 µm	99 ± 1	106.6 ± 0.6	115 ± 1	105.7 ± 0.3	—
Al / 16 µm	16 ± 1	19 ± 2	21.1 ± 0.7	20.2 ± 0.5	18.6 ± 0.6
Al / 520 µm	519 ± 1	534.7 ± 0.3	584 ± 2	539 ± 2	533 ± 4

Effects of the Epoxy-embedding Sample Preparation Method on Samples' Cross Sections

As mentioned above, one of the processes in sample preparation by epoxy-embedding was to polish the cured epoxy from the samples' cross-section side by a lapping machine and rubbing it on a polishing cloth covered by diamond paste, repeatedly, to remove the extra layer of epoxy on top of the samples' cross sections and make the epoxy surface clear enough for imaging. Since the samples' cross sections could have a slight tilt with respect to the imaging surface of the epoxy as well as with respect to each other, not only the extra layer of epoxy on top of the cross sections but also some of the samples' cross sections were polished away during the process to expose all the cross sections. Therefore, as is clear from the above descriptions, the polishing process included many steps of exerting mechanical shear forces to the samples' cross sections. Accordingly, the abnormally higher thicknesses, repeatedly measured by the SEM devices and the optical microscope, which measured samples prepared by epoxy-embedding, could be explained based on smearing the samples' cross sections by the polishing forces, as shown schematically in Figure B-4.

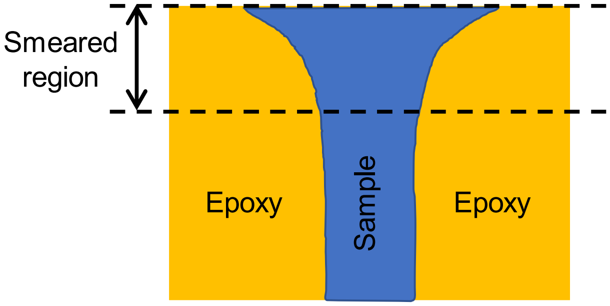

Figure B-4. **A schematic showing a sample's cross section smeared by shearing forces exerted by polishing**

To verify the above hypothesis, focused ion beam SEM (FIB-SEM) was performed by the Helios device at SFU 4D LABS on the 16 μm thick Al foil sample in the puck to reveal its shape underneath the epoxy surface observed during SEM imaging. For this purpose, first, the area chosen for FIB-SEM was covered by a very thin (a few nm thick) Pt layer using the option of ion-beam-induced deposition of the SEM device to protect the underlying region from destructive sputtering of the ion beam, and then the region under the deposited Pt was milled away by the ion beam to reveal the underlying structure. Milling was performed in successive steps, first using high energy beams to quickly dig a trench near the region of interest and then using low energy beams to clean the region of interest from the materials deposited by aggressive milling to uncover the underlying structure. Figure B-5 shows an SEM image taken after milling and cleaning the region of interest underneath the imaging surface of the Al foil, revealing the smeared region underneath the surface. As shown in Figure B-5, the smeared region could extend tens of micrometers deep inside the puck.

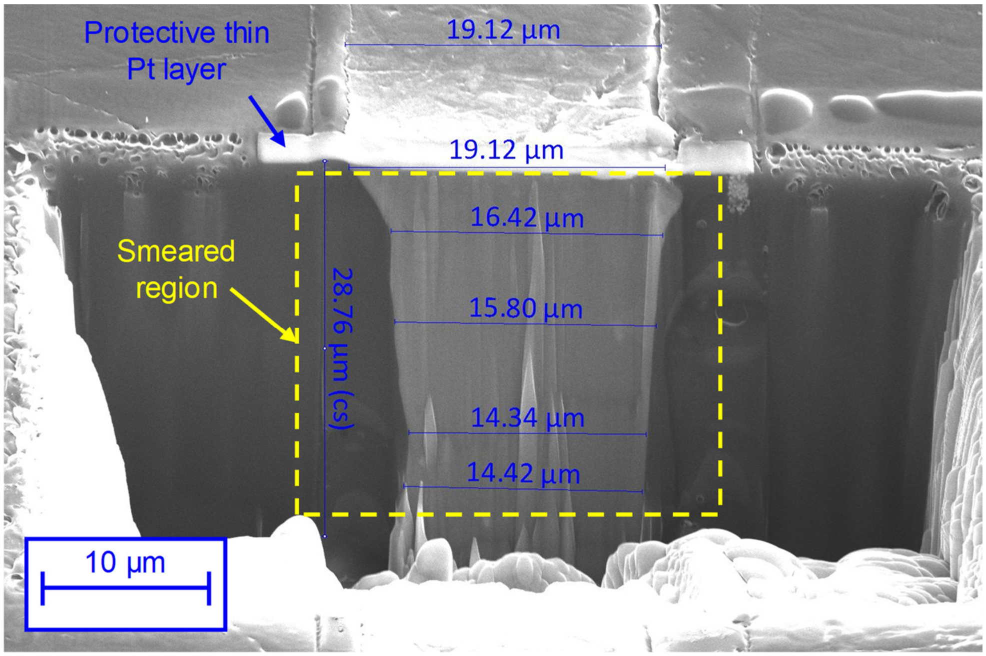

Figure B-5. **SEM image of the milled region underneath the imaging surface of a 16 µm thick Al foil embedded in epoxy, showing the region smeared by polishing forces exterted during the epoxy-embedding sample preparation**

Further verification of the polishing effects was revealed as a more comprehensive scanning of the polished surface was conducted by SEM. Figure B-6 shows nonuniform polishing effects on the cross section of the 16 µm thick Al foil sample, which could be caused by accumulation of chips on the cross section during polishing due to incomplete detachment of the generated chips from the sample. Therefore, as shown above, the method of epoxy-embedding proved to be very unreliable for the Nafion, ETFE, and Al foil samples due to the polishing effects (i.e., smearing and chips accumulation).

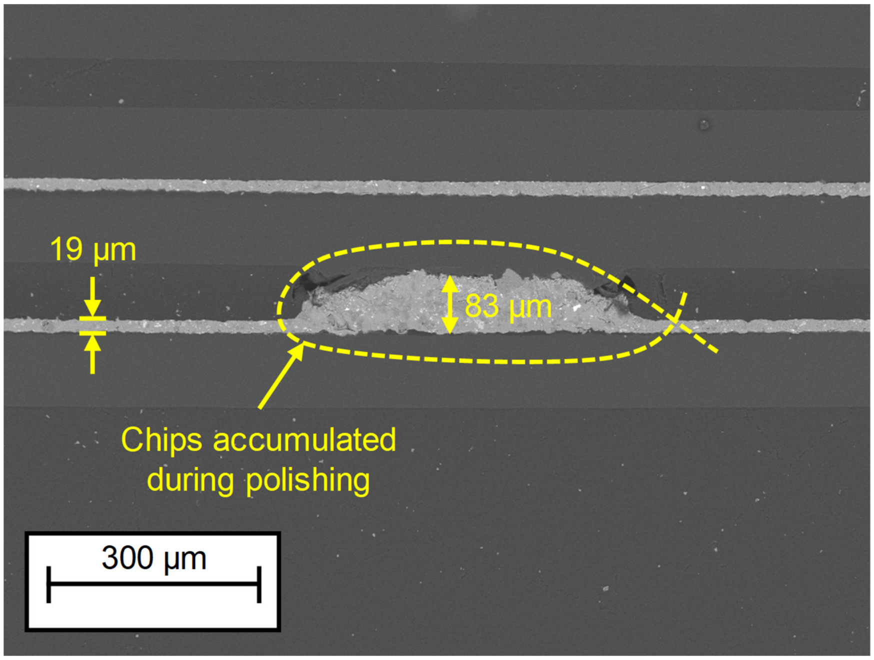

Figure B-6. **SEM image of the polished surface of an epoxy sample puck, showing nonuniform polishing effects as accumulation of chips during polishing on the cross section of a 16 µm thick Al foil**

The polishing effects, especially the smearing effect, would most likely happen to materials having a high tensile strength due to the nature of these effects, which was the case for the materials studied above. For CLs, however, the smearing effect may not be observed due to the very low tensile strength of CLs. One argument for low tensile strength of CLs is that one function of ionomer in CLs is to provide mechanical stability for CLs and prevent them from cracking and flaking; the ionomer, as a binder, merely holds the Pt/C catalyst particles together and can't provide substantial tensile strength for CLs, which could be verified by the ease of scratching away CLs from their substrates. Accordingly, CLs were not expected to resist the aggressive polishing forces and become smeared. However, since polishing proved to affect the other materials' cross sections, the method of SEM sample preparation by epoxy-embedding had a high risk of changing the CLs' cross sections, and there was a fear that what happened to other materials could happen to CLs as well. Further, the chips accumulation effect was still a possibility for CLs embedded in epoxy. Accordingly, the epoxy-embedding sample preparation method could not be fully trusted for CLs, and other sample preparation and thickness measurement methods were developed for cross-checking. The alternative methods are explained in Chapter 3.

Appendix C.

Data of the Microstructural Characterizations

This appendix contains the microstructural data for CL samples of design #1 (introduced in Table 2-1) with different substrates, hot-pressing, and areal Pt loadings, as well as the data of the different CL designs coated and studied in this thesis (see Table 2-1).

Table C- 1. Raw data of CL thickness (from different measurement methods), areal Pt loading, and their ratio for CL samples of design #1 with different substrates, hot-pressing, and areal Pt loadings (errors: STDs)

Substrate	l_{Pt} (µg Pt·cm^{-2})	Hot-pressed	Thickness measurement method	h_{cl} (µm)	h_{cl} / l_{Pt} (µm·(µg Pt·cm^{-2})$^{-1}$)
Al	250 ± 20	No	SEM	7.9 ± 0.4	0.032 ± 0.004
			Densitometer	8.2 ± 0.2	0.034 ± 0.003
		Yes	SEM	8.0 ± 0.3	0.033 ± 0.004
			Densitometer	8.7 ± 0.1	0.036 ± 0.004
	500 ± 50	No	SEM	16.1 ± 0.5	0.032 ± 0.003
			Densitometer	16.0 ± 0.4	0.032 ± 0.003
		Yes	SEM	14.6 ± 0.6	0.029 ± 0.003
			Densitometer	15.7 ± 0.1	0.031 ± 0.003
ETFE	250 ± 20	No	SEM	8.2 ± 0.5	0.033 ± 0.004
			Densitometer	8.3 ± 0.1	0.033 ± 0.003
		Yes	SEM	7.9 ± 0.3	0.031 ± 0.003
			Densitometer	9.3 ± 0.3	0.037 ± 0.004
	500 ± 50	No	SEM	15.6 ± 0.8	0.031 ± 0.003
			Densitometer	15.7 ± 0.4	0.031 ± 0.003
		Yes	SEM	14.9 ± 0.8	0.030 ± 0.003
			Densitometer	16.7 ± 0.1	0.033 ± 0.003

Table C- 2. Porosity data, from different measurement methods, for CL samples of design #1 with different substrates, areal Pt loadings, and hot-pressing (errors: STDs)

Substrate	l_{Pt} (µg Pt·cm^{-2})	Hot-pressed	Porosity measurement/calculation method	Porosity (%)
Al	250 ± 20	No	Densitometer	62 ± 1
			SEM thickness & areal Pt loading	65 ± 9
			Densitometer thickness & areal Pt loading	67 ± 8
		Yes	Densitometer	66 ± 1
			SEM thickness & areal Pt loading	66 ± 9
			Densitometer thickness & areal Pt loading	68 ± 8
	500 ± 50	No	Densitometer	62 ± 1
			SEM thickness & areal Pt loading	65 ± 8
			Densitometer thickness & areal Pt loading	65 ± 8
		Yes	Densitometer	63 ± 2
			SEM thickness & areal Pt loading	61 ± 8
			Densitometer thickness & areal Pt loading	64 ± 8
ETFE	250 ± 20	No	Densitometer	72 ± 1
			SEM thickness & areal Pt loading	66 ± 9
			Densitometer thickness & areal Pt loading	66 ± 8
		Yes	Densitometer	67 ± 1
			SEM thickness & areal Pt loading	64 ± 8
			Densitometer thickness & areal Pt loading	70 ± 9
	500 ± 50	No	Densitometer	64 ± 2
			SEM thickness & areal Pt loading	64 ± 9
			Densitometer thickness & areal Pt loading	64 ± 8
		Yes	Densitometer	65 ± 1
			SEM thickness & areal Pt loading	62 ± 9
			Densitometer thickness & areal Pt loading	66 ± 8

Table C- 3. PSD data, from TEM image analysis, for CL samples of design #1 with different substrates, Pt loadings, and hot-pressing (errors: STDs)

Bin of pore sizes [nm,nm]	Substrate							
	Al				ETFE			
	l_{Pt} (μg Pt·cm^{-2})							
	250 ± 20		500 ± 50		250 ± 20		500 ± 50	
	Hot-pressed							
	No	Yes	No	Yes	No	Yes	No	Yes
	Frequency (%)							
[0,10]	0 ± 0	0 ± 0	0 ± 0	0 ± 0	0 ± 0	0 ± 0	0 ± 0	0 ± 0
[10,20]	0 ± 0	0 ± 0	0 ± 0	0 ± 0	0 ± 0	0 ± 0	0 ± 0	0 ± 0
[20,30]	4.1 ± 0.1	3.8 ± 0.6	3 ± 1	3 ± 2	3 ± 2	3.1 ± 0.2	3 ± 2	3 ± 1
[30,40]	7 ± 1	5 ± 1	4 ± 2	5 ± 3	3 ± 2	4.6 ± 0.3	4 ± 3	5 ± 3
[40,50]	13 ± 2	11 ± 2	8 ± 4	10 ± 7	7 ± 5	10.6 ± 0.8	8 ± 6	10 ± 6
[50,60]	11 ± 2	10 ± 2	8 ± 3	9 ± 4	7 ± 3	10.3 ± 0.4	7 ± 4	9 ± 3
[60,70]	8.5 ± 0.8	7.8 ± 0.3	7 ± 2	8 ± 3	7 ± 1	8.6 ± 0.9	6 ± 2	7 ± 1
[70,80]	6.5 ± 0.9	6.1 ± 0.5	6.3 ± 0.3	6 ± 2	6.1 ± 0.9	7.4 ± 0.9	6 ± 2	7 ± 2
[80,90]	7 ± 2	7.5 ± 0.7	6 ± 1	7 ± 4	6.0 ± 0.7	7 ± 1	6 ± 2	6 ± 1
[90,100]	7 ± 1	6.5 ± 0.8	5.2 ± 0.1	7 ± 2	6 ± 3	7.0 ± 0.2	6 ± 1	6 ± 1
[100,110]	6 ± 2	7.2 ± 0.3	5.7 ± 0.5	6 ± 1	5 ± 1	5.9 ± 0.6	6 ± 2	5.8 ± 0.9
[110,120]	6 ± 1	6 ± 1	6 ± 2	5.5 ± 0.9	5.5 ± 0.9	7 ± 1	6 ± 1	6.4 ± 0.6
[120,130]	5 ± 2	5 ± 3	7 ± 2	6 ± 1	5 ± 1	4.4 ± 0.3	6 ± 1	5 ± 1
[130,140]	5 ± 2	4 ± 1	4.2 ± 0.3	5 ± 1	5 ± 2	6 ± 2	4.9 ± 0.9	5.5 ± 0.4
[140,150]	3.4 ± 0.6	6 ± 4	6 ± 1	4 ± 2	5.0 ± 0.8	5 ± 2	4 ± 2	3 ± 2
[150,160]	5 ± 1	4 ± 2	4 ± 1	3 ± 2	4.6 ± 0.8	5 ± 2	4 ± 2	5 ± 2
[160,170]	1 ± 2	4 ± 1	4 ± 3	3 ± 3	7 ± 3	2.2 ± 0.2	4 ± 3	3 ± 2
[170,180]	1 ± 1	2 ± 1	4 ± 2	1 ± 1	2 ± 2	2.0 ± 0.7	3 ± 2	3 ± 3
[180,190]	0.7 ± 0.6	1 ± 2	2.2 ± 0.7	2 ± 1	3 ± 4	0.6 ± 0.4	3 ± 3	2 ± 3
[190,200]	1 ± 1	2 ± 2	2 ± 2	2 ± 3	2 ± 1	1 ± 1	4 ± 4	1 ± 1
[200,210]	0.3 ± 0.4	1 ± 1	2 ± 1	2 ± 4	2 ± 2	1 ± 1	0.9 ± 0.6	2 ± 3
[210,220]	0.4 ± 0.6	0.5 ± 0.5	2 ± 2	2 ± 2	2 ± 2	0.5 ± 0.9	1 ± 1	3 ± 3
[220,230]	0 ± 0	0.1 ± 0.2	0.8 ± 0.7	1 ± 1	2 ± 2	0 ± 0	1 ± 3	0.5 ± 0.8
[230,240]	0 ± 0	0 ± 0	0.3 ± 0.3	0.9 ± 0.8	0.2 ± 0.3	0 ± 0	2 ± 2	0 ± 0
[240,250]	1 ± 1	0 ± 0	0.5 ± 0.8	0.3 ± 0.6	1 ± 1	0.4 ± 0.7	0.2 ± 0.3	1 ± 1
[250,260]	0.4 ± 0.7	0.4 ± 0.7	0.3 ± 0.5	0 ± 0	2 ± 3	0 ± 0	1 ± 1	0 ± 0
[260,270]	0 ± 0	0 ± 0	0.1 ± 0.1	0.3 ± 0.5	0 ± 0	0 ± 0	1 ± 2	0.2 ± 0.3
[270,280]	0 ± 0	0.4 ± 0.7	0 ± 0	1 ± 1	0.5 ± 0.8	0.7 ± 0.7	0 ± 0	1 ± 1
[280,290]	0 ± 0	0 ± 0	1 ± 1	0.4 ± 0.7	0 ± 0	0 ± 0	1 ± 2	0 ± 0
[290,300]	0 ± 0	0 ± 0	0.8 ± 0.9	0.3 ± 0.6	0.4 ± 0.6	0 ± 0	0 ± 0	0.2 ± 0.3
[300,400]	0 ± 0	0 ± 0	1 ± 2	0 ± 0	1 ± 1	1 ± 1	2 ± 3	0.2 ± 0.3

Table C- 4. Crack density data, from analysis of surface SEM images, for CL samples of design #1 with different substrates, areal Pt loadings, and hot-pressing (errors: STDs)

Substrate	l_{Pt} (µg Pt·cm^{-2})	Hot-pressed	Crack density (%)
Al	250 ± 20	No	5.6 ± 0.8
		Yes	5.6 ± 0.7
	500 ± 50	No	5.9 ± 0.7
		Yes	4.2 ± 0.1
ETFE	250 ± 20	No	5 ± 1
		Yes	5.5 ± 0.2
	500 ± 50	No	5 ± 1
		Yes	5.6 ± 0.4

Table C- 5. Surface roughness data, from a laser microscope, for CL samples of design #1 with different substrates, areal Pt loadings, and hot-pressing (errors: STDs)

Substrate	l_{Pt} (µg Pt·cm^{-2})	Hot-pressed	Surface roughness (µm)
Al	0 (Bare substrate)	No	0.98 ± 0.04
	250 ± 20	No	0.72 ± 0.03
		Yes	0.67 ± 0.01
	500 ± 50	No	0.7 ± 0.1
		Yes	0.69 ± 0.09
ETFE	0 (Bare substrate)	No	0.15 ± 0.02
	250 ± 20	No	0.62 ± 0.01
		Yes	0.61 ± 0.02
	500 ± 50	No	0.72 ± 0.04
		Yes	0.70 ± 0.09

Table C- 6. Surface chemistry data, from XPS measurements, for CL samples of design #1 with different substrates, areal Pt loadings, and hot-pressing (errors: STDs)

Surface	l_{Pt} (µg Pt·cm^{-2})	Hot-pressed	Mass concentration (%)					I/C
			F 1s	O 1s	C 1s	Pt 4f	S 2p	
Normal side on Al	500 ± 50	No	40.8 ± 0.2	4.6 ± 0.2	38.1 ± 0.2	15.0 ± 0.1	1.51 ± 0.03	2.56 ± 0.04
Normal side on ETFE	250 ± 20	No	42.1 ± 0.4	4.40 ± 0.09	37.1 ± 0.3	14.9 ± 0.2	1.5 ± 0.1	2.80 ± 0.07
Normal side on ETFE	250 ± 20	Yes	41.8 ± 0.4	4.1 ± 0.4	37.7 ± 0.3	14.9 ± 0.7	1.5 ± 0.2	2.70 ± 0.05
Decal side on tape	250 ± 20	No	55.8 ± 0.5	5.2 ± 0.3	29.7 ± 0.3	7.4 ± 0.2	1.9 ± 0.2	7.6 ± 0.4
Decal side on tape	250 ± 20	Yes	54.7 ± 0.4	5.3 ± 0.3	30.4 ± 0.1	7.8 ± 0.1	1.9 ± 0.2	6.8 ± 0.1
Decal on NRE-211	250 ± 20	Yes	54.3 ± 0.6	4.9 ± 0.3	30.9 ± 0.5	8.0 ± 0.3	1.9 ± 0.2	6.4 ± 0.4

Table C-7. Porosity, crack density, and crack aspect ratio for all the CL designs (errors: STDs)

Design #	I/C ratio	Dry milling time (hr)	Drying temperature (°C)	Porosity (%)	Crack density (%)	Crack aspect ratio
1	1.1	0	55	59 ± 2	3.1 ± 0.7	4.6 ± 0.6
2	0.7	48	55	45 ± 6	15.3 ± 0.7	37 ± 8
3	0.9	48	55	32 ± 5	15.5 ± 0.8	33 ± 4
4	0.7	24	55	51 ± 2	13.5 ± 0.4	36 ± 3
5	1.1	48	55	24 ± 3	7.8 ± 0.8	8.6 ± 0.7
6	0.9	24	55	43 ± 6	9.3 ± 0.2	23 ± 4
7	1.1	48	24	27 ± 7	14 ± 1	159 ± 44
8	1.1	0	24	57 ± 3	5.4 ± 0.7	6.0 ± 0.2

Appendix D.

Conventional TPS Method for Thin Films as per ISO22007-2

When the nickel element of a Hot Disk testbed is heated, its temperature and, hence, electrical resistivity ($\mathit{\Gamma}$) increases as a function of time, as follows [121]:

$$\mathit{\Gamma}(t) = \{1 + \epsilon \Delta T(t)\}\mathit{\Gamma}(t = 0) = \{1 + \epsilon[\Delta T_{\text{sen-bm}}(t) + \Delta T_{\text{ave}}(t)]\}\mathit{\Gamma}(t = 0) \tag{D.1}$$

where $\mathit{\Gamma}(t = 0)$ is the electrical resistivity of the sensor at the beginning of the test, ϵ is the temperature coefficient of resistivity of the sensor, $\Delta T(t)$ is the sensor's mean temperature increase, $\Delta T_{\text{sen-bm}}(t)$ is the temperature difference between the surface of the nickel sensor and the background material, and $\Delta T_{\text{ave}}(t)$ is the average temperature increase of the surface of the background material. The temperature difference $\Delta T_{\text{sen-bm}}(t)$ becomes constant after a very short time, Δt_{init}, given by [121]:

$$\Delta t_{\text{init}} = \frac{h_{\text{sen-bm}}^2}{\kappa_{\text{sen-bm}}} \tag{D.2}$$

where $h_{\text{sen-bm}}$ and $\kappa_{\text{sen-bm}}$ are, respectively, the overall thickness and thermal diffusivity of the materials between the nickel sensor and the background material.

During a measurement, $\mathit{\Gamma}(t)$ is measured as a function of time [120], and the mean temperature increase of the sensor ($\Delta T(t)$) is calculated from Eq. (D.1), as follows:

$$\Delta T(t) = \Delta T_{\text{sen-bm}}(t) + \Delta T_{\text{ave}}(t) = \frac{1}{\epsilon}\left(\frac{\mathit{\Gamma}(t)}{\mathit{\Gamma}(t = 0)} - 1\right) \tag{D.3}$$

where ΔT_{ave} is obtained from [121]:

$$\Delta T_{\text{ave}}(\tau) = \frac{EP}{\pi^{3/2} r_{\text{sen}} k_{\text{bm}}} \varsigma(\tau) \tag{D.4}$$

where EP is the constant electric power of the sensor, r_{sen} is the radius of the sensor (i.e., the radius of the double spiral disk), k_{bm} is the thermal conductivity of the background material, and τ is a dimensionless time defined by [121]:

$$\tau = \sqrt{\frac{t}{\Theta}} \tag{D.5}$$

where Θ is a characteristic time defined by [121]:

$$\Theta = \frac{r_{\text{sen}}^2}{\kappa_{\text{bm}}} \tag{D.6}$$

where κ_{bm} is the thermal diffusivity of the background material. $\varsigma(\tau)$ in Eq. (D.4) is a dimensionless function, defined as [118, 120]:

$$\varsigma(\tau) = \frac{1}{n_{\text{ring}}^2 \left(n_{\text{ring}} + 1\right)^2} \int_0^{\pi} \frac{1}{s^2} \left[\sum_{e=1}^{n_{\text{ring}}} e \sum_{i=1}^{n_{\text{ring}}} i \cdot \exp\left(-\frac{e^2 + i^2}{4 n_{\text{ring}}^2 s^2}\right) \times I_0 \left(\frac{e \cdot i}{2 n_{\text{ring}}^2 s^2}\right) \right] ds \tag{D.7}$$

where n_{ring} is the number of concentric sources or rings of the double spiral nickel, and I_0 is the modified Bessel function of the zeroth kind.

By combining Eqs. (D.3) and (D.4), the relation between $\Delta T(\tau)$ and $\Delta T_{\text{sen-bm}}(\tau)$ becomes:

$$\Delta T(\tau) = \Delta T_{\text{sen-bm}}(\tau) + \frac{EP}{\pi^{3/2} r_{\text{sen}} k_{\text{bm}}} \varsigma(\tau) \tag{D.8}$$

As $\Delta T_{\text{sen-bm}}(\tau)$ becomes constant shortly after Δt_{init} and $\frac{EP}{\pi^{3/2} r_{\text{sen}} k_{\text{bm}}}$ is a constant for a specific experiment, Eq. (D.8) provides a linear relation between ΔT and $\varsigma(\tau)$ after the time Δt_{init} is elapsed, whose slope and intercept are $\frac{EP}{\pi^{3/2} r_{\text{sen}} k_{\text{bm}}}$ and $\Delta T_{\text{sen-bm}}$, respectively. After determining the steady state temperature difference across the thin materials between the nickel probe and the background material, i.e., $\Delta T_{\text{sen-bm}}$ (note: the temperature would not reach to a steady state in the background material and would evolve transiently), the effective thermal conductivity of the thin materials could be calculated by the following equation which is the solution of steady state 1D heat conduction across a slab:

$$k_{\text{eff}} = \frac{EPh_{\text{sen-bm}}}{2A_{\text{sen}}\,\Delta T_{\text{sen-bm}}} \tag{D.9}$$

where A_{sen} is the area of the sensor. The process of determining $\Delta T_{\text{sen-bm}}$ is, however, an iterative one because the value of κ_{bm} is unknown before a measurement. The iterative process is summarized in Figure D.1. As shown in the figure, after conducting a test and obtaining the temperature increase of the heating element from Eq. (D.3), a value is guessed for κ_{bm}, and then, Θ in Eq. (D.6) and τ in Eq. (D.5) are calculated based on the guessed value. Then, $\varsigma(\tau)$ is calculated, and the curve of $\Delta T(\tau)$ versus $\varsigma(\tau)$ is plotted. According to Eq. (D.8), if κ_{bm} was guessed correctly, the curve would be a line after a short dimensionless time $\Delta \tau_{\text{init}}$ associated with Δt_{init}. Accordingly, the initial nonlinear section of the curve, associated with the initial transient conduction of heat across the thin materials is discarded, and a linear regression is performed on the rest of the data which are registered during the steady state conduction of heat across the thin materials. Since τ is dependent on κ_{bm}, the linear regression analysis is performed on the data points iteratively, as illustrated in Figure D.1. Based on the above theory, as per ISO22007-2 [120], the following procedure is given for measuring thermal conductivity of a thin film:

1. A reference test with the thin film sensor alone between two slabs of the background material to determine effective thermal conductivity of the Kapton layer together with the adhesive ($k_{\text{Kap\&adh}}$)
2. An experiment with the sensor sandwiched between two identical pieces of the sample, supported by the slabs, to determine effective thermal conductivity of the series combination of the adhesive layer, the Kapton layer, and the sample (k_{eff})

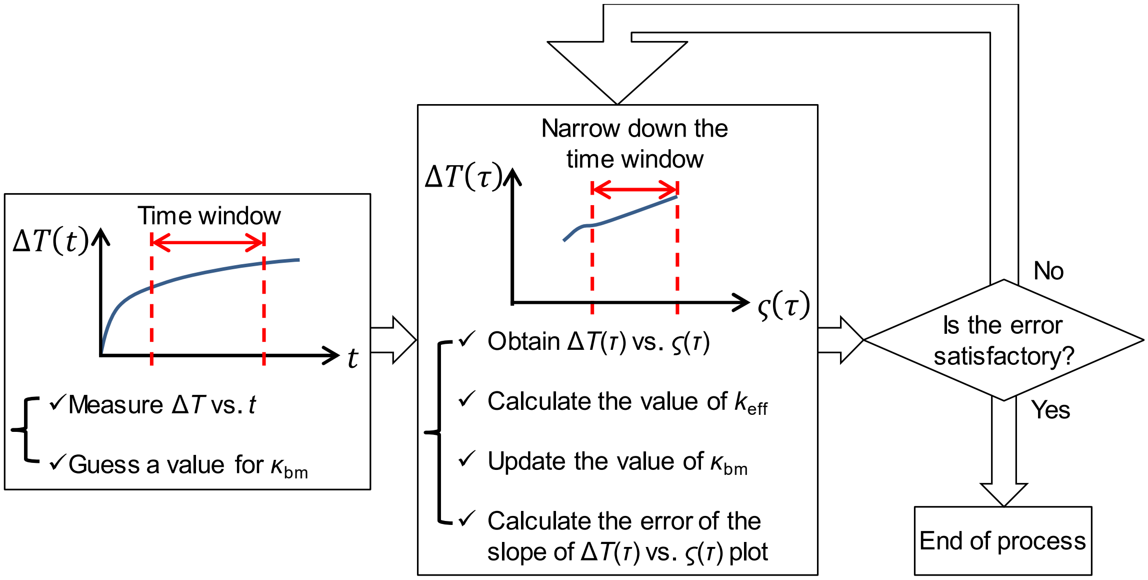

Figure D.1. Iterative process of TPS measurements

Then, according to ISO22007-2 [120], the effective thermal conductivity of the sample (k_s) can be found from [120]:

$$\frac{h_{\mathrm{Kap\&adh}} + h_{\mathrm{s}}}{k_{\mathrm{eff}}} = \frac{h_{\mathrm{s}}}{k_{\mathrm{s}}} + \frac{h_{\mathrm{Kap\&adh}}}{k_{\mathrm{Kap\&adh}}} \tag{D.10}$$

Appendix E.

Uncertainty Analysis

According to Ref. [130], if q is any function of several variables $x,\ldots,z$, then the uncertainty in q, denoted by δq,is calculated by:

$$\delta q = \sqrt{\left(\frac{\partial q}{\partial x}\delta x\right)^2 + \cdots + \left(\frac{\partial q}{\partial z}\delta z\right)^2} \tag{E.1}$$

According to Ref. [131], if a linear regression $\hat{y} = \widehat{sl}x + \hat{b}$ is performed on a set of ordered pairs (x, y), uncertainties of the slope and intercept of the linear regression can be found from:

$$\delta\widehat{sl} = T_{\Omega/2,N-2}s_{sl} \tag{E.2}$$

$$\delta\hat{b} = T_{\Omega/2,N-2}s_{b} \tag{E.3}$$

where $T_{\Omega/2,N-2}$ is the upper $100 \times \Omega/2\%$ point of the t-distribution with $N-2$ degrees of freedom, Ω is the significance level for which a value of 0.05 is mostly used, N is the total number of measurement points, and s_{sl} and s_b are STDs of the slope and intercept of the fitted line, respectively. Moreover, s_{sl} and s_b are calculated from the following equations:

$$s_{sl} = \frac{s_{y,x}}{\sqrt{SS_{xx}}} \tag{E.4}$$

$$s_b = s_{y,x}\sqrt{\left(\frac{1}{N} + \frac{x_{\text{ave}}^2}{SS_{xx}}\right)} \tag{E.5}$$

$$SS_{xx} = \sum_{i=1}^{N}(x_i - x_{\text{ave}})^2 \tag{E.6}$$

$$x_{\text{ave}} = \frac{1}{N}\sum_{i=1}^{N}x_i \tag{E.7}$$

$$s_{y,x} = \sqrt{\frac{SS_E}{N-2}} \tag{E.8}$$

$$SS_E = \sum_{i=1}^{N}(y_i - \hat{y}_i)^2 \tag{E.9}$$

$$\hat{y}_i = \widehat{sl}x_i + \hat{b} \tag{E.10}$$

$$\widehat{sl} = \frac{SS_{xy}}{SS_{xx}} \tag{E.11}$$

$$SS_{xy} = \sum_{i=1}^{N}\left\{\begin{matrix}(x_i - x_{\text{ave}})\\ \times\,(y_i - y_{\text{ave}})\end{matrix}\right\} \tag{E.12}$$

$$y_{\text{ave}} = \frac{1}{N}\sum_{i=1}^{N}y_i \tag{E.13}$$

$$\hat{b} = y_{\text{ave}} - \widehat{sl}x_{\text{ave}} \tag{E.14}$$

If several values of quantity q are measured and average of the measurements is reported as the final value, then, sample standard deviation of the reported average can be obtained from:

$$\text{STD of } q = \sqrt{\frac{\sum_{i=1}^{reps}(q_i - q_{\text{ave}})^2}{reps - 1}} \tag{E.15}$$

where $reps$ is the total number of measurement repetitions and $q_{\text{ave}} = \frac{1}{reps}\sum_{i=1}^{reps} q_i$.

In this thesis, to facilitate showing the data in the tables, the uncertainty of a data point is first rounded to the first significant digit, and then, the data point itself is rounded to the same number of decimal places as the rounded uncertainty. For example, a data point and its uncertainty such as 1.3579 ± 0.004898 are rounded and shown as 1.358 ± 0.005.

Appendix F.

Signal to Noise Ratio Enhancement in Thermal Conductivity Measurements of Designs #2 and #3

The data of this Appendix are tabulated in Appendix G.

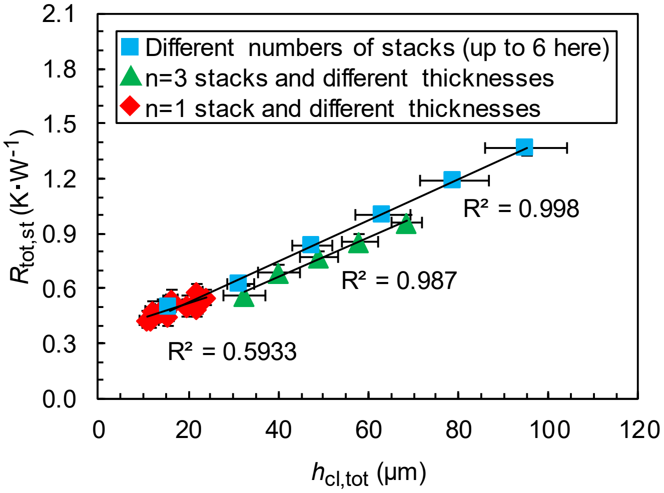

Figure F-1. **Total resistance vs. total CL thickness for design #2 at 1,500 kPa and 29 °C, showing different abilities of the methods in taking the linear signal (error bars: STDs for thickness, random errors for resistance)**

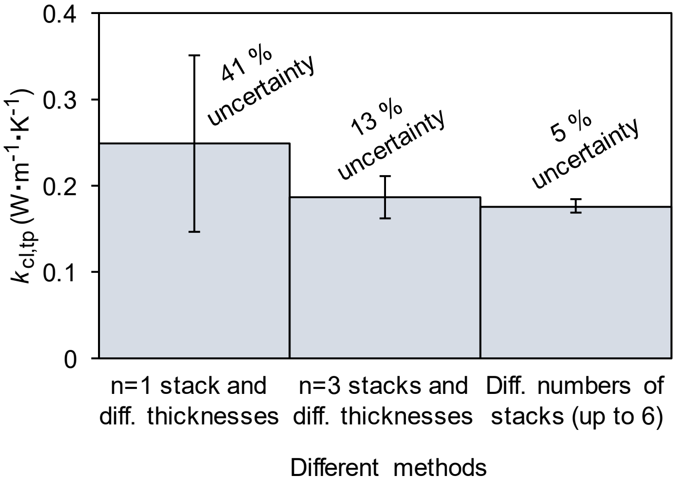

Figure F-2. **Thermal conductivity of design #2 by different methods at 1,500 kPa and 29 °C, showing progression of uncertainty minimzation (error bars: random errors)**

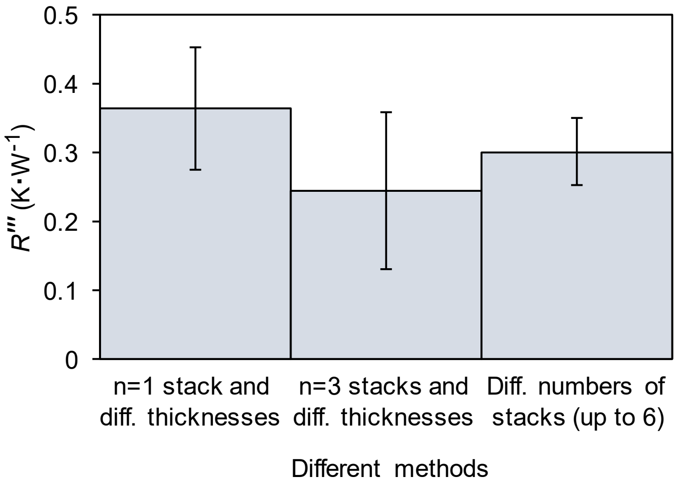

Figure F-3. **Parasitic resistance in measurements of design #2 by different methods at 1,500 kPa and 29 °C, showing the same parasitic resistance (within the error range) in different tests (error bars: random errors)**

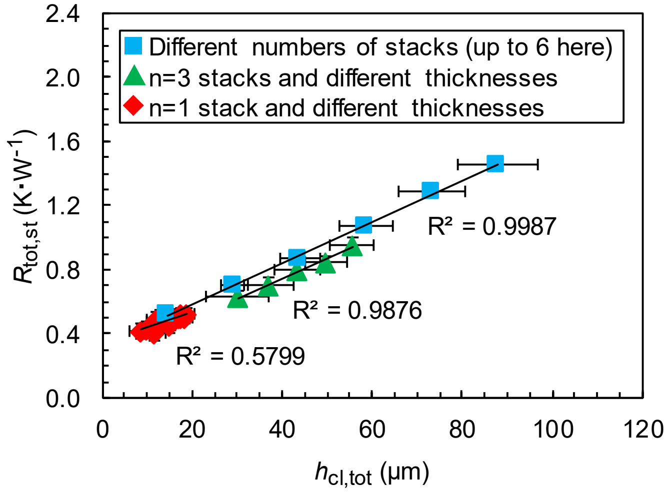

Figure F-4. **Total resistance vs. total CL thickness for design #3 at 1,500 kPa and 29 °C, showing different abilities of the methods in taking the linear signal (error bars: STDs for thickness, random errors for resistance)**

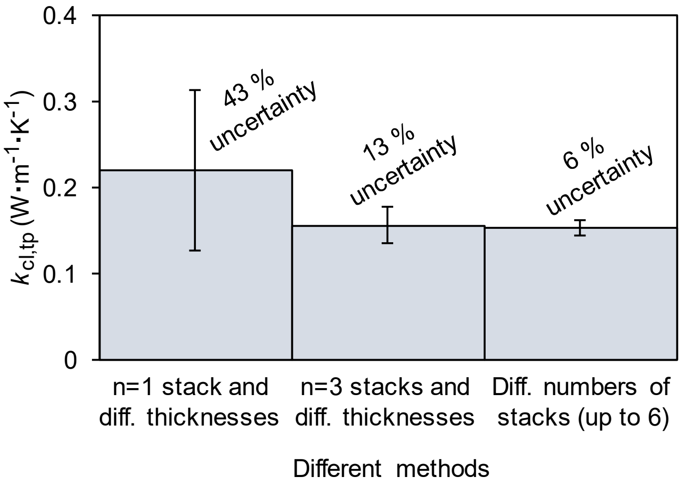

Figure F-5. Thermal conductivity of design #3 by different methods at 1,500 kPa and 29 °C, showing progression of uncertainty minimzation (error bars: random errors)

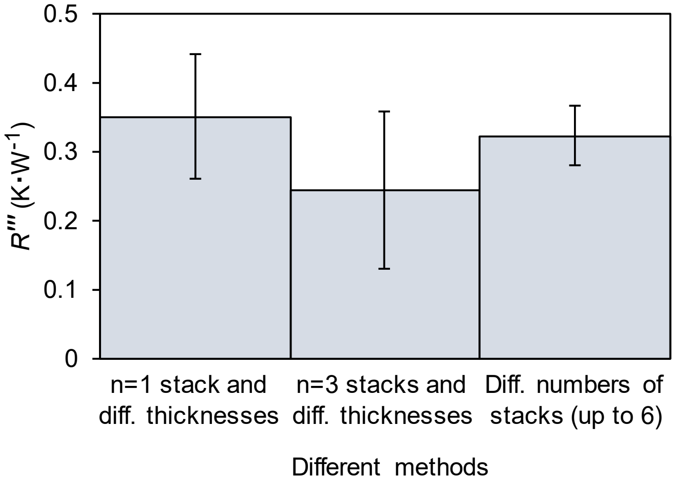

Figure F-6. Parasitic resistance in measurements of design #3 by different methods at 1,500 kPa and 29 °C, showing the same parasitic resistance (within the error range) in different tests (error bars: random errors)

Appendix G.

Data of the Thermal Tests

Table G- 1. Through-plane thermal conductivity tests of ETFE films by TPS (errors: STDs for thickness, random errors for the rest of the data)

P (bar)	h_{etfe} (μm)	k_{app} ($W \cdot m^{-1} \cdot K^{-1}$)		R_{tot} ($K \cdot W^{-1}$)		R' ($K \cdot W^{-1}$)	k_{etfe} ($W \cdot m^{-1} \cdot K^{-1}$)
		Arbitrary reference	Measured reference	Arbitrary reference	Measured reference		
2.1	11 ± 1	4.6 ± 0.7	0.29 ± 0.03	0.577 ± 0.001	0.554 ± 0.007	0.46 ± 0.05	0.17 ± 0.01
	24 ± 1	0.49 ± 0.03	0.199 ± 0.002	0.644 ± 0.005	0.669 ± 0.002		
	50 ± 1	0.226 ± 0.002	0.158 ± 0.002	0.878 ± 0.003	0.933 ± 0.004		
	105 ± 1	0.204 ± 0.001	0.183 ± 0.002	1.249 ± 0.002	1.247 ± 0.008		
	204 ± 1	0.177 ± 0.001	0.176 ± 0.001	2.127 ± 0.005	2.063 ± 0.005		
4.2	11 ± 1	-0.8 ± 0.2	0.28 ± 0.01	0.553 ± 0.005	0.534 ± 0.003	0.44 ± 0.06	0.17 ± 0.01
	24 ± 1	0.72 ± 0.06	0.215 ± 0.004	0.621 ± 0.004	0.633 ± 0.003		
	50 ± 1	0.236 ± 0.002	0.165 ± 0.001	0.865 ± 0.003	0.891 ± 0.002		
	105 ± 1	0.213 ± 0.001	0.191 ± 0.001	1.218 ± 0.001	1.193 ± 0.003		
	204 ± 1	0.182 ± 0.001	0.177 ± 0.001	2.087 ± 0.004	2.026 ± 0.003		
6.2	11 ± 1	-0.49 ± 0.08	0.24 ± 0.01	0.539 ± 0.006	0.529 ± 0.003	0.43 ± 0.05	0.18 ± 0.01
	24 ± 1	1.0 ± 0.1	0.232 ± 0.008	0.609 ± 0.005	0.608 ± 0.005		
	50 ± 1	0.249 ± 0.001	0.175 ± 0.001	0.850 ± 0.001	0.854 ± 0.003		
	105 ± 1	0.217 ± 0.001	0.196 ± 0.001	1.208 ± 0.002	1.163 ± 0.004		
	204 ± 1	0.186 ± 0.001	0.178 ± 0.001	2.054 ± 0.003	2.004 ± 0.010		
8.3	11 ± 1	-0.29 ± 0.04	0.25 ± 0.01	0.517 ± 0.007	0.522 ± 0.003	0.42 ± 0.05	0.177 ± 0.010
	24 ± 1	1.0 ± 0.1	0.231 ± 0.003	0.607 ± 0.005	0.606 ± 0.002		
	50 ± 1	0.258 ± 0.006	0.180 ± 0.001	0.840 ± 0.006	0.840 ± 0.003		
	105 ± 1	0.222 ± 0.001	0.200 ± 0.001	1.193 ± 0.004	1.144 ± 0.002		
	204 ± 1	0.189 ± 0.001	0.178 ± 0.003	2.032 ± 0.004	2.00 ± 0.02		

Table G- 2. Through-plane thermal conductivity tests of ETFE films by GHF (errors: STDs for thickness, random errors for the rest of the data)

P (bar)	h_{etfe} (μm)	R_{tot} (K·W^{-1})	TCR (K·W^{-1})	k_{etfe} (W·m^{-1}·K^{-1})
3	11 ± 1	0.45 ± 0.02	0.31 ± 0.08	0.17 ± 0.01
	24 ± 1	0.60 ± 0.03		
	50 ± 1	0.90 ± 0.03		
	105 ± 1	1.41 ± 0.03		
	204 ± 1	2.66 ± 0.07		
6	11 ± 1	0.42 ± 0.02	0.29 ± 0.08	0.18 ± 0.01
	24 ± 1	0.58 ± 0.02		
	50 ± 1	0.88 ± 0.03		
	105 ± 1	1.37 ± 0.03		
	204 ± 1	2.61 ± 0.07		
9	11 ± 1	0.41 ± 0.02	0.28 ± 0.09	0.18 ± 0.01
	24 ± 1	0.56 ± 0.02		
	50 ± 1	0.87 ± 0.03		
	105 ± 1	1.35 ± 0.03		
	204 ± 1	2.59 ± 0.08		
12	11 ± 1	0.40 ± 0.02	0.27 ± 0.09	0.18 ± 0.01
	24 ± 1	0.55 ± 0.02		
	50 ± 1	0.86 ± 0.09		
	105 ± 1	1.33 ± 0.03		
	204 ± 1	2.57 ± 0.08		

Table G- 3. **Through-plane thermal conductivity tests of Nafion films by TPS (errors: STDs for thickness, random errors for the rest of the data)**

P (bar)	h_{Nafion} (μm)	k_{app} by arbitrary reference ($\mathrm{W \cdot m^{-1} \cdot K^{-1}}$)	R_{tot} ($\mathrm{K \cdot W^{-1}}$)	R' ($\mathrm{K \cdot W^{-1}}$)	k_{Nafion} ($\mathrm{W \cdot m^{-1} \cdot K^{-1}}$)
2.1	10 ± 1	-1.1 ± 0.3	0.560 ± 0.004	0.508 ± 0.005	0.25 ± 0.01
	16 ± 1	1.1 ± 0.3	0.596 ± 0.006		
	26 ± 1	0.46 ± 0.01	0.651 ± 0.002		
	48 ± 1	0.344 ± 0.007	0.767 ± 0.004		
4.2	10 ± 1	-0.29 ± 0.02	0.524 ± 0.004	0.470 ± 0.007	0.25 ± 0.01
	16 ± 1	-3 ± 1	0.561 ± 0.003		
	26 ± 1	0.79 ± 0.06	0.620 ± 0.003		
	48 ± 1	0.398 ± 0.009	0.738 ± 0.004		
6.2	10 ± 1	-0.185 ± 0.001	0.504 ± 0.001	0.450 ± 0.008	0.24 ± 0.01
	16 ± 1	-0.67 ± 0.08	0.541 ± 0.004		
	26 ± 1	1.31 ± 0.03	0.603 ± 0.001		
	48 ± 1	0.44 ± 0.01	0.722 ± 0.003		
8.3	10 ± 1	-0.171 ± 0.001	0.490 ± 0.001	0.435 ± 0.009	0.24 ± 0.01
	16 ± 1	-0.49 ± 0.02	0.527 ± 0.002		
	26 ± 1	1.9 ± 0.7	0.590 ± 0.006		
	48 ± 1	0.48 ± 0.02	0.710 ± 0.006		
10.4	10 ± 1	-0.147 ± 0.008	0.480 ± 0.005	0.424 ± 0.009	0.24 ± 0.01
	16 ± 1	-0.38 ± 0.03	0.517 ± 0.004		
	26 ± 1	5 ± 2	0.581 ± 0.003		
	48 ± 1	0.53 ± 0.02	0.702 ± 0.005		

Table G- 4. Through-plane thermal conductivity tests of Nafion films by GHF (errors: STDs for thickness, random errors for the rest of the data)

P (bar)	h_{Nafion} (μm)	R_{tot} ($K \cdot W^{-1}$)	*TCR* ($K \cdot W^{-1}$)	k_{Nafion} ($W \cdot m^{-1} \cdot K^{-1}$)
3	10 ± 1	0.29 ± 0.01	0.20 ± 0.03	0.21 ± 0.02
	16 ± 1	0.34 ± 0.01		
	26 ± 1	0.46 ± 0.02		
	48 ± 1	0.65 ± 0.02		
6	10 ± 1	0.28 ± 0.01	0.19 ± 0.02	0.21 ± 0.02
	16 ± 1	0.33 ± 0.01		
	26 ± 1	0.44 ± 0.01		
	48 ± 1	0.63 ± 0.02		
9	10 ± 1	0.27 ± 0.01	0.018 ± 0.02	0.22 ± 0.02
	16 ± 1	0.32 ± 0.01		
	26 ± 1	0.43 ± 0.01		
	48 ± 1	0.61 ± 0.02		
12	10 ± 1	0.27 ± 0.01	0.17 ± 0.02	0.22 ± 0.01
	16 ± 1	0.31 ± 0.01		
	26 ± 1	0.42 ± 0.01		
	48 ± 1	0.61 ± 0.02		

Table G- 5. Through-plane thermal conductivity tests of GDLs by TPS (errors: STDs for thickness, random errors for the rest of the data)

P (bar)	Sample	h_{gdl} (μm)	k_{app} by arbitrary reference ($W \cdot m^{-1} \cdot K^{-1}$)	R_{tot} ($K \cdot W^{-1}$)	R' ($K \cdot W^{-1}$)	k_{gdl} ($W \cdot m^{-1} \cdot K^{-1}$)
1.0	24BA	189 ± 1	0.1193 ± 0.0006	2.313 ± 0.008	0.39 ± 0.09	0.135 ± 0.003
	34BA	272 ± 1	0.1355 ± 0.0002	3.150 ± 0.004		
2.0	24BA	185 ± 1	0.1666 ± 0.0010	1.687 ± 0.007	0.33 ± 0.06	0.188 ± 0.004
	34BA	267 ± 1	0.1876 ± 0.0003	2.288 ± 0.003		
3.1	24BA	180 ± 1	0.2185 ± 0.0005	1.403 ± 0.002	0.31 ± 0.05	0.228 ± 0.005
	34BA	262 ± 1	0.2380 ± 0.0009	1.898 ± 0.005		
4.1	24BA	176 ± 1	0.2772 ± 0.0003	1.231 ± 0.001	0.30 ± 0.04	0.260 ± 0.005
	34BA	258 ± 1	0.2898 ± 0.0008	1.663 ± 0.003		
5.1	24BA	172 ± 1	0.338 ± 0.002	1.112 ± 0.003	0.29 ± 0.04	0.289 ± 0.007
	34BA	254 ± 1	0.348 ± 0.002	1.500 ± 0.006		
6.1	24BA	169 ± 1	0.418 ± 0.002	1.023 ± 0.002	0.28 ± 0.04	0.314 ± 0.008
	34BA	250 ± 1	0.407 ± 0.003	1.379 ± 0.005		
7.1	24BA	165 ± 1	0.510 ± 0.008	0.954 ± 0.006	0.28 ± 0.04	0.337 ± 0.008
	34BA	246 ± 1	0.4663 ± 0.0008	1.284 ± 0.001		
8.1	24BA	162 ± 1	0.608 ± 0.007	0.898 ± 0.003	0.27 ± 0.04	0.358 ± 0.009
	34BA	243 ± 1	0.531 ± 0.004	1.208 ± 0.005		
9.2	24BA	159 ± 1	0.753 ± 0.003	0.851 ± 0.001	0.27 ± 0.03	0.377 ± 0.007
	34BA	239 ± 1	0.601 ± 0.003	1.144 ± 0.002		
10.2	24BA	156 ± 1	0.91 ± 0.03	0.811 ± 0.008	0.26 ± 0.04	0.39 ± 0.01
	34BA	236 ± 1	0.675 ± 0.003	1.090 ± 0.002		

Table G- 6. Through-plane thermal conductivity tests of GDLs by GHF (errors: STDs for thickness, random errors for the rest of the data)

P (bar)	Sample	h_{gdl} (μm)	R_{tot} ($K \cdot W^{-1}$)	TCR ($K \cdot W^{-1}$)	k_{gdl} ($W \cdot m^{-1} \cdot K^{-1}$)
1.0	24BA	189 ± 1	3.08 ± 0.03	0.7 ± 0.2	0.16 ± 0.01
	34BA	272 ± 1	4.10 ± 0.05		
2.0	24BA	185 ± 1	1.89 ± 0.03	0.2 ± 0.2	0.22 ± 0.01
	34BA	267 ± 1	2.64 ± 0.04		
3.1	24BA	180 ± 1	1.42 ± 0.02	0.0 ± 0.1	0.26 ± 0.02
	34BA	262 ± 1	2.04 ± 0.03		
4.1	24BA	176 ± 1	1.16 ± 0.02	0.0 ± 0.1	0.30 ± 0.02
	34BA	258 ± 1	1.70 ± 0.02		
5.1	24BA	172 ± 1	0.99 ± 0.02	-0.0 ± 0.1	0.33 ± 0.02
	34BA	254 ± 1	1.48 ± 0.02		
6.1	24BA	169 ± 1	0.87 ± 0.02	-0.06 ± 0.09	0.36 ± 0.02
	34BA	250 ± 1	1.31 ± 0.02		
7.1	24BA	165 ± 1	0.78 ± 0.02	-0.07 ± 0.08	0.39 ± 0.02
	34BA	246 ± 1	1.19 ± 0.02		
8.1	24BA	162 ± 1	0.71 ± 0.02	-0.07 ± 0.08	0.41 ± 0.03
	34BA	243 ± 1	1.09 ± 0.02		
9.2	24BA	159 ± 1	0.65 ± 0.02	-0.07 ± 0.07	0.44 ± 0.03
	34BA	239 ± 1	1.02 ± 0.02		
10.2	24BA	156 ± 1	0.60 ± 0.02	-0.08 ± 0.07	0.46 ± 0.03
	34BA	236 ± 1	0.95 ± 0.01		

Table G- 7. Through-plane thermal conductivity tests of CL samples of design #1 by TPS at different pressures, 29 °C, and room RH (errors: STDs for thickness, random errors for the rest of the data)

P (bar)	$h_{cl,tot}$ (μm)	k_{app} by arbitrary ref. ($W \cdot m^{-1} \cdot K^{-1}$)	R_{tot} ($K \cdot W^{-1}$)	R' ($K \cdot W^{-1}$)	$k_{cl,tp}$ ($W \cdot m^{-1} \cdot K^{-1}$)
2.1	15 ± 1	0.2002 ± 0.0010	2.057 ± 0.007	1.92 ± 0.05	0.22 ± 0.03
	28.7 ± 0.8	0.1971 ± 0.0003	2.178 ± 0.002		
6.2	15 ± 1	0.2113 ± 0.0005	1.979 ± 0.003	1.84 ± 0.05	0.21 ± 0.02
	28.7 ± 0.8	0.2063 ± 0.0007	2.107 ± 0.005		
10.4	15 ± 1	0.2167 ± 0.0002	1.944 ± 0.002	1.81 ± 0.05	0.21 ± 0.02
	28.7 ± 0.8	0.2111 ± 0.0006	2.072 ± 0.005		
14.6	15 ± 1	0.2213 ± 0.0007	1.916 ± 0.004	1.78 ± 0.05	0.22 ± 0.03
	28.7 ± 0.8	0.216 ± 0.001	2.037 ± 0.009		

Table G- 8. Through-plane thermal conductivity tests of CL samples of design #1 by GHF at different pressures, 29 °C, and room RH (errors: STDs for thickness, random errors for the rest of the data)

P (bar)	$h_{cl,tot}$ (μm)	R_{tot} ($K \cdot W^{-1}$)	TCR ($K \cdot W^{-1}$)	$k_{cl,tp}$ ($W \cdot m^{-1} \cdot K^{-1}$)
4	8.7 ± 0.7	0.44 ± 0.01	0.36 ± 0.08	0.21 ± 0.03
	23.9 ± 0.8	0.59 ± 0.02		
6	8.7 ± 0.7	0.38 ± 0.01	0.30 ± 0.08	0.21 ± 0.03
	23.9 ± 0.8	0.52 ± 0.01		
8	8.7 ± 0.7	0.34 ± 0.01	0.26 ± 0.07	0.21 ± 0.03
	23.9 ± 0.8	0.48 ± 0.01		
10	8.7 ± 0.7	0.32 ± 0.01	0.24 ± 0.07	0.22 ± 0.03
	23.9 ± 0.8	0.46 ± 0.01		
12	8.7 ± 0.7	0.30 ± 0.01	0.22 ± 0.07	0.22 ± 0.03
	23.9 ± 0.8	0.43 ± 0.01		
14	8.7 ± 0.7	0.28 ± 0.01	0.20 ± 0.07	0.22 ± 0.03
	23.9 ± 0.8	0.42 ± 0.01		

Table G- 9. **Data of single-stack tests of through-plane thermal conductivity for design #1 at 1,500 kPa, 29 °C, and room RH by GHF (errors: STDs for thickness, random errors for the rest of the data)**

$h_{cl,tot}$ (μm)	R_{tot} (K·W^{-1})	R''' (K·W^{-1})	$k_{cl,tp}$ (W·m^{-1}·K^{-1})
15 ± 2	0.49 ± 0.04	0.33 ± 0.05	0.26 ± 0.08
15 ± 2	0.44 ± 0.04		
15 ± 2	0.44 ± 0.05		
19 ± 2	0.49 ± 0.05		
19 ± 2	0.46 ± 0.05		
19 ± 2	0.45 ± 0.05		
22 ± 2	0.52 ± 0.04		
22 ± 2	0.50 ± 0.04		
22 ± 2	0.49 ± 0.04		
23 ± 3	0.52 ± 0.05		
23 ± 3	0.46 ± 0.05		
23 ± 3	0.47 ± 0.05		
26 ± 2	0.55 ± 0.05		
26 ± 2	0.55 ± 0.04		
26 ± 2	0.55 ± 0.05		
29 ± 2	0.56 ± 0.04		
29 ± 2	0.56 ± 0.04		
29 ± 2	0.57 ± 0.04		

Table G- 10. Data of single-stack tests of through-plane thermal conductivity for design #1 at 1,500 kPa, 29 °C, and room RH by TPS (errors: STDs for thickness, random errors for the rest of the data)

$h_{cl,tot}$ (µm)	k_{app} by arbitrary reference (W·m^{-1}·K^{-1})	R_{tot} (K·W^{-1})	R''' (K·W^{-1})	$k_{cl,tp}$ (W·m^{-1}·K^{-1})
15 ± 1	0.2213 ± 0.0007	1.916 ± 0.004	1.8 ± 0.05	0.19 ± 0.05
22 ± 2	0.2167 ± 0.0005	1.988 ± 0.004		
29 ± 2	0.216 ± 0.001	2.037 ± 0.009		
15 ± 1	0.2196 ± 0.0007	1.926 ± 0.005		
21 ± 2	0.2191 ± 0.0004	1.973 ± 0.003		
28 ± 2	0.222 ± 0.001	1.998 ± 0.007		
17 ± 1	0.2151 ± 0.0003	1.954 ± 0.002		
21 ± 2	0.216 ± 0.002	2.00 ± 0.01		
25 ± 2	0.220 ± 0.001	2.012 ± 0.007		

Table G- 11. Data of 3-stacks tests of through-plane thermal conductivity for design #1 at 1,500 kPa, 29 °C, and room RH by GHF (errors: STDs for thickness, random errors for the rest of the data)

$h_{cl,tot}$ (µm)	R_{tot} (K·W^{-1})	R''' (K·W^{-1})	$k_{cl,tp}$ (W·m^{-1}·K^{-1})
44 ± 5	0.68 ± 0.04	0.28 ± 0.05	0.21 ± 0.01
56 ± 7	0.80 ± 0.04		
67 ± 7	0.92 ± 0.05		
78 ± 7	1.02 ± 0.05		
88 ± 6	1.10 ± 0.05		

Table G- 12. Data of through-plane thermal conductivity tests by the method of different numbers of stacks for design #1 at 1,500 kPa, 29 °C, and room RH by GHF (errors: STDs for thickness, random errors for the rest of the data)

# of stacks	$h_{cl,tot}$ (μm)	R_{tot} (K·W^{-1})	R''' (K·W^{-1})	$k_{cl,tp}$ (W·m^{-1}·K^{-1})
1	29 ± 1	0.64 ± 0.04	0.37 ± 0.05	0.21 ± 0.01
2	57 ± 2	0.87 ± 0.05		
3	86 ± 4	1.21 ± 0.05		
4	114 ± 5	1.46 ± 0.06		
5	143 ± 6	1.73 ± 0.07		
6	172 ± 7	1.98 ± 0.07		

Table G- 13. Through-plane thermal conductivity tests of design #1 by GHF at different temperatures, 1,500 kPa, and uncontrolled RH (errors: STDs for thickness, random errors for the rest of the data)

T (°C)	# of stacks	$h_{cl,tot}$ (μm)	R_{tot} (K·W^{-1})	R''' (K·W^{-1})	$k_{cl,tp}$ (W·m^{-1}·K^{-1})
29	1	32 ± 1	0.60 ± 0.05	0.30 ± 0.06	0.21 ± 0.01
	6	193 ± 6	2.12 ± 0.07		
40	1	32 ± 1	0.61 ± 0.05	0.32 ± 0.07	0.22 ± 0.02
	6	193 ± 6	2.08 ± 0.08		
58	1	32 ± 1	0.56 ± 0.05	0.28 ± 0.06	0.23 ± 0.02
	6	193 ± 6	1.94 ± 0.07		
74	1	32 ± 1	0.53 ± 0.05	0.26 ± 0.06	0.24 ± 0.02
	6	193 ± 6	1.85 ± 0.06		
90	1	32 ± 1	0.50 ± 0.05	0.25 ± 0.06	0.25 ± 0.02
	6	193 ± 6	1.77 ± 0.06		

Table G- 14. Data of through-plane thermal resistance tests for stacks of one and six 50 μm thick Al foil samples at 1,500 kPa and 29 °C (errors: STDs for thickness, random errors for resistance)

Number of samples	$h_{\mathrm{Al,tot}}$ (μm)	R_{tot} (K·W^{-1})
1	50 ± 1	0.32 ± 0.04
6	300 ± 6	0.30 ± 0.04

Table G- 15. Data of single-stack tests of through-plane thermal conductivity for design #2 at 1,500 kPa, 29 °C, and room RH by GHF (errors: STDs for thickness, random errors for the rest of the data)

$h_{\mathrm{cl,tot}}$ (μm)	R_{tot} (K·W^{-1})	R''' (K·W^{-1})	$k_{\mathrm{cl,tp}}$ (W·m^{-1}·K^{-1})
12 ± 2	0.45 ± 0.05	0.36 ± 0.09	0.25 ± 0.10
11 ± 2	0.43 ± 0.05		
12 ± 2	0.43 ± 0.05		
14 ± 2	0.47 ± 0.05		
14 ± 2	0.49 ± 0.05		
12 ± 2	0.48 ± 0.05		
16 ± 1	0.55 ± 0.05		
16 ± 1	0.49 ± 0.04		
15 ± 1	0.44 ± 0.05		
16 ± 2	0.51 ± 0.05		
14 ± 2	0.49 ± 0.05		
16 ± 2	0.51 ± 0.05		
20 ± 1	0.51 ± 0.05		
22 ± 1	0.49 ± 0.04		
20 ± 1	0.50 ± 0.05		
22 ± 1	0.54 ± 0.05		
22 ± 1	0.58 ± 0.05		
24 ± 1	0.55 ± 0.04		

Table G- 16. **Data of 3-stacks tests of through-plane thermal conductivity for design #2 at 1,500 kPa, 29 °C, and room RH by GHF (errors: STDs for thickness, random errors for the rest of the data)**

$h_{cl,tot}$ (μm)	R_{tot} (K·W^{-1})	R''' (K·W^{-1})	$k_{cl,tp}$ (W·m^{-1}·K^{-1})
32 ± 5	0.56 ± 0.05	0.24 ± 0.10	0.19 ± 0.02
40 ± 5	0.69 ± 0.04		
49 ± 4	0.77 ± 0.04		
58 ± 4	0.86 ± 0.04		
68 ± 3	0.96 ± 0.05		

Table G- 17. **Data of through-plane thermal conductivity tests by the method of different numbers of stacks for design #2 at 1,500 kPa, 29 °C, and room RH by GHF (errors: STDs for thickness, random errors for the rest of the data)**

# of stacks	$h_{cl,tot}$ (μm)	R_{tot} (K·W^{-1})	R''' (K·W^{-1})	$k_{cl,tp}$ (W·m^{-1}·K^{-1})
1	16 ± 2	0.50 ± 0.03	0.30 ± 0.05	0.18 ± 0.01
2	32 ± 3	0.63 ± 0.03		
3	48 ± 5	0.83 ± 0.03		
4	63 ± 6	1.00 ± 0.03		
5	79 ± 8	1.19 ± 0.04		
6	95 ± 9	1.37 ± 0.04		

Table G- 18. **Data of single-stack tests of through-plane thermal conductivity for design #3 at 1,500 kPa, 29 °C, and room RH by GHF (errors: STDs for thickness, random errors for the rest of the data)**

$h_{cl,tot}$ (μm)	R_{tot} (K·W^{-1})	R''' (K·W^{-1})	$k_{cl,tp}$ (W·m^{-1}·K^{-1})
9 ± 2	0.41 ± 0.05	0.35 ± 0.09	0.22 ± 0.09
12 ± 2	0.40 ± 0.05		
10 ± 2	0.43 ± 0.05		
14 ± 2	0.47 ± 0.04		
13 ± 2	0.46 ± 0.04		
12 ± 2	0.48 ± 0.04		
16 ± 2	0.49 ± 0.05		
14 ± 2	0.49 ± 0.04		
12 ± 2	0.49 ± 0.04		
15 ± 1	0.45 ± 0.04		
13 ± 1	0.50 ± 0.05		
15 ± 1	0.49 ± 0.04		
17 ± 2	0.50 ± 0.04		
17 ± 2	0.50 ± 0.04		
16 ± 2	0.51 ± 0.04		
19 ± 2	0.53 ± 0.04		
18 ± 2	0.53 ± 0.04		
19 ± 2	0.50 ± 0.03		

Table G- 19. Data of 3-stacks tests of through-plane thermal conductivity for design #3 at 1,500 kPa, 29 °C, and room RH by GHF (errors: STDs for thickness, random errors for the rest of the data)

$h_{cl,tot}$ (μm)	R_{tot} (K·W^{-1})	R''' (K·W^{-1})	$k_{cl,tp}$ (W·m^{-1}·K^{-1})
30 ± 7	0.63 ± 0.04	0.24 ± 0.10	0.16 ± 0.02
37 ± 6	0.71 ± 0.04		
43 ± 5	0.80 ± 0.04		
50 ± 5	0.85 ± 0.04		
56 ± 5	0.96 ± 0.04		

Table G- 20. Data of through-plane thermal conductivity tests by the method of different numbers of stacks for design #3 at 1,500 kPa, 29 °C, and room RH by GHF (errors: STDs for thickness, random errors for the rest of the data)

# of stacks	$h_{cl,tot}$ (μm)	R_{tot} (K·W^{-1})	R''' (K·W^{-1})	$k_{cl,tp}$ (W·m^{-1}·K^{-1})
1	15 ± 1	0.52 ± 0.03	0.32 ± 0.04	0.15 ± 0.01
2	29 ± 3	0.70 ± 0.03		
3	44 ± 4	0.87 ± 0.04		
4	59 ± 6	1.08 ± 0.04		
5	73 ± 7	1.29 ± 0.04		
6	88 ± 9	1.46 ± 0.04		

Table G- 21. Data of through-plane thermal conductivity tests by the method of different numbers of stacks (only the first and last data points are shown here) for all the CL designs at 1,500 kPa, 29 °C, and room RH by GHF (errors: STDs for thickness, random errors for the rest of the data)

Design #	I/C ratio	Dry milling time (hr)	Drying temperature (°C)	$h_{\mathrm{cl,tot}}$ (µm)	R_{tot} (K·W^{-1})	$k_{\mathrm{cl,tp}}$ (W·m^{-1}·K^{-1})
1	1.1	0	55	29 ± 1	0.64 ± 0.04	0.21 ± 0.01
				172 ± 7	1.98 ± 0.07	
2	0.7	48	55	16 ± 2	0.50 ± 0.03	0.18 ± 0.01
				95 ± 9	1.37 ± 0.04	
3	0.9	48	55	15 ± 1	0.52 ± 0.03	0.15 ± 0.02
				88 ± 9	1.46 ± 0.04	
4	0.7	24	55	40 ± 1	0.98 ± 0.06	0.24 ± 0.04
				127 ± 5	1.70 ± 0.08	
5	1.1	48	55	9 ± 2	0.52 ± 0.05	0.07 ± 0.02
				55 ± 11	1.75 ± 0.07	
6	0.9	24	55	14 ± 2	0.52 ± 0.04	0.19 ± 0.03
				82 ± 10	1.22 ± 0.05	
7	1.1	48	24	10 ± 3	0.63 ± 0.04	0.07 ± 0.03
				58 ± 20	1.97 ± 0.09	
8	1.1	0	24	16.2 ± 0.4	0.54 ± 0.04	0.20 ± 0.02
				97.2 ± 2.4	1.33 ± 0.05	

Appendix H.

Data of the Electrical Tests

Table H- 1. **Data of calibration check of the micro-ohm meter and the in-plane sample holder, using standard resistors (errors: random errors)**

Nominal resistance of standard resistor (Ω)	Measured resistance of standard resistor by direct connection (Ω)	Measured resistance of standard resistor in the in-plane sample holder (Ω)
0.01	0.00979 ± 0.00008	0.00982 ± 0.00007
0.1	0.10115 ± 0.00009	0.10140 ± 0.00006
1	0.9980 ± 0.0003	0.9987 ± 0.0001
10	9.9483 ± 0.0006	9.9467 ± 0.0006
100	97.08 ± 0.01	97.127 ± 0.006
1000	997 ± 0	997.03 ± 0.06
10000	9990.3 ± 0.6	9989.7 ± 0.6
100000	99740 ± 50	99710 ± 10

Table H- 2. **Data of calibration check of the in-plane sample holder by measuring strips of a 50 μm thick Al foil with 1 cm width (errors: STDs for probing length, random errors for the rest of the data)**

Len_{Al} (mm)	R_{tot} (mΩ)	ECR (mΩ)	σ_{Al} / 10^6 (S·m^{-1})
300 ± 1	18.3 ± 0.1	0.5 ± 0.1	34 ± 4
250 ± 1	15.5 ± 0.2		
200 ± 1	12.4 ± 0.1		
150 ± 1	9.4 ± 0.2		
100 ± 1	6.4 ± 0.1		
50 ± 1	3.5 ± 0.1		

Table H- 3. Data of two-samples tests of through-plane electronic conductivity for design #2 at 1,500 kPa, 21 °C, and room RH (errors: STDs for thickness, random errors for the rest of the data)

$h_{cl,tot}$ (μm)	R_{tot} (Ω)	R'''' (Ω)	$\sigma_{cl,tp}$ ($S \cdot m^{-1}$)
5.4 ± 0.8	0.28 ± 0.02	0.21 ± 0.03	0.16 ± 0.03
5.4 ± 0.8	0.26 ± 0.01		
5.4 ± 0.8	0.279 ± 0.008		
8 ± 2	0.310 ± 0.002		
8 ± 2	0.287 ± 0.003		
8 ± 2	0.311 ± 0.005		
12 ± 1	0.362 ± 0.004		
12 ± 1	0.345 ± 0.001		
12 ± 1	0.327 ± 0.007		
11 ± 3	0.337 ± 0.004		
11 ± 3	0.37 ± 0.02		
11 ± 3	0.373 ± 0.005		
15 ± 2	0.445 ± 0.010		
15 ± 2	0.411 ± 0.005		
15 ± 2	0.395 ± 0.003		
19 ± 1	0.447 ± 0.003		
19 ± 1	0.41 ± 0.01		

Table H- 4. **Data of six-samples tests of through-plane electronic conductivity for design #2 at 1,500 kPa, 21 °C, and room RH (error bars: STDs for thickness, random errors for the rest of the data)**

$h_{cl,tot}$ (μm)	R_{tot} (Ω)	R'''' (Ω)	$\sigma_{cl,tp}$ (S·m^{-1})
16 ± 2	0.76 ± 0.01	0.62 ± 0.07	0.18 ± 0.03
24 ± 5	0.93 ± 0.03		
34 ± 5	1.00 ± 0.01		
44 ± 6	1.09 ± 0.01		
56 ± 4	1.24 ± 0.03		

Table H- 5. **Data of in-plane electronic conductivity measurements of design #1 by measuring CL srtips with 1 cm width at 21 °C and room RH (errors: STDs for probing length, random errors for the rest of the data)**

Len_{cl} (mm)	R_{tot} (kΩ)	ECR (kΩ)	$\sigma_{cl,ip}$ (S·m^{-1})
58 ± 1	1.560 ± 0.006	0.01 ± 0.02	526 ± 36
48 ± 1	1.3092 ± 0.0004		
38 ± 1	1.0298 ± 0.0008		
28 ± 1	0.7605 ± 0.0004		
18 ± 1	0.49433 ± 0.00008		

Table H- 6. **Data of two-samples tests of through-plane electronic conductivity for design #1 at different pressures, 29 °C, and room RH (errors: STDs for thickness, random errors for the rest of the data)**

P (bar)	$h_{\mathrm{cl,tot}}$ (µm)	R_{tot} (Ω)	R'''' (Ω)	$\sigma_{\mathrm{cl,tp}}$ (S·m^{-1})
3	15.2 ± 0.8	0.377 ± 0.004	0.32 ± 0.06	0.6 ± 0.1
	29 ± 1	0.424 ± 0.009		
6	15.2 ± 0.8	0.359 ± 0.004	0.31 ± 0.05	0.6 ± 0.1
	29 ± 1	0.405 ± 0.007		
9	15.2 ± 0.8	0.345 ± 0.004	0.30 ± 0.05	0.6 ± 0.1
	29 ± 1	0.389 ± 0.006		
12	15.2 ± 0.8	0.332 ± 0.002	0.28 ± 0.05	0.6 ± 0.1
	29 ± 1	0.375 ± 0.006		
15	15.2 ± 0.8	0.322 ± 0.003	0.28 ± 0.05	0.6 ± 0.1
	29 ± 1	0.363 ± 0.006		

Table H- 7. **Data of twelve-samples tests of through-plane electronic conductivity for design #1 at different temperatures, 1,500 kPa, and uncontrolled RH (errors: STDs for thickness, random errors for the rest of the data)**

T (°C)	$h_{\mathrm{cl,tot}}$ (µm)	R_{tot} (Ω)	R'''' (Ω)	$\sigma_{\mathrm{cl,tp}}$ (S·m^{-1})
22	89 ± 4	1.77 ± 0.02	1.5 ± 0.2	0.58 ± 0.09
	172 ± 7	2.05 ± 0.02		
43	89 ± 4	1.69 ± 0.02	1.4 ± 0.2	0.59 ± 0.08
	172 ± 7	1.97 ± 0.02		
62	89 ± 4	1.58 ± 0.02	1.3 ± 0.2	0.66 ± 0.09
	172 ± 7	1.82 ± 0.02		
79	89 ± 4	1.49 ± 0.01	1.2 ± 0.2	0.7 ± 0.1
	172 ± 7	1.72 ± 0.02		

Table H- 8. Data of through-plane electronic conductivity tests for all the CL designs at 1,500 kPa, 21 °C, and room RH (errors: STDs for thickness, random errors for the rest of the data)

Design #	I/C ratio	Dry milling time (hr)	Drying temperature (°C)	# of CL samples in the stack	$h_{\mathrm{cl,tot}}$ (µm)	R_{tot} (Ω)	$\sigma_{\mathrm{cl,tp}}$ (S·m^{-1})
1	1.1	0	55	12	88 ± 4	1.77 ± 0.01	0.6 ± 0.1
					172 ± 7	2.05 ± 0.03	
2	0.7	48	55	6	16 ± 2	0.76 ± 0.01	0.18 ± 0.03
					56 ± 4	1.24 ± 0.03	
3	0.9	48	55	6	30 ± 7	0.58 ± 0.02	0.10 ± 0.03
					56 ± 5	1.09 ± 0.04	
4	0.7	24	55	12	78 ± 2	2.47 ± 0.02	0.25 ± 0.03
					127 ± 5	2.86 ± 0.01	
5	1.1	48	55	12	53 ± 5	0.90 ± 0.01	0.06 ± 0.02
					76 ± 6	1.61 ± 0.04	
6	0.9	24	55	12	82 ± 2	2.24 ± 0.01	0.09 ± 0.02
					109 ± 5	2.83 ± 0.04	
7	1.1	48	24	12	31 ± 2	1.18 ± 0.04	0.027 ± 0.004
					58 ± 4	3.15 ± 0.03	
8	1.1	0	24	24	101 ± 5	2.59 ± 0.06	0.6 ± 0.1
					194 ± 5	2.93 ± 0.02	

Table H- 9. Data of in-plane electronic conductivity tests for all the CL designs at 21 °C and room RH (errors: STDs for thickness, random errors for the rest of the data)

Design #	I/C ratio	Dry milling time (hr)	Drying temperature (°C)	*Len*$_{cl}$ (mm)	*R*$_{tot}$ (kΩ)	$\sigma_{cl,ip}$ (S·m^{-1})
1	1.1	0	55	58 ± 1	1.560 ± 0.006	526 ± 36
				18 ± 1	0.49433 ± 0.00008	
2	0.7	48	55	58 ± 1	7.03 ± 0.04	160 ± 14
				18 ± 1	2.57 ± 0.04	
3	0.9	48	55	58 ± 1	5.02 ± 0.01	265 ± 20
				18 ± 1	1.893 ± 0.003	
4	0.7	24	55	58 ± 1	6.535 ± 0.004	192 ± 21
				18 ± 1	2.078 ± 0.007	
5	1.1	48	55	58 ± 1	2.955 ± 0.008	407 ± 98
				18 ± 1	0.94 ± 0.01	
6	0.9	24	55	58 ± 1	4.25 ± 0.02	313 ± 31
				18 ± 1	1.424 ± 0.003	
7	1.1	48	24	58 ± 1	19.33 ± 0.07	68 ± 20
				18 ± 1	6.41 ± 0.01	
8	1.1	0	24	58 ± 1	1.55 ± 0.01	501 ± 38
				18 ± 1	0.4936 ± 0.0003	

Appendix I.

Derivation of Porosity of Agglomerate Clusters

Porosity of the agglomerate clusters around the micropores, $\varepsilon_{\mathrm{ac}}$ in Eq. (6.24), is defined as the ratio of volume of pores inside the mesoscale unit cell to total volume of the mesoscale unit cell or, equivalently, one minus the ratio of volume of solid parts of the mesoscale unit cell to the total volume of the mesoscale unit cell as follows:

$$\varepsilon_{\mathrm{ac}} = 1 - \frac{V_{\mathrm{Pt}} + V_{\mathrm{C}} + V_{\mathrm{ion}}}{V_{\mathrm{meu}}} = 1 - \frac{n_{\mathrm{Pt}}\frac{4}{3}\pi r_{\mathrm{Pt}}^{3} + n_{\mathrm{C}}\frac{4}{3}\pi r_{\mathrm{C}}^{3}(1-\varepsilon_{\mathrm{C}}) + h_{\mathrm{ion}}(2A_{\mathrm{ion}})}{\left[2\left(r_{\mathrm{agg}} - \omega_{\mathrm{agg}}\right)\right]^{3}} \tag{I.1}$$

where n_{Pt} and n_{C} are the number of platinum particles and the number of carbon particles inside an agglomerate, respectively, ε_{C} is the porosity of each individual carbon particle, A_{ion} is the surface area of ionomer on half of an aggregate (see Eq. (6.27)), and ω_{agg} is the overlap depth of the aggregates (see Figure A-1).

Having the relation for h_{ion} from Eq. (J.3), the relation between n_{Pt} and n_{C} from Eq. (J.1), the relation for n_{C} from Eq. (J.4), and the geometrical relations of the aggregates from Eqs. (A.1) and (A.2), the relation for $\varepsilon_{\mathrm{ac}}$ becomes:

$$\begin{aligned}\varepsilon_{\mathrm{ac}} = 1 - \sqrt{2}\pi^{2}(1-\varepsilon_{\mathrm{C}})&\left[1 + l_{\mathrm{Pt/C}}\frac{\rho_{\mathrm{C}}}{\rho_{\mathrm{Pt}}} + \frac{\rho_{\mathrm{C}} l_{\mathrm{ion}}\left(1 + l_{\mathrm{Pt/C}}\right)}{\rho_{\mathrm{ion}}(1 - l_{\mathrm{ion}})}\right] \\ &\times \frac{\left\{\frac{4}{3} - \left[1 - \cos\left(\frac{\theta_{\mathrm{agg}}}{2}\right)\right]\left(3\sin^{2}\left(\frac{\theta_{\mathrm{agg}}}{2}\right) + \left[1 - \cos\left(\frac{\theta_{\mathrm{agg}}}{2}\right)\right]^{2}\right)\right\}}{48\cos^{3}\left(\frac{\theta_{\mathrm{agg}}}{2}\right)}\end{aligned} \tag{I.2}$$

where θ_{agg} is the overlap angle of the aggregates (see Figure A-1).

Appendix J.

Derivation of Thickness of the Ionomer Film around the Aggregates

Relation for ionomer thickness, h_{ion}, is obtained from the CL composition defined by its platinum and ionomer loadings. The platinum loading, denoted by $l_{\mathrm{Pt/C}}$, and the ionomer loading, denoted by l_{ion}, are defined as:

$$l_{\mathrm{Pt/C}} = \frac{m_{\mathrm{Pt}}}{m_{\mathrm{C}}} = \frac{\rho_{\mathrm{Pt}} n_{\mathrm{Pt}} \frac{4}{3}\pi r_{\mathrm{Pt}}^3}{\rho_{\mathrm{C}} n_{\mathrm{C}} \frac{4}{3}\pi r_{\mathrm{C}}^3 (1-\varepsilon_{\mathrm{C}})} = \left(\frac{1}{1-\varepsilon_{\mathrm{C}}}\right)\left(\frac{\rho_{\mathrm{Pt}}}{\rho_{\mathrm{C}}}\right)\left(\frac{n_{\mathrm{Pt}}}{n_{\mathrm{C}}}\right)\left(\frac{r_{\mathrm{Pt}}}{r_{\mathrm{C}}}\right)^3 \tag{J.1}$$

$$l_{\mathrm{ion}} = \frac{m_{\mathrm{ion}}}{m_{\mathrm{ion}} + m_{\mathrm{Pt}} + m_{\mathrm{C}}} = \frac{\rho_{\mathrm{ion}} h_{\mathrm{ion}} (2A_{\mathrm{ion}})}{\rho_{\mathrm{ion}} h_{\mathrm{ion}} (2A_{\mathrm{ion}}) + \rho_{\mathrm{Pt}} n_{\mathrm{Pt}} \frac{4}{3}\pi r_{\mathrm{Pt}}^3 + \rho_{\mathrm{C}} n_{\mathrm{C}} \frac{4}{3}\pi r_{\mathrm{C}}^3 (1-\varepsilon_{\mathrm{C}})} \tag{J.2}$$

where n_{Pt} and n_{C} are the number of platinum particles and the number of carbon particles in an aggregate, respectively, and ε_{C} is the porosity of each individual carbon particle. By combining Eqs. (J.1) and (J.2), the following relation is obtained for h_{ion}:

$$h_{\mathrm{ion}} = \frac{4\pi \rho_{\mathrm{C}} n_{\mathrm{C}} r_{\mathrm{C}}^3 l_{\mathrm{ion}} \left(1 + l_{\mathrm{Pt/C}}\right)(1-\varepsilon_{\mathrm{C}})}{3\rho_{\mathrm{ion}} (2A_{\mathrm{ion}})(1 - l_{\mathrm{ion}})} \tag{J.3}$$

where n_{C} can be obtained by dividing the volume of an aggregate (see Figure A-1) by the volume of a nanoscale unit cell (see Figure 6-1) and then multiplying the result by the number of carbon particles in the unit cell. Noting that a nanoscale unit cell contains four one-eighth particles in an FCC arrangement (see Figure 6-4), n_{C} could be obtained as:

$$n_{\mathrm{C}} = \frac{\frac{4}{3}\pi r_{\mathrm{agg}}^3 - \frac{\pi}{6}\omega_{\mathrm{agg}}\left(3a_{\mathrm{agg}}^2 + \omega_{\mathrm{agg}}^2\right) \times 6}{\left(\sqrt{2} r_{\mathrm{C}}\right)^3} \times \frac{1}{2} \tag{J.4}$$